Hydroformylation of alkenes using "heterogenized" complexes of rhodium

By

Cornelia Maria Joubert

A dissertation in fulfilment of the requirement of the degree of PhD in Chemistry in the Department of Chemistry and Polymer Science, University of Stellenbosch

Supervisor: Prof. S.F. Mapolie

December 2018

Declaration

By submitting this thesis electronically, I declare that the entirety of the work contained therein is my own, original work, that I am the authorship owner thereof (unless to the extent explicitly otherwise stated) and that I have not previously in its entirety or in part submitted it for obtaining any qualification.

December 2018

Abstract

This thesis describes the synthesis of a range of siloxane functionalized rhodium complexes with chelating ligands. The complexes were immobilized onto mesoporous silica, thereby producing novel MCM-41 and SBA-15 immobilized rhodium catalysts that could be applied in the hydroformylation of alkenes.

Neutral and cationic model and siloxane functionalized complexes containing the Schiff base ligand scaffolds N-(2-diphenylphosphino)benzylidene-alkylamine, N-(2-pyridinylmethylene)-1-alkylimine and N-alkylsalicylaldimine (where alkyl equals n-propyl or 3-(triethoxysilyl)propyl-) were prepared by reacting the appropriate ligand with the rhodium precursors $[RhCl(CO)_2]_2$ or $[RhCl(COD)]_2$. These ligands differed with regard to the chelating atoms utilized. Ligands with N,P, N,N and N,O chelating units were synthesized. Analogous cationic complexes were prepared using 2-(1-alkyl-1*H*-1,2,3-triazol-4-yl)pyridine, where alkyl equals octyl or 3-(triethoxysilyl)propyl as chelating ligands. The ligands were prepared by using copper-assisted azide-alkyne Huisgen cycloaddition.

The complexes were characterized by Fourier transform infrared spectroscopy, nuclear magnetic resonance (NMR) (^{1}H, ^{13}C and ^{31}P) spectroscopy, mass spectrometry analysis and elemental analysis. During characterization of the complexes by ^{1}H NMR, two unusual phenomena were observed which were further investigated using advanced NMR techniques. Firstly, an unusually large shift of the imine signal in the ^{1}H NMR spectrum of the cationic N,N Schiff base complex was shown to be due to close ion-pairing of the complex with the tetraphenylborate counter-ion in chloroform. The ion-pairing effect as well as the influence of the solvent was investigated using nuclear Overhauser spectroscopy, heteronuclear Overhauser spectroscopy, and diffusion ordered spectroscopy. Secondly, a chemical exchange process involving the olefinic protons of the 1,5-cyclooctadiene ligand on the cationic N,N Schiff base complex and the pyridyl-triazole complex was investigated using variable temperature NMR as well as some computational methods. The dynamic behaviour was tentatively attributed to the breaking a metal-ligand bond and subsequent rotation of the ligand around the remaining bond.

The immobilized complexes were characterized by a range of solid-state techniques namely Fourier transform infrared spectroscopy, nitrogen adsorption/desorption surface analysis, powder X-ray diffraction, scanning and transmission electron microscopy, inductively coupled plasma optical emission spectroscopy (ICP-OES), and solid-state ^{29}Si NMR. These analyses gave insight into the chemical and physical properties of the immobilized catalysts. The metal loading of the immobilized systems were determined using ICP-OES, and this allowed for the

rhodium loadings during catalysis being kept constant. In this way was therefore possible to compare the model and immobilized systems directly.

The model complexes and their immobilized counterparts were applied as catalyst precursors in the hydroformylation of 1-octene. The conversion and selectivity of the reaction were found to be influenced by reaction parameters such as temperature and pressure, with an increase in pressure leading to an increase in both conversion and aldehyde selectivity. In general it was observed that the model catalysts gave moderate conversions, with the pyridyl-triazole complex converting 85% of the starting material after 2 hours. The cationic complexes were generally more active than the neutral complexes, likely due to the metal centre on the cationic complexes being more electron deficient, leading to faster alkene coordination. Initially, a high selectivity towards internal octenes was obtained in these reactions. This is due to the rapid rate of isomerization mediated by these catalysts. As the reactions progressed, the internal octenes were hydroformylated to give branched aldehydes, leading to an increase in aldehyde selectivity with a concomitant decrease in aldehyde regioselectivity. The highest regioselectivity obtained was a ratio of nonanal to 2-methyloctanal of 3 to 1, using the neutral Schiff base chlorocarbonyl complex. The complexes were therefore not very regioselective.

The immobilized catalysts gave higher activity than their model counterparts in all cases, with only slight differences being observed between the immobilized MCM-41 and SBA-15 systems. The recyclability of the systems were however poor, with dramatic losses in turnover number being observed upon the re-use of the catalysts. The filtrate obtained after recovering the solid catalysts was analyzed by ICP-OES and it was found that the rhodium leaching was quite significant, which explained the loss of activity.

From some preliminary mechanistic studies it was found that the replacement of the 1,5-cyclooctadiene ligand on the cationic N,N Schiff base complex by two carbonyl ligands occurred within seconds at room temperature and atmospheric pressure. Attempts to observe the rhodium hydride (a known step in the hydroformylation reaction mechanism) using high-pressure ^{1}H NMR was unsuccessful, leading to the conclusion that the rhodium hydride species was either present only in low abundance or that it had a relatively short life-time. When the complex was heated in a high-pressure NMR tube in the presence of 30 bar syngas and 1-octene, the disappearance of the terminal alkene proton signals and the formation of new signals in the aldehyde region could be observed in the ^{1}H NMR spectrum over a time period of two hours, confirming the formation of major hydroformylation products.

Opsomming

Hierdie tesis beskryf die sintese van ‘n reeks siloksaan-gefunksioneerde rhodiumkomplekse met chelerende ligande. Die komplekse is op mesoporieuse silika geïmmobiliseer en op so ‘n manier is nuwe MCM-41 en SBA-15 geïmmobiliseerde katalisatore wat in die hidroformilering van alkene toegepas kon word geproduseer.

Neutrale en kationiese model en siloksaan-gefunksioneerde komplekse gebasseer op die Schiff basis ligand raamweke N-(2-difenielfosfien)bensielidien-alkielamien, N-(2-pyridienmetileen)-1-alkielamine en N-alkielsalisielaldimien (waar alkiel wys na n-propiel of 3-(triëtoksiesiliel)propiel-) is berei deur die gepaste ligand met òf $[RhCl(CO)_2]_2$ òf $[RhCl(COD)]_2$ te reageer. Die ligande verskil ten opsigte van die chelaatatome wat in die struktuur teenwoordig is. Ligande met N,P, N,N en N,O chelaatsisteme is gesintetiseer. Kationiese komplekse is berei deur 2-(1-alkiel-1*H*-1,2,3-triasool-4-iel)piridien, waar alkiel wys na oktiel of 3-(triëtoksiesiliel)propiel, as chelaat-ligande te gebruik. Die ligande is berei deur koper-aangedrewe asied-alkyn Huisgen siklo-addisie.

Die komplekse is gekarakteriseer deur van FT-IR spektroskopie, KMR (^{1}H, ^{13}C en ^{31}P) spektroskopie, ESI-MS en mikroanalise gebruik te maak. Tydens die karakterisering van die komplekse deur ^{1}H KMR is daar twee onverwagse verskynsels, naamlik ‘n onverwags groot verskuiwing van die imien-sein in die ^{1}H KMR spektrum van die kationiese N,N Schiff basis komples asook ‘n opmerklike verskil tussen die vorms van die 1,5-siklo-oktadiëen olefien protone in die kationiese Schiff basis N,N kompleks en die piridieltriasool kompleks se sein in die ^{1}H KMR, opgelet. Gevorderde KMR tegnieke is gebruik om die bogenoemde te ondersoek. Daar is gewys dat eersgenoemde te danke was aan intieme ioonparing tussen die katioon en die tetrafenielboraat teenioon in chloroform. Beide die ioonparingseffek en die invloed van die oplosmiddel is deur NOESY, HOESY en DOSY eksperimente ondersoek. Die tweede verskynsel was ‘n chemiese uitruilingsproses, waarby die olefien-protone van die 1,5-siklo-oktadiëen ligand in die kationiese Schiff basis N,N kompleks en die piridiel-triasoolkompleks betrokke was. Hierdie is deur veranderlike temperatuur KMR en berekeningsmetodes ondersoek. Die dinamiese gedrag is aan die splitsing van ‘n ligand-metaal binding en daaropvolgende rotasie van die ligand om die oorblywende binding toegeskryf.

Die geïmmobiliseerde komplekse is deur ‘n reeks vaste fase tegnieke naamlik FT-IR, stikstof adsorbsie/desorpsie oppervlakanalise, poeier X-straal diffraksie, skandeer- en transmissie-elektronmikroskopie, IKP-OES en vastetoestand ^{29}Si KMR gekarateriseer. Hierdie analises het meer insig oor die chemiese en fisiese eienskappe van die geïmmobiliseerde katalisatore verskaf. Die hoeveelheid metaal in die geïmmobiliseerde sisteme is deur ICP-OES bepaal, en

sodoende was dit moontlik om die rhodiumladings tydens katalitiese reaksies konstant te hou. Op hierdie manier was dit dus moontlik om die model en geïmmobiliseerde sisteme direk (by dieselfde metaalkonsentrasie) te vergelyk.

Die modelkomplekse en hulle geïmmobiliseerde ewekniëe is as katalisator-voorlopers in die hidroformilering van 1-okteen gebruik. Daar is gevind dat die omsetting en selektiwiteit van die reaksie beïnvloed kon word deur reaksieparameters soos temperatuur en druk. ‘n Verhoging in druk lei byvoorbeeld tot ‘n hoër omsetting en aldehied-selektiwiteit. Oor die algemeen is daar gesien dat die modelkatalisatore matige omsetting gee, met die piridiel-triasoolkompleks wat 85% van die 1-okteen na 2 ure na produkte omgeskakel het. Die kationiese komplekse was oor die algemeen meer aktief as die neutral komplekse, waarskynlik as gevolg van die feit dat die metaal in die kationiese komplekse minder elektronryk is en dat die koördinering van die alkeen dus vinniger kan plaasvind. Aanvanklik is daar meer interne oktene gevorm in hierdie reaksies. Met verloop van tyd word die interne oktene gehidroformileer na vertakte aldehiede, wat gelei het tot ‘n hoër aldehied-selektiwiteit en te gelyketyd tot ‘n afname in regioselektiwiteit. Die hoogste regioselektiwiteit wat verkry is (met die gebruik van die neutrale chloorkarboniel Schiff basis kompleks), was ‘n verhouding van nonanal tot 2-metieloktanaal van 3 tot 1. Die komplekse toon dus nie hoë regioselektiwiteit nie.

Die geïmmobiliseerde katalisatore het hoër aktiwiteit as hulle model-ewekniëe getoon, alhoewel daar slegs klein verskille tussen die geïmmobiliseerde MCM-41 en SBA-15 sisteme. Die herwinbaarheid van die sisteme was egter teleurstellend in dat groot afnames in die omsettingsgetal gesien is met die hergebruik van die katalisatore. Na die vastetoestand katalisatore herwin is, is die filtraat deur IKP-OES geanaliseer en daar is gevind dat ‘n beduidende hoeveelheid van die rhodium uitgeloog is. Die afname in aktiwiteit kan dus hieraan toegeskryf word.

Vanaf voorlopige meganistiese studies is daar gesien dat die verplasing van die 1,5-siklo-oktadiëenligand op die kationiese Schiff basis N,N kompleks met twee karbonielligande baie maklik was en dat dit binne sekondes by kamertemperatuur en atmosferiese druk gebeur. Pogings om die rhodiumhidried (‘n bekende stap in die hidroformuleringsmeganisme) met hoë-druk KMR waar te neem was onsuksesvol, wat tot die gevolgtrekking gelei het dat die hidried spesie òf in lae konsentrasies teenwoordig was, òf dat die spesie ‘n relatiewe kort leeftyd het. Wanneer die kompleks die kationiese Schiff basis N,N kompleks in ‘n hoë-druk KMR buis in die teenwoordigheid van 30 bar sintese-gas en 1-okteen verhit is, kon die verdwyning van die terminale alkeen se protonseine, asook die vorming van nuwe seine in die

aldehied-omgewing in die ^{1}H KMR spektrum oor ‘n tydperk van twee ure opgemerk word, wat die vorming van hidroformuleringsprodukte bevestig het.

Acknowledgements

Firstly, I want to thank my supervision, Prof. Selwyn Mapolie, for his guidance, support and patience throughout the pursuit of this degree. Thanks for providing direction when I needed it, and for guiding me to ask the interesting questions.

I would also like to thank my colleagues, past and present, of the Organometallic Research Group at Stellenbosch University: Drs. Hennie Kotzé, Andrew Swarts and Angelique Blanckenberg, Derik Wilbers, Jacquin October, Cassiem Joseph, Ené Slazus, Annick van Niekerk and Laura Leckie for the many interesting discussions, willingness to help and countless memorable moments whether in the lab, at Bosberaad or at CATSA.

The support staff of the Inorganic Chemistry building, namely Sylette, Malcolm, Johnny, Chalon, Moebarik, Jabu and Peta provided invaluable assistance during the time I spent in the building. Thank you for always helping out with a smile.

I would like to thank the staff of the Central Analytical Facility at the University of Stellenbosch for assisting with various analytical techniques. I would also like to thank Dr. Izak Kotze from the University of Witwatersrand for assistance with 2D NMR techniques.

Financial support from the DST-NRF through the c*change Centre for Excellence in Catalysis is greatly appreciated. I would also like to thank c*change for fostering a community of young catalysis scientists in South Africa.

Thanks to my friends and family for their encouragement and support during the years.

Lastly I would like to thank my husband, Jedri, for his support throughout this project. Thank you for always allowing me to bounce ideas off of you and for asking (insightful) questions that no self-respecting chemist would think of asking.

Conference Contributions

Corli Joubert and Prof S.F. Mapolie

Poster presentation titled: ***New siloxane functionalized rhodium complexes for application as hydroformylation catalysts***

Catalysis Society of South Africa (CATSA), Port Edward (Wild Coast Sun), South Africa, 2013

Corli Joubert and Prof S.F. Mapolie

Poster presentation titled: ***New siloxane functionalized rhodium complexes and their application as catalysts in the hydroformylation of 1-octene***

Catalysis Society of South Africa (CATSA), Johannesburg (St. George's Hotel), South Africa, 2014

Corli Joubert and Prof S.F. Mapolie

Poster presentation titled: ***The application of new siloxane functionalized rhodium complexes in the hydroformylation of 1-octene***

Catalysis Society of South Africa (CATSA), Hermanus (Arabella Hotel and Spa), South Africa, 2015

Corli Joubert and Prof S.F. Mapolie

Oral presentation titled: ***Counter-ion effect on the behaviour of silica supported cationic rhodium complexes as hydroformylation catalysts***

Catalysis Society of South Africa (CATSA), Cathkin Park (Champagne Sports Resort), South Africa, 2016

Table of Contents

List of Figures

Chapter 1

Chapter 2

Chapter 5

List of Schemes

Chapter 1

Chapter 2

Chapter 3

List of Tables

Chapter 2

Chapter 3

Chapter 4

Chapter 5

Abbreviations

δ	chemical shift
γ	gyromagnetic ratio
Å	Angstrom
acac	acetylacetone
ATR	attenuated total reflectance
BDA	bis-3,4-diazaphospholane
BET	Brunauer-Emmett-Teller
BJH	Barret-Joyner-Halenda
BMI	1-*n*-butyl-3-methylimidazolium
cm^{-1}	wavenumber
CTAB	cetyltrimethylammonium bromide
COD	1,5-cyclooctadiene
d	doublet
DAB	1,4-aminobutane
DCM	dichloromethane
DMSO	dimethyl sulfoxide
DOSY	diffusion ordered spectroscopy
ESI-MS	electrospray ionization mass spectrometry
FT-IR	Fourier transform infrared spectroscopy
h	hour
GC-FID	gas chromatography with flame ionization detector
HOESY	heteronuclear nuclear Overhauser effect spectroscopy
Hz	Hertz
ICP-OES	inductively coupled plasma optical emission spectroscopy

m	multiplet
m/z	mass-to-charge ratio
MAS	magic angle spinning
MCM	Mobil crystalline material
Mhz	megahertz
mL	milliliters
min	minute(s)
mol	mole
mmol	millimole
mPa	millipascal
n:iso	normal to iso
nm	nanometer
NMR	nuclear magnetic resonance
NOESY	nuclear Overhause effect spectroscopy
P/P_0	relative pressure
PEG	polyethylene glycol
Ph	phenyl
PEI	polyethyleneimine
PHP	poly-*N,N*-diallyl-*N*-methylaminodihydrophosphate
PGSE	pulse gradient spin-echo
PPh_3	triphenylphosphine
ppm	chemical shift
q	quartet
RGO	reduced graphene oxide
s	singlet
SBA	Santa Barbara amorphous

SEM	scanning electron microscopy
t	triplet
TEM	transmission electron microscopy
TEOS	tetraethylorthosilicate
TGA	thermal gravimetric analysis
THF	tetrahydrofuran
TPPTS	tri(*m*-sulfonyl)triphenylphosphine
TOF	turnover frequency
TON	turnover number
V	volt
W	Watt
WPC	water-soluble poly-*N,N*-diallyl-*N,N*-dimethylammonium chloride
XRD	X-ray diffraction

CHAPTER 1 : THE USE OF IMMOBILIZED CATALYSTS IN THE HYDROFORMYLATION REACTION

1.1 Hydroformylation

Hydroformylation, also known as the oxo process, was discovered in 1938 by Otto Roelen while he was doing research in the area of Fischer-Tropsch synthesis.[1,2] This reaction is catalysed by transition metal complexes and involves the *cis* addition of carbon monoxide and hydrogen to an olefin substrate to yield aldehydes in one-step fashion with 100% atom economy and is shown in Scheme 1.1.[3]

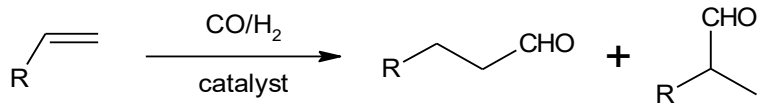

Scheme 1.1 The hydroformylation reaction.

The hydroformylation reaction is one of the most important applications of homogeneous catalysis in the chemical industry today.[4,5] The reaction was initially mainly applied to bulk synthesis of short-chain aldehydes, but the demand for the production of new aldehydes, mainly derived from long-chain olefins, as precursors for high-value chemicals is growing.[6–9]

Cobalt was the first transition metal that was used to catalyze the hydroformylation reaction.[1] Some early research was conducted on the effect of various additives and ligands on the cobalt-catalyzed reaction.[10–12] In 1965 Wilkinson and co-workers described the use of rhodium to catalyze the hydrogenation reaction, and soon after they reported the first use of rhodium as a hydroformylation catalyst.[13,14] Since then the majority of research effort has been focused on improving the rhodium-catalyzed hydroformylation reaction in terms of activity and selectivity by designing new ligand systems.[15–20] Complexes based on alternative metals, mainly ruthenium and iridium, have also been studied as hydroformylation catalysts, but at this stage none of these systems display comparable activity to that of the rhodium systems.[21-23]

1.2 Immobilization of catalysts

The chief problem that is still encountered when using homogeneous catalysts is the issue of removing the catalyst from the product stream. Successful removal of the catalyst will not only result in obtaining a cleaner product, but will also allow the catalyst to be re-used, thus reducing the overall cost of the process.[24–26] One strategy for achieving this goal is the immobilization of homogeneous catalysts onto solid supports. It is envisioned that, in this way, the often superior activity and selectivity of homogeneous catalysts could be retained, while permanent immobilization onto the support will allow for the catalysts to be recovered and re-used.[27] Practically many of these so-called “heterogenized” systems suffer from reduced activity and catalyst deactivation due to the metal leaching from the support.

Many different supports, both organic and inorganic, have been studied over the years. Most of these supports have several properties in common such as chemical, thermal and mechanical stability and high surface areas.[2] A number of examples of the use of supported hydroformylation catalysts will be discussed.

1.2.1 Organic Supports

1.2.1.1 Dendrimers

Dendrimers are monodispersed, highly symmetrical macromolecules with key features such as a core, branching points and terminal groups, as shown in Figure 1.1, which can be modified.[28]

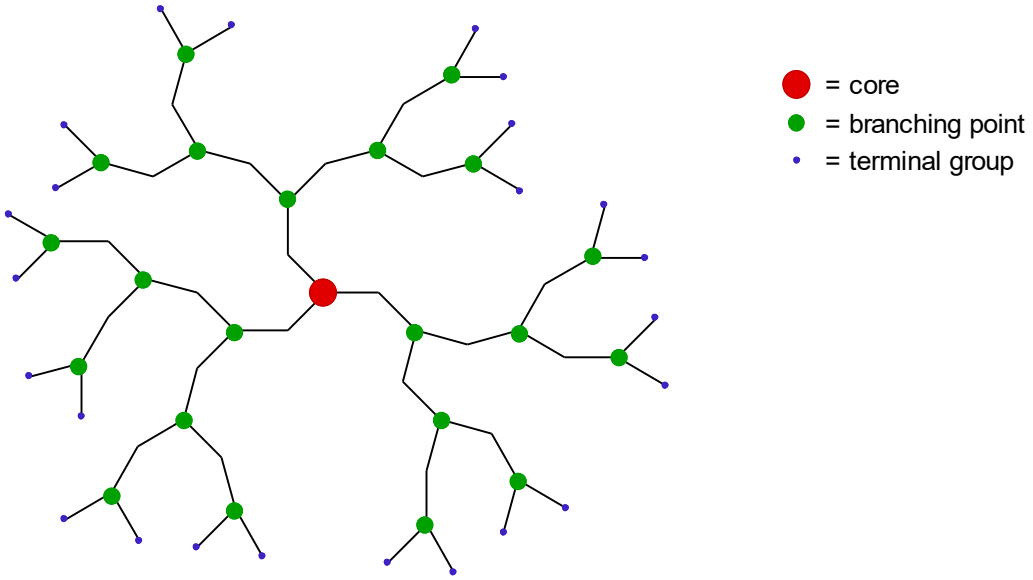

Figure 1.1 Key features of a dendrimer.[28]

The first attempted dendrimer synthesis was described in 1978 by Vögtle and co-workers.[28,29] The concept of using dendrimers as catalysts or catalyst supports can be traced back to some

of the early publications on dendrimers.[30] Dendrimers of sufficient size can be removed from the product stream *via* ultrafiltration and these catalysts can possibly be re-used.[31,32]

Reetz *et al.* reported the first use of a dendrimer catalyst in the hydroformylation reaction in 1997.[29] They used the 1,4-diaminobutane (DAB) polyamino dendrimer as starting point, and functionalized the terminal amines with Ph_2PCH_2OH to afford the phosphine-functionalized dendrimer. The dendrimer ligand was then reacted with $[Rh(cod)_2BF_4]$ to form dendrimer-supported metal complexes, shown in Figure 1.2. The complexes were applied in the hydroformylation of 1-octene and gave quantitative conversion to aldehydes with a ratio of linear (normal) to branched (*iso*) of 1.5:1. This ratio is commonly reported as the *n:iso* ratio.

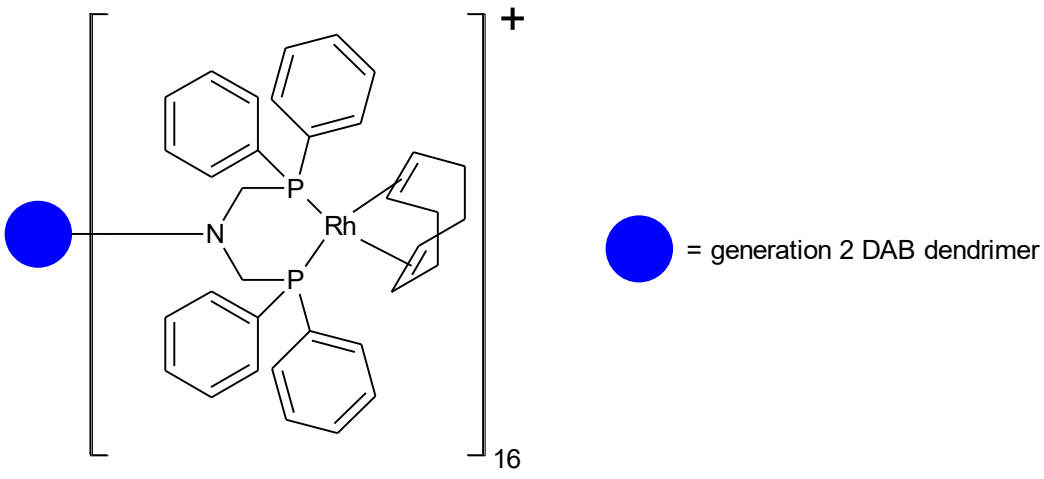

Figure 1.2 Dendrimeric rhodium complex synthesized by Reetz *et al*.[29]

Further work on the application of homogeneous dendritic systems as hydroformylation catalysts was done by Antonels *et al.*[33] They utilized the DAB dendrimer scaffold (generations 1 and 2) and reacted the terminal amines with 2-pyridinecarboxaldehyde in a Schiff base condensation reaction to yield their ligands. The ligands were then reacted with $[RhCl(COD)]_2$ to form the rhodium complexes. An example can be seen in Figure 1.3. The catalysts were applied in the hydroformylation of 1-octene. Both the dendritic catalysts as well as a monomeric analogue gave 98% conversion after 8 hours, with aldehydes and octene isomers being formed. The *n:iso* ratio was determined after 2 hours and it was found that the second generation dendrimer showed higher selectivity towards branched aldehydes (*n:iso* ratio 1.5:1) when compared to the first generation dendrimer and the monomeric analogue (*n:iso* ratio 2.6:1).

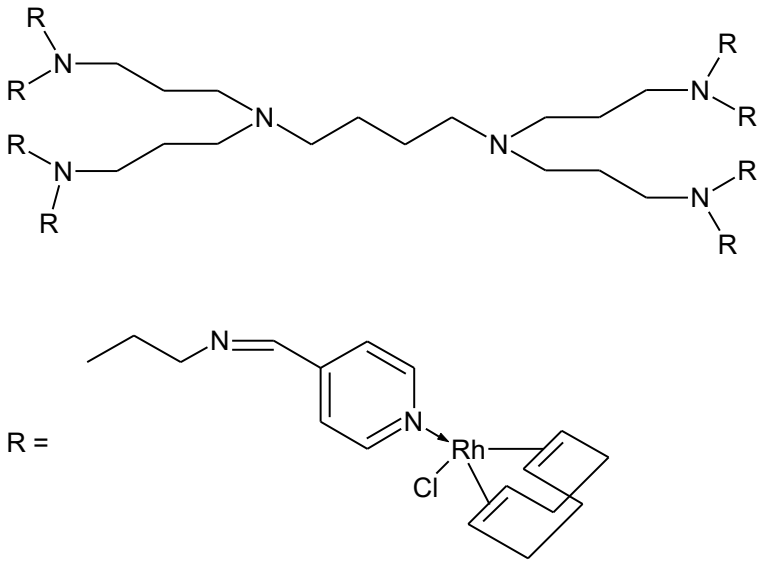

Figure 1.3 DAB generation 2 metallodendrimer.[33]

Smith and co-workers also explored the catalytic properties of some medium-sized dendrimers.[34,35] They developed tris-2-(2-pyridylimine ethyl) ligands from tris(2-aminoethyl)amine and 2-pyridinecarboxaldehyde. The ligands were then reacted with either $[RhCl(CO)_2]_2$ (to form neutral complexes) or $[RhCl(COD)]_2$ and $NaPF_6$ (to form cationic complexes). The catalysts were evaluated in the hydroformylation of 1-octene and both systems showed >99% conversion of 1-octene after 8 hours. The chemoselectivity was mostly towards aldehydes, with selectivity of greater than 85% obtained for both catalyst systems. The regioselectivity was mostly towards nonanal (*n:iso* ratio 15.6:1 and 2.12:1 for the neutral and cationic complexes respectively), with the dendritic systems being more selective than the analogous mononuclear systems (*n:iso* ratio 0.89:1 and 0.69:1 respectively). Unfortunately the authors do not comment on the recyclability of these catalysts.

In general, the literature shows that dendritic catalytic systems have slightly lower activities than their mononuclear analogues (the homogeneous system). However, no drastic difference in selectivity is observed. Although the idea of recycling dendritic catalysts via ultrafiltration is often mentioned, no examples of this could be found for dendrimer-catalyzed hydroformylation reactions.

1.2.1.2 Polymer supported catalysts

In 1970 Moffat reported the immobilization of cobalt complexes on a crosslinked poly-2-vinylpyridine polymer.[36] This is the first report of polymers being used as support for hydroformylation catalysts. It was found that the $HCo(CO)_4$ species was preferentially bound to the polymer over $Co_2(CO)_8$. The heterogenized system outperformed homogeneous catalyst systems in impure feeds, with the polymer serving as a reservoir which regulates the

amount of cobalt in the system. Čapka *et al.* prepared a phosphine-functionalized styrene-divinylbenzene copolymer and reacted it with $RhCl_3$ in order to obtain polymer-supported rhodium complexes.[37] These were applied in the hydroformylation of 1-heptene and gave a mixture of *n*-octanal and *iso*-octanal.

Nozaki *et al.* studied the use of Rh(I) complexes of the chiral phosphine-phosphite, (*R*, *S*)-BINAPHOS for asymmetric hydroformylation, initially in homogeneous systems and later in heterogenized systems. Vinyl-BINAPHOS was subjected to radical copolymerization with styrene derivatives to form polymers incorporating the ligand, as shown in Figure 1.4. Rh(acetylacetonate) was then added to form the complex. The immobilized catalysts were applied in the hydroformylation of styrene and could be re-used once with no loss in conversion and only a small decrease in enantioselectivity.[38]

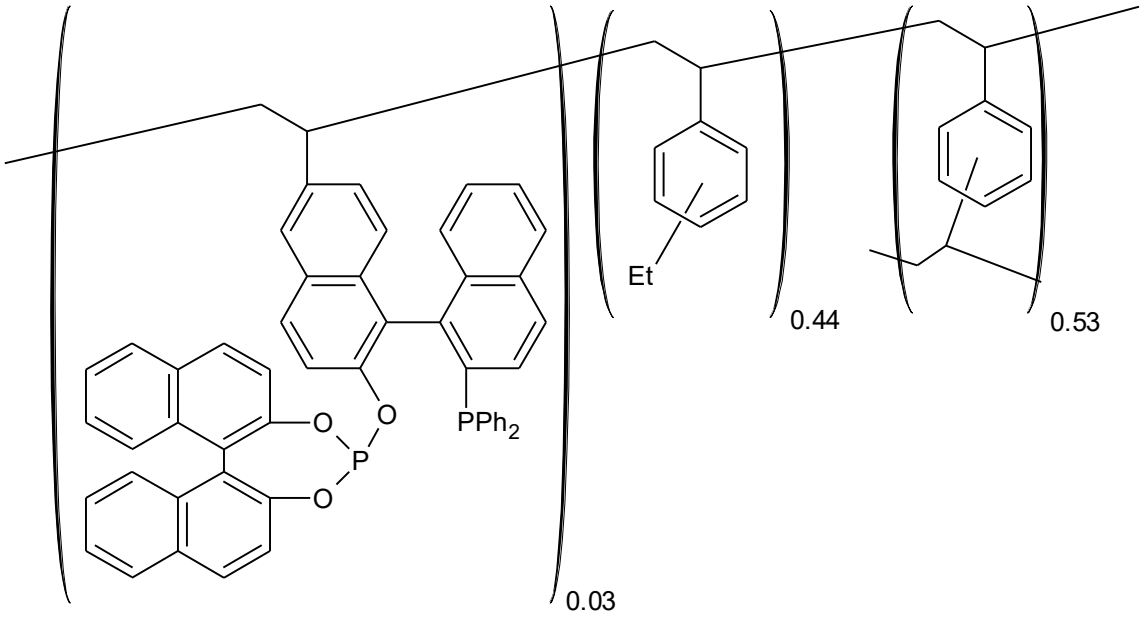

Figure 1.4 Polymer incorporating BINAPHOS ligand.[38]

Slivinskii *et al.* used different nitrogen-containing polymers as macroligands for rhodium coordination.[39] First, polyethyleneimine (PEI), water-soluble poly-*N,N*-diallyl-*N,N*-dimethylammonium chloride (WPC) and poly-*N,N*-diallyl-*N*-methylaminodihydrophosphate (PHP) supported $RhCl_3$ complexes were compared in the hydroformylation of 2-butene. It was found that the reaction rate was quite slow for the PEI-supported catalyst compared to the WPC and PHP-supported catalysts, with the latter two reaching reaction rates close to that of analogous conventional homogeneous catalysis. The PEI-supported catalyst shows higher selectivity towards 2-methylbutanal (98%) than the WPC and PHP systems (78% and 79%, respectively). Modification of these catalysts with erythritol phosphate caused an increase in reaction rate and selectivity, with all systems showing 98% selectivity or more towards

2-methylbutanal. The selectivity drops significantly for the WPC and PHP systems after recycling the systems once.

Smith and co-workers used chitosan, a biopolymer, as support for rhodium complexes. The chitosan was first modified *via* Schiff base condensation to form N,N and P,N chelating donor sites.[40] $[RhCl(CO)_2]_2$ was then added to form the supported complexes. An example is shown in Scheme 1.2.

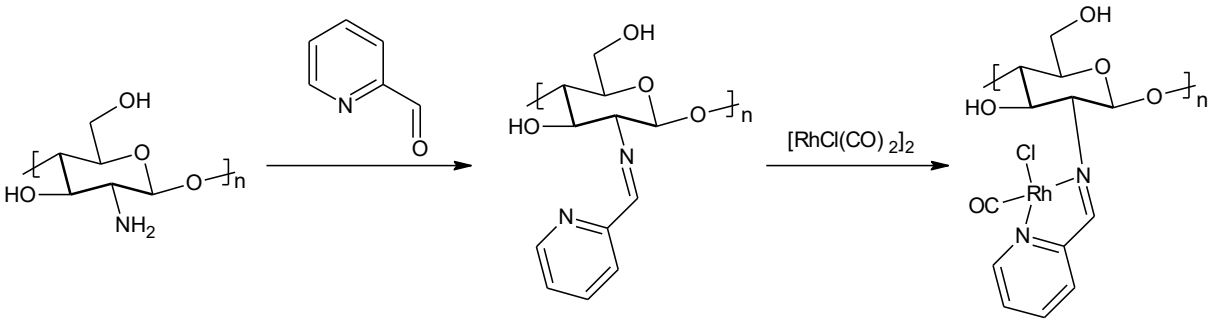

Scheme 1.2 Chitosan-supported rhodium complex.[40]

Mononuclear analogues of the complexes were prepared as well. The catalysts were tested in the hydroformylation of 1-octene. While the mononuclear complexes showed higher conversion at the beginning of the reaction, the conversion of 1-octene was similar for all catalysts after a 10-hour period. The low initial activity of the supported catalysts was ascribed to an induction period for these catalysts, where the syngas is first diffused into the solvent resulting in slower access to the rhodium sites on the chitosan. The catalysts showed high selectivity towards aldehydes, with the iminophosphine catalysts being more selective towards nonanal (70% and 72% respectively) than the iminopyridyl catalysts (57% and 68% respectively). Leaching studies showed that 0.02% (iminophosphine catalyst) and 0.05% (pyridine-imine catalyst) rhodium was lost over a time period of 2 hours.

Adint and Landis studied the immobilization of bis-3,4-diazaphospholanes (BDA) onto polymer resin bead supports with the aim of preparing enantioselective hydroformylation catalysts with high turnover frequencies and recyclability.[41] (*S*,*S*)-tetra-acid bis-3,4-diazaphospholane was fluorinated on the hydroxyl sites, followed by reaction with the amine-terminated beads. The immobilized ligands were then reacted with *S*-methylbenzylamine to generate the asymmetrical ligands as shown in Figure 1.5. Any remaining amines were capped to deactivate the polymer surface, and then the functionalized beads were reacted with $Rh(acac)(CO)_2$.

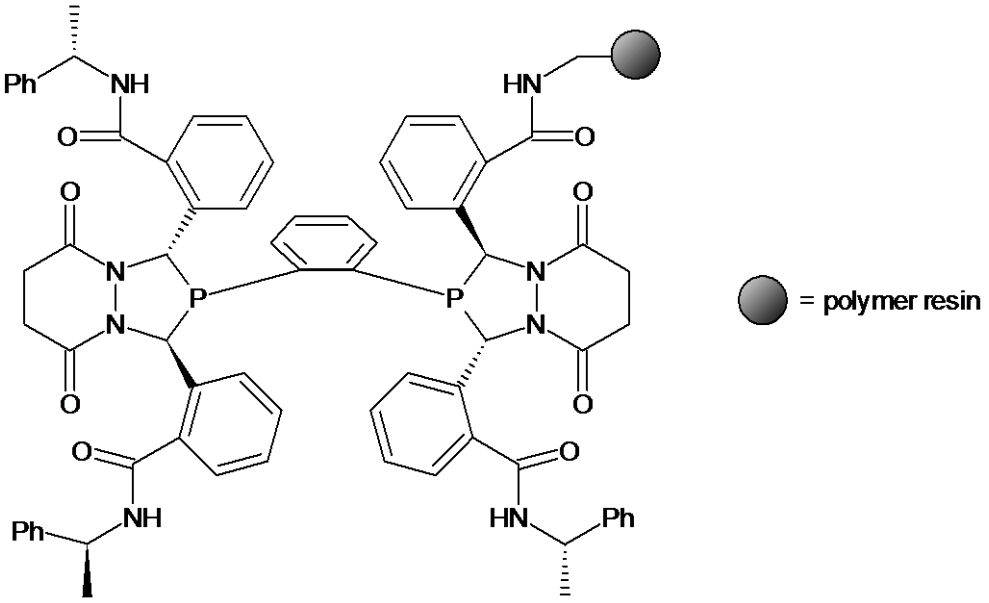

Figure 1.5 Asymmetric ligand linked to polymer resin.[41]

The catalyst was evaluated in the hydroformylation of styrene. The catalyst showed a preference for the formation of branched aldehydes. It was found that the *n:iso* ratio was below 0.083:1 and decreased to 0.067:1 with the re-use of the same batch of catalyst up to four times. The hydroformylation of styrene is commonly regioselective to the branched aldehyde. An enantiomeric excess of above 65% of the *S* isomer was found throughout. The amount of rhodium leaching was 2.5% for the first run and below the point of detection for the subsequent four runs. It was found that the turnover frequency was approximately four times lower than that of an analogous homogeneous catalyst.

Sun *et al.* attempted to minimize leaching of rhodium metal by making use of a porous organic polymer composed of suitable organic ligands.[42] Porous organic polymers have high surface areas, excellent stabilities and designable pore walls.[43–45] These polymers also possess good swelling properties, which endow the organic framework with high flexibility.[46] This could enhance the mobility of the catalytic sites in the polymer framework. Vinyl-functionalized diphosphine monomers based on 1,2-bis(diphenylphosphino)ethane, bis(diphenylphosphino)-methane and 1,2-bis-(diphenylphosphino)benzene, shown in Figure 1.6, were used to synthesize three different insoluble porous organic polymers *via* free-radical polymerization.

The polymers were treated with $Rh(CO)_2(acac)$ to give the catalyst precursor. The catalysts were then tested in the hydroformylation of styrene. These catalysts gave quantitative conversion of styrene after 20 hours, with very high selectivity towards aldehydes, with the branched aldehyde being formed in 88% yield.

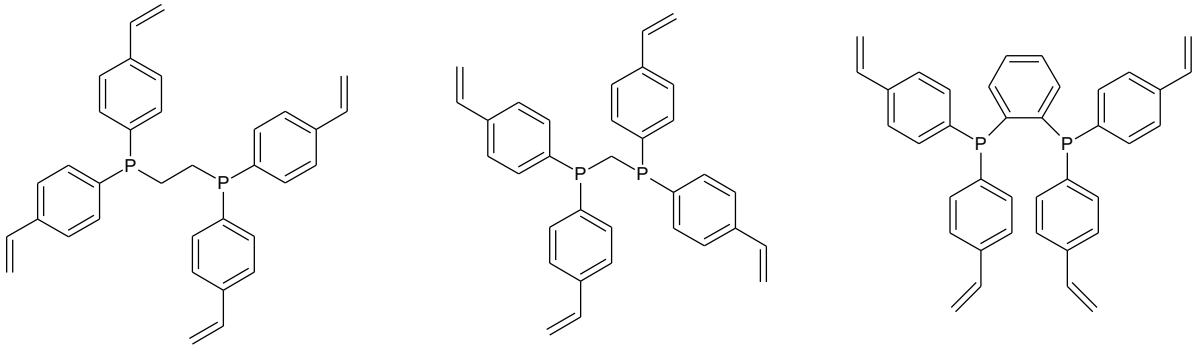

Figure 1.6 Diphosphine monomers used to prepare porous organic polymers.[42]

The catalyst was recycled five times without loss of activity and regioselectivity. ICP-OES studies show that the quantity of rhodium in solution after each run was <10 ppb. This is attributed to the high ligand concentration in the support, which allows for Rh complex retention.

Polymers have been used as hydroformylation supports for a long time as described in this section, and generally seem to work fairly well. Numerous recycling studies have been carried out, and rhodium leaching is quite low. Although the activity is lower than that of homogeneous systems in most cases, this is offset by the ability of the catalysts to be recycled.

1.2.2 Biphasic systems

1.2.2.1 Aqueous biphasic hydroformylation catalysts

In aqueous biphasic catalysis, a water-soluble catalyst remains dissolved in water, while the reactants and products are confined to the organic layer. The products can therefore be separated from the catalyst with relative ease, and the catalyst can be recycled as shown in Figure 1.7.

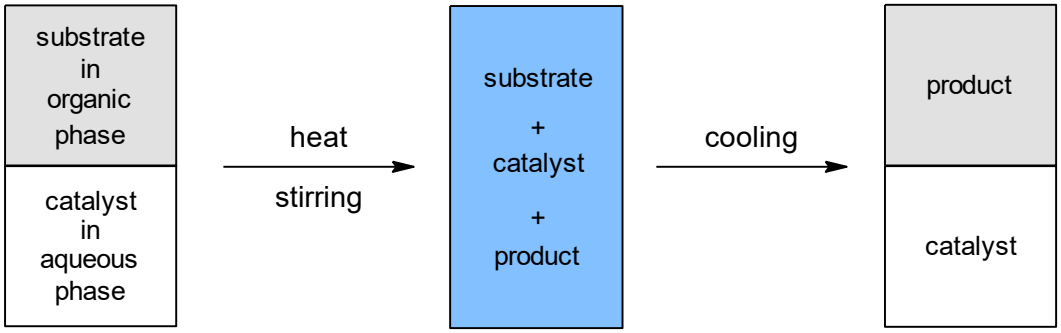

Figure 1.7 Diagram showing principle of aqueous biphasic catalysis.[47]

The most well-known industrial application of this principle is in the Ruhrchemie/Rhône-Poulenc process, where tri(*m*-sulfonyl)triphenylphosphine (TPPTS), shown in Figure 1.8, is used as ligand to keep the rhodium in the aqueous phase.[48]

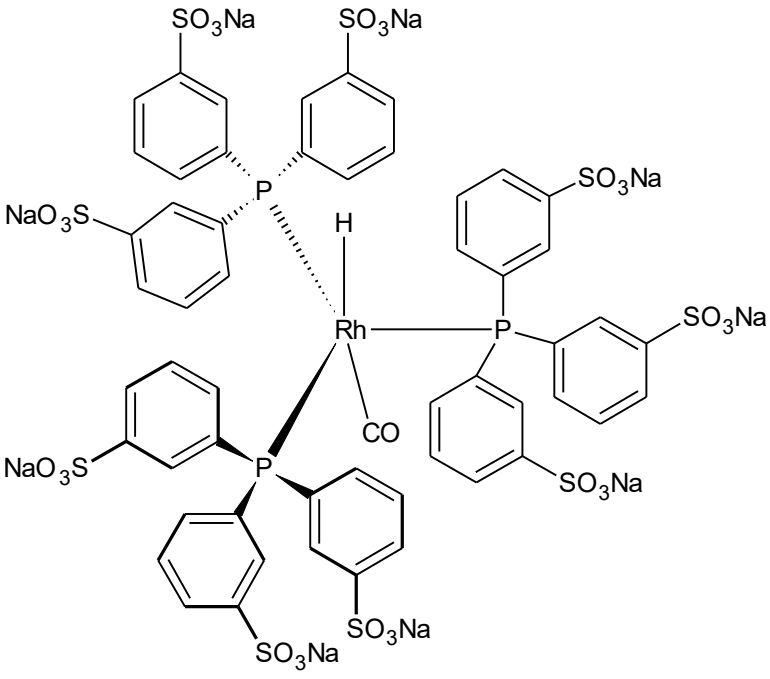

Figure 1.8 The TPPTS ligand used in the Ruhrchemie/Rhône-Poulenc process.[48]

The process works exceedingly well when propene and butenes are used as substrates, with the rhodium loss being less than 10^{-9} g per kg *n*-butyraldehyde produced. The process does not work that well with longer chain olefins, although numerous methodologies to improve catalyst recovery, such as adding surfactants to the reaction mixture, have been investigated to overcome this problem.

Several such surfactants were studied by Fu *et al*.[49] They utilized various cationic gemini and trimeric surfactants, shown in Figure 1.9, to promote the aqueous biphasic hydroformylation of higher olefins.

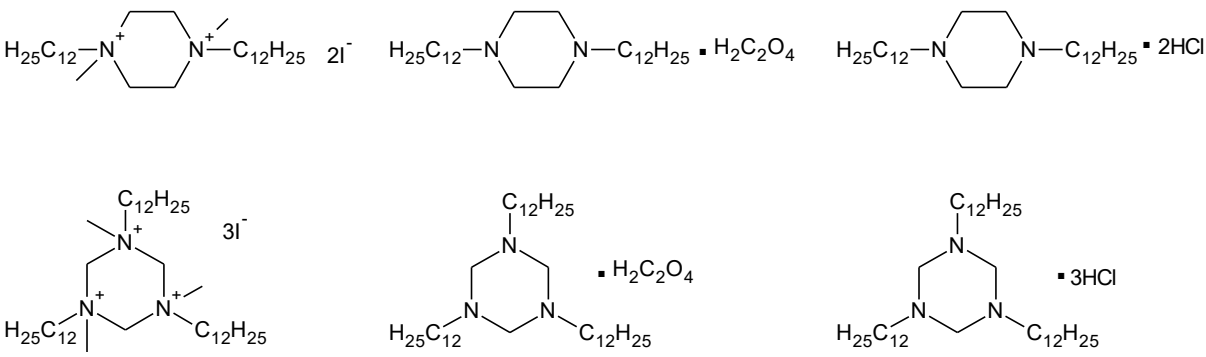

Figure 1.9 Surfactants used by Fu *et al*. [49]

The catalyst used in this study in conjunction with the ionic liquids was $RhCl(CO)(TPPTS)_2$/(TPPTS). Several of these surfactants caused an increase in the turnover frequency of the hydroformylation of 1-octene when added to the reaction. No apparent structure-activity relationship was observed. It was also seen that the turnover promoting effect increased as the concentration of the surfactant was increased, up to a concentration of 6 mmol surfactant per litre. Recycling studies were carried out using one of the surfactants, and the catalyst was re-used 6 times with only a slight loss in activity.

Fu *et al*. later combined the surfactant and ligand properties into one molecule by synthesizing a surface-active sulfonated phosphine with a hydrophobic tail (Figure 1.10).[50] DMOPPS (sulfonated n-$C_{12}H_{25}OC_6H_4P(C_6H_{14}$-$p$-$CH_3O)_2$) was prepared by reacted the phosphine DMOPP with concentrated sulphuric acid for 5 hours. Transmission electron microscopy (TEM) imaging was used to show that these ligands did indeed form micellar structures in water.

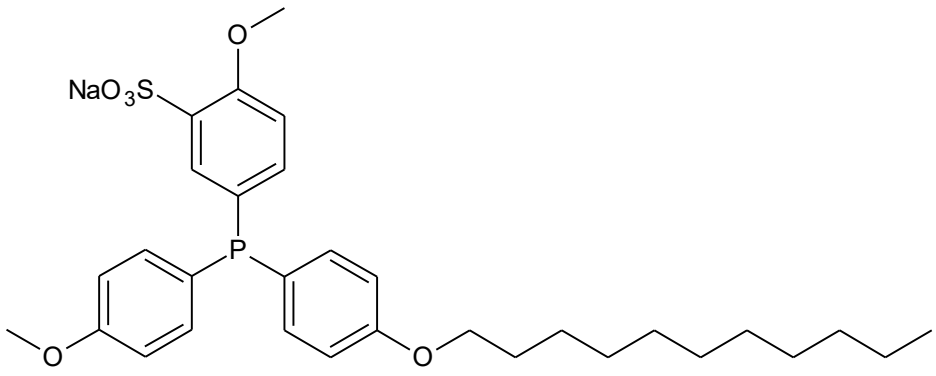

Figure 1.10 Amphiphilic sulfonated phosphine ligand.[50]

These ligands were reacted with $RhCl(CO)(TPPTS)_2$ to generate the catalyst *in situ*. The catalyst performed well in the hydroformylation of 1-octene, 1-decene and 1-dodecene, with TOF numbers higher than 600. The activity was much lower for longer chain olefins. The

catalyst was re-used five times with the TOF dropping only slightly. Some rhodium was leached into the organic phase – at first, the losses were in the order of 0.02 ppm, but the losses increased to 0.1 ppm after the third run. The addition of fresh DMOPPS seemed to help curb the rhodium loss.

Moving away from the TPPTS systems, another approach was taken by Hager *et al*. in which sulfonated salicylaldimine diaminobutane dendrimers were synthesized and reacted with rhodium metal precursors to form the complexes as catalyst precursors (Figure 1.11).[47]

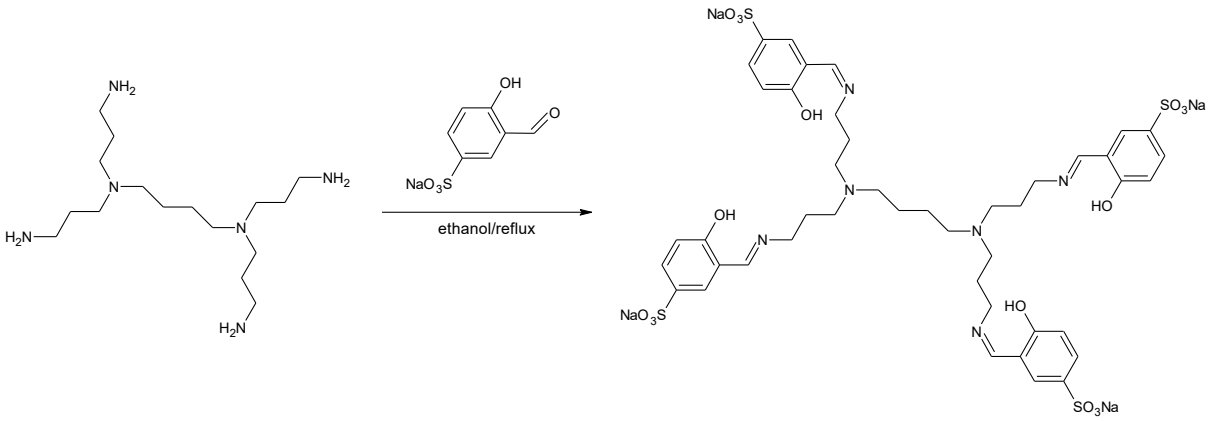

Figure 1.11 Synthesis of first generation water-soluble DAB dendrimer.[47]

A monomeric model catalyst was also synthesized. The complexes performed moderately well in the hydroformylation of 1-octene, with turnover frequencies between 189 and 309 moles of product formed per hour. The turnover frequencies could be increased by increasing the reaction temperature. The catalysts were re-used and showed rhodium leaching between 9% and 22% after being re-used five times. Less rhodium was leached from the dendrimeric catalysts as compared to the monomeric systems, possibly due to the excess of nitrogen atoms found in the dendrimeric skeleton.

The same research group later used the monomeric water-soluble rhodium complex as model to incorporate a ferrocene moiety into the structure, hoping that the bimetallic complex, shown in Figure 1.12) might show improved results.[51]

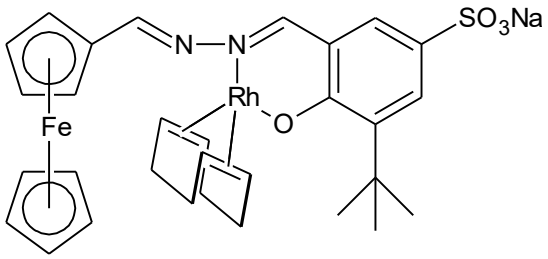

Figure 1.12 Example of a heterobimetallic precatalyst.[51]

While these complexes were active in the hydroformylation of 1-octene, their activity was lower than that of the monometallic counterparts. The catalysts could also be recycled, but the 1-octene conversion dropped significantly after the second re-use.

While aqueous biphasic hydroformylation has a proven track record as an immobilization method for hydroformylation catalysis, it is still primarily being used in the hydroformylation of shorter chain olefins. Although numerous systems for the hydroformylation of longer chain olefins have been developed, the rhodium leaching from these systems remains quite high by comparison to the Ruhrchemie/Rhône-Poulenc process.

1.2.2.2 The use of ionic liquids in hydroformylation

The use of ionic liquids in hydroformylation catalysis is relatively new compared to other immobilization methods. Chauvin *et al*. reported the first use of ionic liquid for biphasic hydroformylation in 1995.[52] They used room temperature ionic liquids based on 1-*n*-butyl-3-methylimidazolium (BMI) salts in conjunction with the rhodium precursor complex $[Rh(CO)_2(acac)]$ and PPh_3 as ligand. The salt is shown in Figure 1.13.

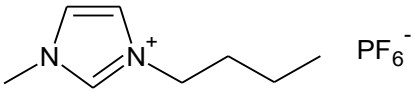

Figure 1.13 1-*n*-butyl-3-methylimidazolium hexafluorophosphate salt.[52]

The ionic liquid catalyst system gave a slightly higher turnover frequency in the hydroformylation of 1-pentene than that of the homogeneous complex. The *n:iso* ratio was also increased from 2:1 in the homogeneous system to 3:1. The catalyst was recycled, but leaching of rhodium into the organic phase was observed. The authors postulated that the use of a better tailored, possibly cationic, rhodium precursor could curb the leaching to a large extent.

One example of such a tailored rhodium complex is reported by Chen *et al*.[53] They synthesized a novel rhodium(III) complex with phosphine ligands, with the ligands based on the structure of their chosen ionic liquids, 1-*n*-butyl-3-methylimidazolium tetrafluoroborate and 1-(2-piperid-1-yl-ethyl)-3-methylimidazolium tetrafluoroborate. They also synthesized various other ligands to be used in conjunction with the complex. The structures of these are shown in Figure 1.14.

It was found that the addition of a P,N cationic ligand gave excellent conversion of 1-octene, with a selectivity of 90% towards aldehydes and an *n:iso* ratio of 2.8:1. The addition of the monodentate phosphorous-containing ligand supressed the activity of the catalyst. This is

ascribed to the formation of over-stable complexes, which prohibit the formation of the active Rh(I)-H species.

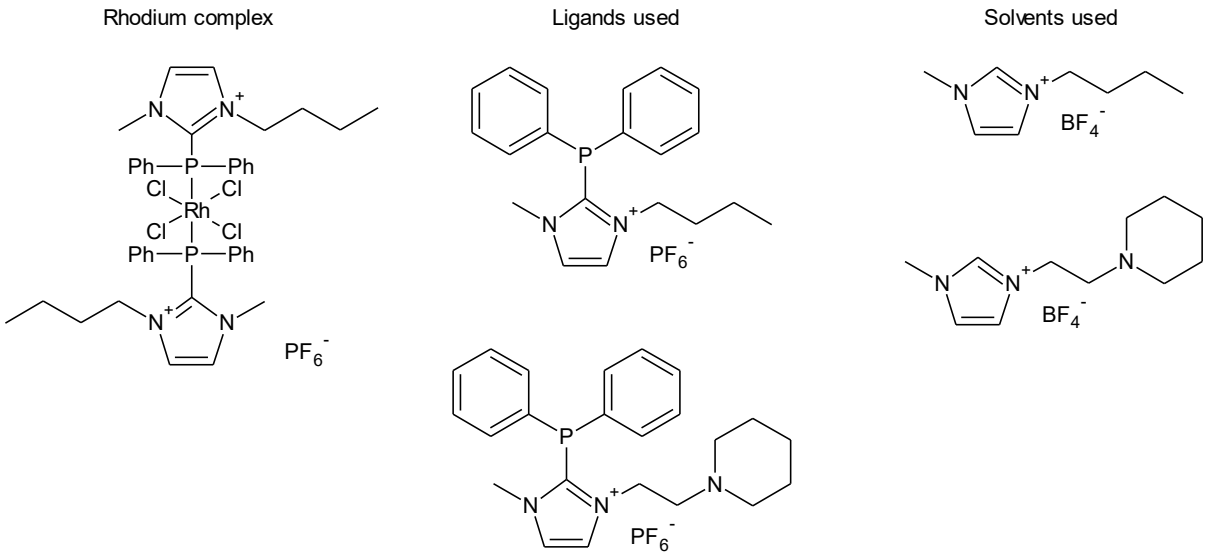

Figure 1.14 Complex (left), ligands (centre) and ionic liquids (right) used by Chen *et al*.[53]

The catalytic system utilizing the bidentate P,N ligand was then re-used. In [Bmim][BF_4], leaching was a problem and after 4 uses, the conversion dropped from 96% to 22%. When [PEmim][BF_4] was used as solvent, the catalyst could be re-used seven times without a significant drop in the conversion. It should, however be noted that the time needed for the conversion increased and the TOF drops from 613 h^{-1} to 81^{-1}. The amount of rhodium leaching into the organic phase is below the rhodium detection limit (ICP-OES), and it is therefore not rhodium loss which is responsible for the decrease in TOF. The authors speculated that a more stable dimeric rhodium complex could be forming which could be responsible for the low activity.

Jin *et al*. followed a slightly differently approach, moving away from the traditional imidazolium-based ionic liquids.[54] They used polyether guanidinium methanesulfonates as ionic liquids, which are liquids at the temperatures at which hydroformylation is usually carried out, but solids at room temperature. For the rhodium source and ligand, they employed the commonly used $RhCl_3$ and TPPTS, which were stirred together prior to the start of the hydroformylation reaction (Figure 1.15).

This catalyst system was applied in the hydroformylation of 1-octene, 1-decene, 1-dodecene and 1-tetradecene. It was found that the conversion increased through the first few cycles of re-use, and that the longer chain alkenes required more cycles to reach the optimum conversion. For 1-octene, for example, the conversion in the first cycle was 36% and this increased to 98% in the third cycle, while for 1-tetradecene the initial conversion was 6%,

which increased to 84% after 6 cycles. This suggests that the activity is controlled by the amount of active catalyst species in the ionic liquid phase. The lower conversion of the longer chain alkenes was attributed to lower solubility of these alkenes in the ionic liquids.

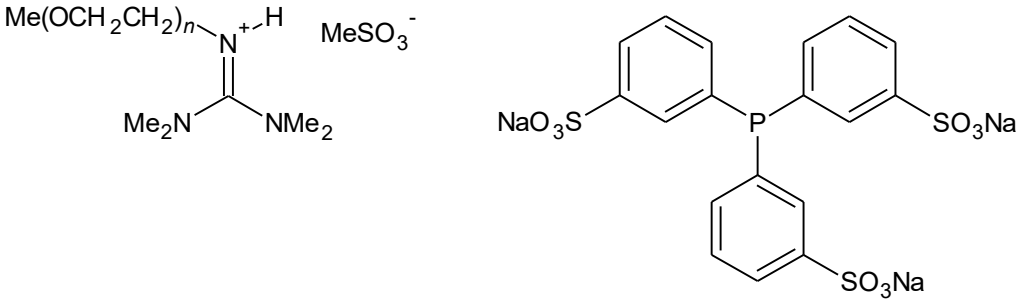

Figure 1.15 Ionic liquid (left) and ligand (right) used by Jin *et al*.[54]

High selectivity towards aldehydes (>90%) and moderate *n:iso* ratios (in the range of 2.0:1 to 2.4:1) were obtained throughout. The catalyst was re-used 35 times in the hydroformylation of 1-octene with the activity dropping from 98% to 85%. The total rhodium loss was 0.07%. The use of an ionic liquid which is solid at room temperature makes separation of the product and catalyst phases quite facile – the product phase can simply be decanted after completion of the reaction.

A related area which has garnered quite a lot of interest is the use of supported ionic liquid catalysts. In this method, an ionic liquid is covalently bonded to a support material. When this surface is treated with additional ionic liquid, multiple layers of ionic liquid forms on the support. This then serves as reaction phase in which the homogeneous catalyst is dissolved. An early example is the work done by Mehnert *et al*. who used silica gel as support.[55] An imidazolium-based ionic liquid was immobilized as shown in Scheme 1.3.

The rhodium precursor, dicarbonylacetylacetonate rhodium, was treated with tri(*m*-sulfonyl) triphenylphosphine *tris*(1-butyl-3-methyl-imidazolium) salt. This was then combined with the supported ionic liquid. The supported catalysts were applied in the hydroformylation of 1-hexene, and gave TOF values of 65 and 60 mole aldehyde per mole rhodium per minute, respectively. These values are higher than that of the same catalyst in an ionic liquid biphasic system, which is tentatively attributed to a higher concentration of the active rhodium species at the interface. It was found that the ionic liquid partially dissolved in the organic phase at high aldehyde concentrations, and the aldehyde concentration was kept below 50% to supress rhodium leaching.

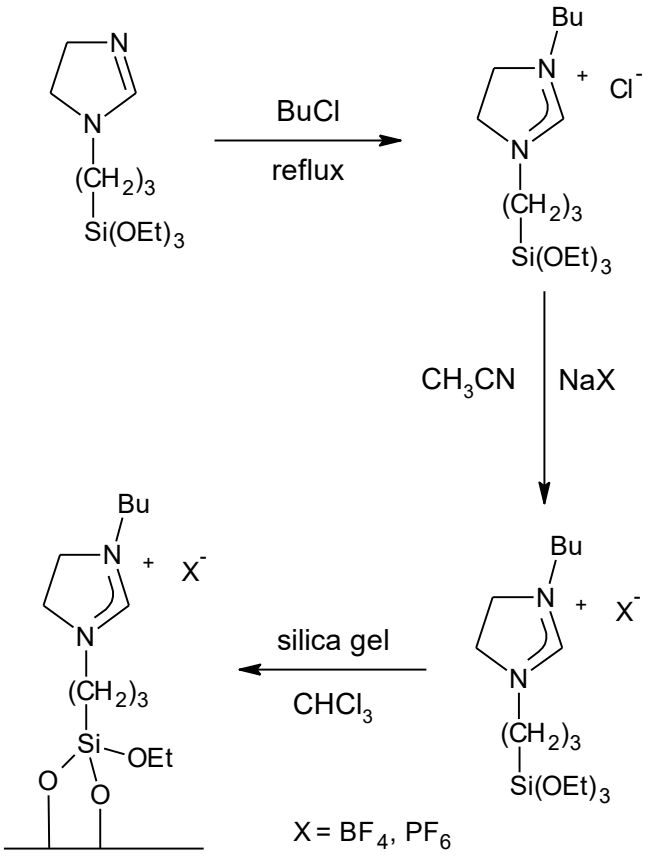

Scheme 1.3 Synthesis of silica-immobilized ionic liquid.[55]

Weiß *et al*. studied carbon as support for ionic liquids in the hydroformylation reaction.[56] Pristine carbon showed very low activities, but after surface modification the activities were much improved. A number of approaches were taken in the surface modification, including treating the carbon material with concentrated nitric acid. The catalysts were then prepared by reacting these modified supports with a mixture of the rhodium metal precursor, the ligand 4,5-*bis*(diphenylphosphino)-9,9-dimethylxanthene (also known as xantphos) and the ionic liquid 1-ethyl-3-methylimidazolium *bis*(trifluoromethylsulfonyl)imide ([EMIM][NTf_2]). The catalysts were applied in the hydroformylation of propene and a TOF of 215 h^{-1} was found. The *n:iso* ratio was 13:1. The high *n:iso* ratio was attributed to the use of the xantphos ligand. The increased activity was ascribed to the high nitrogen content of the support, which plays a role in modifying the ligand during catalysis.

Both traditionally used and supported ionic liquids show great promise as immobilization methods for rhodium-catalyzed hydroformylation. Activities are generally high and, when the right ligands and ionic liquids are chosen, the leaching of the rhodium into the organic phase can be largely suppressed.

1.2.3 Inorganic Supports

1.2.3.1 Carbon supported catalysts

Carbon materials are considered good catalyst supports due to their thermal and chemical inertness, high surface areas and surface morphology properties.[57] These materials have also been tested as catalyst supports in the hydroformylation reaction.

Zhang *et al.* prepared a range of carbon-supported noble metal catalysts to study in the hydroformylation of 1-hexene.[58] Metal nitrate aqueous solutions were used to impregnate active carbon materials, which were subsequently dried and finally reduced under hydrogen at 673 K for 6 hours to yield the supported metal nanoparticles. The metals used were cobalt, palladium, ruthenium, platinum and rhodium. These catalysts were then used in the hydroformylation of 1-hexene. It was found that the rhodium and ruthenium catalysts gave the highest conversion of 1-hexene after 2 hours (99.6% and 92.8% respectively), followed by the cobalt catalyst with a 68.1% conversion. When the products were analysed it was found that the ruthenium catalyst was selective towards isomerization, with only 7% of the products being aldehydes. The rhodium and cobalt catalysts, on the other hand, showed high selectivity towards aldehydes, with 82% and 84% of the products formed being aldehydes, respectively.

The hydroformylation of mixed octenes by rhodium on activated carbon was studied by Ma *et al.*[59] They also prepared the homogeneous catalysts $RhCl(CO)(TPPTS)_2$ (for use in biphasic catalysis) and $[Rh(CH_3COO)_2]_2$-Ph_3PO. For the preparation of supported catalysts, five different activated carbon supports which vary in surface area, pore diameter and pore volume were used. The carbon was impregnated first with an aqueous solution of rhodium trichloride and then with an aqueous solution of phosphoric acid, followed by calcination.

After hydroformylation of mixed octenes by these three groups of catalysts, it was found that the catalysts supported on activated carbon outperformed the biphasic catalyst in terms of conversion and turnover frequency, and came close to the conversion of the homogeneous catalyst although having a lower turnover frequency. Furthermore, the supported catalyst could be recycled three times before any significant loss of conversion occurred, whereas the biphasic and especially the homogeneous catalysts showed a dramatic loss in conversion after only one catalytic run.

Alper and co-workers reported the covalent immobilization of a rhodium complex onto the surface of activated carbon.[60] The carbon support was functionalized by first treating it with a solution of HNO_3 at 80°C until dryness, followed by a reaction with $SOCl_2$ in diethyl ether. The acid-chloride functionalized support was then dried under vacuum at 40°C. Two methods were then followed to anchor the desired complex onto the carbon: (i) the ligand was bonded to the

support followed by reaction with a rhodium precursor salt to form the complex, and (ii) the complex was synthesized prior to being bound to the support (Scheme 1.4).

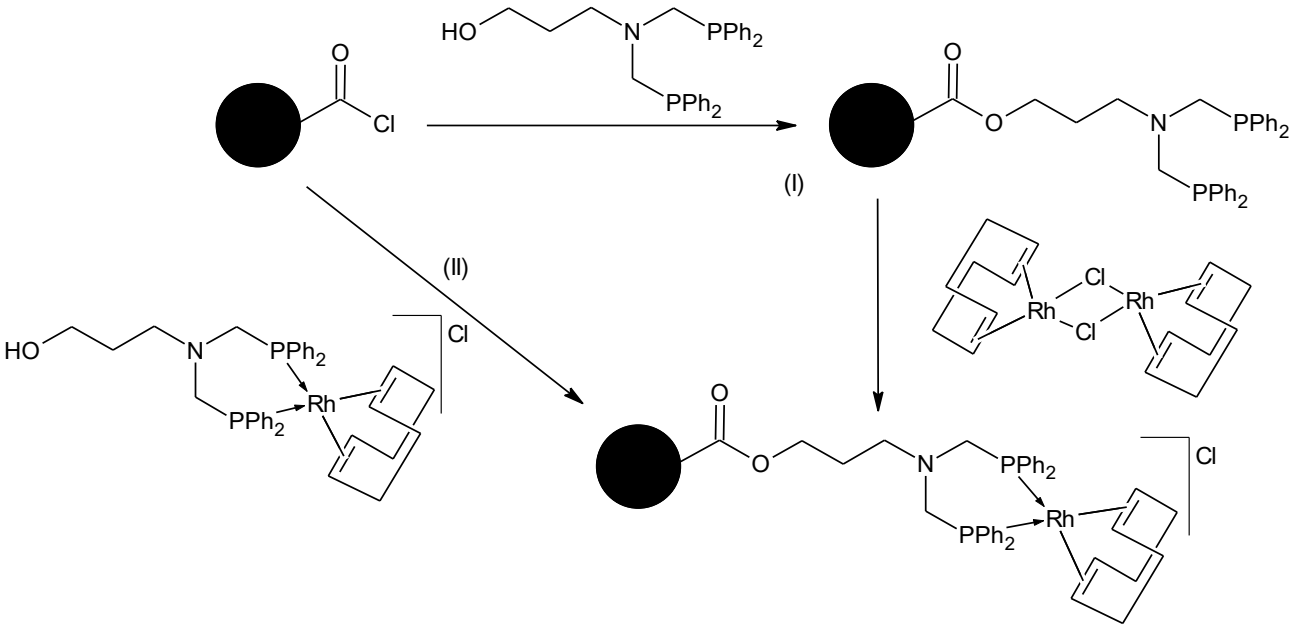

Scheme 1.4 Synthetic routes to obtain Rh complex covalently bonded to the activated carbon support.[60]

These catalysts were then tested in the hydroformylation of 1-octene, with $[RhCl(COD)]_2$ as homogeneous reference. The concentration of rhodium was kept constant throughout. In the first catalytic run, the homogeneous catalyst and catalyst obtained by route II showed 100% conversion, with catalyst obtained by route I giving 80% conversion. While the homogeneous catalyst had higher selectivity towards aldehydes, it had a lower *n:iso* ratio and thus the total amount of nonanal obtained for all three systems is comparable. The immobilized catalysts were re-used for a further three catalytic runs. The total leaching expressed as a percentage of rhodium after all four runs for the catalysts obtained by route I and II is 59% and 43%, respectively. ^{31}P NMR analysis showed the presence of phosphine ligands in the solution, indicating that part of the complex is in the solution as well. The ester linkage was presumably cleaved under the catalytic conditions. The higher leaching for route I could indicate that some of the rhodium salt is deposited onto the carbon support and not covalently bonded to the carbon support.

A variety of other carbon-derived materials are also available as catalyst supports. Graphene oxide has abundant oxygen-containing groups on the sheet surfaces, which can improve the material's hydrophilicity and stability, while also serving as nucleation sites to anchor metal ions.[61] Graphene oxide with metal ions on the surface can also be simultaneously reduced to form reduced graphene oxide (RGO) supported metal nanoparticles. Tan *et al.* reported the

first RGO supported catalysts for hydroformylation in 2015.[62] The graphene oxide was mixed with an aqueous solution of $Rh(NO_3)_3$ in an ethylene-glycol water solution and then heated for 10 hours. The reaction mixture was then filtered, washed and dried to give the metal nanoparticles supported on the graphene oxide.

The catalyst was evaluated in the hydroformylation of 1-hexene. Complete conversion was obtained after 4 hours. After 1 hour, heptanal and internal hexenes were formed in almost equal amounts, but after 4 hours the selectivity was towards aldehydes. The *n:iso* ratio was 4.0 after one hour, but decreased to 1.1 after 4 hours. This was attributed to the internal hexenes undergoing hydroformylation to form branched aldehydes.

Carbon materials have the potential to be effective supports for hydroformylation catalysts, however, at this stage, rhodium leaching from the support remains a major problem.

1.2.3.2 Silica supported catalysts

Silica has been a widely used catalyst support in catalysis due to its ease of preparation, thermal stability and high surface area.[63–65] The silanol groups present on the silica surface makes the material particularly suited to immobilization of complexes, since the former can be reacted in a simple condensation reaction with a suitable moiety, such as a siloxane, in the metal complex.

In 1975, Arai *et al.* prepared a styrene and divinylbenzene copolymer in the presence of silica gel which resulted in the silica being coated with polymer.[66] The polymer was first brominated followed by phosphination to yield a silica-stabilized polymer with phosphine binding sites. This polymer was treated with $[RhCl(CO)_2]_2$ to afford the catalyst as shown in Figure 1.16. For comparison, three other catalysts consisting of silica gel directly impregnated with $[RhCl(CO)(PPh_3)_2]$, $RhCl_3$ and rhodium metal respectively were prepared as well.

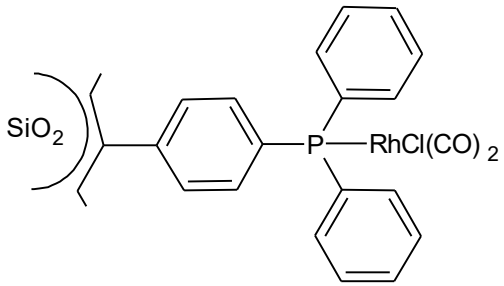

Figure 1.16 Rhodium complex immobilized on silica gel.[66]

The hydroformylation reactions were carried out in the gas phase with either ethylene or propylene being used as substrate. The amount of rhodium used in all reactions was kept the

same. It was found that the polymer-stabilized catalyst far outperformed all the catalysts in which rhodium was directly impregnated onto the silica gel. Both the $[RhCl(CO)(PPh_3)_2]$ and rhodium metal catalysts showed no activity, while the $RhCl_3$ catalyst showed moderate activity for up to 2 hours, after which the rate of propional formation dropped. This was attributed to the leaching of $[RhCl(CO)]_2$ from the silica. The polymer-supported system showed no drop in the rate of propional formation, indicating a more stable system.

In the same year, Allum *et al.* reported the functionalization of silica with ligands that were able to complex rhodium precursors.[67] Phosphorous, nitrogen, oxygen and sulphur donor ligands were synthesized. Some of these ligands were reacted with $[Rh(acac)(CO)_2]$ and $[RhCl(CO)_2]_2$ to form the complexes immobilized onto silica. They also prepared simple rhodium complexes functionalized with a siloxane moiety which could then be covalently bonded to silica. The silica-immobilized complexes were tested in the hydroformylation of 1-hexene.[68] For the phosphorous-linked complexes it was found that, after 75 hours on stream, the conversion of 1-hexene to heptanal was quantitative, with the selectivity towards aldehydes being more than 90%. When the phosphorous systems were compared to the nitrogen systems it was found that the rhodium leaching was lower for the phosphorous systems, with <0.07 ppm rhodium being detected for the former and between 4 and 45 ppm rhodium for the latter system. The authors attributed the greater stability of the phosphorous-linked systems to the presence of multiple phosphorous donor sites on the silica that could bind to the rhodium.

Van Leeuwen and co-workers studied the immobilization of a xanthene-based diphosphine rhodium complex, with the ligand shown in Figure 1.17, onto silica using both a sol-gel technique and a direct anchoring technique.[69] The sol-gel technique was chosen because of its diversity, the low temperatures at which the catalyst can be bound to the support, and reported suppression of metal leaching.[70,71] To prepare the sol-gel catalyst the ligand, $[Rh(acac)(CO)_2]$ and tetramethyl orthosilicate was stirred in THF/H_2O to obtain a gel. The gel was then dried and crushed into a free-flowing silica.

Various routes and additives were used when immobilizing the catalyst onto commercially available silica, but only two will be discussed here: (i) the ligand was immobilized onto silica, followed by the addition of a rhodium precursor, and (ii) the ligand and rhodium precursor were reacted to form the complex, which was then subsequently immobilized onto the silica.

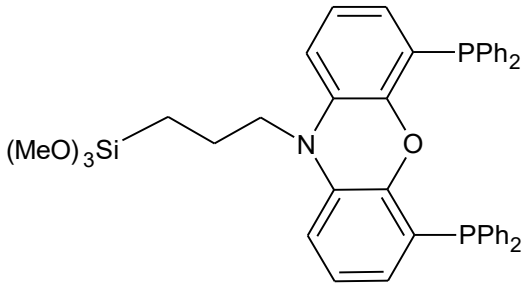

Figure 1.17 Xanthene-based diphosphine ligand used for immobilization.[69]

Adint and Landis immobilized the asymmetric hydroformylation catalyst shown in Figure 1.5 on silica gel as well as on a polymer resin as discussed in Section 1.2.1.2. They used two different methods of immobilization – in one case the complex was modified with 3-aminopropyltriethoxysilane before immobilization, and in the other the silica was treated with the amine, followed by reacting this functionalized silica with the rhodium complex. The catalysts were applied in the hydroformylation of styrene, but exhibited lower conversion, regioselectivity and enantioselectivity than their polymer-immobilized or homogeneous counterparts. Rhodium leaching was found to be less than 1%. While the results were slightly disappointing, this remains one of the very few examples of asymmetric hydroformylation performed with a silica-immobilized catalyst.

More recently, ordered mesoporous silica has been investigated with great interest as catalyst supports. These silica materials have a higher surface area than that of conventional SiO_2, as well as well-ordered pores with large pore volumes. Mesopores are defined by their pore size, which is between 2 and 50 nanometres. The most widely used of these mesoporous silica materials have been MCM-41, developed by the Mobil Corporation, and SBA-15, developed by the University of Santa Barbara in the mid-1990s.[72,73] This silica is synthesized *via* the combination of a templating agent and a silica source in water. The pH is usually controlled by the addition of an acid or a base. By changing these factors, properties of the silica like the surface area, pore volume, pore size and pore structure can be controlled.

The most commonly accepted mechanism for the formation of the ordered mesoporous silicas is the liquid crystal templating mechanism.[74] This mechanism involves the arrangement of the surfactant molecules to form micelles with the hydrophobic part towards the center of the micelle. The micelles pack to form micellar rods, which arrange to form a hexagonal array. The silica is added by introducing a source such a tetraethylorthosilicate. The silica forms a layer around the hexagonal array, and finally the templating agent is removed *via* calcination, leaving mesoporous silica containing even hexagonal pores, as shown in Scheme 1.5.

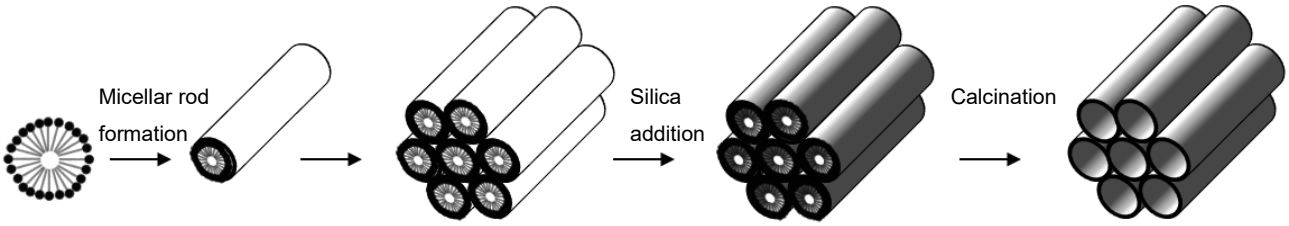

Scheme 1.5 Synthesis of mesoporous silica *via* the liquid crystal templating method.[74]

Marras *et al.* immobilized the xanthene-based diphosphine ligand shown in Figure 1.17 onto SBA-15 with the hope of exceeding the activity obtained for this ligand immobilized onto sol-gel or conventional silica.[69,75] SBA-15 with a pore diameter of 10 nm was prepared and the ligand was immobilized by refluxing it with the silica in toluene. $[Rh(acac)(CO)_2]$ was subsequently added to form the active complex. They compared this catalyst with a homogeneous analogue as well as an analogous complex immobilized onto SiO_2. The silica gel supported catalyst showed a much lower TOF (8 mol product per mol rhodium per hour) than that of the homogeneous catalyst (120 h^{-1}) under the similar conditions. The SBA-15 supported catalyst, however, had a TOF of 195 h^{-1} under the similar conditions, thus outperforming the homogeneous catalyst. The regioselectivity was slightly higher for the homogeneous catalyst, with an *n:iso* ratio of 41, compared to that of 35 for the SBA-15 supported catalyst. More importantly, the SBA-15 supported catalyst could be recycled up to 14 times with no significant loss of activity and selectivity, and with less than 3 ppb rhodium metal leaching (according to ICP-OES analysis).

Bae *et al.* studied the effect of the pore structure of mesoporous silica-supported rhodium catalysts on 1-octene hydroformylation.[76] They used MCM-41 (typical pore size of 2-3 nm), SBA-15 (typical pore size of 4-6 nm) and amorphous silica (typical pore size 8-10 nm). The amorphous silica has a disordered pore structure, while the other two silicas have ordered hexagonal pores. The silica was functionalized with γ-aminopropylmethyl dimethoxysilane (AEAPMDMS) and reacted with $Rh_4(CO)_{12}$ to yield the immobilized catalyst. In all cases there was a decrease in the surface area and pore size after functionalization of the silica. The catalysts were applied in the hydroformylation of 1-octene. All the catalysts showed high conversion of 1-octene to internal octene isomers and C9 aldehydes. It was found that, in terms of aldehyde yield, SBA-15 performed the best, followed by the amorphous silica and then MCM-41. From this, it would seem that both pore size and pore structure plays a role in the catalysis.

Dastgir *et al*. synthesized rhodium N-heterocyclic carbene complexes and immobilized these onto MCM-41 for application in the hydroformylation in 1-octene.[77] First, two imidazolium salts, (tmpMes)HI and (tmp^{t}Bu)HI, were synthesized *via* the reaction of

(3-iodopropyl)trimethoxysilane and *N*-mesitylimidazole or *N*-*tert*-butylimidazole. The silver complexes of these ligands were synthesized in an reaction with AgO_2, followed by transmetallation with $[RhCl(COD)]_2$ to form the final complex, as shown in Scheme 1.6.

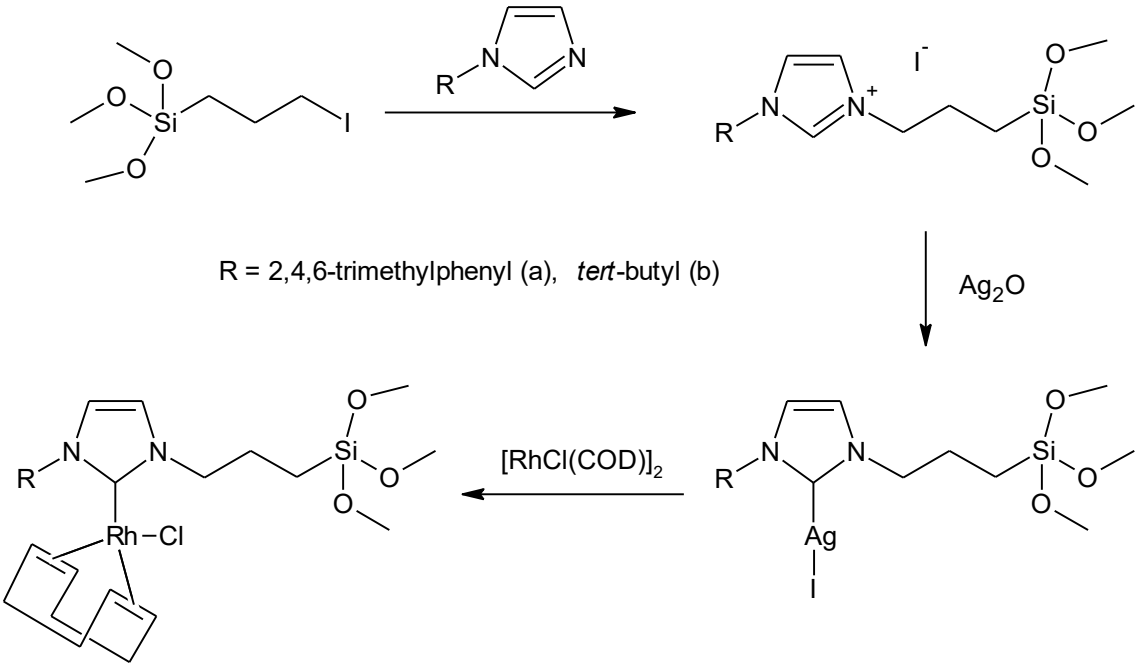

Scheme 1.6 Synthesis of imidazolium salts and rhodium complexes.[77]

The MCM-41 support was pre-functionalized with Ph_2SiCl_2 by following a literature procedure.[78] This was done to deactivate the silanol groups on the outer surface of the silica, and force the catalyst into the pores. The functionalized silica was reacted with the siloxane-functionalized rhodium complexes to complete the catalyst immobilization procedure. The catalysts were found to give 100% conversion of 1-octene after 18 hours. Both catalysts exhibited high selectivity towards aldehydes, with the 2,4,6-trimethylphenyl catalyst **a** also yielding some alcohols (20% of the yield). The catalysts were re-used for a further seven catalytic runs with no loss in activity or selectivity. The selectivity towards aldehydes actually increased from 80% to a maximum of 98% in the case of catalyst **a**. The *n:iso* ratio showed a steady but small decrease in subsequent catalytic runs throughout for both catalysts. This was tentatively attributed to changes in the microstructure of MCM-41 during recycling.

1.2.4 Other modes of immobilization

Various other methods of immobilization have also been explored over the years. One such method is the use of coated magnetic nanoparticles as support, as studied by Shaikh *et al.*[79] Iron oxide nanoparticles are simple to prepare from low-cost materials, have a high surface area and can easily be functionalized to allow for suitable ligands to be anchored on their surface. The group synthesized a *bis*(diphenylphosphinomethyl)dopamine (bpd) ligand which

was anchored onto the iron nanoparticles as shown in Scheme 1.7. For the hydroformylation reactions, $RhCl_3$ or $[Rh(NBD)Cl]_2$ was added to form the active Rh complex *in situ*.

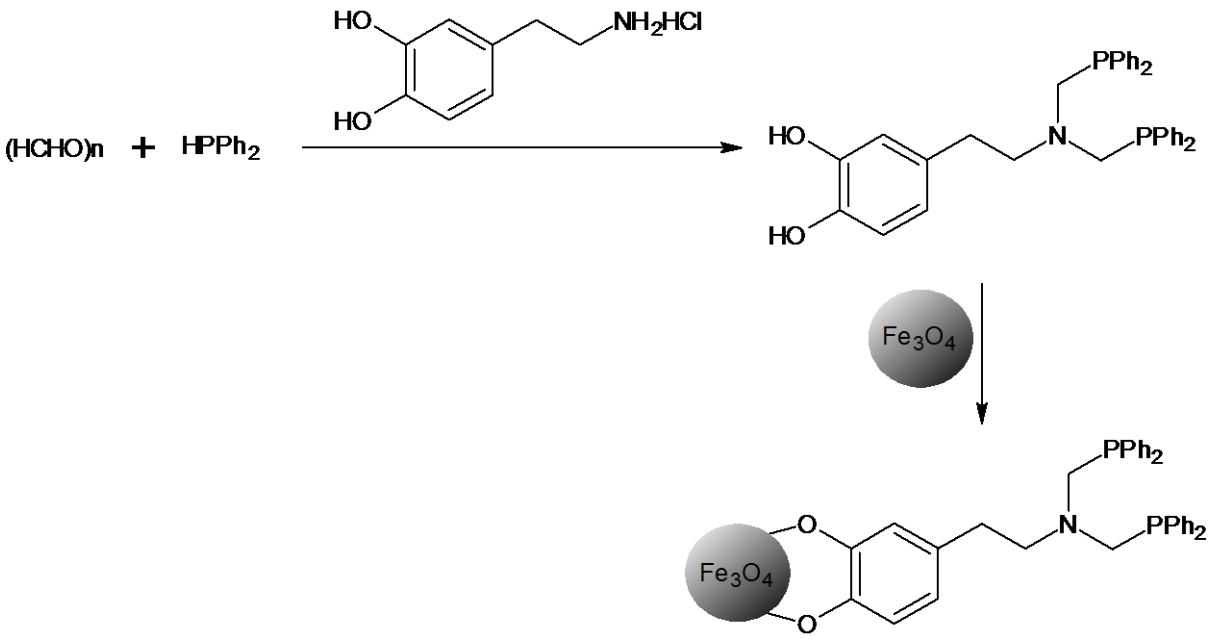

Scheme 1.7 Preparation of immobilized bpd ligand onto magnetic nanoparticles.[79]

The catalyst was tested in the hydroformylation of styrene as well as some substituted styrene derivatives. It was found that the catalyst gave quantitative conversion of the olefins after 16 to 24 hours. The *n:iso* ratio was influenced by the reaction temperature. It varied very little when different substrates were tested, with the lowest being 0.85 for 4-vinylanisole, and the highest 1.32 for nitrostyrene. The catalyst, with no new Rh(I) added, could be re-used seven times in the hydroformylation of styrene without significant loss of activity.

Cardozo *et al.* employed triphenylphosphine core functionalized cross-linked micelles with $[Rh(acac)(CO)_2]$ as nanoreactors for the aqueous biphasic nanoreactors for the hydroformylation of 1-octene. The hydrophobic core of the micelle provides a good environment for the hydroformylation reaction, while the hydrophilic shell confines the micelle to the aqueous phase and so presumably prevents rhodium metal leaching. The micelles were synthesized according to a previously reported procedure and the structure is shown in Figure 1.18.[80] $[Rh(acac)(CO)_2]$ in 1-decanal was added to form the catalyst *in situ*.

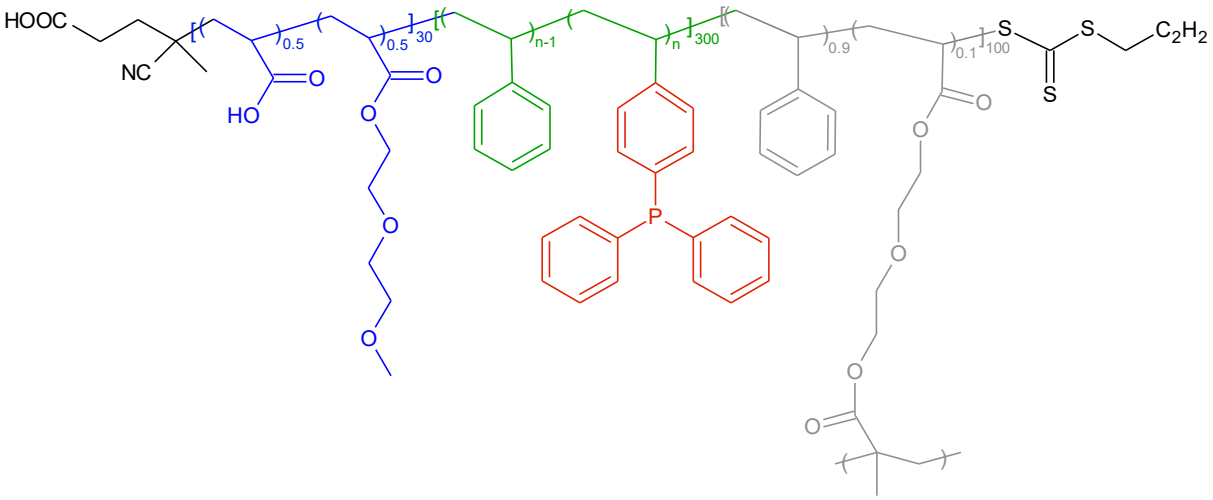

Figure 1.18 Polymeric backbone of micelles. Phosphine ligand used to coordinate to metal shown in red.[80]

This catalyst was tested in the hydroformylation of 1-octene, and was found to have an adequate turnover frequency value of 473 h^{-1}. The products formed were mostly aldehydes (90%), with some octene isomers being formed as well. The *n:iso* ratio was 2.7. The catalyst was re-used a further four times with no significant loss of TOF, and a small decrease in *n:iso* ratio. Rhodium leaching was low, being <2.7 ppm for all cycles. It is assumed that the rhodium is being lost into the organic phase together with the micelle nanoreactor, and not being leached from the nanoreactor.

Hydrotalcites are synthetic anionic clays with positively charged sheets containing exchangeable interlayer anions.[81] These anions can be replaced with a variety of organic and inorganic anions. Sharma *et al*. studied the intercalation of $HRh(CO)(TPPTS)_3$ in the interlayer spaces of Mg-Al hydrotalcite and the application of this catalyst material in the hydroformylation of alkenes.[82] The structural make-up of the catalytic material is shown in Figure 1.19.

Quantitative conversion of most linear alkenes was obtained after ten hours, with the conversion dropping for alkenes longer than 1-decene. The selectivity for aldehydes was 98% for 1-pentene and also dropped with increasing chain length, being 56% for 1-tridecene. The catalyst could be re-used seven times without loss in conversion, and with only slight loss in selectivity for aldehydes. The rhodium metal loss after seven cycles was 1.5 weight %.

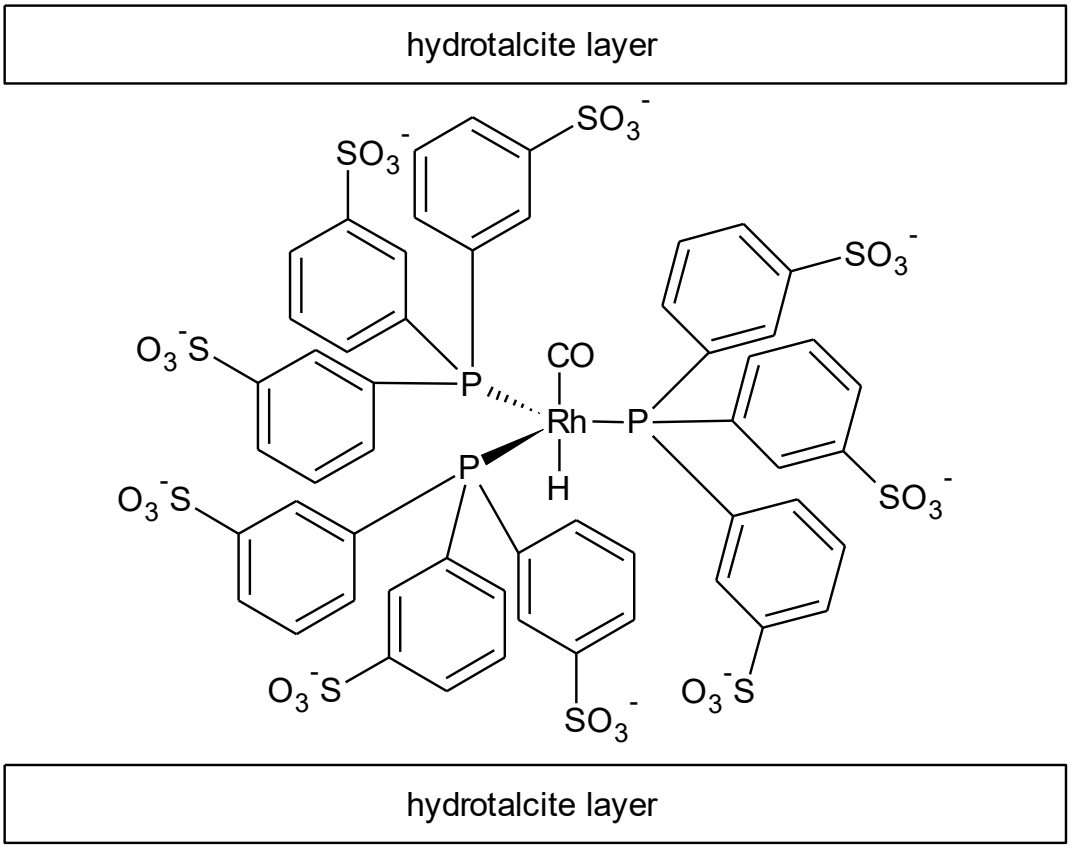

Figure 1.19 Intercalation of the complex $HRhCO(TPPTS)_3$ in the interlayer space of hydrotalcite.[82]

The techniques discussed in this section are less commonly found in the literature than, for example, immobilization on silica or biphasic hydroformylation.

1.3 Concluding remarks

From the literature it is clear that the search for a recyclable hydroformylation catalyst, capable of hydroformylating both short-chain and long-chain alkenes is still ongoing. While the Ruhrchemie-Rhône-Poulenc process has met with great industrial success, it is not applicable in the hydroformylation of longer-chain alkenes.

Some support materials, such as dendrimers and metal-organic frameworks, have the potential to be recycled and re-used, however, cases of this actually being reported are extremely limited in published work. Other supports, such as polymers, silica and ionic liquids, have a clear track record of being both active and recyclable, with rhodium leaching being extremely low in several cases.

The ease of synthesis, low cost, ease of functionalization and thermal and chemical stability of silica makes it an excellent choice as support. Mesoporous silica has the additional advantage of having larger surface areas and regular hexagonal channels, thereby increasing

the amount of catalyst that can be immobilized onto the surface when compared to amorphous silica.

It is clear that the choice of ligand also plays an important role in the activity and selectivity of the catalyst, as well as the ability of the catalyst to be recycled. This will be discussed further in Chapter 2.

1.4 Project objectives

The aims of this study were

1. To synthesize a range of ligands with N,P, N,N and N,O donor atoms, with some of these incorporating a siloxane tether. These ligands were then used to synthesize both neutral and cationic rhodium complexes.
2. To immobilize the siloxane functionalized complexes onto mesoporous silica and characterize these immobilized catalyst systems.
3. To apply the catalysts in the hydroformylation of 1-octene and compare the activity and selectivity of the different catalyst systems.
4. To recycle the immobilized catalysts in order to determine to what extent they could be re-used for hydroformylation.

Chapter two discusses the choice of ligands for the study, as well as the synthesis and characterization of the ligands and complexes. This includes Schiff base ligands and their complexes, as well as some triazole-based ligands and complexes. Various analytical and spectroscopic techniques were used to fully characterize the compounds.

During the characterization of the synthesized Schiff base complexes, some interesting solution behaviour and dynamic character of the complexes were observed. These behaviours were studied using various techniques, including advanced NMR techniques, and the results of these studies is reported in **Chapter three**.

The immobilization of the functionalized complexes is discussed in **Chapter four**. The catalysts were covalently linked to the silica surface *via* condensation of the siloxane functionality on the ligands with the silanol groups on the silica surface. The native silica and immobilized catalysts were characterized using a wide range of solid-stage techniques, including nitrogen adsorption to determine the surface area and pore sizes, scanning and transmission electron microscopy to observe some physical features and ICP-OES to determine the metal loading on the silica.

Chapter five discusses the application of the catalysts in the hydroformylation of 1-octene. The reaction parameters were optimised using a model catalyst. Subsequently, the various catalysts, both homogeneous and immobilized, were used and the results were compared.

The immobilized catalysts were recycled, and the effect of the supports on the catalytic reaction was also examined. Some preliminary mechanistic studies were also done.

1.5 References

1 B. Cornils, W. A. Herrmann and M. Rasch, *Angew. Chem. Int. Ed.*, 1994, **33**, 2144–2163.

2 Â. C. B. Neves, M. J. F. Calvete, T. M. V. D. Pinho e Melo and M. M. Pereira, *European J. Org. Chem.*, 2012, 6309–6320.

3 P. W. N. M. van Leeuwen and C. Claver, *Rhodium-catalyzed hydroformylaztion*, Kluwer Academic Publishers, Dordrecht, 2000.

4 G. W. Parshall and S. D. Ittel, *Homogeneous Catalysis: The Applications and Chemistry of Catalysis by Soluble Transition Metal Complexes*, Wiley, New York, 1992.

5 B. Cornils and W. A. Herrmann, *Aqueous-phase organometallic catalysis : concepts and applications*, Wiley, New York, 1998.

6 M. Torrent, M. Solà and G. Frenking, *Chem. Rev.*, 2000, **100**, 439–494.

7 J. Klosin and C. R. Landis, *Acc. Chem. Res.*, 2007, **40**, 1251–1259.

8 A. F. Peixoto, D. S. de Melo, T. F. Fernandes, Y. Fonseca, E. V. Gusevskaya, A. M. S. Silva, R. R. Contreras, M. Reyes, A. Usubillaga, E. N. dos Santos, M. M. Pereira and J. C. Bayón, *Appl. Catal. A Gen.*, 2008, **340**, 212–219.

9 Y. Deng, H. Wang, Y. Sun and X. Wang, *ACS Catal.*, 2015, **5**, 6828–6837.

10 M. Van Boven, N. H. Alemdaroglu and J. M. L. Penningep, *Ind. Eng. Chem. Res.*, 1975, **14**, 2–7.

11 R. Laï and E. Ucciani, *J. Mol. Catal. A: Chem.*, 1978, **4**, 401–410.

12 W. Cornely and B. Fell, *J. Mol. Catal A: Chem..*, 1982, **16**, 89–94.

13 J. F. Young, J. A. Osborn, F. H. Jardine and G. Wilkinson, *Chem. Commun.*, 1965, 131–132.

14 D. Evans, J. A. Osborn and G. Wilkinson, *Inorg. Phys. Theor.*, 1968, **566**, 3133–3142.

15 T. T. Adint, G. W. Wong and C. R. Landis, *J. Org. Chem.*, 2013, **78**, 4231–4238.

16 P. Dydio, R. J. Detz and J. N. H. Reek, *J. Am. Chem. Soc.*, 2013, **135**, 10817–10828.

17 H. Fernández-Pérez, J. Benet-Buchholz and A. Vidal-Ferran, *Org. Lett.*, 2013, **15**, 3634–3637.

18 K. Dong, X. Fang, R. Jackstell and M. Beller, *Chem. Commun.*, 2015, **51**, 5059–5062.

19 L. Rovira, M. Vaquero and A. Vidal-Ferran, *J. Org. Chem.*, 2015, **80**, 10397–10403.

20 Z. Yu, M. S. Eno, A. H. Annis and J. P. Morken, *Org. Lett.*, 2015, **17**, 3264–3267.

21 K. Takahashi, M. Yamashita, Y. Tanaka and K. Nozaki, *Angew. Chemie Int. Ed.*, 2012, **51**, 4383–4387.

22 I. Piras, R. Jennerjahn, R. Jackstell, A. Spannenberg, R. Franke and M. Beller, *Angew. Chem. Int. Ed. Engl.*, 2011, **50**, 280–284.

23 J. Pospech, I. Fleischer, R. Franke, S. Buchholz and M. Beller, *Angew. Chemie Int. Ed.*, 2013, **52**, 2852–2872.

24 A. E. C. Collis and I. T. Horváth, *Catal. Sci. Technol.*, 2011, **1**, 912–919.

25 I. R. Shaikh, *Journal of Catalysts*, 2014, 1–35.

26 I. Vural Gürsel, T. Noël, Q. Wang and V. Hessel, *Green Chem.*, 2015, **17**, 2012–2026.

27 F. Ungváry, *Coord. Chem. Rev.*, 2007, **251**, 2072–2086.

28 O. A. Matthews, A. N. Shipway and J. F. Stoddart, *Prog. Polym. Sci.*, 1998, **23**, 1–56.

29 M. T. Reetz, G. Lohmer and R. Schwicardi, *Angew. Chemie Int. Ed.*, 1997, **6**, 1526–1529.

30 D. Tomalia, J. R. Baker, J. Dewald, M. Hall, G. Kallos, S. Martin, J. Roeck, J. Ryder and P. Smith, *Macromolecules*, 1986, **19**, 2466–2468.

31 D. Wang and D. Astruc, *Coord. Chem. Rev.*, 2013, **257**, 2317–2334.

32 D. Astruc, D. Wang, C. Deraedt, L. Liang, R. Ciganda and J. Ruiz, *Synthesis.*, 2015, **47**, 2017–2031.

33 N. C. Antonels, J. R. Moss and G. S. Smith, *J. Organomet. Chem.*, 2011, **696**, 2003–2007.

34 B. C. E. Makhubela, A. M. Jardine, G. Westman and G. S. Smith, *Dalton Trans.*, 2012, **41**, 10715–10723.

35 E. B. Hager, B. C. E. Makhubela and G. S. Smith, *Dalton Trans.*, 2012, **41**, 13927–13935.

36 A. Moffat, *J. Catal.*, 1970, **18**, 193–199.

37 M. Čapka, P. Svoboda, M. Černý and J. Hetflejš, *Tetrahedron Lett.*, 1971, **12**, 4787–4790.

38 K. Nozaki, F. Shibahara, Y. Itoi, E. Shirakawa, T. Ohta, H. Takaya and T. Hiyama, *Bull. Chem. Soc. Jpn.*, 1999, **72**, 1911–1918.

39 E. V. Slivinskii and N. V. Kolesnichenko, *Russ. Chem. Bull.*, 2004, **53**, 2449–2454.

40 B. C. E. Makhubela, A. Jardine and G. S. Smith, *Green Chem.*, 2012, **14**, 338–347.

41 T. T. Adint and C. R. Landis, *J. Am. Chem. Soc.*, 2014, **136**, 7943–7953.

42 Q. Sun, M. Jiang, Z. Shen, Y. Jin, S. Pan, L. Wang, X. Meng, W. Chen, Y. Ding, J. Li and F.-S. Xiao, *Chem. Commun.*, 2014, **50**, 11844–11847.

43 F. Wang, J. Mielby, F. H. Richter, G. Wang, G. Prieto, T. Kasama, C. Weidenthaler, H.-J. Bongard, S. Kegnaes, A. Fürstner and F. Schüth, *Angew. Chemie Int. Ed.*, 2014, **53**, 8645–8648.

44 P. Kuhn, A. Thomas and M. Antonietti, *Macromolecules*, 2009, **42**, 319–326.

45 Y. Zhang and S. N. Riduan, *Chem. Soc. Rev.*, 2012, **41**, 2083–2094.

46 V. Davankov and A. V. Pastukhov, *J. Phys. Chem. B*, 2011, **115**, 15188–15195.

47 E. B. Hager, B. C. E. Makhubela and G. S. Smith, *Dalton Trans.*, 2012, **41**, 13927–13935.

48 C. W. Kohlpaintner, R. W. Fischer and B. Cornils, *Appl. Catal. A Gen.*, 2001, **221**, 219–225.

49 H. Fu, M. Li, H. Mao, Q. Lin, M. Yuan, X. Li and H. Chen, *Catal. Commun.*, 2008, **9**, 1539–1544.

50 H. Fu, M. Li, J. Chen, R. Zhang, W. Jiang, M. Yuan, H. Chen and X. Li, *J. Mol. Catal. A Chem.*, 2008, **292**, 21–27.

51 S. Siangwata, N. Baartzes, B. C. E. Makhubela and G. S. Smith, *J. Organomet. Chem.*, 2015, **796**, 26–32.

52 Y. Chauvin, L. Mussmann and H. Olivier, *Angew. Chem. Int. Ed. Engl.*, 1996, **34**, 2698–2700.

53 S.-J. Chen, Y.-Y. Wang, W.-M. Yao, X.-L. Zhao, G. VO-Thanh and Y. Liu, *J. Mol. Catal. A Chem.*, 2013, **378**, 293–298.

54 X. Jin, D. Yang, X. Xu and Z. Yang, *Chem. Commun.*, 2012, **48**, 9017–9019.

55 C. P. Mehnert, R. A. Cook, N. C. Dispenziere and M. Afeworki, *J. Am. Chem. Soc.*, 2002, **124**, 12932–12933.

56 A. Weiss, M. Munoz, A. Haas, F. Rietzler, H. P. Steinrueck, M. Haumann, P. Wasserscheid and B. J. M. Etzold, *ACS Catal.*, 2016, **6**, 2280–2286.

57 F. Rodríguez-Reinoso, *Carbon N. Y.*, 1998, **36**, 159–175.

58 Y. Zhang, K. Nagasaka, X. Qiu and N. Tsubaki, *Ratio*, 2004, **276**, 103–111.

59 Z. Ma, X. Liu, G. Yang and C. Liu, *Fuel Process. Technol.*, 2009, **90**, 1241–1246.

60 M. C. Román-Martínez, J. a. Díaz-Auñón, C. Salinas-Martínez De Lecea and H. Alper, *J. Mol. Catal. A Chem.*, 2004, **213**, 177–182.

61 D. R. Dreyer, S. Park, C. W. Bielawski and R. S. Ruoff, *Chem. Soc. Rev.*, 2010, **39**, 228–240.

62 M. Tan, G. Yang, T. Wang, T. Vitidsant, J. Li, Q. Wei, P. Ai, M. Wu, J. Zheng and N. Tsubaki, *Catal. Sci. Technol.*, 2016, **6**, 1162–1172.

63 M. Kaur, S. Sharma and P. M. S. Bedi, *Chinese J. Catal.*, 2015, **36**, 520–549.

64 A. Corma and H. Garcia, *Adv. Synth. Catal.*, 2006, **348**, 1391–1412.

65 M. Opanasenko, P. Štěpnička and J. Čejka, *RSC Adv.*, 2014, **4**, 65137–65162.

66 H. Arai, T. Kaneko and T. Kunugi, *Chem. Lett.*, 1975, 265–268.

67 K. Allum, R. Hancock and I. Howell, *J. Organomet. Chem.*, 1975, **87**, 203–216.

68 K. Allum, R. Hancock, I. Howell, R. Pikethly and P. Robinson, *J. Catal.*, 1976, **43**, 322–330.

69 A. J. Sandee, J. N. Reek, P. C. Kamer and P. W. van Leeuwen, *J. Am. Chem. Soc.*, 2001, **123**, 8468–8476.

70 E. Lindner, T. Schneller, F. Auer and H. Mayer, *Angew. Chem. Int. Ed. Engl.*, 1999, **38**, 2154–2174.

71 J. Blum, A. Rosenfeld, N. Polak, O. Israelson, H. Schumann and D. Avnir, *J. Mol. Catal. A Chem.*, 1996, **107**, 217–223.

72 J. S. Beck, J. C. Vartuli, W. J. Roth, M. E. Leonowicz, C. T. Kresge, K. D. Schmitt, C. T.-W. Chu, D. H. Olson, E. W. Sheppard, S. B. McCullen, J. B. Higgins and J. L. Schlenkert, *J. Am. Chem. Soc.*, 1992, **114**, 10834–10843.

73 D. Zhao, J. Feng, Q. Huo, N. Melosh, G. Fredrickson, B. Chmelka and G. Stucky, *Science (80-.).*, 1998, **279**, 548–52.

74 C. T. Kresge, M. E. Leonowicz, W. J. Roth, J. C. Vartuli and J. S. Beck, *Nature*, 1992, **359**, 710–712.

75 F. Marras, J. Wang, M.-O. Coppens and J. N. H. Reek, *Chem. Commun.*, 2010, **46**, 6587–6589.

76 J. A. Bae, K.-C. Song, J.-K. Jeon, Y. S. Ko, Y.-K. Park and J.-H. Yim, *Microporous Mesoporous Mater.*, 2009, **123**, 289–297.

77 S. Dastgir, K. S. Coleman and M. L. H. Green, *Dalton Trans.*, 2011, **40**, 661–672.

78 D. S. Shephard, W. Zhou, T. Maschmeyer, J. M. Matters, C. L. Roper, S. Parsons, B. F. G. Johnson and M. J. Duer, *Angew. Chemie - Int. Ed.*, 1998, **37**, 2719–2723.

79 M. N. Shaikh, M. Bououdina, A. A. Jimoh, M. A. Aziz, A. Helal, A. S. Hakeem, Z. H. Yamani and T.-J. Kim, *New J. Chem.*, 2015, **39**, 7293–7299.

80 X. Zhang, A. F. Cardozo , S. Chen , W. Zhang, C. Julcour , M. Lansalot, J.-F. Blanco , F. Gayet , H. Delmas , B. Charleux , E. Manoury , F. D'Agosto and R. Poli , *Chem. - A Eur. J.*, 2014, **20**, 15505–15517.

81 F. Cavani, F. Trifirò and A. Vaccari, *Catal. Today*, 1991, **11**, 173–301.

82 S. K. Sharma, P. A. Parikh and R. V. Jasra, *J. Mol. Catal. A Chem.*, 2010, **316**, 153–162.

CHAPTER 2 : SYNTHESIS OF SCHIFF BASE AND TRIAZOLE LIGANDS AND THEIR RHODIUM COMPLEXES

2.1 Rhodium complexes in hydroformylation

The choice of ligand has always played an important role in the rhodium-catalysed hydroformylation reaction. Phosphine- and phosphite-based ligands have been commonly used, and are among the most well-studied today.[1–6] These ligands are known form active and selective hydroformylation catalysts in conjunction with rhodium, with linear to branched ratios greater than 10:1 being common, and ratios greater than 50:1 being reported in a few cases.[6] The activity and selectivity of the catalyst systems is usually attributed to the phosphorous donor atoms, as well as the bulky structure of the ligands. A few examples of such ligands are shown in Figure 2.1.

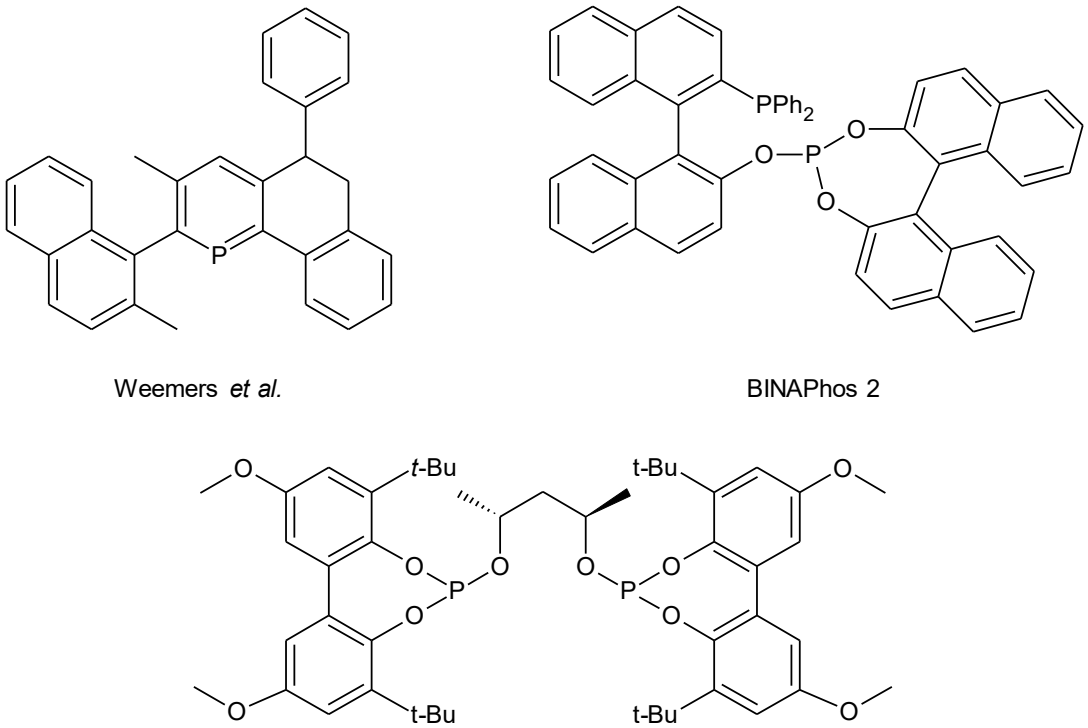

Weemers *et al.*

BINAPhos 2

(*R*,*R*) CHIRAPHITE

Figure 2.1 Some examples of phosphine and phosphite ligands used as ligands in the hydroformylation reaction.[2–4]

The use of nitrogen-donor ligands in hydroformylation is less well-studied, especially with regards to the mechanism of hydroformylation with complexes containing these type of ligands. Schiff base ligands, first described by Hugo Schiff in 1864, allow for the synthesis of a range of ligands which vary with regards to the donor atoms.[7] These ligands are synthesized *via* the condensation of an amine and an aldehyde. By changing the starting aldehyde, one of the donor atoms can be varied to, among others, phosphorous, nitrogen or oxygen. The influence of these different chelating ligands can then be studied. Another advantage of Schiff base ligands, with the eye on immobilization, is the ease with which the siloxane functionality can be incorporated into the ligand structure. This will be discussed in more detail in Section 2.1.1.

One type of nitrogen-containing ligands that have received some attention in the literature related to hydroformylation are the hemilabile P,N type ligands. Andrieu *et al*. studied various amino-phosphane ligands in conjunction with $[RhCl(COD)]_2$ using high-pressure spectroscopic techniques (Figure 2.2).[8]

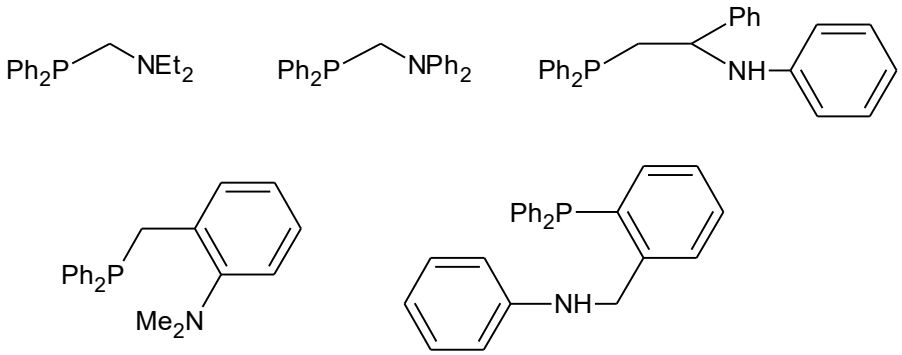

Figure 2.2 P,N ligands used together with $[RhCl(COD)]_2$ in hydroformylation reactions by Andrieu *et al*.[8]

The authors found that the complexes form *in situ*, as monodentate $[RhCl(CO)_2(\kappa^1\text{-}P\text{-}P,N)]$ complexes under hydroformylation conditions. The uncoordinated amino group assists in the formation of the rhodium-hydride active species due to the basicity of the nitrogen, as well as its distance from the metal centre playing a role in this process.

Maura *et al*. later synthesized a range of pyridine-based *N*-phosphanylamindine ligands in order to study their coordination to rhodium (Figure 2.3).[9]

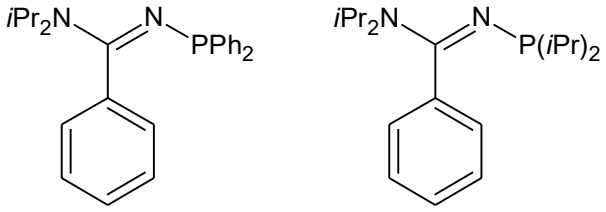

Figure 2.3 *N*-phosphanylamidine ligands used in hydroformylation together with rhodium precursors used by Maura *et al*.[9]

These complexes were also evaluated in the hydroformylation of 1-octene. It was found that, during the reaction, the ligands coordinated in a monodentate fashion to the rhodium, with only the phosphorous donor atom coordinating. The most effective complex gave a turnover number of 725 mol product formed per mol rhodium after 6 hours under optimal conditions. The *n:iso* ratio was below 2.22 in all cases, indicating that these ligands do not influence regioselectivity to a large extent.

Recently, the group of Smith published a number of papers in which they report the use of P,N Schiff base ligands in hydroformylation catalysis.[10–12] These catalysts gave turnover numbers in the range of 223 – 261 h^{-1}, with selectivity towards aldehydes and *n:iso* ratios of 2.6:1 – 2.7:1 after 2 hours. The P,N ligands therefore do show some moderate selectivity towards the formation of the linear aldehyde. Some other Schiff base ligands, containing N,N and N,O donor atoms, were studied as well.[13–15] Some examples of these are shown in Figure 2.4. These catalysts give reasonable conversions and turnover frequencies in the range of 250 – 310 h^{-1}, with good selectivity towards aldehydes. The *n:iso* ratio for these catalysts were however fairly low, ranging from 1.3:1 to 0.7:1.

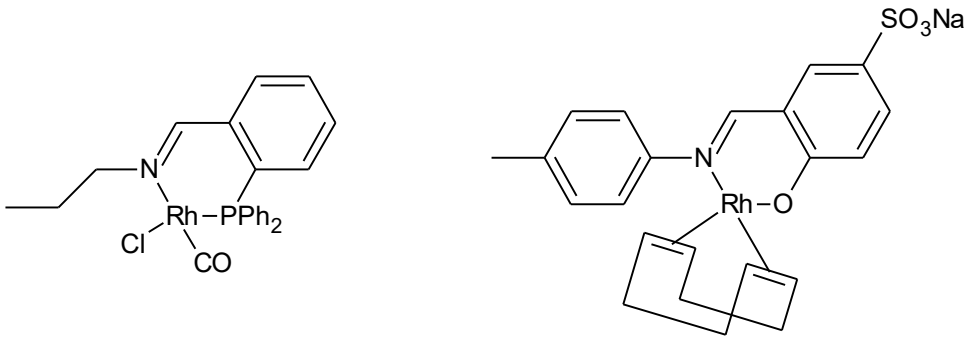

Antonels *et al*. Matsinha *et al*.

Figure 2.4 Examples of Schiff base rhodium complexes.[10,14]

From the available literature it is clear that Schiff base rhodium complexes are relatively active in the hydroformylation reaction. The selectivity towards aldehydes is high, but the regioselectivity is fairly mediocre when compared with the best-performing phosphine ligands.

There is thus a need to gain greater insight into the reaction mechanism using the latter complexes during the hydroformylation reaction, in order that the ligand systems might be tailored to improve both chemo- and regioselectivity.

2.1.1 Functionalization of ligands for silica immobilization

As discussed in Chapter 1, the recycling of hydroformylation catalysts is an area that has attracted much attention - mainly due to the high cost of rhodium. There are a number of ways in which the recycling can be done, one of which is to immobilize the catalyst onto a solid support such as silica. The immobilization of a metal complex onto silica can be achieved through either a convergent or sequential immobilization process. When the convergent method is followed, the discrete metal complex containing a siloxane moiety is first synthesized and isolated, followed by the immobilization of this complex onto silica. This is in contrast to the sequential process, where the ligand is first immobilized onto, or synthesized directly on the silica, followed by the metal precursor addition to form the complex. The two methods are illustrated in Scheme 2.1.

Numerous examples of both approaches can be found in the literature, with the sequential method being the more common approach.[16–20] A possible drawback of this method is that there is uncertainty over whether all the metal is actually bound to the immobilized ligand, as some of the metal salts may temporarily be adsorbed onto the silica surface. We followed the convergent route in order to have more control regarding the exact environment of the metal centres.

Schiff base ligands allow for easy incorporation of a siloxane moiety into the ligand. For example, 3-aminopropyltriethoxysilane is reacted with an appropriate aldehyde to form a bidentate pyridine-imine ligand. The use of Schiff bases can however have some drawbacks in that it limits the amine that can be used to one containing a siloxane functionality. This prohibits the incorporation of functional groups with varying electronic and steric properties. These types of variations are often used in ligand design in order to study the effects on catalysis. Another issue that might be encountered is that the imine bond could be prone to hydrolysis under certain reaction conditions, and this could lead to the metal leaching from the support. Some possible alternatives to siloxane functionalized imines are therefore also investigated in this chapter.

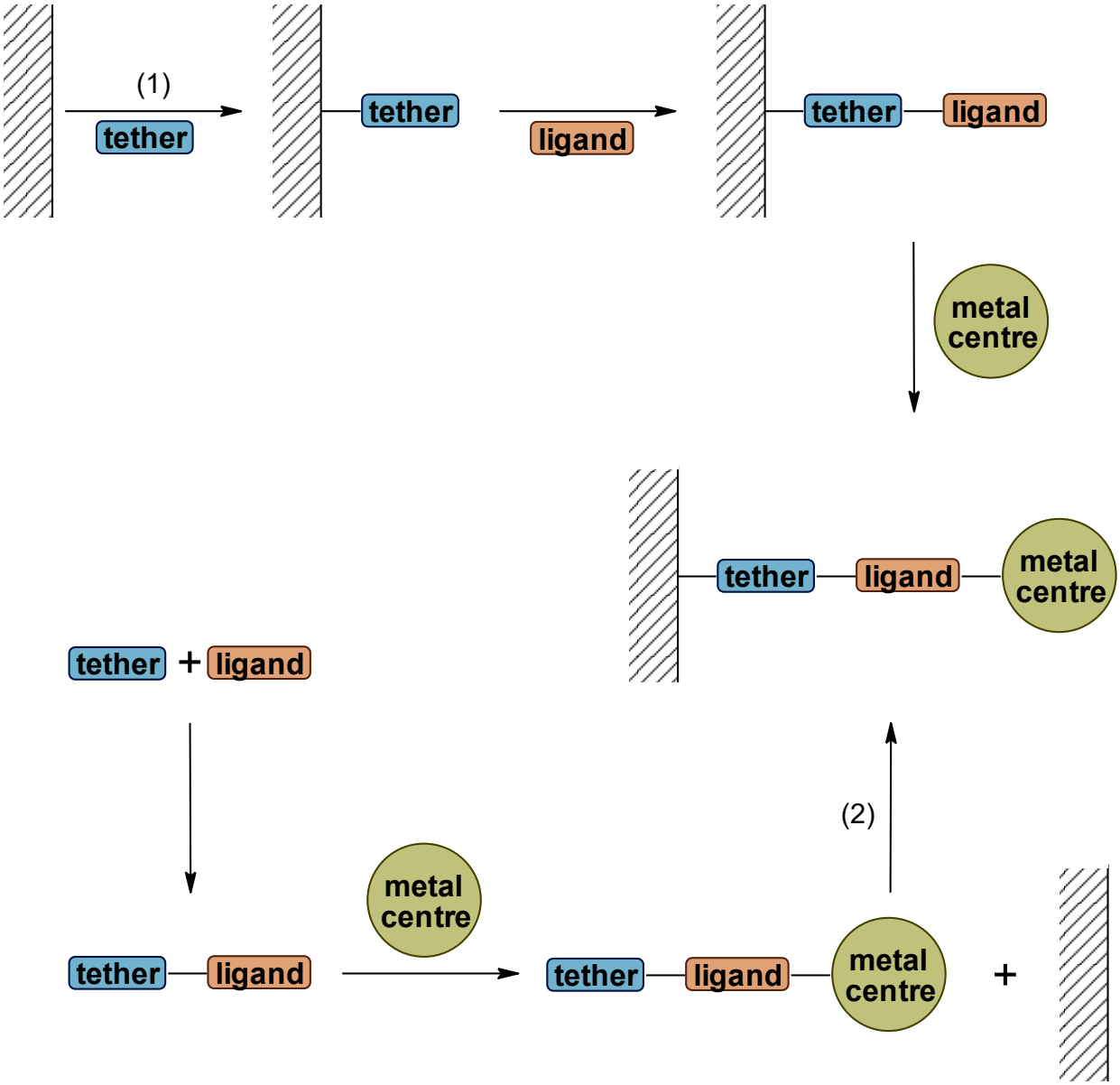

Scheme 2.1 Two methods of immobilization: sequential (1) and convergent (2) immobilization.

2.2 Results and discussion

2.2.1 Ligands and complexes synthesized in this thesis

This chapter discusses *inter alia* the synthesis and characterization of six Schiff base ligands and their rhodium complexes, as well as two pyridyl-triazole ligands and their rhodium complexes. A summary of the ligands and complexes together with their abbreviations is given below in Figures 2.6 – 2.9.

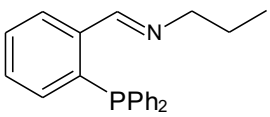

L2.1

N-(2-Diphenylphosphino)benzylidene-propanamine

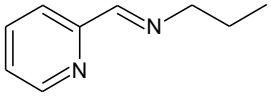

L2.2

N-(2-Pyridinylmethylene)-1-propanamine

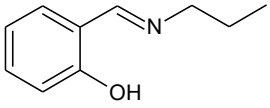

L2.3

N-Propylsalicylaldimine

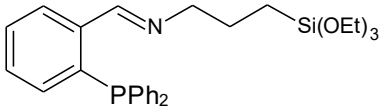

L2.4

N-(2-Diphenylphosphino)benzylidene-3-(triethoxysilyl)-1-propanamine

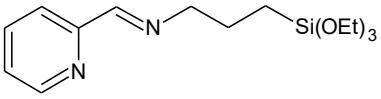

L2.5

N-(2-Pyridinylmethylene)-3-(triethoxysilyl)-1-propanamine

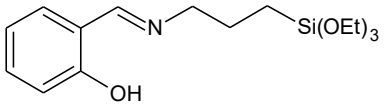

L2.6

Salicylidene-3-aminopropyltriethoxysilane

Figure 2.5 Schiff base ligands L2.1 - L2.2 described in this chapter.

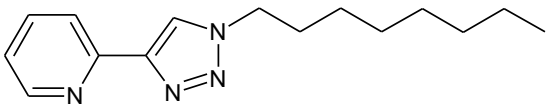

L2.7

2-(1-Octyl-1 *H*-1,2,3-triazol-4-yl)pyridine

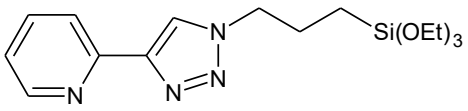

L2.8

2-(1-[3-(Triethoxysilyl)propyl]-1 *H*-1,2,3-triazol-4-yl)pyridine

Figure 2.6 Pyridyl-triazole ligands L2.7 and L2.8 described in this chapter.

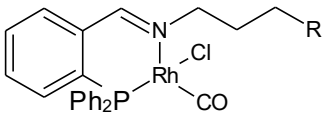

C2.1

N-(2-Diphenylphosphino)benzylidene-propanamine rhodium(I) chlorocarbonyl complex

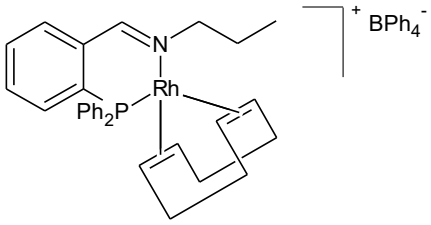

C2.2

N-(2-Diphenylphosphino)benzylidene-propanamine rhodium(I)1,5-cyclooctadiene complex

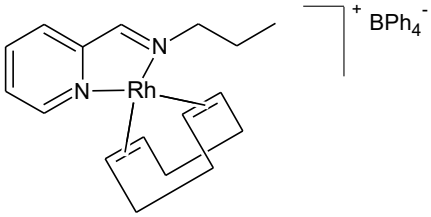

C2.3

N-(2-Pyridinylmethylene)-1-propanamine rhodium(I)1,5-cyclooctadiene complex

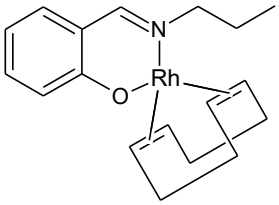

C2.4

N-Propylsalicylaldimine rhodium(I)1,5-cyclooctadiene complex

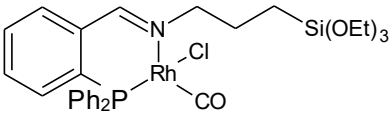

C2.5

N-(2-Diphenylphosphino)benzylidene-3-(triethoxysilyl)-1-propanamine rhodium(I) chlorocarbonyl complex

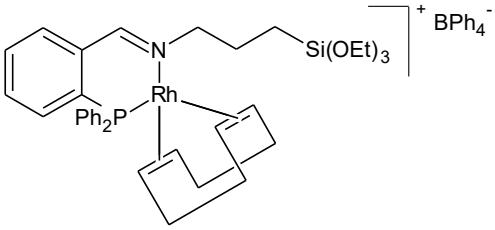

C2.6

N-(2-Diphenylphosphino)benzylidene-3-(triethoxysilyl)-1-propanamine rhodium(I)1,5-cyclooctadiene complex

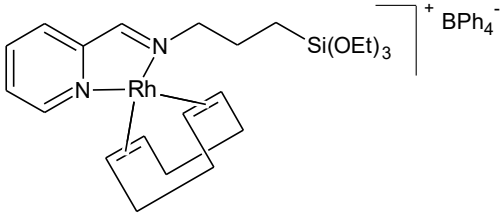

C2.7

N-(2-Pyridinylmethylene)-3-(triethoxysilyl)-1-propanamine rhodium(I)1,5-cyclooctadiene complex

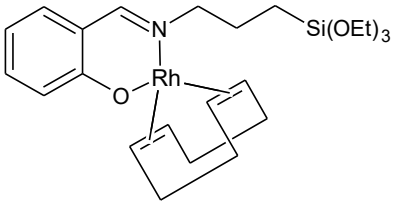

C2.8

Salicylidene-3-aminopropyltriethoxysilane rhodium(I)1,5-cyclooctadiene complex

Figure 2.7 Schiff base rhodium complexes C2.1 - C2.8 described in this chapter.

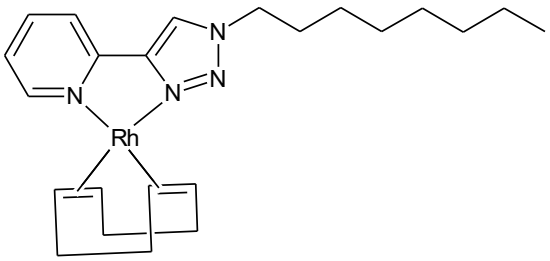

L2.9
2-(1-Octyl-1 *H*-1,2,3-triazol-4-yl)pyridine rhodium(I)1,5-cyclooctadiene complex

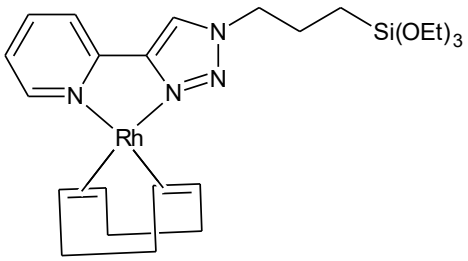

L2.10
2-(1-[3-(Triethoxysilyl)propyl]-1 *H*-1,2,3-triazol-4-yl)pyridine rhodium(I)1,5-cyclooctadiene complex

Figure 2.8 Pyridyl-triazole rhodium complexes described in this chapter.

2.2.2 Synthesis and characterization of Schiff base ligands L2.1 – L2.6

Six ligands were synthesized *via* Schiff base condensation as shown in Scheme 2.2. The synthetic routes were adapted from literature procedures.[12,15] Three different aldehydes were employed to synthesize the so-called 'model ligands', using propylamine as amine, while siloxane-functionalized ligands were prepared using 3-aminopropyltriethoxysilane as amine. The aldehydes differ in the substituent *ortho* to the aldehyde carbon, giving rise to different donor atoms in each ligand. Three different chelates, namely N,P, N,O and N,N, were prepared in this manner. In the case of **L2.2** – **L2.6**, the aldehyde and the amine were reacted in a 1:1 ratio in diethyl ether with the addition of magnesium sulphate to remove any water formed as by-product. For **L2.1** it was found that the reaction produced a higher yield of the product when the reaction was done in the absence of added solvent, employing an excess of propylamine as both reactant and solvent in the absence of magnesium sulphate.

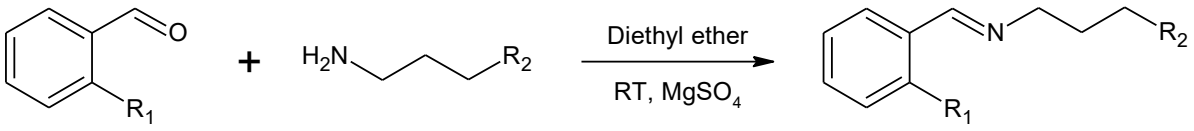

L2.1: $R_1 = PPh_2$, $R_2 = H$
L2.3: $R_1 = OH$, $R_2 = H$
L2.4: $R_1 = PPh_2$, $R_2 = Si(OEt)_3$
L2.6: $R_1 = OH$, $R_2 = Si(OEt)_3$

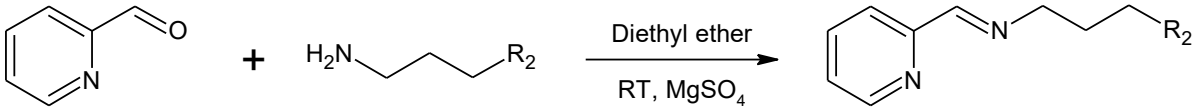

L2.2: $R_2 = H$
L2.5: $R_2 = Si(OEt)_3$

Scheme 2.2 Synthesis of Schiff base ligands L2.1 – L2.6.

The model ligands were found to be air-stable over long periods of time, while the siloxane functionalized ligands decomposed over time when stored at room temperature in air. The moisture-sensitive ligands changed from oils into gel-like residues, with changes being observed in the siloxane region of the infrared spectra as shown in Figure 2.9. The peak at 1074 cm^{-1} appears sharp and well defined shortly after synthesis of the ligand. When the infrared spectrum is collected after the ligand was left for one year at ambient conditions, the peak shows significant broadening and is shifted to 1033 cm^{-1}. This indicates that the siloxane moieties are gradually undergoing hydrolysis and self-condensation. The functionalized ligands were therefore stored in a glovebox under nitrogen conditions or prepared shortly before use.

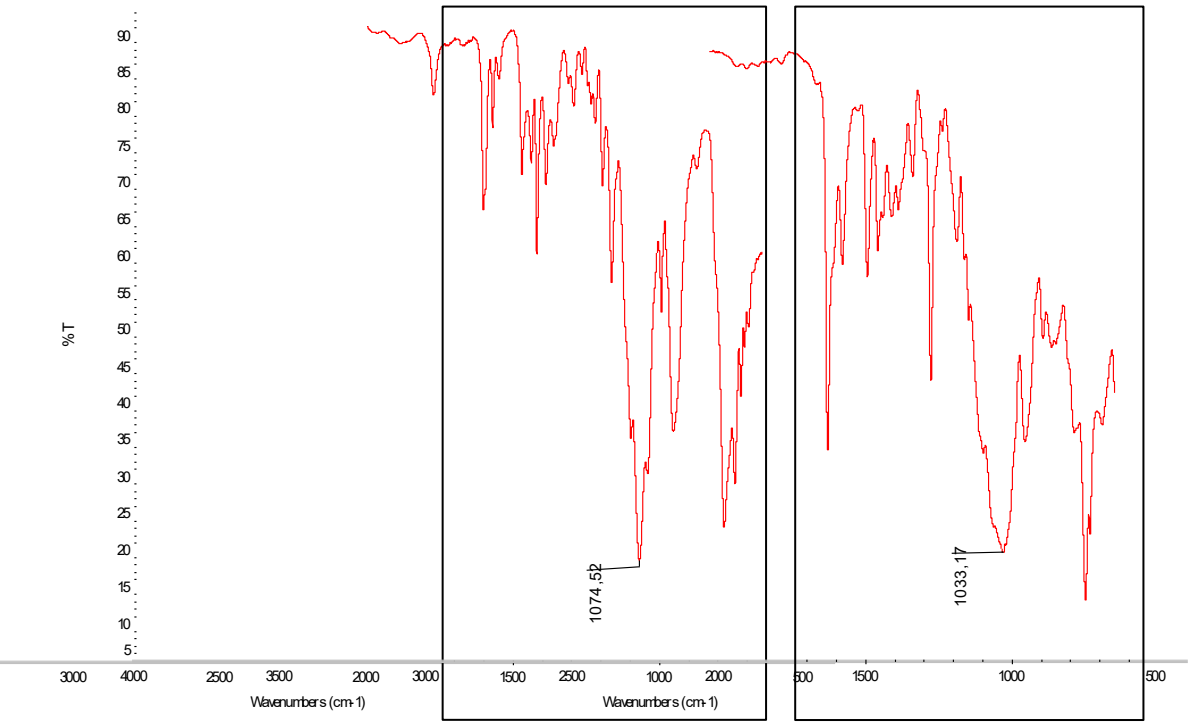

Figure 2.9 Fingerprint region of the infrared spectrum of L2.6 shortly after synthesis (left) and after 1 year under ambient conditions (right). Note the broadening of the peak at 1033 cm^{-1}.

2.2.2.1 Characterization of Schiff base ligands using FT-IR spectroscopy

The successful formation of the Schiff base ligands was monitored by the disappearance of the aldehyde (C=O) band in the region of 1728 cm^{-1} – 1740 cm^{-1} in the infrared spectrum and the appearance of a new band in the region 1630 cm^{-1} – 1650 cm^{-1}. This latter band is due to the C=N stretch in the formed imine. In the case of **L2.2** and **L2.5**, the pyridine C=N band was seen at 1586 cm^{-1} and the C=C bonds were observed at 1566 cm^{-1}. These bands in the infrared spectrum are also commonly observed in literature.[10,21]

For the siloxane functionalized ligands, the characteristic Si-O stretch at 1071 cm^{-1} was observed as well. Normally, broadening of this band indicates hydrolysis of the siloxane functionalities which could ultimately lead to self-condensation, as seen for the ligands over a long time period. This band was therefore carefully monitored throughout the synthetic process.

Selected IR vibrations are shown in Table 2.1 below:

Table 2.1 Selected IR vibrations of Schiff base ligands L2.1 – L2.6.[a]

Ligand	Imine:	Pyridine ring:		Siloxane:	
	$\nu_{C=N}$ cm^{-1}	$\nu_{C=N}$ cm^{-1}	$\nu_{C=C}$ cm^{-1}	$\nu_{Si-O-Si}$ cm^{-1}	ν_{Si-OH} cm^{-1}
L2.1	1636	-	-	-	-
L2.2	1649	1586	1566	-	-
L2.3	1631	-	-	-	-
L2.4	1636	-	1584	1068	740
L2.5	1648	1586	1567	1071	769
L2.6	1632	-	-	1071	768

[a] Oils recorded as neat samples using an ATR accessory

A typical IR spectrum, that of the functionalized iminophosphine ligand **L2.4**, is shown below in Figure 2.10. The imine peak at 1635 cm^{-1} is clearly visible, as is the strong siloxane stretching band at 1067 cm^{-1}

Figure 2.10 IR spectrum of functionalized N,P ligand L2.4 showing the peaks indicative of the siloxane moiety at 1067 cm^{-1}, 950 cm^{-1} and 740 cm^{-1}.

2.2.2.2 Characterization of Schiff base ligands using ^{1}H NMR spectroscopy

Along with infrared spectroscopy, ^{1}H NMR spectroscopy was very useful to determine the successful formation of the ligands. The disappearance of the aldehyde proton resonance in the region of 10.42 ppm was monitored along with the appearance of a new resonance, due to the imine proton, in the 8.30 ppm – 8.90 ppm region. The siloxane functionalized ligands also show characteristic resonances, namely a triplet at 1.22 pm and a quartet at 3.79 ppm, due to the methylene and methyl protons of the siloxane moiety.

Selected ^{1}H NMR resonances are shown in Table 2.2 below.

Table 2.2 Selected ^{1}H NMR data for Schiff base ligands L2.1 – L2.6.[a]

Ligand	Siloxane functionality:		Imine:
	$Si(OCH_2C\underline{H}_3)_3$ (ppm)	$Si(OC\underline{H}_2CH_3)_3$ (ppm)	$N{=}C\underline{H}$ (ppm)
L2.1	-	-	8.88
L2.2	-	-	8.62
L2.3	-	-	8.34
L2.4	1.22 (t, 9H)	3.80 (q, 6H)	8.89
L2.5	1.21 (t, 9H)	3.81 (q, 6H)	8.62
L2.6	1.24 (t, 9H)	3.82 (q, 6H)	8.35

[a] Recorded in chloroform-*d* at 25 °C

2.2.3 Synthesis of Schiff base rhodium complexes

The synthesis of the rhodium complexes were carried out using two different rhodium precursors, namely di-μ-chloro-tetracarbonyldirhodium(I) $[RhCl(CO)_2]_2$ for **C2.1** and **C.2.5** and the chloro(1,5-cyclooctadiene)rhodium(I) dimer $[RhCl(COD)]_2$ for **C2.2**, **C2.3**, **C2.4**, **C2.6**, **C2.7** and **C2.8**. $[RhCl(CO)_2]_2$ was synthesized by adapting a literature procedure from Deeming *et al.*[22] Instead of bubbling carbon monoxide through the solution, the reaction was allowed to proceed at 15 bar CO for 6 hours. The orange residue obtained after solvent removal was then purified *via* sublimation under vacuum and the product was obtained as red-orange needle-shaped crystals.

$[RhCl(COD)]_2$ was initially synthesized by following a literature procedure.[23] The 18 hour reaction gave a yield of between 50% and 60%. Drawing inspiration from a procedure for the synthesis of a ruthenium metal precursor in a microwave reactor by Tönnemann *et al.*, we developed a microwave synthesis method for the synthesis of $[RhCl(COD)]_2$.[24] In this procedure, $RhCl_3{\cdot}H_2O$ was dissolved in a 1:5 mixture of water and ethanol and reacted with an excess of 1,5-cyclooctadiene in a microwave reactor at a temperature of 100 °C, using a power of 100 W. A dark yellow solid was obtained. Using this method, the reaction was completed in 5 minutes and the yield was improved to between 70% and 75%.

The neutral N,P complexes **C2.1** and **C2.5** were synthesized by first dissolving 2 equivalents of the appropriate ligand in THF, and then adding 1 equivalent of $[RhCl(CO)_2]_2$, dissolved in THF, dropwise to the ligand solution.[10] After stirring at room temperature for a short time, an orange solid formed. The solvent was then reduced, hexane was added to precipitate more of the product, which was collected by filtration. The synthesis of these complexes is shown in Scheme 2.3.

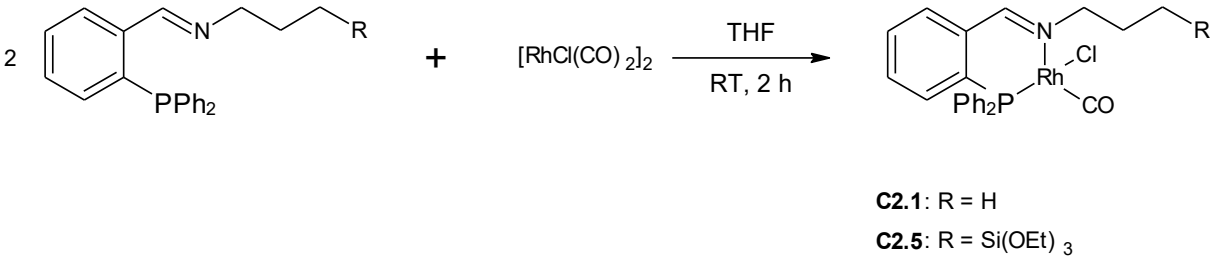

C2.1: R = H
C2.5: R = Si(OEt)$_3$

Scheme 2.3 Synthesis of neutral rhodium complexes C2.1 and C2.5.

The cationic N,P and N,N rhodium complexes **C2.2**, **C2.3**, **C2.6** and **C2.7** were synthesized by adapting a literature procedure which is shown in Scheme 2.4.[21] For these complexes, the chloride counter-ion was exchanged with the larger tetraphenylborate counter-ion, as this made isolating solid complexes much easier. Tetraphenylborate was chosen as counter-ion over other commonly used counter-ions such as tetrafluoroborate and hexafluorophosphate, since the latter two yield complexes which are fairly soluble in methanol, making purification of these complexes more difficult.

In order to synthesize the N,P and N,N rhodium complexes, $[RhCl(COD)]_2$ was dissolved in DCM and two equivalents of the appropriate ligand dissolved in DCM was added dropwise to the metal precursor solution. An immediate colour change (yellow to dark orange for **C2.2** and **C2.6**, yellow to dark purple for **C2.3** and **C2.7**) was observed. The solvent was removed and the residue re-dissolved in methanol since the counter-ion salt used, sodium tetraphenylborate is highly soluble in methanol. The solution was cooled to 0°C and the counter-ion was added. A solid formed immediately upon addition of the counter-ion. The products were isolated by filtration and washed with methanol to remove excess sodium tetraphenylborate, as well as the formed solid chloride.

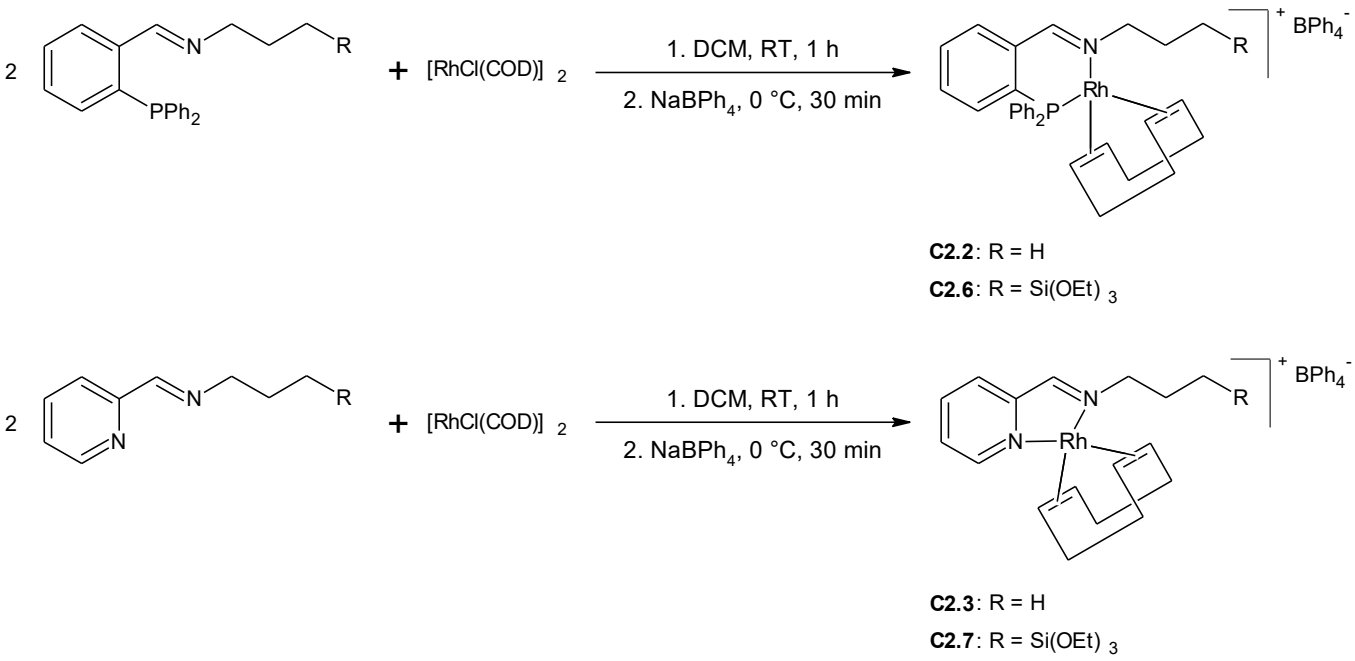

Scheme 2.4 Synthesis of cationic rhodium complexes C2.2, C2.3, C2.6 and C2.7.

All the complexes were isolated as air-stable solids in moderate yields. During the analysis of the complexes it was found that they are unstable in solution and started to decompose after approximately 36 hours in both chloroform and acetone. The N,P complexes **C2.2** and **C2.6** melt above 120°C, while the N,N complexes **C2.3** and **C2.7** have fairly low melting points, both melting at under 100°C.

The neutral N,O complexes, **C2.4** and **C2.8**, were synthesized following a literature procedure.[15] Potassium hydroxide was added to the ligand in solution to assist in the deprotonation of the –OH group, after which the metal precursor was added to the solution. A yellow solid product was obtained after recrystallization. Both the model and functionalized complexes were air-stable solids with relatively low melting points, with **C2.4** melting between 75 and 78°C and **C2.8** melting between 89 and 92°C. The synthesis is illustrated in Scheme 2.5.

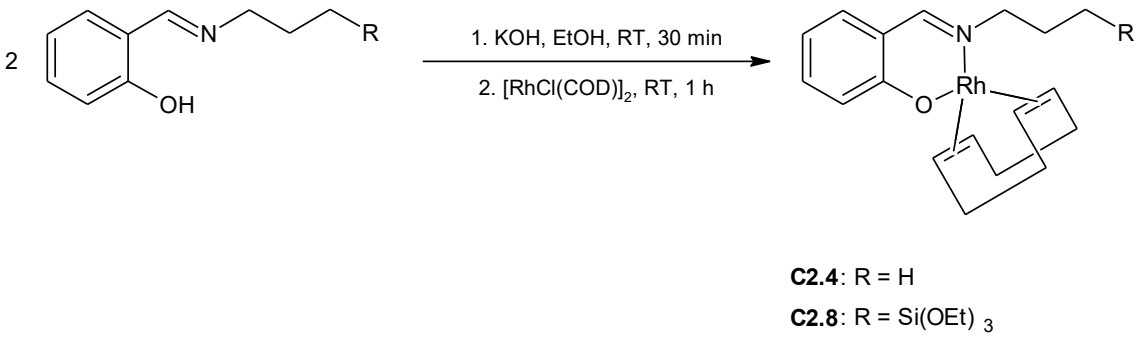

Scheme 2.5 Synthesis of neutral rhodium complexes C2.4 and C2.8.

2.2.3.1 Characterization of Schiff base rhodium complexes using FT-IR spectroscopy

FT-IR spectroscopy provided a quick and facile method to monitor coordination of the ligands to the metal centre, since the imine band shows a shift towards a lower wavenumber upon complexation. Selected IR vibrations are shown in Table 2.3.

Table 2.3 Selected IR vibrations of Schiff base rhodium complexes C2.1 – C2.8.[a]

Complex	$\nu_{C=N}$ cm^{-1} (imine)		Siloxane		$B(Ph)_4^-$
	Ligand	Complex	$\nu_{Si-O-Si}$ cm^{-1}	ν_{Si-OH} cm^{-1}	ν_{B-C} cm^{-1}
C2.1	1636	1627	-	-	-
C2.2	1636	1626	-	-	703
C2.3	1649	1624	-	-	700
C2.4	1631	1599	-	-	-
C2.5	1636	1626	1070	953	-
C2.6	1636	1622	1073	957	702
C2.7	1648	1625	1070	952	702
C2.8	1632	1630	1065	953	-

[a] Solids recorded as neat samples using an ATR accessory

The imine band shifted from the region of 1631 cm^{-1} – 1649 cm^{-1} in the free ligands to between 1599 cm^{-1} – 1630 cm^{-1} in all complexes. This shift is due to the change in the C=N bond character after complexation. When the nitrogen donor site binds to the rhodium, the C=N bond order is weakened and a shift to lower wavenumber occurs. For the cationic complexes **C2.2**, **C2.3**, **C2.6** and **C2.7**, two very intense bands at 735 cm^{-1} and 700 cm^{-1} due to the tetraphenylborate counter-ion were observed.[25] The siloxane band in the N,O complex **C2.8** showed a small degree of broadening, indicating that some hydrolysis and self-condensation of the siloxane moiety may have occurred during the synthesis of this complex in the presence of potassium hydroxide.

2.2.3.2 Characterization of Schiff base rhodium complexes using ^{1}H NMR spectroscopy

In the ^{1}H NMR spectra of the complexes, the peak due to the imine proton resonance was monitored, as this proton is the most affected by the change in the bond character upon binding to the metal centre. This peak showed an upfield shift in the complex in most cases. Interestingly, while this shift was 0.93 ppm for the carbonyl chloride complexes, **C2.1** and **C2.5**, containing the N,P chelate ligand, and 0.43 ppm and 0.42 ppm for the N,O complexes **C2.4** and **C2.8** respectively, the shift was 2.38 ppm for **C2.3.** This shift is unusually large. The pyridine protons of complex **C2.3** also show rather large upfield shifts relative to the shifts of the benzene protons of **C2.1** and **C2.4**.

The imine proton of the cationic N,P complex **C2.2** with COD as co-ligand is obscured by the aromatic protons. The siloxane functionalized equivalent of **C2.3**, **C2.7** was insoluble in chloroform-*d* and the ^{1}H NMR spectrum was therefore recorded in deuterated acetone. The imine proton of **C2.7** in acetone-d_6 showed only a slight downfield shift from 8.34 ppm to 8.46 ppm after complexation. The ^{1}H spectrum of the model complex **C2.3** was subsequently also recorded in acetone-d_6, and in this solvent the imine proton only showed a slight downfield shift from 8.34 ppm in the ligand to 8.46 ppm after complexation. The large upfield shift of the imine proton is therefore solvent dependent.

Due to cationic complexes such **C2.3** being generally sparingly soluble in chloroform-*d*, reports of examples of such a large shift in the imine proton resonance in the literature are rather limited. Most of the ^{1}H NMR spectra of analogous complexes reported have been recorded in acetone-d_6 or DMSO-d_6 and, as discussed above, no unusually large shifts of the imine protons after complexation have been noted.

Vuong *et al*. reported the synthesis of a series of imidazolylidene-1,2,3-triazole cationic rhodium complexes for which a similar shift for certain signals can be observed.[26] In the case of the ligand and complex shown in Scheme 2.6, the triazole proton (indicated in blue) shifts from 8.32 ppm in the ligand to 6.64 in the ^{1}H NMR of complex recorded in chloroform-*d*. Unfortunately, the authors do not comment on this unusually large shift of the triazole proton resonance.

Given that such shifts are fairly significant for several of the complexes, we decided to investigate this phenomenon in more detail using 1D and 2D NMR spectroscopy techniques. The results of this study is reported in Chapter 3.

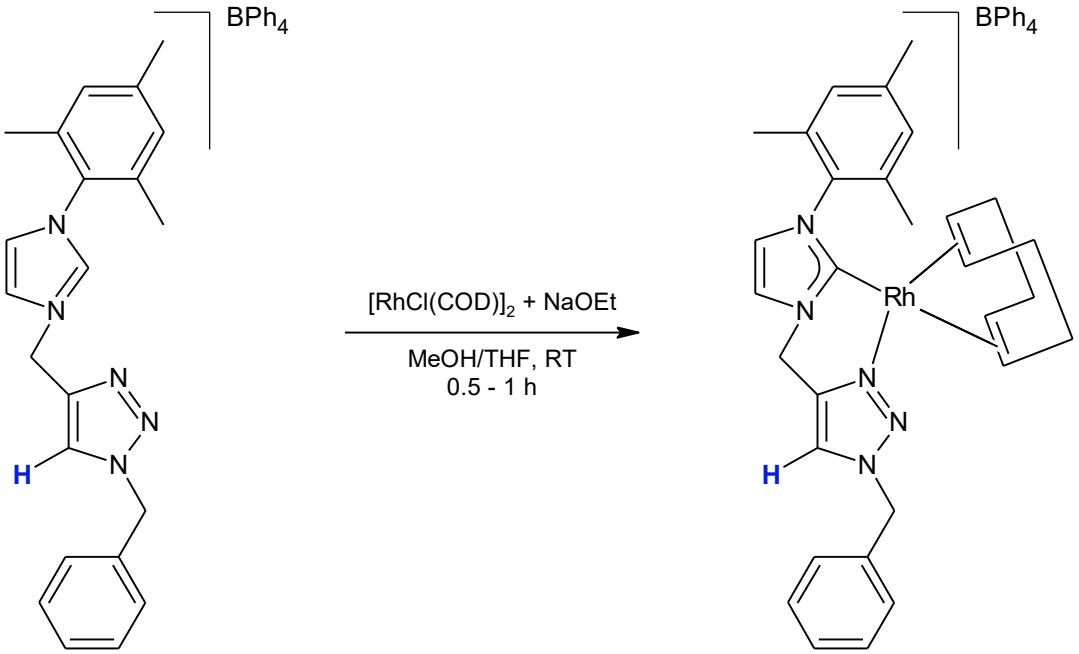

Scheme 2.6 Rhodium complex synthesized by Vuong *et al*.[26] A large upfield shift of the triazole proton (blue) in chloroform-*d*, similar to that observed for C2.3 in chloroform-*d*, was reported.

The protons of the 1,5-cyclooctadiene ligand were also visible in **C2.2**, **C2.3**, **C2.4**, **C2.6**, **C2.7** and **C2.8**. These were shifted from their positions in the chloro(1,5-cyclooctadiene)rhodium(I) dimer, indicating that complexation had taken place. In the N,N binding complexes **C2.3** and **C2.7** the olefinic protons of the 1,5-cyclooctadiene appear as a singlet at 4.25 ppm, while in the N,P and N,O complexes **C2.2**, **C2.4**, **C2.6** and **C2.8** they are split into a doublet, appearing at 5.22 and 3.56 ppm in **C2.2** and 4.56 ppm and 3.72 ppm in **C2.4**. The same splitting patterns were observed by Smith and co-workers for the N,O complex.[15] They tentatively attributed the splitting of the olefinic COD protons to the asymmetric environment created by the bidentate N,O ligand as shown in Figure 2.11, with two of the protons being *trans* to the nitrogen donor atom (H_1, shown in red) and the other two *trans* to the oxygen donor atoms (H_2, shown in blue).

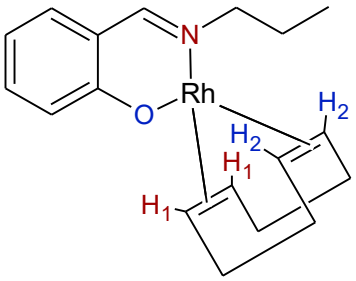

Figure 2.11 N,O complex C2.4, indicating the different environments of the olefinic COD protons. Two protons (blue) are *trans* to the oxygen donor atoms and two (red) are *trans* to the nitrogen atom.

Table 2.4 Selected ^{1}H NMR data for Schiff base complexes C2.1 - C2.8.[a]

Complex	Imine		1,5-cyclooctadiene		Siloxane functionality:	
	Ligand (ppm)	Complex (ppm)	Olefinic (ppm)	Aliphatic (ppm)	$Si(OCH_2C\underline{H}_3)_3$ (ppm)	$Si(OC\underline{H}_2CH_3)_3$ (ppm)
C2.1	8.88	7.95	-	-	-	-
C2.2	8.88	*obscured*	5.22 (s, 2H), 3.56 (s, 2H)	2.41 (s, 4H), 1.56 (s, 4H)	-	-
C2.3	8.62	6.24	4.25 (s, 4H)	2.49 (s, 4H), 2.03 (d, 4H)	-	-
C2.4	8.34	7.91	4.56 (m, 2H), 3.72 (m, 2H)	2.50 (m, 4H), 1.94 (m, 4H)	-	-
C2.5	8.89	8.28	-	-	1.07 (t, 9H)	3.17 (q, 6H)
C2.6	8.89	*obscured*	5.50 (s, 2H), *obscured*	2.44 (s, 4H), 1.53 (s, 4H)	1.13 (t, 9H)	3.74 (q, 6H)
C2.7	8.34[b]	8.46[b]	4.28 (s, 4H)	2.51 (m, 4H), 2.05 (m 4H)	1.21 (t, 9H)	3.81 (q, 6H)
C2.8	8.35	7.93	4.55 (m, 2H), 3.72 (m, 2H)	2.48 (m, 4H),1.94 (m, 4H)	1.24 (t, 9H)	3.82 (q, 6H)

[a] Recorded in chloroform-*d* at 25 °C [b] Recorded in acetone-d_6 at 25 °C

2.2.3.3 Characterization of Schiff base rhodium complexes using ESI-MS, melting point and microanalysis

ESI-MS data, microanalyses and melting points of complexes **C2.1** – **C2.8** are summarized in Table 2.5. The rhodium carbonyl complexes **C2.1** and **C2.5** decomposed without melting above 228°C and 248°C respectively. The remainder of the complexes melted below 160°C, with the siloxane functionalized complexes having slightly higher melting points than the model complexes, except in the case of the cationic N,P complexes **C2.2** and **C2.6**.

Microanalysis of the model complexes **C2.1 – C2.4** showed good agreement with the calculated values. Due to the sensitive nature of the functionalized complexes, accurate microanalysis results could not be obtained for complexes **C2.5** – **C2.8**.

Table 2.5 ESI-MS, microanalysis and melting points of complexes C2.1 – C2.8.

	Molecular formula	ESI-MS $[M]^+$ (m/z)	Microanalysis: Calculated (Found)			Melting Point
		Calculated (Found)	C	H	N	(°C)
C2.1	$C_{23}H_{21}ClNOPRh$	462.0 (462.0)	66.04 (65.76)	6.48 (6.25)	12.84 (12.50)	228 (dec.)
C2.2	$C_{54}H_{53}BNPRh$	543.1 (542.5)	75.27 (74.94)	6.32 (6.30)	1.63 (1.95)	157 – 159
C2.3	$C_{41}H_{43}BN_2Rh$	359.1 (359.1)	72.58 (72.27)	6.54 (6.54)	4.13 (4.43)	79 – 82
C2.4	$C_{18}H_{23}NORh$	374.1 (374.1)	57.91 (57.21)	6.48 (6.69)	3.75 (3.62)	75 – 78
C2.5	$C_{29}H_{36}ClNO_4PRhSi$	661.0 (661.0)	52.77 (55.90)	5.50 (5.78)	2.12 (1.91)	248 (dec.)
C2.6	$C_{60}H_{68}BNO_3PRhSi$	704.7 (704.7)	70.38 (61.8)	6.69 (5.94)	1.37 (2.18)	134 - 137
C2.7	$C_{47}H_{58}BN_2O_3RhSi$	521.5 (521.2)	67.14 (62.40)	6.95 (6.70)	3.33 (4.45)	92 – 96
C2.8	$C_{24}H_{38}NO_4RhSi$	535.6 (536.5)	53.82 (48.0)	7.15 (6.53)	2.62 (2.73)	89 – 92

The mass spectrum for complex **C2.1** shows the $[M - Cl]^+$ ion as the base peak with an m/z of 462.0. The molecular ion is not observed. For **C2.3**, the parent ion $[M]^+$ is observed as the base peak with an m/z of 359.1. Peaks at m/z 211.0, 252.0 and 293.1 were found to be due

to rhodium-1,5-cyclooctadiene and its acetonitrile adducts (Figure 2.12). A peak is also seen at 149.1, which is due to the protonated ligand **L2.2**.

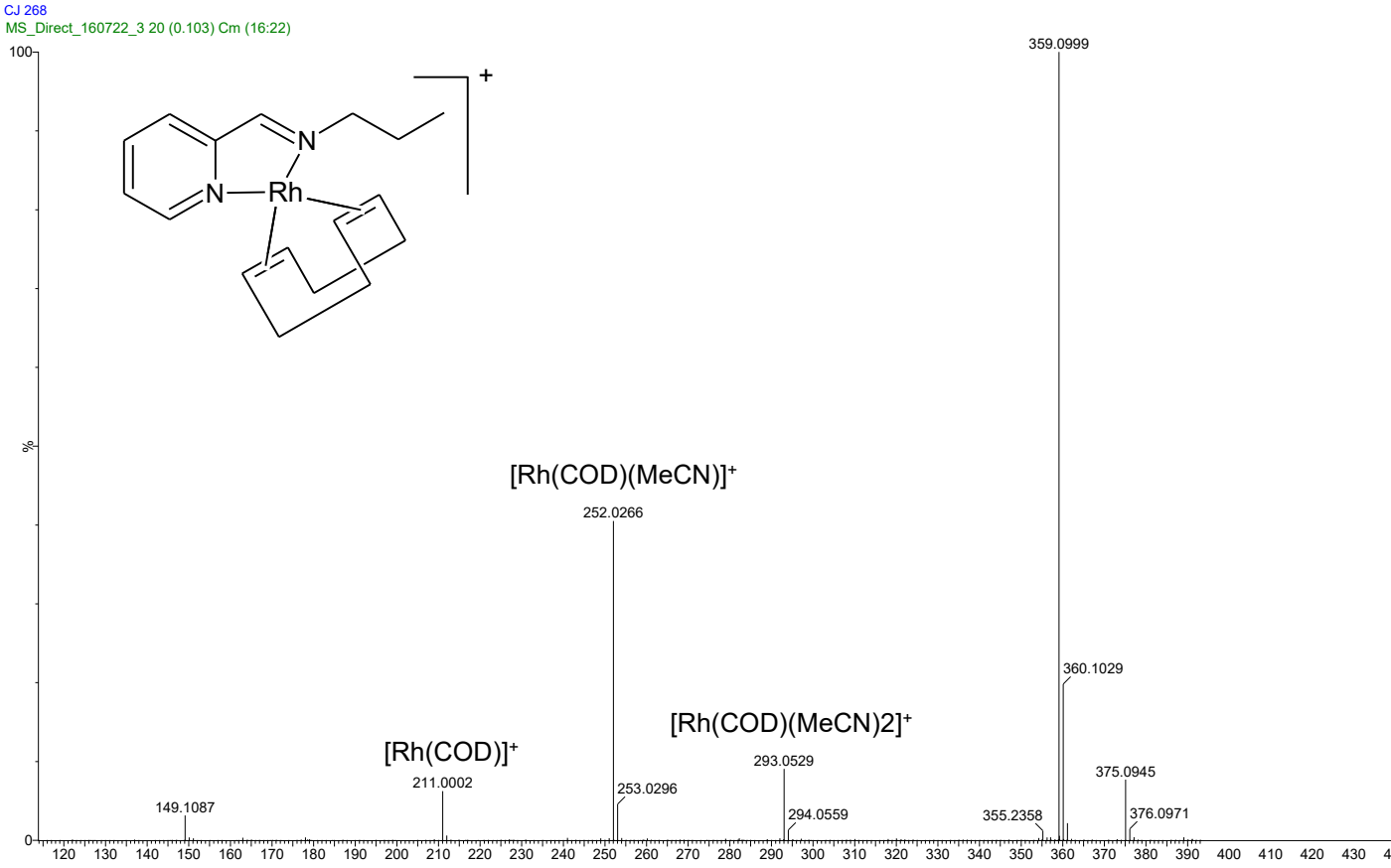

Figure 2.12 ESI-MS (positive mode) spectrum of model complex C2.3. The parent ion $[M]^+$ can be observed at 359.1.

The same rhodium-1,5-cyclooctadiene adducts are seen in the spectrum of **C2.4**, and the adduct with one molecule of acetonitrile is indeed the base peak in this spectrum. The molecular ion is observed in very low abundance as $[M + H]^+$ at an m/z of 354.1. The protonated ligand **L2.3** can also be observed at m/z 164.1.

The mass spectrum of model complex **C2.3** was recorded in the negative mode as well, to confirm the presence of the counter-ion. The base peak, which is the only peak observed, corresponds to the counter-ion ($[M]^-$ = 319.16) and therefore confirms the presence of the tetraphenylborate counter-ion in the complex. The mass spectrum is shown in Figure 2.13.

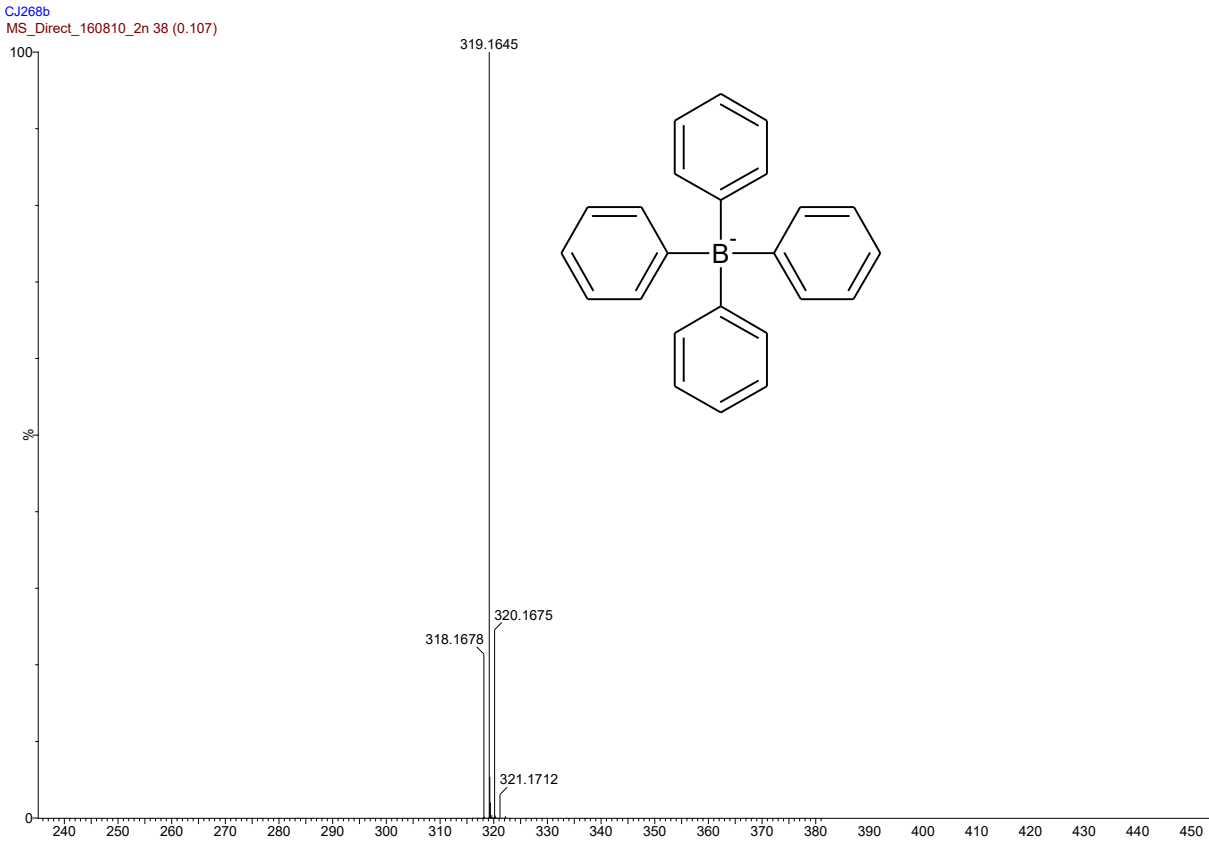

Figure 2.13 ESI-MS (negative mode) of functionalized complex C2.3, confirming the presence of the tetraphenylborate anion.

2.2.4 Synthesis and characterization of pyridyl-triazole ligands L2.7 and L2.8

Another type of N,N bidentate ligand was synthesized by making use of the facile azide-alkyne Huisgen cycloaddition to synthesize a pyridyl-triazole ligand. The siloxane functionality would be linked to the binding site through a triazole ring instead of through an imine. A water-soluble close analogue of the ligand was recently synthesized by Scrivanti *et al*. and was effective in the biphasic hydroformylation of styrene and 1-hexene.[27] By varying the azide used, it was possible to synthesize both a model and siloxane functionalized version of the ligand. The model ligand was synthesized from 2-ethynylpyridine and octyl bromide using a one-pot reaction method, shown in Scheme 2.7.

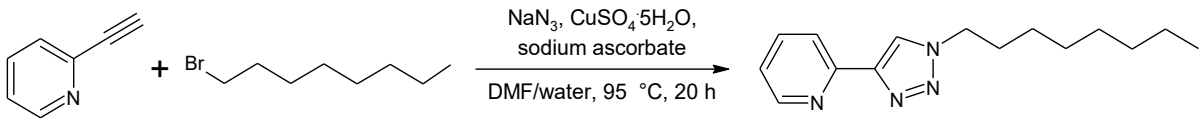

Scheme 2.7 Synthesis of model triazole ligand.

For the siloxane functionalized ligand, the appropriate azide was first synthesized and isolated, followed by the cycloaddition reaction using *tris*(triphenylphosphine)copper(I) bromide as

catalyst.[28] A microwave reactor was used to shorten the time of the reaction, and after extraction with hexane the two ligands were obtained as pale yellow oils. The synthesis of the ligand is illustrated in Scheme 2.8.

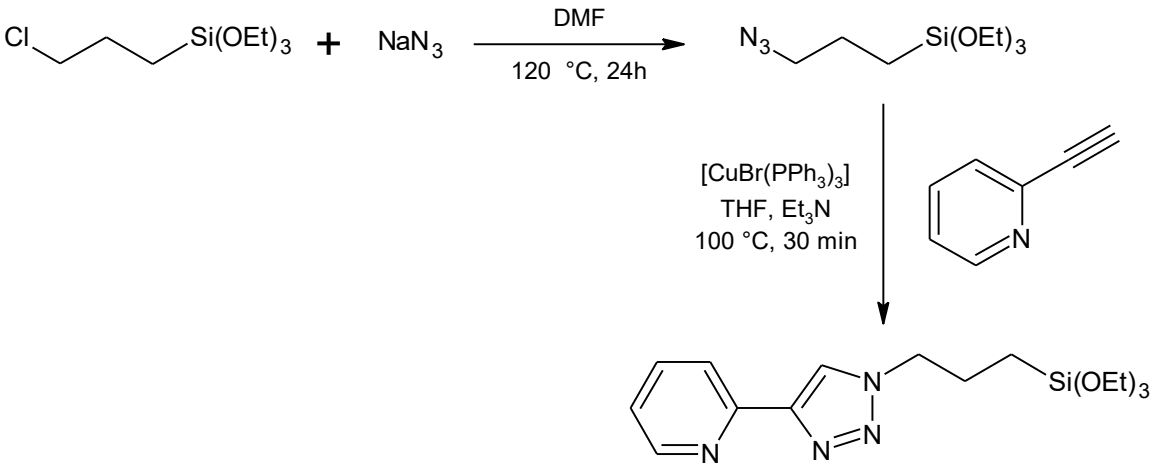

Scheme 2.8 Synthesis of siloxane functionalized triazole ligand.

2.2.4.1 Characterization of pyridyl-triazole ligands L2.7 and L2.8 using FT-IR spectroscopy

The infrared spectra of these ligands do not contain as much information about the formation of the ligands as in the case of ligands **2.1** to **2.8**. In these spectra the disappearance of the azide N≡N band in the 2090 cm^{-1} is monitored, as well as the shape and position of the siloxane asymmetric Si-O-Si stretch at 1071 cm^{-1}.

2.2.4.2 Characterization of pyridyl-triazole ligands L2.7 and L2.8 using ^{1}H NMR spectroscopy

^{1}H NMR spectroscopy proved an invaluable tool in the characterization of the pyridyl-triazole ligands. The proton on the unsubstituted carbon of the triazole ring resonates as a singlet at 8.13 ppm and is easy to distinguish from the other aromatic resonances. The presence of this signal confirms the successful formation of the triazole ring. A summary of selected resonances is given in Table 2.6

Table 2.6 Selected ^{1}H NMR data for triazole ligand L2.7 and L2.8.[a]

Ligand	Triazole proton (CH) (ppm)	Aromatic protons (ppm)
L2.7	8.13	8.58 (d, 1H), 8.19 (d, 1H), 7.78 (td, 1H), 7.23 (m, 1H)
L2.8	8.14	8.54 (d, 1h), 8.15 (*obscured by triazole*, 1H), 7.74 (td, 1H), 7.19 (m, 1H)

[a] Recorded in chloroform-*d* at 25 °C

2.2.5 Synthesis and characterization of pyridyl-triazole rhodium complexes C2.9 and C2.10

With the pyridyl-triazole ligands successfully obtained, the synthesis of their rhodium complexes followed as shown in Scheme 2.9. Since these ligands had two nitrogen donor atoms, the cationic rhodium complexes were synthesized using the same procedure that was used for **C2.3** and **C2.7**. Both complexes **C2.9** and **C2.10** were isolated as bright yellow solids.

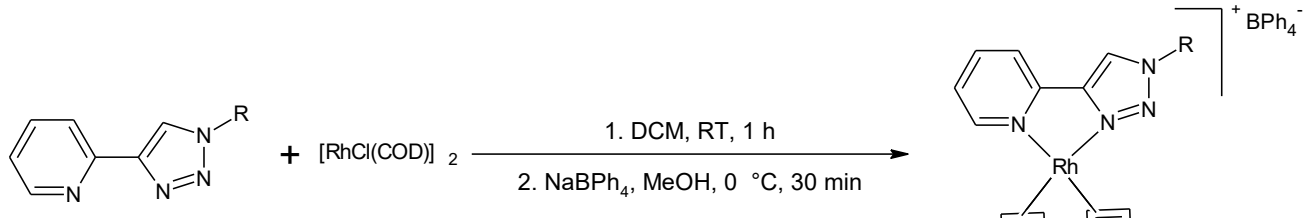

C2.9: R = octyl
C2.10: R = propyltriethoxysilane

Scheme 2.9 Synthesis of pyridyl-triazole rhodium complexes C2.9 and C2.10.

2.2.5.1 Characterization of pyridyl-triazole complexes C2.9 and C2.10 using FT-IR spectroscopy

As in the case for the pyridyl-triazole ligands, the infrared spectroscopy was not adequate for the characterization of the complexes. The intense peak at 700 cm^{-1} due to the presence of the tetraphenylborate counter-ion, as well as the presence of the siloxane bands in the region of 1073 cm^{-1} to 1068 cm^{-1} in the case of the siloxane functionalized complex were observed in the infrared spectrum.

2.2.5.2 Characterization of pyridyl-triazole complexes C2.9 and C2.10 using ^{1}H NMR spectroscopy

The ^{1}H NMR for these complexes were recorded in chloroform-*d*. For the triazole proton, a very large upfield shift relative to the analogous ligand was observed in both complexes, similar to that observed for the imine proton in **C2.3**. The resonance shifted from 8.13 ppm and 8.14 ppm in the ligands, to 5.75 pm and 5.79 ppm in the respective complexes.

Table 2.7 Selected ^{1}H NMR data for triazole complexes C2.9 and C2.10.[a]

Complex	Ligand triazole proton (CH) (ppm)	Complex triazole proton (CH) (ppm)
C2.9	8.13	5.75
C2.10	8.14	5.79

[a] Recorded in chloroform-*d* at 25 °C

Another rather striking observation was the line shape of the olefin 1,5-cyclooctadiene protons. While these ^{1}H NMR signals appear as a single peak in the Schiff base N,N complex **C2.3** and as two multiplets in the Schiff base N,O complex **C2.4**, the COD proton signals are seen as a very low intensity broad doublet in the ^{1}H NMR spectrum of the pyridyl-triazole complexes. This phenomenon was investigated further using variable temperature NMR. The results of this study are reported in Chapter 3.

2.2.5.3 Characterization of pyridyl-triazole complexes using ESI-MS, melting point and microanalysis

The ESI-MS data, microanalyses and melting points for complexes **C2.9** and **C2.10** are shown in Table 2.8. Both complexes melt above 130°C, with the melting point of the functionalized complex **C2.10** being slightly higher than that of the model complex **C2.9**. Microanalysis data for the two complexes showed good agreement with the expected values.

For **C2.9**, the parent ion $[M]^+$ is observed as the base peak with an m/z of 469.2. As was the case for the cationic complexes discussed in Section 2.2.3.3, peaks due to rhodium-1,5-cyclooctadiene and its acetonitrile adducts were observed at m/z 211.0, 252.0 and 293.1. In the case of **C2.10**, the parent ion was also observed as base peak, in this case at an m/z of 561.2.

Table 2.8 ESI-MS, microanalysis and melting points of complexes C2.9 and C2.10.

	Molecular Formula	ESI-MS $[M]^+$ (m/z)	Microanalysis: Calculated (Found)			Melting Point
		Calculated (Found)	C	H	N	(°C)
C2.9	$C_{47}H_{54}BN_4Rh$	469.4 (469.2)	71.76 (71.39)	6.66 (6.78)	7.12 (7.48)	134-136
C2.10	$C_{48}H_{58}BN_4O_3RhSi$	561.6 (561.2)	65.45 (64.03)	6.62 (6.34)	6.36 (7.19)	146 - 149

From these analyses, it was concluded that new model and siloxane functionalized triazole rhodium complexes had been successfully synthesized, which could be applied in hydroformylation reactions.

2.2.6 Attempts at expansion of triazole series

The pyridyl-triazole ligands described above have the drawback in that they are limited in the terms of the nature of the substituent on the triazole. The necessity of an alkyne-functionalized reactant restricts the number of possible ligands that can be synthesized. If, however, the triazole ring contained an aldehyde functionality, a number of amines could be reacted with the aldehyde to form various substituted imines as shown in Figure 2.14, which could provide the required rhodium binding site together with a triazole nitrogen.

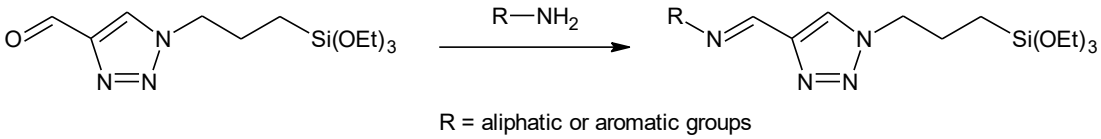

Figure 2.14 Proposed reaction scheme to form new substituted triazole ligands.

In a paper by Dai *et al*., the synthesis of an alcohol-functionalized triazole and its subsequent oxidation is described.[29] The procedure was modified to include a siloxane moiety which would serve as linker to the silica surface.

2.2.6.1 Synthesis and characterization of (1-propyltriethoxysilane-1*H*-1,2,3-triazol-4-yl)methanol

An initial attempt to synthesize this ligand in a microwave reactor resulted in a bright yellow, highly insoluble product. A more conventional method was therefore used. Propargyl alcohol and 3-azidotriethoxysilane was reacted in a 1.5:1 ratio in THF. Copper iodide was used a catalyst, and diisopropylamine was added to act as base. The reaction was allowed to proceed for 24 hours, and subsequently filtered. The solvent was removed from the filtrate to yield a light yellow oil. The synthetic scheme is shown in Scheme 2.10.

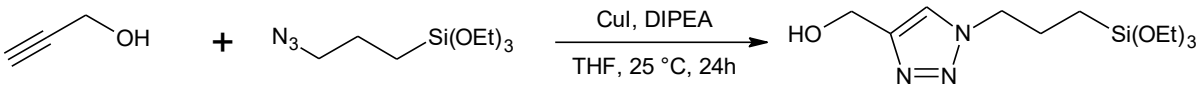

Scheme 2.10 Synthesis of alcohol-functionalized triazole.

An FT-IR spectrum showed a clear hydroxyl peak at 3050 cm^{-1}, while the siloxane asymmetric Si-O-Si stretch peaks were also clearly visible at 1064 cm^{-1}. Most importantly, no azide peak was observed.

In the ^{1}H NMR, the characteristic triazole proton was observed at 7.56 ppm. The siloxane moiety showed the expected peaks at 1.22 ppm and 3.82 ppm. The successful synthesis of a triazole containing both important elements – a hydroxyl group and a siloxane moiety was therefore confirmed.

2.2.6.2 Oxidation of alcohol-functionalized triazole

With the alcohol-functionalized triazole in hand, the next step was oxidation to the corresponding aldehyde. Continuing from the paper by Dai *et al.*, oxidation was first attempted using manganese oxide. Jones oxidation was avoided initially, due to the impact that the acidic conditions might have on the pH-sensitive siloxane functionality.

An excess of manganese oxide was added to the alcohol-functionalized triazole, and the mixture was heated under reflux in ethyl acetate for 24 hours (Scheme 2.11). The manganese oxide was filtered off, and once the solvent was removed from the filtrate, infrared spectroscopy was used to determine whether oxidation had taken place. A peak in the region of 1680 – 1720 cm^{-1} would indicate successful oxidation. Unfortunately, no such peak could be seen in the infrared spectrum.

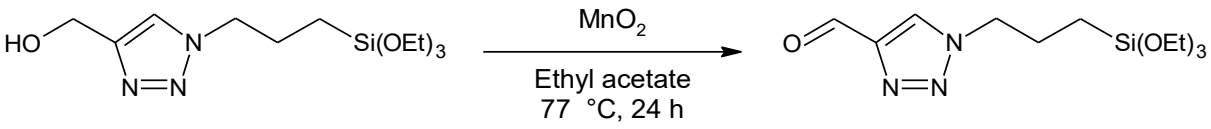

Scheme 2.11 Oxidation of alcohol functionality using manganese oxide.

The reaction was repeated to run for 72 hours under reflux, again using ethyl acetate as solvent. After filtration and solvent removal, the infrared spectrum, shown Figure 2.15, revealed a small peak at 1698 cm^{-1}. This indicated that some oxidation had taken place, however, it was clear that conversion was very low.

The difference in the oxidation rates between this molecule and the molecules reported by Dai *et al*. is possibly due to the substituent on the N-1 nitrogen of the triazole. The reported

compounds all contain a substituted phenyl moiety, whereas our system has a propyl-triethoxysilane moiety in that position. The electron-withdrawing nature of the phenyl rings could possibly help to facilitate the oxidation reaction in the published triazoles.

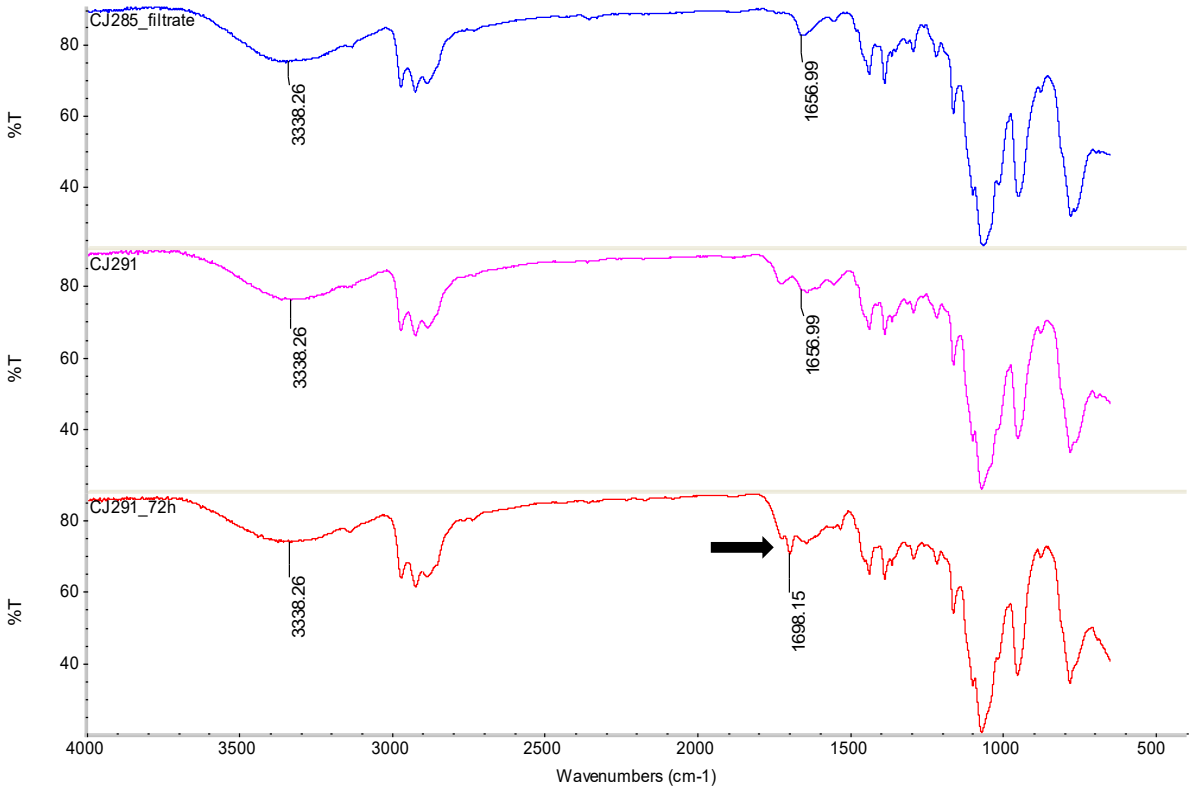

Figure 2.15 Infrared spectra of triazole-alcohol (top), oil after 24 hours at reflux (middle) and after 72 hours at reflux (bottom). The carbonyl peak is expected around 1700 cm^{-1}.

A literature search revealed some microwave-assisted oxidation methods using manganese oxide.[30] An excess of manganese oxide and the alcohol-functionalized triazole was dissolved in ethyl acetate and allowed to react in the microwave reactor for 30 minutes at 104°C using 100 W of power. The reaction was unsuccessful. Neither changing the solvent to diethyl ether, nor increasing the time to 1 hour yielded any better results.

Faced with these results, it was decided instead to use the Jones reagent for the oxidation reaction. The bright orange reactant was prepared according to a literature procedure.[31] The alcohol-functionalized triazole was dissolved in acetone and cooled to 0°C. An equimolar amount of the Jones reagent was added dropwise and the reaction was stirred at 0°C for 20 minutes (Scheme 2.12).

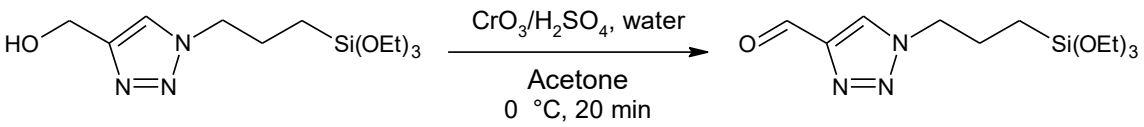

Scheme 2.12 Oxidation of alcohol-triazole with Jones reagent.

The solution was filtered and a pale yellow residue was obtained after removal of the solvent. Infrared spectroscopy, shown in Figure 2.16, indicated that the oxidation had successfully taken place with a very strong peak at 1697 cm^{-1}, and that the siloxane functionality was still intact, although the peak is slightly broader.

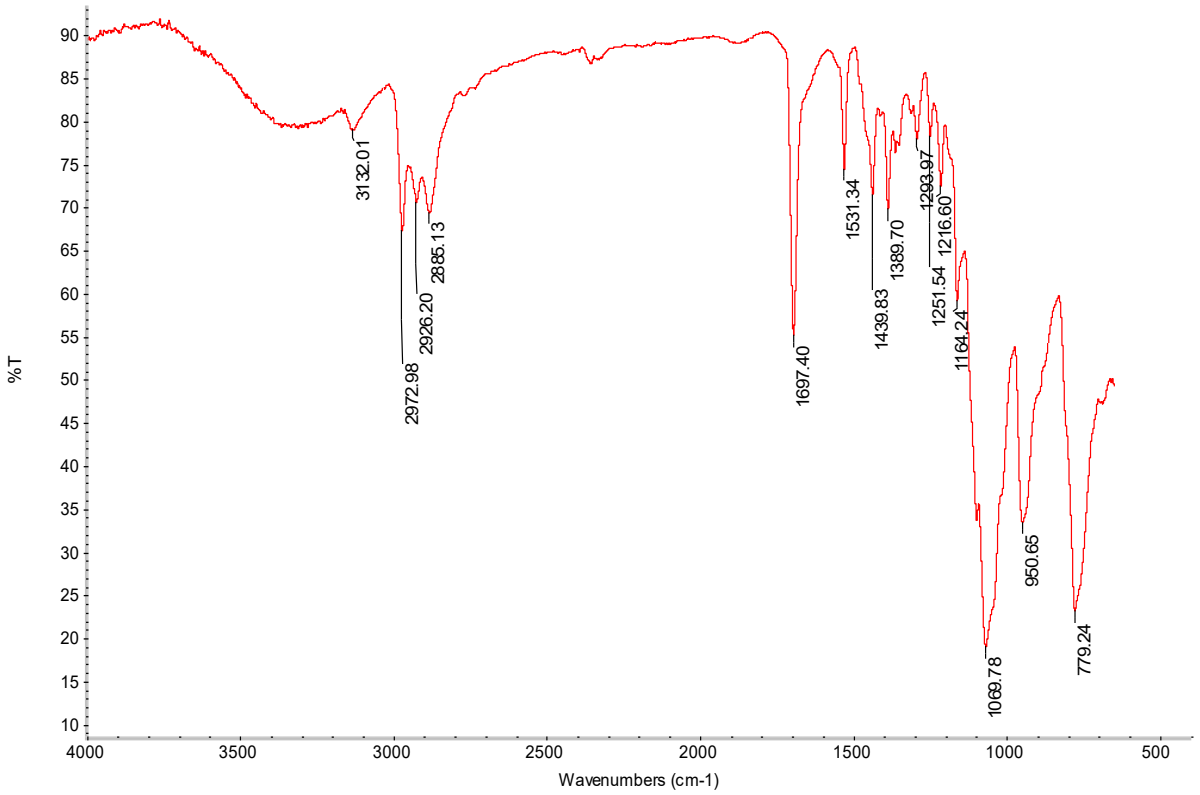

Figure 2.16 Infrared spectrum after Jones oxidation. Note the carbonyl peak at 1697 cm^{-1}, indicating that oxidation has occurred.

^{1}H NMR spectroscopy showed that two new peaks had formed in the downfield region – a peak at 10.15 ppm, attributed to the aldehyde proton, and at 8.14 ppm, attributed to the triazole proton of the aldehyde-functionalized triazole. Unfortunately the spectrum, shown in Figure 2.17, shows that quite a lot of the alcohol was left as well.

Attempts to increase the yield by increasing the time of the reaction lead to hydrolysis and self-condensation of the siloxane moieties, as observed by infrared spectroscopy. Column chromatography was also attempted, but the product decomposed on the column and could not be isolated. This synthetic route was therefore abandoned.

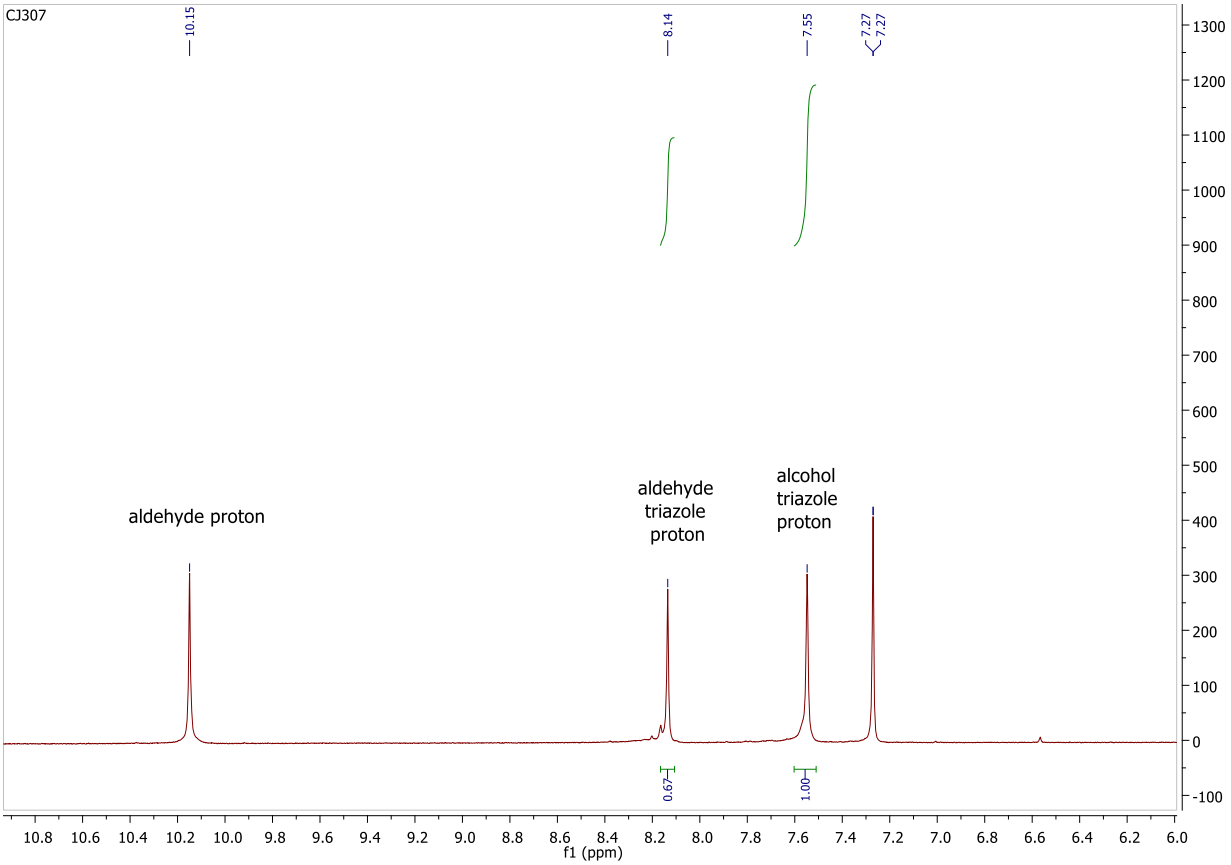

Figure 2.17 ^{1}H NMR spectrum of oxidized product showing the presence of both aldehyde and alcohol functionalized triazoles, indicating incomplete oxidation of the alcohol.

2.3 Concluding remarks

Six ligands, three of which contain siloxane functionalities, were synthesized *via* Schiff base condensation. The ligands were reacted with either $[RhCl(CO)_2]_2$ or $[RhCl(COD)]_2$ to produce eight rhodium complexes. A microwave synthesis technique was developed for the synthesis of $[RhCl(COD)]_2$, which shortened the reaction time and improved the yield of this metal precursor. Four of these complexes were cationic, and were isolated as tetraphenylborate salts. The complexes were characterized using FT-IR spectroscopy, ^{1}H, ^{13}C and (where applicable) ^{31}P NMR spectroscopy, mass spectrometry and microanalysis. The melting points were also recorded. Some difficulty was experienced in the mass spectrometry and microanalysis characterization of the functionalized complexes, as these complexes are sensitive to air and moisture.

Two pyridyl-triazole ligands, one of which contained a siloxane functionality, were synthesized using azide-alkyne Huisgen cycloaddition. Using $[RhCl(COD)]_2$ as metal source, cationic complexes of the ligands were prepared with tetraphenylborate as counter-ion. The

complexes were characterized using the same range of techniques mentioned for the Schiff base complexes. It should be noted that the pyridyl-triazole complex appeared to be somewhat more stable under ambient conditions than the Schiff base complexes as more accurate mass spectrometry and microanalysis results were obtained.

Two interesting phenomena were noticed during the ^{1}H NMR characterization of the rhodium complexes. Firstly, the imine and triazole proton signals of **C2.3** and **C2.9** exhibited unusually large upfield shifts in the ^{1}H spectra (recorded in chloroform-*d*) after complexation. Secondly, two low, broad peaks were observed in the ^{1}H NMR spectrum of **C2.9**, representing the olefinic COD protons. This was in contrast to the spectrum of **C2.3**, where the olefinic COD protons are observed as a single, narrower peak. A more thorough investigation of these phenomena is described in Chapter 3.

Following the successful synthesis of the pyridyl-triazole complexes, it was attempted to synthesize new diimine complexes with the siloxane functionality being incorporated through a triazole ring. This *inter alia* entailed the oxidation of an alcohol group to an aldehyde group. Unfortunately, an oxidation method which could yield high amounts of the aldehyde while still preserving the integrity of the siloxane functionality could not be found at this stage.

2.4 Experimental section

2.4.1 General remarks and instrumentation

All reactions were carried out under a nitrogen atmosphere making use of standard Schlenk techniques. Highly air-sensitive materials were stored in a nitrogen purged glovebox and all manipulations with these materials were carried out in the glovebox to prevent decomposition or oxidation. A CEM Discover microwave reactor was used for certain reactions.

Fourier transform infrared (FR-IR) spectra were recorded using an ATR accessory on a Nicolet Avatar 330 FT-IR spectrometer. ^{1}H and ^{13}C NMR spectra were recorded on an Agilent Inova instrument at 300, 400 and 600 MHz for ^{1}H and 75, 100, 150 MHz for ^{13}C. ESI mass spectra were recorded by direct injection into a stream of acetonitrile and 0.1 % formic acid employing a cone coltage of 15 V using a Water API Quattro Micro spectrometer. A Thermo Elemental Analyzer CHNS-O was used for the accurate determination of the elemental composition of samples.

2.4.2 Materials

Reagents were purchased from Sigma-Aldrich and used as received. Solvents were purchased from Sigma-Aldrich and Kimix Chemicals and were dried over alumina molecular sieves in Sigma Aldrich Innovative Technology solvent purifiers in the case of dichloromethane

(DCM), tetrahydrofurane (THF), diethyl ether, toluene and hexane, and by refluxing over dry magnesium turnings and iodine in the case of ethanol and methanol.

2.4.3 Synthesis of model and functionalized ligands L2.1 – L2.6

2.4.3.1 Synthesis of model ligands L2.1 – L2.3

N-propylamine (0.236 g, 4 mmol) in dry diethyl ether (4 mL) was added to a stirring solution of the appropriate aldehyde (4 mmol) in dry diethyl ether (4 mL) in a Schlenk tube, followed by the addition of a small amount of $MgSO_4$. The solution was stirred for 24 hours at room temperature and then filtered to remove the $MgSO_4$. The solvent was subsequently removed from the filtrate to yield the products as oils.

***N*-(2-Diphenylphosphino)benzylidene-propanamine** ligand **L2.1** $C_{22}H_{21}NP$ – aldehyde used: 2-Diphenylphosphinobenzaldehyde. Orange oil, yield 82%. IR: FT-IR, *v*/cm^{-1}: 1636 (s, imine, C=N). ^{1}H NMR (300 MHz, $CDCl_3$): δ (ppm) = 0.74 (t, $^3J_{H\text{-}H}$ = 7.6 Hz, 3H, $NCH_2CH_2C\mathbf{H_3}$), 1.53 (m, 2H, $NCH_2C\mathbf{H_2}CH_3$), 3.44 (td, $^3J_{H\text{-}H}$ = 7.0 and $^4J_{H\text{-}H}$ = 1.2 Hz, 2H, $NC\mathbf{H_2}CH_2CH_3$), 6.87 (m, 1H, Ar), 7.27 (m, 5H, Ar), 7.33 (m, 5H, Ar), 7.38 (t, $^3J_{H\text{-}H}$ = 7 Hz, 1H, Ar), 7.66 (m, 1H, Ar), 7.98 (m, 1H, Ar), 8.88 (d, $^4J_{H\text{-}P}$ = 4.6 Hz, 1H, *imine*-C**H**).

***N*-(2-Pyridinylmethylene)-1-propanimine** ligand **L2.2** $C_9H_{11}N_2$ – aldehyde used: 2-Pyridinecarboxaldehyde. Yellow oil, yield 85%. IR: FT-IR, *v*/cm^{-1}: 1649 (s, imine, C=N), 1586 (m, pyridine, C=N), 1566 (m, pyridine, C=N). ^{1}H NMR (300 MHz, $CDCl_3$): δ (ppm) = 0.94 (t, $^3J_{H\text{-}H}$ = 7.6 Hz, 3H, $NCH_2CH_2C\mathbf{H_3}$), 1.74 (m, 2H, $NCH_2C\mathbf{H_2}CH_3$), 3.62 (td, $^3J_{H\text{-}H}$ = 7.0 and $^4J_{H\text{-}H}$ = 1.2 Hz, 2H, $NC\mathbf{H_2}CH_2CH_3$), 7.27 (m, 1H, Pyr), 7.71 (td, $^3J_{H\text{-}H}$ = 7.6 and $^4J_{H\text{-}H}$ = 1.2 Hz, 1H, Pyr), 7.97 (d, $^3J_{H\text{-}H}$ = 7.6 Hz,1H, Pyr), 8.35 (s, 1H, *imine*-C**H**), 8.62 (d, $^3J_{H\text{-}H}$ = 4.7 Hz, 1H, Pyr).

***N*-propylsalicylaldimine** ligand **L2.3** $C_{10}H_{11}NO$ – aldehyde used: Salicylaldehyde. Yellow oil, yield 92%. IRL FT-IR, *v*/cm^{-1}: 1631 (s, imine, C=N). ^{1}H NMR (300 MHz, $CDCl_3$): δ (ppm) = 1.00 (t, $^3J_{H\text{-}H}$ = 7.0 Hz, 3H, $NCH_2CH_2C\mathbf{H_3}$), 1.75 (m, 2H, $NCH_2C\mathbf{H_2}CH_3$), 3.57 (td, $^3J_{H\text{-}H}$ = 7.0 Hz and $^4J_{H\text{-}H}$ = 1.2 Hz, 2H, $NC\mathbf{H_2}CH_2CH_3$), 6.88 (t, $^3J_{H\text{-}H}$ = 8.0 Hz, 1H, Ar), 6.99 (d, $^3J_{H\text{-}H}$ = 8.0 Hz, 1H, Ar), 7.28 (m, 2H, Ar), 8.34 (s, 1H, *imine*-C**H**), 13.69 (s, 1H, Ar-O**H**).

2.4.3.2 Synthesis of siloxane functionalized ligands L2.4 – L2.6

3-Aminopropyltriethoxysilane (0.885 g, 4 mmol) in dry diethyl ether (4 mL) was added to a stirring solution of the appropriate aldehyde (4 mmol) in dry diethyl ether (4 mL) in a Schlenk tube, followed by the addition of a small amount of $MgSO_4$. The solution was stirred for 3 hours at room temperature and then filtered to remove the $MgSO_4$. The solvent was subsequently removed to yield the products as oils.

***N*-(2-Diphenylphosphino)benzylidene-3-(triethoxysilyl)-1-propanamine** ligand **L2.4** $C_{28}H_{36}NO_3PSi$ – aldehyde used: 2-Diphenylphosphinobenzaldehyde. Orange oil, yield 88%. IR: FT-IR, *v*/cm^{-1}: 1636 (m, imine, C=N), 1068 (s, Si-O). ^{1}H NMR (300 MHz, $CDCl_3$): δ (ppm) = 0.55 (t, $^3J_{H-H}$ = 7.6 Hz, 2H, $NCH_2CH_2C\mathbf{H_2}Si$), 1.22 (t, $^3J_{H-H}$ = 7 Hz, 9H, $SiOCH_2C\mathbf{H_3}$), 1.66 (m, 2H, $NCH_2C\mathbf{H_2}CH_3$), 3.48 (t, $^3J_{H-H}$ = 7.0 Hz, 2H, $NC\mathbf{H_2}CH_2CH_3$), 3.79 (q, $^3J_{H-H}$ = 7.0 Hz, 6H, $SiOC\mathbf{H_2}CH_3$), 6.88 (t, 1H, Ar), 7.27 (m, 5H, Ar), 7.33 (m, 5H, Ar), 7.38 (t, $^3J_{H-H}$ = 7.0 Hz, 1H, Ar), 7.66 (m, 1H, Ar), 7.99 (m, 1H, Ar), 8.89 (d, $^4J_{H-P}$ = 4.7 Hz, 1H, *imine*-C**H**).

***N*-(2-Pyridinylmethylene)-3-(triethoxysilyl)-1-propanimine** ligand **L2.5** $C_{15}H_{26}N_2O_3Si$ – aldehyde used: 2-Pyridinecarboxalhydehyde. Yellow oil, yield 84%. IR: FT-IR, *v*/cm^{-1}: 1648 (s, imine, C=N), 1586 (m, pyridine, C=N), 1567 (m, pyridine, C=N), 1071 (s, Si-O). ^{1}H NMR (300 MHz, $CDCl_3$): δ (ppm) = 0.69 (t, $^3J_{H-H}$ = 7.6 Hz, 2H, $NCH_2CH_2C\mathbf{H_3}Si$), 1.21 (t, $^3J_{H-H}$ = 7.0, 9H, $SiOCH_2C\mathbf{H_3}$), 1.85 (m, 2H, $NCH_2C\mathbf{H_2}CH_3$), 3.65 (td, $^3J_{H-H}$ = 7.0 and $^4J_{H-H}$ = 1.2 Hz, 2H, $NC\mathbf{H_2}CH_2CH_3$), 3.82 (q, $^3J_{H-H}$ = 7.0, 6H, $SiOC\mathbf{H_2}CH_3$), 7.28 (m, 1H, Pyr), 7.71 (m, 1H, Pyr), 7.96 (m, 1H, Pyr), 8.36 (d, $^3J_{H-H}$ = 6.5, 1H, *imine*-C**H**), 8.62 (m, 1H, Pyr).

Salicylidene-3-aminopropyltriethoxysilane ligand **L2.6** $C_{16}H_{26}NO_4Si$ – aldehyde used: Salicylaldehyde. Yellow oil, yield 93%. IR: FT-IR, *v*/cm^{-1}: 1632 (s, imine, C=N), 1071 (s, Si-O). ^{1}H NMR (300 MHz, $CDCl_3$): δ (ppm) = 0.70 (t, $^3J_{H-H}$ = 7.0 Hz, 2H, $NCH_2CH_2C\mathbf{H_2}Si$), 1.24 (t, $^3J_{H-H}$ = 7.0 Hz, 9H, $SiOCH_2C\mathbf{H_3}$), 1.84 (m, 2H, $NCH_2C\mathbf{H_2}CH_2Si$), 3.61 (t, $^3J_{H-H}$ = 7.0 Hz, 2H, $NC\mathbf{H_2}CH_2CH_3$), 3.85 (q, $^3J_{H-H}$ = 7.0 Hz, 6H, $SiOC\mathbf{H_2}CH_3$), 6.88 (t, $^3J_{H-H}$ = 8.0 Hz, 1H, Ar), 6.98 (d, $^3J_{H-H}$ = 8.0 Hz, 1H, Ar), 7.28 (m, 2H, Ar), 8.35 (s, 1H, *imine*-C**H**), 13.62 (s, 1H, Ar-O**H**).

2.4.4 Synthesis of pyridyl-triazole ligands L2.7 and L2.8

2.4.4.1 Synthesis of 2-(1-Octyl-1*H*-1,2,3-triazol-4-yl)pyridine ligand L2.7

2-Ethynylpyridine (0.309 g, 3 mmol) was dissolved in 7.5 mL of a DMF/water mixture (4:1). To this solution, sodium azide (0.234 g, 3.6 mmol), copper(II) sulfate pentahydrate (0.150 g, 0.6 mmol), sodium ascorbate (0.594 g, 3 mmol) and 1-bromooctane (0.637 g, 3.3 mmol) was added. A yellow-brown murky solution formed which was stirred at 95°C for 20 hours. DCM (20 mL) and 25% ammonia (20 mL) were added to the dark brown solution and the organic layer was separated from the solution. The organic layer was then washed with distilled water (2 x 10 mL) and had a yellow-brown colour. Finally, the organic layer was washed with brine (2 x 10 mL) and dried over $MgSO_4$. The $MgSO_4$ was filtered off and the solvent was removed from the filtrate to yield a yellow-brown solid.

$C_{15}H_{22}N_4$. Yellow-brown solid, yield 63%. IR: FT-IR, *v*/cm^{-1}: 1595 (s, pyridine, C=N), 1568 (m, pyridine, C=N). ^{1}H NMR (300 MHz, $CDCl_3$): δ (ppm) = 0.87 (t, $^3J_{H-H}$ = 7.1 Hz, 3H $CH_2CH_2C\mathbf{H_3}$),

1.28 (m, 10H, $NCH_2CH_2C\mathbf{H_2}C\mathbf{H_2}C\mathbf{H_2}C\mathbf{H_2}C\mathbf{H_2}CH_3$), 1.95 (m, 2H, $NCH_2C\mathbf{H_2}CH_2$), 4.41 (t, $^3J_{H\text{-}H}$ = 7.1 Hz, 2H, $NC\mathbf{H_2}CH_2CH_2$), 7.23 (m, 1H, Pyr), 7.78 (td, $^3J_{H\text{-}H}$ = 7.6 Hz and $^4J_{H\text{-}H}$ = 1.7 Hz, 1H, Pyr), 8.13 (s, 1H, *triazole*-C**H**), 8.19 (d, $^3J_{H\text{-}H}$ = 7.6 Hz, 1H, Pyr), 8.58 (d, $^3J_{H\text{-}H}$ = 4.1 Hz, 1H, Pyr).

2.4.4.2 Synthesis of 2-(1-[3-(Triethoxysilyl)propyl]-1*H*-1,2,3-triazol-4-yl) pyridine ligand L2.8

The ligand **L2.8** was synthesized *via* a microwave-assisted click reaction. 2-Ethynylpyridine (0.103 g, 1 mmol) and 3-azidopropyl triethyoxysilane (0.248, 1 mmol) was dissolved in THF (0.5 mL) and trimethylamine (0.5 mL). To this, $[CuBr(PPh_3)_3]$ (0.016 g, 0.02 mmol) was added. The reaction was allowed to proceed in the microwave reactor for 30 minutes at 100 °C using 100 W of power. The reaction mixture was then cooled to room temperature and the solvent removed. Hexane (15 mL) was added to the residue and this was stirred overnight. The hexane was decanted and the solvent removed to obtain the product as a yellow oil.

$C_{16}H_{26}N_4O_3Si$. Yellow oil, yield 68%. IR: FT-IR, ν/cm^{-1}: 1602 (m, pyridine, C=N), 1570 (m, pyridine, C=N), 1070 (s, siloxane, Si-O). ^{1}H NMR (300 MHz, $CDCl_3$): δ (ppm) = 0.62 (t, $^3J_{H\text{-}H}$ = 8.2 Hz, 2H, $CH_2CH_2C\mathbf{H_2}Si$), 1.19 (t, $^3J_{H\text{-}H}$ = 7 Hz, 9H, $SiOCH_2C\mathbf{H_3}$), 2.05 (m, 2H, $CH_2C\mathbf{H_2}CH_2Si$), 3.79 (q, $^3J_{H\text{-}H}$ = 7 Hz, 6H, $SiOC\mathbf{H_2}CH_3$), 4.39 (t, $^3J_{H\text{-}H}$ = 7.1 Hz, 2H, $C\mathbf{H_2}CH_2CH_2Si$), 7.19 (m, 1H, Pyr), 7.74 (td, $^3J_{H\text{-}H}$ = 7.6 Hz and $^4J_{H\text{-}H}$ = 1.2 Hz, 1H, Pyr), 8.14 (s, 1H, *triazole*-C**H**), 8.15 (d, 1H, Pyr), 8.54 (d, $^3J_{H\text{-}H}$ = 4.1 Hz, 1H, Pyr).

2.4.5 Synthesis of $[RhCl(COD)]_2$ in the microwave reactor

1,5-cyclooctadiene (0.28 mL, 2.2 mmol) was added to a solution of $RhCl_3$ (0.100 g, 0.477 mmol) in a ethanol (4.2 mL) and water (0.8 mL) mixture. The red-brown solution was reacted in a microwave reactor at 100°C and a maximum power of 200W for 5 minutes. The colour had changed to yellow, with a yellow precipitate also forming. The precipitate was filtered off and washed with cold ethanol (2 x 5 mL).

Yellow solid, yield 74%. ^{1}H NMR (300 MHz, $CDCl_3$): δ (ppm) = 1.77 (m, 4H, C**H₂**-*COD*), 2.53 (m, 4H, C**H₂**-*COD*), 4.24 (s, 4H, C**H**-*COD*).

2.4.6 Synthesis of model and functionalized rhodium complexes C2.1 – C2.8

2.4.6.1 Synthesis of model and functionalized neutral rhodium complexes C2.1 and C2.5

$[RhCl(CO)_2]_2$ (0.083 g, 0.25 mmol) was dissolved in dry THF (4 mL) and added dropwise to a stirring solution of **L2.1** or **L2.4** (0.50 mmol) in dry THF (6 mL). An orange precipitate started to form in the solution after 45 minutes. The reaction was stirred for a total of 2 hours at room

temperature. The solvent volume was then reduced and dry hexane (15 mL) was added. The reaction flask was left at low temperature overnight after which a powder was filtered off.

***N*-(2-Diphenylphosphino)benzylidene-propanamine rhodium(I) chlorocarbonyl** complex **C2.1**: Bright orange powder, yield 67%. Mp: 228°C (decomposed without melting). IR: FT-IR, *v*/cm^{-1}: 1987 (s, carbonyl), 1627 (w, imine, C=N). ^{1}H NMR (300 MHz, $CDCl_3$): δ (ppm) = 0.47 (t, $^{3}J_{H\text{-}H}$ = 7.4 Hz, 3H, $NCH_2CH_2C\mathbf{H_3}$), 1.72 (m, 2H, $NCH_2C\mathbf{H_2}CH_3$), 4.12 (t, $^{3}J_{H\text{-}H}$ = 7 Hz, 2H, $NC\mathbf{H_2}CH_2CH_3$), 6.91 (m, 1H, Ar), 7.46 (m, 12H, Ar), 7.57, (m, 1H, Ar) 7.95 (s, 1H, *imine*-C**H**). ^{13}C {^{1}H} NMR (75 MHz, $CDCl_3$): δ (ppm) = 10.6 ($NCH_2CH_2\mathbf{C}H_3$), 24.1 (*(*$NCH_2\mathbf{C}H_2CH_3$), 66.7 (*(*$N\mathbf{C}H_2CH_2CH_3$), 126.9, 127.2, 128.6, 128.7, 130.9, 131.0, 131.1, 131.3, 131.8, 132.5, 132.5, 133.8, 135.1, 137.0 (Ar), 163.6 (*imine*-**C**H), 189.2 (CO). ^{31}P{^{1}H} NMR (121 MHz, $CDCl_3$): δ (ppm) = 49.0 (d, $^{1}J_{P\text{-}Rh}$ = 168.6 Hz). Elemental Analysis (%): Calc. for $C_{23}H_{21}ClNOPRh$: C, 66.04; H, 6.48; N, 12.84; Found: C, 65.76; H, 6.25; N, 12.50. MS (ESI, *m/z*): 462.0 [M –Cl]$^{+}$.

***N*-(2-Diphenylphosphino)benzylidene-3-(triethoxysilyl)-1-propanamine rhodium(I) chloro-carbonyl** complex complex **C2.5**: Mp: 248°C (decomposed without melting). IR: FT-IR, *v*/cm^{-1}: 1988 (s, carbonyl), 1625 (w, imine, C=N). ^{1}H NMR (300 MHz, DMSO-d6): δ (ppm) = 0.85 (t, $^{3}J_{H\text{-}H}$ = 7.1 Hz, 2H, $NCH_2CH_2C\mathbf{H_2}Si$), 1.07 (t, $^{3}J_{H\text{-}H}$ = 7.0 Hz, 9H, $SiOCH_2C\mathbf{H_3}$), 2.52 (m, 2H, $NCH_2C\mathbf{H_2}CH_3$), 3.71 (q, $^{3}J_{H\text{-}H}$ = 7 Hz, 6H, $SiOC\mathbf{H_2}CH_3$) 4.37 (t, $^{3}J_{H\text{-}H}$ = 7 Hz, 2H, $NC\mathbf{H_2}CH_2CH_3$), 7.26 (m, 1H, Ar), 7.60 (m, 12H, Ar), 8.05 (m, 1H, Ar) 8.28 (s, 1H, *imine*-C**H**). ^{13}C {^{1}H} NMR (75 MHz, DMSO-d6): δ (ppm) = 6.6 ($NCH_2CH_2\mathbf{C}H_2Si$), 19.0 ($SiOCH_2\mathbf{C}H_3$), 29.3 *(*$NCH_2\mathbf{C}H_2CH_2Si$), 49.1 *(*$N\mathbf{C}H_2CH_2CH_2Si$), 56.5 ($SiO\mathbf{C}H_2CH_3$), 122.5 – 133.83 (Ar), 165.1 (*imine*-**C**), 201.7 (CO). ^{31}P{^{1}H} NMR (121 MHz, DMSO-d6): δ (ppm) = 30.3 (d, $^{1}J_{P\text{-}Rh}$ = 168.6 Hz). Elemental Analysis (%): Calc. for $C_{29}H_{36}ClNO_4PRhSi$: C, 52.77; H, 5.50; N, 2.12; Found: C, 55.90; H, 5.78; N, 1.91. MS (ESI, *m/z*): 661.0 [M –Cl]$^{+}$.

2.4.6.2 Synthesis of model and functionalized cationic rhodium complexes C2.2, C2.3, C2.6 and C2.7

L2.1, L2.2, L2.4 or **L2.5** (0.2 mmol) was dissolved in dry DCM (2 mL) and added dropwise to a stirring solution of $[RhCl(COD)]_2$ (0.1 mmol) in dry DCM (4 mL). Upon addition of the ligand, the solution changed colour from yellow to bright orange for **C2.2** and **C2.6,** and to dark purple for **C2.3** and **C2.7**. The solution was stirred at room temperature for 1 hour. The solvent was removed, leaving a residue which was dissolved in dry methanol (8 mL) and cooled to 0°C. $NaBPh_4$ (0.2 mmol) was added and a orange (**C2.2** and **C2.6**) or purple-red (**C2.3** and **C2.7**) precipitate formed in the solution. The reaction was stirred for a further 30 minutes at 0°C after which the solid was filtered off and washed with dry methanol.

***N*-2(Diphenylphosphino)benzylidine-propanamine rhodium(I)1,5-cyclooctadiene** complex **C2.2**: Orange solid, yield 55%. Mp: 156°C - 158°C. IR: FT-IR, *v*/cm^{-1}: 1626 (w, imine,

C=N), 703 (s, tetraphenylborate, B-C). ^{1}H NMR (300 MHz, $CDCl_3$): δ (ppm) = 0.39 (t, $^{3}J_{H-H}$ = 7.0 Hz, 3H, $NCH_2CH_2C\mathbf{H_3}$), 1.33 (m, 2H, $NCH_2C\mathbf{H_2}CH_3$), 2.17 (m, 4H, $C\mathbf{H_2}$-*COD*), 2.41 (s, 4H, $C\mathbf{H_2}$-*COD*), 2.86 (t, $^{3}J_{H-H}$ = 7.0 Hz, 2H, $NC\mathbf{H_2}CH_2CH_3$), 3.56 (s, 2H, C**H**-*COD*), 5.22 (s, 2H, C**H**-*COD*), 6.86 (t, $^{3}J_{H-H}$ = 7.0 Hz, 4H, *BPh₄*-Ar), 7.00 (t, $^{3}J_{H-H}$ = 7.0 Hz, 8H, *BPh₄*-Ar), 7.07 (m, 1H, Ar), 7.29 (m, 5H, Ar, *masked by CDCl₃ signal*), 7.45 (s, 8H, *BPh₄*-Ar), 7.49 (t, $^{3}J_{H-H}$ = 7.6 Hz, 7H, Ar), 7.54 (t, $^{3}J_{H-H}$ = 7.0 Hz, 2H, Ar). ^{13}C {^{1}H} NMR (125 MHz, $CDCl_3$): δ (ppm) = 10.4 ($NCH_2CH_2\mathbf{C}H_3$), 25.2 (*(*$NCH_2\mathbf{C}H_2CH_3$), 31.3 ($\mathbf{C}H_2$-*COD*), 66.7 ($N\mathbf{C}H_2CH_2CH_3$), 84.5 (**C**H-*COD*), 121.6, 123.4, 125.6, 127.1, 127.2, 128.3, 128.7, 129.1, 129.6, 131.9, 129.2, 129.6, 131.9, 132.2, 132.6, 133.7, 136.2 (Ar) 164.5 (q, $^{1}J_{C-B}$ = 49.4 Hz, *BPh₄*-**C**), 167.1 (*imine*-**C**H). ^{31}P{^{1}H} NMR (121 MHz, $CDCl_3$): δ (ppm) = 34.04 (d, $^{1}J_{P-Rh}$ = 152.7 Hz). Elemental Analysis (%): Calc. for $C_{54}H_{53}BNPRh$: C, 75.27; H, 6.32; N, 1.63; Found: C, 74.94; H, 6.30; N, 1.95. MS (ESI, *m/z*): 542.5 $[M]^+$.

***N*-(2-Pyridinylmethylene)-1-propanimine rhodium(I)1,5-cyclooctadiene** complex **C2.3**: Red solid, yield 52%. Mp: 79°C - 82°C. IR: FT-IR, *v*/cm^{-1}: 1624 (w, imine, C=N), 1596 (m, pyridine, C=N), 1577 (w, pyridine, C=N), 700 (s, tetraphenylborate, B-C). ^{1}H NMR (300 MHz, $CDCl_3$): δ (ppm) = 0.87 (t, $^{3}J_{H-H}$ = 7.4 Hz, 3H, $NCH_2CH_2C\mathbf{H_3}$), 1.40 (m, 2H, $NCH_2C\mathbf{H_2}CH_3$), 2.03 (d, J_{H-H} = 8.2 Hz, 4H, $C\mathbf{H_2}$-*COD*), 2.49 (s, 4H, $C\mathbf{H_2}$-*COD*), 2.72 (t, $^{3}J_{H-H}$ = 7.4 Hz, 2H, $NC\mathbf{H_2}CH_2CH_3$), 4.25 (s, 4H, C**H**-*COD*), 6.24 (s, 1H, *imine*-C**H**), 6.71 (d, $^{3}J_{H-H}$ = 7.8 Hz, 1H, Ar), 6.89 (t, $^{3}J_{H-H}$ = 7.1 Hz, 4H, *BPh₄*-Ar), 6.96 (m, 1H, Ar, *masked by BPh₄ signal*), 7.01 (t, $^{3}J_{H-H}$ = 7.4 Hz, 8H, *BPh₄*-Ar), 7.16 (d, $^{3}J_{H-H}$ = 5.1 Hz, 1H, Ar), 7.44 (m, 1H, Ar, *masked by BPh₄ signal*), 7.47 (s, 8H, *BPh₄*-Ar). ^{13}C {^{1}H} NMR (75 MHz, $CDCl_3$): δ (ppm) = 10.8 ($NCH_2CH_2\mathbf{C}H_3$), 24.7 *(*$NCH_2\mathbf{C}H_2CH_3$), 29.8 ($\mathbf{C}H_2$-*COD*), 57.6 ($N\mathbf{C}H_2CH_2CH_3$), 85.1 (**C**H-*COD*), 121.6, 125.5, 128.0, 135.8, 140.4, 147.4, 154.3, 163.7 (q, $^{1}J_{C-B}$ = 49.4 Hz, *BPh₄*-**C**), 170.5 (*imine*-**C**H). Elemental Analysis (%): Calc. for $C_{41}H_{43}BN_2Rh$: C, 72.58; H, 6.54; N, 4.13; Found: C, 72.27; H, 6.54; N, 4.43. MS (ESI, *m/z*): 359.1 $[M]^+$.

***N*-2(Diphenylphosphino)benzylidine-3-(triethoxysilyl)-1-propanamine rhodium(I)1,5-cyclo-octadiene** complex **C2.6**: Pale orange solid, yield 49%. Mp: 134°C – 137°C. IR: FT-IR, *v*/cm^{-1}: 1622 (w, imine, C=N), 702 (s, tetraphenylborate, B-C). ^{1}H NMR (300 MHz, $CDCl_3$): δ (ppm) = 0.87 (t, $^{3}J_{H-H}$ = 8.2 Hz, 2H, $NCH_2CH_2C\mathbf{H_2}Si$), 1.15 (t, $^{3}J_{H-H}$ = 7 Hz, 9H, $SiOCH_2C\mathbf{H_3}$), 2.08 (m, 2H, $NCH_2C\mathbf{H_2}CH_2Si$), 2.11 (m, 4H, $C\mathbf{H_2}$-*COD*), 2.41 (s, 4H, $C\mathbf{H_2}$-*COD*), 3.7 (t, $^{3}J_{H-H}$ = 7.0 Hz, 2H, $NC\mathbf{H_2}CH_2CH_3$), 3.56 (s, 2H, C**H**-*COD*), 3.71 (q, $^{3}J_{H-H}$ = 7 Hz, 6H, $SiOC\mathbf{H_2}CH_3$), 5.22 (s, 2H, C**H**-*COD*), 6.86 (t, $^{3}J_{H-H}$ = 7.0 Hz, 4H, *BPh₄*-Ar), 7.04 (t, $^{3}J_{H-H}$ = 7.0 Hz, 8H, *BPh₄*-Ar), 7.07 (m, 1H, Ar), 7.29 (m, 5H, Ar, *masked by CDCl₃ signal*), 7.51 (s, 8H, *BPh₄*-Ar), 7.53 (t, $^{3}J_{H-H}$ = 7.6 Hz, 7H, Ar), 7.62 (t, $^{3}J_{H-H}$ = 7.0 Hz, 2H, Ar). ^{13}C {^{1}H} NMR (125 MHz, $CDCl_3$): δ (ppm) = 8.2 ($NCH_2CH_2\mathbf{C}H_2Si$), 17.9 ($SiOCH_2\mathbf{C}H_3$), 27.2 *(*$NCH_2\mathbf{C}H_2CH_2Si$), 30.4 ($\mathbf{C}H_2$-*COD*), 42.7 (*propyl*-$\mathbf{C}H_2$), 57.3 ($N\mathbf{C}H_2CH_2CH_2Si$), 82.5 (**C**H-*COD*), 121.2, 124.9, 125.0, 126.4, 128.1,

128.7, 131.0, 131.2, 131.9, 133.0, (Ar) 145.6 (*imine*-**C**H), 164.1 (q, $^{1}J_{C\text{-}B}$ = 49.4 Hz, *BPh*$_4$-**C**), 169.7 (*imine*-**C**H). $^{31}P\{^{1}H\}$ NMR (121 MHz, $CDCl_3$): δ (ppm) = 30.06 (d, $^{1}J_{P\text{-}Rh}$ = 152.7 Hz). Elemental Analysis (%): Calc. for $C_{60}H_{68}BNO_3PRhSi$: C, 70.38; H, 6.69; N, 1.37; Found: C, 61.80; H, 5.94; N, 2.18. MS (ESI, *m/z*): 704.7 $[M]^+$.

***N*-(2-Pyridinylmethylene)-3-(triethoxysilyl)-1-propanimine rhodium(I)1,5-cyclooctadiene** complex **C2.7**: Pale red solid, yield 47%. Mp: 92°C – 96°C. IR: FT-IR, *v*/cm^{-1}: 1625 (w, imine, C=N), 1595 (m, pyridine, C=N), 1579 (w, pyridine, C=N), 1070 (m, Si-O), 702 (s, tetraphenylborate, B-C). ^{1}H NMR (300 MHz, acetone-d6): δ (ppm) = 0.87 (t, $^{3}J_{H\text{-}H}$ = 7.0 Hz, 3H, $NCH_2CH_2C\mathbf{H_3}$), 1.26 (t, $^{3}J_{H\text{-}H}$ = 7.1 Hz, 9H, $SiOCH_2C\mathbf{H_3}$), 1.40 (m, 2H, $NCH_2C\mathbf{H_2}CH_3$), 2.03 (m, 4H, $C\mathbf{H_2}$-*COD*), 2.49 (m, 4H, $C\mathbf{H_2}$-*COD*), 2.81 (t, $^{3}J_{H\text{-}H}$ = 7.4 Hz, 2H, $NC\mathbf{H_2}CH_2CH_3$), 3.86 (q, $^{3}J_{H\text{-}H}$ = 6.9 Hz, 6H, $SiOC\mathbf{H_2}CH_3$), 4.28 (s, 4H, C**H**-*COD*), 6.40 (s, 1H, *imine*-C**H**), 6.71 (d, $^{3}J_{H\text{-}H}$ = 7.8 Hz, 1H, Ar), 6.88 (t, $^{3}J_{H\text{-}H}$ = 7.1 Hz, 4H, *BPh*$_4$-Ar), 7.02 (t, $^{3}J_{H\text{-}H}$ = 7.4 Hz, 8H, *BPh*$_4$-Ar), 7.16 (d, $^{3}J_{H\text{-}H}$ = 5.1 Hz, 1H, Ar), 7.26 (m, 1H, Ar) 7.45 (s, 8H, *BPh*$_4$-Ar), 7.16 (m, 1H, Ar). $^{13}C\ \{^{1}H\}$ NMR (125 MHz, $CDCl_3$): δ (ppm): 7.7 ($NCH_2CH_2\mathbf{C}H_2Si$), 18.5 ($SiOCH_2\mathbf{C}H_3$), 24.4 ($NCH_2\mathbf{C}H_2CH_2Si$), 30.5 ($\mathbf{C}H_2$-*COD*), 52.7 ($N\mathbf{C}H_2CH_2CH_2Si$), 58.7 ($SiO\mathbf{C}H_2CH_3$), 75.9.3 (**C**H-*COD*), 115.6, 122.9, 136.8, 144.0, 149.8, (Ar), 157.8 (*imine*-**C**H), 164.5 (q, $^{1}J_{C\text{-}B}$ = 49.4 Hz, *BPh*$_4$-**C**). Elemental Analysis (%): Calc. for $C_{47}H_{58}BN_2O_3RhSi$: C, 67.14; H, 6.95; N, 3.33; Found: C, 62.40; H, 6.70; N, 4.45. MS (ESI, *m/z*): 521.5 $[M]^+$.

2.4.6.3 Synthesis of model and functionalized neutral rhodium complexes C2.4 and C2.8

KOH (0.25 mL, 1 M in ethanol) was added to a solution of **L2.3** or **L2.6** and (0.1 mmol) in ethanol (2 mL) and DCM (2 mL). The reaction was stirred for 30 minutes at room temperature. $[RhCl(COD)]_2$ (0.05 mmol) was added to the reaction as a solid, after which the reaction was allowed to proceed for a further 90 minutes. The solution was then filtered to give a yellow solution and the solvent was removed from the filtrate to yield a yellow solid.

***N*-propylsalicylaldimine rhodium(I)1,5-cyclooctadiene** complex **C2.4**: Yellow solid, yield 45%. Mp 75 - 78°C. IR: FT-IR, *v*/cm^{-1}: 1599 cm^{-1} (m, imine, C=N). ^{1}H NMR (300 MHz, $CDCl_3$): δ (ppm) = 0.93 (t, $^{3}J_{H\text{-}H}$ = 7.6 Hz, 3H, $NCH_2CH_2C\mathbf{H_3}$), 1.72 (m, 2H, $NCH_2C\mathbf{H_2}CH_3$), 1.94 (m, 4H, $C\mathbf{H_2}$-*COD*), 2.50 (m, 4H, $C\mathbf{H_2}$-*COD*), 3.09 (t, $^{3}J_{H\text{-}H}$ = 7.6 Hz, 2H, $NC\mathbf{H_2}CH_2CH_3$), 3.72 (m, 2H, C**H**-*COD*), 4.56 (m, 2H, C**H**-*COD*), 6.56 (t, $^{3}J_{H\text{-}H}$ = 7.1 Hz, 1H, Ar), 6.85 (d, $^{3}J_{H\text{-}H}$ = 8.2 Hz, 1H, Ar), 7.15 (dd, $^{3}J_{H\text{-}H}$ = 7.6 Hz and $^{4}J_{H\text{-}H}$ = 1.8 Hz, 1H, Ar), 7.30 (td, $^{3}J_{H\text{-}H}$ = 6.5 Hz and $^{4}J_{H\text{-}H}$ = 1.8 Hz, 1H, Ar, *masked by CDCl*$_3$ *signal*), 7.91 (s, 1H, *imine*-C**H**). $^{13}C\ \{^{1}H\}$ NMR (125 MHz, $CDCl_3$): δ (ppm): 11.3 ($NCH_2CH_2\mathbf{C}H_3$), 27.3 ($NCH_2\mathbf{C}H_2CH_3$), 31.8 ($\mathbf{C}H_2$-*COD*), 61.1 ($N\mathbf{C}H_2CH_2CH_3$), 84.9 (**C**H-*COD*), 114.3, 119.2, 121.4, 134.4, 134.9, (Ar), 165.9 (*imine*-**C**H).

Elemental Analysis (%): Calc. for $C_{18}H_{23}NORh$: C, 57.91; H, 6.48; N, 3.75; Found: C, 57.21; H, 6.69; N, 3.62. MS (ESI, *m/z*): 374.1 $[M+H]^+$.

Salicylidene-3-aminopropyltriethoxysilane rhodium(I)1,5-cyclooctadiene complex **C2.8**: Yellow solid, yield 42%. Mp 89 - 92°C. IR: FT-IR, *v*/cm^{-1}: δ (ppm) = 0.60 (t, $^3J_{H-H}$ = 8.2 Hz, 2H, $NCH_2CH_2C\mathbf{H_2}Si$), 1.25 (t, $^3J_{H-H}$ = 7.6 Hz, 9H, $SiOCH_2C\mathbf{H_2}$) 1.80 (m, 2H, $NCH_2C\mathbf{H_2}CH_2Si$), 1.88 (m, 4H, $C\mathbf{H_2}$-*COD*), 2.48 (m, 4H, $C\mathbf{H_2}$-*COD*), 3.12 (m, 2H, $NC\mathbf{H_2}CH_2CH_2Si$), 3.72 (m, 2H, C**H**-*COD*), 3.83 (q, $^3J_{H-H}$ = 6.4 Hz, 6H, $SiOC\mathbf{H_2}CH_3$), 4.55 (s, 2H, C**H**-*COD*), 6.56 (m, 1H, Ar), 6.83 (m, 1H, Ar), 7.15 (m, 1H, Ar), 7.29 (m, 1H, Ar, *masked by $CDCl_3$ signal*), 7.93 (s, 1H, *imine*-C**H**). ^{13}C $\{^1H\}$ NMR (125 MHz, $CDCl_3$): δ (ppm): 4.3 ($NCH_2CH_2\mathbf{C}H_2Si$), 13.6 ($SiOCH_2\mathbf{C}H_3$), 24.2 ($NCH_2\mathbf{C}H_2CH_2Si$), 27.0 ($\mathbf{C}H_2$-*COD*), 53.6 ($SiO\mathbf{C}H_2CH_3$), 66.42 ($N\mathbf{C}H_2CH_2CH_2Si$), 80.3 (**C**H-*COD*), 114.4, 116.6, 122.44, 129.6, 130.1, 165.2 (Ar), 160.5 (*imine*-**C**H). Elemental Analysis (%): Calc. for $C_{24}H_{38}NO_4RhSi$: C, 53.82; H, 7.15; N, 2.62; Found: C, 48.0; H, 6.53; N, 2.73. MS (ESI, *m/z*): 536.4 $[M+H]^+$.

2.4.7 Synthesis of pyridyl-triazole cationic rhodium complexes C2.9 and C2.10

The complexes were synthesized by dissolving $[RhCl(COD)]_2$ (0.1 mmol) in DCM (2 mL) and adding the ligand (0.2 mmol) dissolved in DCM (4 mL) dropwise to the stirring solution. An immediate colour change from yellow to brown was observed. The reaction was allowed to proceed for 1 hour at room temperature. The solvent was then removed and the residue redissolved in MeOH (10 mL). The reaction was cooled to 0°C and $NaBPh_4$ (0.2 mmol) was added. A precipitate formed and the reaction was stirred for a further hour at 0°C after which the solid was filtered off and washed with methanol.

2.4.7.1 Synthesis of 2-(1-Octyl-1*H*-1,2,3-triazol-4-yl)pyridine rhodium(I)1,5-cyclooctadiene complex C2.9

Model pyridyl-triazole ligand **L2.7** used. Product obtained as a yellow solid, yield 48%. Mp: 134°C - 136°C. ^1H NMR (300 MHz, $CDCl_3$): δ (ppm) = 0.91 (t, $^3J_{H-H}$ = 7.0 Hz, 3H, $CH_2CH_2C\mathbf{H_3}$), 1.20 (s, broad, 2H, $CH_2CH_2C\mathbf{H_2}CH_3$), 1.28 (m, 8H, $NCH_2CH_2C\mathbf{H_2}C\mathbf{H_2}C\mathbf{H_2}C\mathbf{H_2}CH_2CH_3$), 1.63 (m, 2H, $NCH_2C\mathbf{H_2}CH_2CH_2$), 2.10 (d, $^3J_{H-H}$ = 8.2 Hz, 4H, $C\mathbf{H_2}$-*COD*), 2.53 (s, 4H, $C\mathbf{H_2}$-*COD*), 3.80 (t, $^3J_{H-H}$ = 7.6 Hz, 2H, $NC\mathbf{H_2}CH_2CH_2$), 4.81 (br d, $^3J_{H-H}$ = 211.5 Hz, 4H, C**H**-*COD*), 5.79 (s, 1H, *triazole*-C**H**), 6.85 (t, $^3J_{H-H}$ = 7.0 Hz, 4H, *BPh_4*-Ar), 6.99 (t, $^3J_{H-H}$ = 7.1 Hz, 8H, *BPh_4*-Ar), 7.03 (m, 1H, Pyr, *obscured by BPh_4 signal*), 7.12 (t, $^3J_{H-H}$ = 6.4 Hz, 1H, Pyr), 7.43 (d, $^3J_{H-H}$ = 5.2 Hz, 1H, Pyr), 7.51 (s, 8H, *BPh_4*-Ar), 7.63 (t, $^3J_{H-H}$ = 8.2 Hz, 1H, Pyr). ^{13}C $\{^1H\}$ NMR (125 MHz, $CDCl_3$): δ (ppm): 14.1 (*octyl*-$\mathbf{C}H_3$), 22.6, 26.2, 28.8, 29.0, 29.7, 30.3 (*octyl*-$\mathbf{C}H_2$), 31.7 ($\mathbf{C}H_2$-*COD*), 51.8 (*octyl*-$\mathbf{C}H_2$), 84.9 (**C**H-*COD*), 121.9, 122.5, 124.5, 125.3, 136.0, 141.0, 147.7 (Ar), 164.4 (q, $^1J_{C-B}$ = 49.4 Hz, *BPh_4*-**C**). Elemental Analysis (%): Calc. for $C_{47}H_{54}BN_4Rh$: C, 71.76; H, 6.66; N, 7.12; Found: C, 71.39; H, 6.78; N, 7.48. MS (ESI, *m/z*): 469.2 $[M]^+$..

2.4.7.2 Synthesis of 2-(1-[3-(Triethoxysilyl)propyl]-1*H*-1,2,3-triazol-4-yl) pyridine rhodium(I)1,5-cyclooctadiene complex C2.10

Functionalized pyridyl-triazole ligand **L2.8** used. Product obtained as a dark yellow solid, yield 42%. Mp: 146 – 149 °C. ^{1}H NMR (300 MHz, $CDCl_3$): δ (ppm) = 0.50 (m, 2H, $NCH_2CH_2C\mathbf{H_2}Si$), 1.24 (t, $^{3}J_{H\text{-}H}$ = 4.7 Hz, 9H, $SiOCH_2C\mathbf{H_3}$), 1.78 (m, 2H, $NCH_2C\mathbf{H_2}CH_2Si$), 2.11 (d, $^{3}J_{H\text{-}H}$ = 8.2 Hz, 4H, $C\mathbf{H_2}$-*COD*), 2.53 (s, 4H, $C\mathbf{H_2}$-*COD*), 3.81 (m, 2H, $NC\mathbf{H_2}CH_2CH_2Si$, *obscured by* $SiOC\mathbf{H_2}CH_3$ *signal*) 3.84 (m, 6H, $SiOC\mathbf{H_2}CH_3$, *obscured by* $NC\mathbf{H_2}CH_2CH_2Si$ *signal*) 4.79 (br d, $^{3}J_{H\text{-}H}$ = 110.3 Hz, 4H, C**H**-*COD*), 5.75 (s, 1H, *triazole*-C**H**), 6.84 (t, $^{3}J_{H\text{-}H}$ = 7.1 Hz, 4H, BPh_4-*Ar*), 6.99 (t, $^{3}J_{H\text{-}H}$ = 7.0 Hz, 8H, BPh_4-*Ar*), 7.03 (m, 1H, Pyr, *obscured by* BPh_4 *signal*), 7.13 (td, $^{3}J_{H\text{-}H}$ = 7.1 Hz and $^{4}J_{H\text{-}H}$ = 1.2 Hz, 1H, Pyr), 7.44 (d, $^{3}J_{H\text{-}H}$ = 5.3 Hz, 1H, Pyr), 7.50 (s, 8H, BPh_4-*Ar*), 7.65 (td, $^{3}J_{H\text{-}H}$ = 7.7 Hz and $^{4}J_{H\text{-}H}$ = 1.2 Hz, 1H, Pyr). ^{13}C {^{1}H} NMR (125 MHz, $CDCl_3$): δ (ppm) = 6.4 ($NCH_2CH_2\mathbf{C}H_2Si$), 17.8 ($SiOCH_2\mathbf{C}H_3$), 24.3 (**C**H_2-COD), 31.3 ($NCH_2\mathbf{C}H_2CH_2Si$), 39.9 ($N\mathbf{C}H_2CH_2CH_2Si$), 58.1 ($SiO\mathbf{C}H_2CH_3$), 83.7 (**C**H-COD), 119.2, 121.3, 125.1, 125.9, 126.8, 127.3, 128.8, 129.3, 136.1 (Ar), 163.8 (q, $^{1}J_{C\text{-}B}$ = 49.4 Hz, BPh_4-**C**). Elemental Analysis (%): Calc. for $C_{48}H_{58}BN_4O_3RhSi$: C, 65.45; H, 6.62; N, 6.36; Found: C, 64.03; H, 6.34; N, 7.19. MS (ESI, *m/z*): 561.2 $[M]^+$.

2.4.7.3 Synthesis of (1-propyltriethoxysilane-1*H*-1,2,3-triazol-4-yl)methanol

Propargyl alcohol (0.086 mL, 1.5 mmol), 3-azidopropyltriethoxysilane (0.247 g, 1 mmol) was dissolved in THF (8 mL). Copper(I) iodide (0.004 g, 0.02 mmol) was added and remained suspended in the clear reaction solution. Upon the addition of diisopropylamine (0.8 mL), the colour of the solution changed to yellow. The reaction was stirred at 25°C for 24 hours, during which time the colour darkened slightly. The solution was filtered to yield an orange solution. The solvent was removed from the solution and a yellow oil was obtained.

Yellow oil, yield 76%. IR: FT-IR, *v*/cm^{-1}: 3050 cm^{-1} (m, O-H), 1064 (s, Si-O). ^{1}H NMR (300 MHz, $CDCl_3$): δ (ppm) = 0.62 (t, $^{3}J_{H\text{-}H}$ = 8.2 Hz, 2H, $CH_2CH_2C\mathbf{H_2}Si$), 1.22 (t, $^{3}J_{H\text{-}H}$ = 7.1 Hz, 9H, $SiCH_2C\mathbf{H_3}$), 2.03 (m, 2H, $CH_2C\mathbf{H_2}CH_2Si$), 3.82 (q, $^{3}J_{H\text{-}H}$ = 7 Hz, 6H, $SiC\mathbf{H_2}CH_3$), 4.37 (t, $^{3}J_{H\text{-}H}$ = 7.1 Hz, 2H, $C\mathbf{H_2}CH_2CH_2Si$), 4.80 (s, 2H, $HOC\mathbf{H_2}$), 7.56 (s, 1H, *triazole*-C**H**).

2.5 References

1 N. V. Dubrovina, L. Domke, I. A. Shuklov, A. Spannenberg, R. Franke, A. Villinger and A. Börner, *Tetrahedron*, 2013, **69**, 8809–8817.

2 J. J. M. Weemers, W. N. P. Van Der Graaff, E. A. Pidko, M. Lutz and C. Müller, *Chem. - A Eur. J.*, 2013, **19**, 8991–9004.

3 I. Mon, D. A. Jose and A. Vidal-Ferran, *Chem. - A Eur. J.*, 2013, **19**, 2720–2725.

4 C. F. Czauderna, D. B. Cordes, A. M. Z. Slawin, C. Mueller, J. I. Van Der Vlugt, D. Vogt and P. C. J. Kamer, *Eur. J. Inorg. Chem.*, 2014, 1797–1810.

5 S. H. Chikkali, J. I. Van Der Vlugt and J. N. H. Reek, *Coord. Chem. Rev.*, 2014, **262**, 1–15.

6 B. R. James, P. W. N. M. Van Leeuwen, S. D. Ittel, A. Nakamura, R. L. Richards and A. Yamamoto, *Rhodium Catalyzed Hydroformylation*, Kluwer Academic Publishers, 2002.

7 P. G. Cozzi, *Chem. Soc. Rev.*, 2004, **33**, 410–421.

8 J. Andrieu, J. Camus, P. Richard, R. Poli, L. Gonsalvi, F. Vizza and M. Peruzzini, *Eur. J. Inorg. Chem.*, 2006, 51–61.

9 R. Maura, J. Steele, L. Vendier, D. Arquier, S. Bastin, M. Urrutigoïty, P. Kalck and A. Igau, *J. Organomet. Chem.*, 2011, **696**, 897–904.

10 N. C. Antonels, B. Therrien, J. R. Moss and G. S. Smith, *Inorg. Chem. Commun.*, 2009, **12**, 716–719.

11 N. C. Antonels, J. R. Moss and G. S. Smith, *J. Organomet. Chem.*, 2011, **696**, 2003–2007.

12 B. C. E. Makhubela, A. Jardine and G. S. Smith, *Green Chem.*, 2012, **14**, 338–347.

13 B. C. E. Makhubela, A. M. Jardine, G. Westman and G. S. Smith, *Dalton Trans.*, 2012, **41**, 10715.

14 L. C. Matsinha, S. F. Mapolie and G. S. Smith, *Dalton Trans.*, 2015, **44**, 1240–1248.

15 E. B. Hager, B. C. E. Makhubela and G. S. Smith, *Dalton Trans.*, 2012, **41**, 13927–13935.

16 S. Nakagaki, G. K. B. Ferreira, A. L. Marçal and K. J. Ciuffi, *Curr. Org. Synth.*, 2014, **11**, 67–88.

17 Y. Pérez, I. del Hierro, L. Zazo, R. Fernández-Galán and M. Fajardo, *Dalton Trans.*, 2015, **44**, 4088–101.

18 C. Sarmah, D. Sahu and P. Das, *Catal. Commun.*, 2013, **41**, 75–78.

19 M. Vasconcellos Dias, M. S. Saraiva, P. Ferreira and M. J. Calhorda, *Organometallics*, 2015, **34**, 1465–1478.

20 T. Baskaran, R. Kumaravel, J. Christopher, S. Radhakrishnan and A. Sakthivel, *Catal. Letters*, 2015, **145**, 851–859.

21 B. C. E. Makhubela, A. Jardine and G. S. Smith, *Green Chem.*, 2012, **14**, 338–347.

22 A. J. Deeming and P. J. Sharratt, *J. Organomet. Chem.*, 1975, **99**, 447–453.

23 J. Chatt and M. Venanzi, L, *J. Chem. Soc*, 1957, 4735–4741.

24 J. Tönnemann, J. Risse, Z. Grote, R. Scopelliti and K. Severin, *Eur. J. Inorg. Chem.*, 2013, 4558–4562.

25 I. P. Kovalev, Y. N. Kolmogorov, Y. A. Strelenko, A. V Ignatenko, M. G. Vinogradov and G.- Nikishin, 1990, **385**, 173–184.

26 K. Q. Vuong, M. G. Timerbulatova, M. B. Peterson, M. Bhadbhade and B. A. Messerle, *Dalton Trans.*, 2013, **42**, 14298–308.

27 A. Scrivanti, V. Beghetto, M. Alam, S. Paganelli, P. Canton, M. Bertoldini and E. Amadio, *Inorg. Chim. Acta.*, 2017, **455**, 613–617.

28 N. Moitra, J. J. E. Moreau, X. Cattoen and M. Wong Chi Man, *Chem. Commun.*, 2010, **46**, 8416–8418.

29 Z.-C. Dai, Y.-F. Chen, M. Zhang, S.-K. Li, T.-T. Yang, L. Shen, J.-X. Wang, S.-S. Qian, H.-L. Zhu and Y.-H. Ye, *Org. Biomol. Chem.*, 2015, **13**, 477–486.

30 B. L. Hayes, *Microwave Synthesis: Chemistry at the speed of light*, CEM Publishing, 2002.

31 P. Sambasiva Rao, C. Kurumurthy, B. Veeraswamy, G. Santhosh Kumar, P. Shanthan Rao, R. Pamanji, J. Venkateswara Rao and B. Narsaiah, *Bioorganic Med. Chem. Lett.*, 2013, **23**, 1225–1227.

CHAPTER 3 : NMR STUDIES OF RHODIUM 1,5-CYCLOOCTADIENE COMPLEXES

3.1 Introduction

Nuclear magnetic resonance spectroscopy is an indispensable analytical technique for modern chemists and biochemists. The importance of the field is underlined by the fact that the 1991 Nobel Prize in Chemistry was awarded to Richard Ernst for his work in developing experimental NMR spectroscopy techniques.[1]

NMR spectroscopy is most commonly used for structure elucidation and can be used to study substances from small organic molecules to high molecular weight macromolecules such as proteins. Various so-called two dimensional NMR techniques can give further insight into the structure of compounds and their behaviour in solution.[2–4] These techniques make use of more advanced pulse sequences than what is commonly used for simple NMR spectroscopy. NMR spectroscopy can also be used to study dynamic effects in molecules, from intramolecular interconversions in cyclical molecules like cyclohexene, to intermolecular processes like the binding of a substrate to an enzyme.[1,5]

In this current investigation we applied NMR spectroscopy to probe:

a) ionic interactions that give rise to some peculiar NMR spectra for some of the complexes reported in Chapter 2 and

b) the kinetics of a dynamic process that was observed in a number of the complexes reported in Chapter 2.

A short introduction into the use of NMR to study such processes is therefore given.

3.1.1 Ion pairing in organometallic chemistry

Ion pairs are defined as pairs of oppositely charged ions with a common solvation shell, held together essentially by Coulombic forces. The pairs need to be kinetically and thermodynamically stable. The concept was first introduced by Bjerrum in 1925. Since then, various types of ion pairs have been defined, including contact ion pairs, solvent-separated ion pairs and solvent-shared ion pairs.[6]

Contact (also called intimate) ion pairs are ion pairs where there is no solvent molecule between the two ions, as shown in (a) in Figure 3.1. Solvent-separated (or loose) ion pairs are ion pairs where each ion is completely surrounded by solvent molecules (b). A further distinction is made for the situation where only one solvent shell separates the two ions, and these ion pairs are called solvent-shared ion pairs (c).

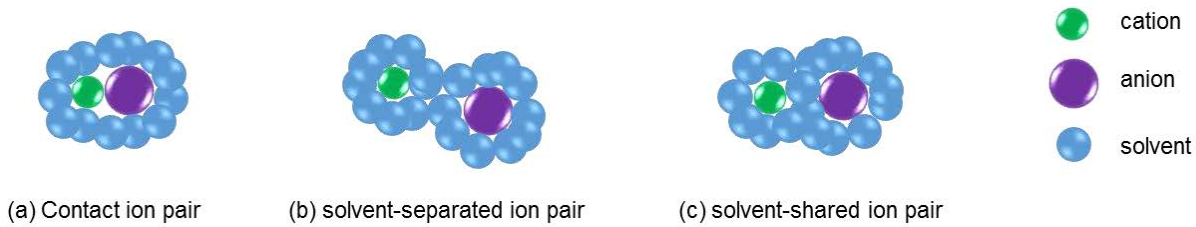

Figure 3.1 Examples of different types of ion pairs.[6]

The above definitions can also be applied to ion pairs of organometallic complexes. For transition metal complexes there also exists the possibility of a so-called 'inner-sphere ion pair', where one of the ligands is replaced with the anion.

The solvent in which the organometallic complex is dissolved plays an important role to determine which type of ion pair will be present. It has been found that solvents with low dielectric constants, e.g. chloroform, dichloromethane and toluene, generally lead to the formation of contact ion pairs. In solvents with high dielectric constants, like methanol and acetone, solvent-separated ion pairs are more commonly found.[7]

Given that several ionic complexes were prepared as part of this thesis, the effects of ion pairing is of particular interest in the larger context of this project, since it can have dramatic effects on the catalytic behaviour of transition metal complexes as described by Macchioni in a 2005 review. In this particular article, a number of catalytic reactions is reviewed, including olefin polymerization, Diels-Alder reactions and carbonylation reactions to name but a few.[6]

The main method of studying ion pairs in solution is NMR spectroscopy. Both nuclear Overhauser effect (NOE) NMR spectroscopy and pulse gradient spin echo (PGSE) spectroscopy are commonly used, and these techniques are briefly discussed below.

3.1.1.1 The use of nuclear Overhauser effect spectroscopy to study ion pairing

NOE spectroscopy relies on the detection of inter-ionic dipolar interactions. When studying ion pairs, NOE spectroscopy is used to investigate interactions between atoms of the cations (usually hydrogen) and those of the anions (hydrogen or fluorine). These spectra can be used to determine the relative positions of the ions.

Zuccaccia *et al*. applied this technique to determine the position of a hexafluorophosphate counter-ion relative to a ruthenium cationic complex.[8] The heteronuclear nuclear Overhauser effect spectrum, shown in Figure 3.2, clearly show interionic interactions between the fluorine atoms of the counter-ion and some of the protons on the cation. Strong interactions are observed between the fluorine atoms of the counter-ion and the CH_2 protons and the 5/5' protons. There is also a weak interionic contact between the PMe_3 protons and the counter-ion, but its intensity is rather small. This indicates that the counter-ion mainly occupies space to the right of the cation as drawn in Figure 3.2.

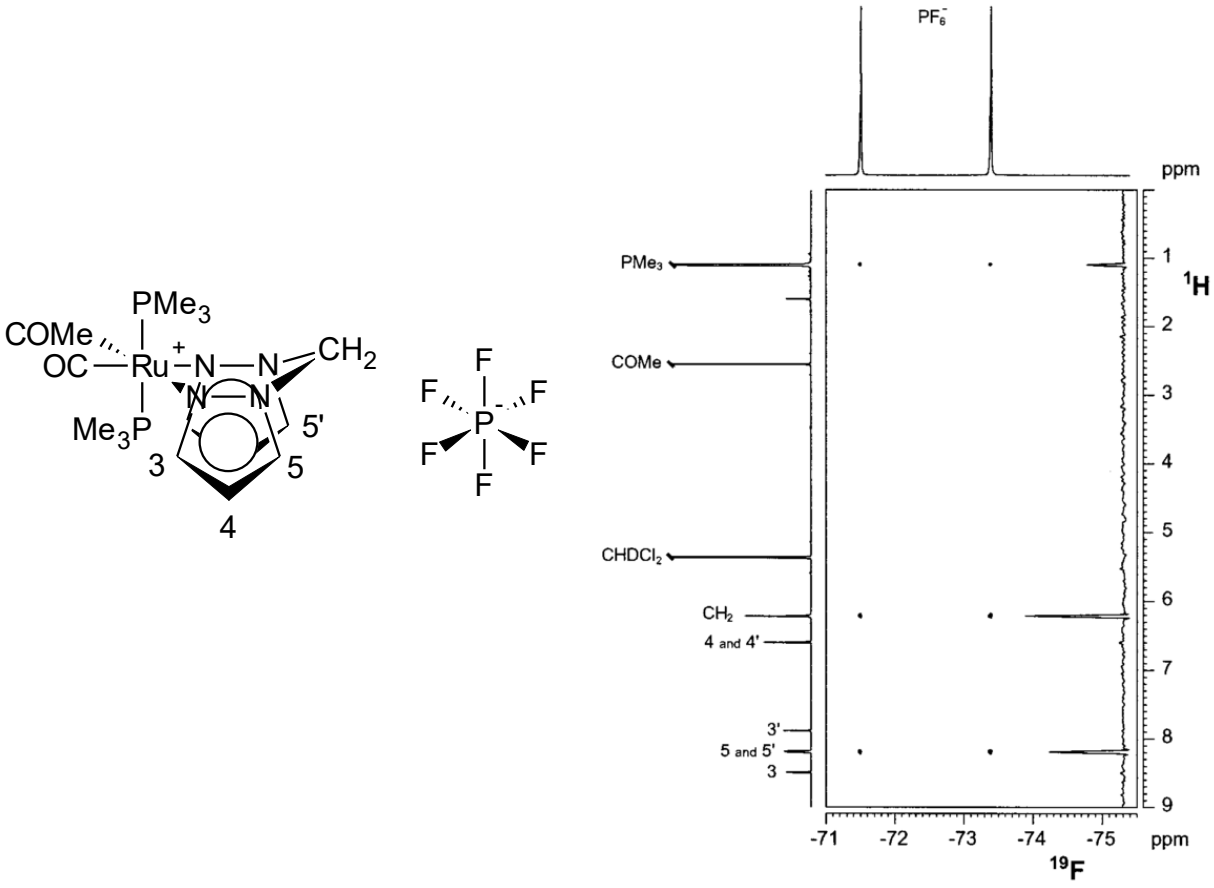

Figure 3.2 Ruthenium complex investigated by Zuccaccia *et al*. (left), showing region-specific interactions. ^{19}F, ^{1}H-HOESY spectrum of the ruthenium complex (right).[8]

3.1.1.2 The use of pulse gradient spin echo spectroscopy to study ion pairing

Pulse gradient spin echo (PGSE) spectroscopy or its 2D variant, diffusion ordered NMR spectroscopy (DOSY), is a useful tool to determine the diffusion rate of molecular entities. In these experiments, a series of spin-echo spectra are measured with varying pulsed field gradient strengths. This leads to differing values of the measured intensity of the measured NMR signal. The diffusion coefficient is obtained from Equation 3.1

$$\ln\left(\frac{I}{I_0}\right) = -(\gamma_X \delta)^2 G^2 \left(\Delta - \frac{\delta}{3}\right) D \qquad (3.1)$$

where I is the measured intensity of the NMR signal, I_0 is the maximum intensity of the NMR signal, γ is the gyromagnetic ratio of the X nucleus, δ is the length of the gradient pulse, G is the gradient strength, Δ is the delay between the midpoints of the gradients, and D is the diffusion coefficient. By varying the gradient strength one can obtain a set of values for I, and by plotting $\ln(I/I_0)$ against G^2 the value for D can be obtained from the slope of the graph.

In order to compare ions in different solvents, the Stokes-Einstein equation (Equation 3.2), which takes solvent viscosity into account, is used to calculate the hydrodynamic radii of the ions. In this equation k_B represents Boltzmann's constant, T is the temperature, η is the solvent viscosity and r_H the hydrodynamic radius.

$$D = \frac{k_B T}{6\pi\eta r_H} \qquad (3.2)$$

The use of these techniques is well known in literature and has been the subject of some recent reviews.[6,7,9]

3.1.2 Cation-π stacking interactions

Noncovalent interactions involving aromatic rings are amongst other phenomena that could play an important role in chemical conformational control and molecular recognition. These interactions include π-π stacking, XH/π interactions (X = O, N, C) and cation-π interactions. Many biological molecules exhibit these types of interactions and understanding these processes is often pivotal in the field of drug design.[10,11] For example, the binding of the anti-Alzheimer's drug E2020 to the active site of the enzyme acetylcholinesterase involves a number of noncovalent interactions in which the π systems of aromatic groups play an important role (Figure 3.3).

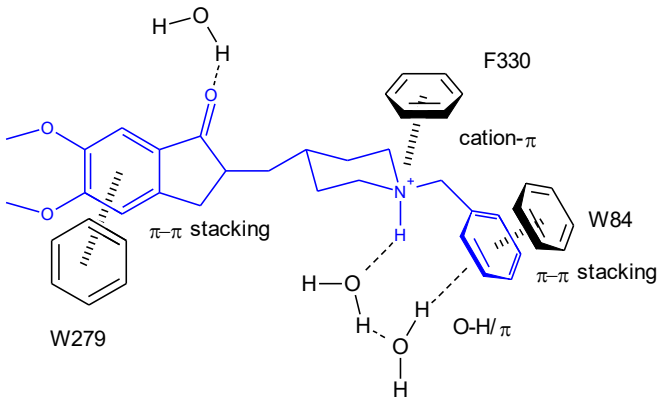

Figure 3.3 Binding mode of the anti-Alzheimer's drug E2020 (blue) within the active site of acetylcholinesterase from *Torpedo californica*.[10] W279, F330 and W84 are different aromatic residues within the enzyme's binding pocket.

Cation-π interactions, or the electrostatic attraction between a cation and the negative electrostatic potential associated with the face of a simple π system, play an important role in biological ligand recognition and catalysis. Cations taking part in this type of interaction in biological systems include simple inorganic ions (Li^+, K^+ and Na^+), protonated amines (RNH_3^+) and quaternary ammonium ions.[12]

Interactions involving aromatic rings also play a role in the structure of metal complexes. Milčić *et al.* screened crystal structures of metal complexes in the Cambridge Structural Database in order to find interactions between ligands coordinated to a metal centre and aromatic groups.[13] These authors found numerous examples of metal complexes in which there is close contact between an aromatic ring and a hydrogen atom from two different ligands on the metal. In all of the observed cases, the hydrogen atom interacting with the aromatic group is directed towards the aromatic ring. These hydrogen atoms were found to possess a partial positive charge, induced by the metal charge. The authors used DFT calculations to determine that the energy of interactions in a model Co^{3+} complex was about 4 kcal/mol.

Cation-π interactions have predominantly been studied in the solid state by analysing the crystal structures of molecules or complexes where such interactions are suspected.[14–16] Not surprisingly, studies of this phenomenon in solution are less commonly found in the literature. Richter *et al.* used NOESY and fluorescence spectroscopy to study the intramolecular cation-π stacking interactions of *N*-methyl-pyridinium iodides.[11] It was found that there were no NOESY cross-peaks between the pyridyl and phenyl ring proton signals of flexible neutral phenylalkyl pyridines. However conversion of these species to the corresponding methylpyridinium salts resulted in distinct cross-peaks between the pyridinium and phenyl proton signals in the NOE spectra. This indicates that the phenyl and pyridyl are in close proximity. The proposed structure that one of these species would adopt in solution is shown in Figure 3.4. The adoption of this conformation is most likely facilitated by a cation-π interaction.

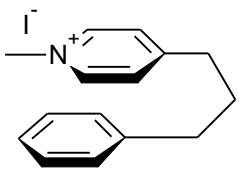

Figure 3.4 Conformation of *N*-methyl-pyridinium iodine salt in dichloromethane solution as determined by NOE spectroscopy.[11]

3.1.3 Dynamic NMR spectroscopy

NMR spectroscopy can be used to detect molecular motion over a wide range of timescales, from picoseconds to several seconds.[5] Various types of molecular motion can have an effect on the NMR spectrum; these include molecular vibrations, local rotations of molecular groups, internal molecular flexibility, chemical exchange, molecular rotations and translational motion.

Of these types of motion, molecular vibrations, local rotations and molecular rotations of small molecules occur on the picosecond timescale and are typically too fast to detect using NMR, but can be observed in some cases.[17] Molecular flexibility, molecular rotations of large molecules such proteins, translational motion and chemical exchange are more commonly observed and can occur from a nanosecond to the second timescale.[18–20]

Chemical exchange is the most commonly observed to influence an NMR spectrum, and is discussed in more detail in the following section.[5,21]

3.1.3.1 Chemical exchange

Chemical exchange is observed when some dynamic process translates certain nucleus from one magnetic environment to a different one.[21] This process may or may not involve the breaking and re-forming of chemical bonds. It can also occur when the conformation of a molecule changes around a relatively rigid bond. This process can occur over a wide range of timescales, from a few nanoseconds, to seconds. A common example of this process is the exchange of the *N*-methyl groups of *N*,*N*-dimethylformamide as shown in Scheme 3.1. Because of the resonance between the unshared electron pair on the nitrogen atom and the C=O double bond, the central C-N nitrogen bond has some double bond character and rotation around the bond is restricted.[22]

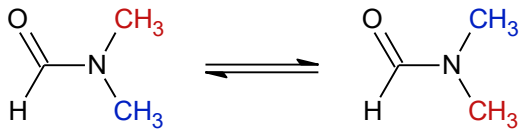

Scheme 3.1 Chemical exchange between methyl groups in N,N-dimethylformamide.[22]

NMR spectroscopy can be used to study chemical exchange phenomena even when the system is in equilibrium because the molecular motion itself is studied, rather than a change in concentration of two chemical species. This gives it an advantage over other techniques such as infrared or ultraviolet spectroscopy.[1,5]

3.1.3.2 Conformational exchange

Conformational exchange is an intramolecular process where some of the nuclei of a molecule can be found in two different magnetic environments and therefore exchange their environments. Some examples of conformational site exchange that can occur in organic molecules are molecules with a hindrance to internal rotation, ring inversion, and valence tautomerism.[1,22] If both conformations are in equal concentration, this process is called symmetric two-site exchange. The process is commonly depicted as shown below (Scheme 3.2).

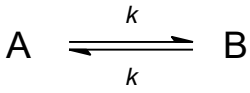

Scheme 3.2 Symmetric site-exchange.

In this depiction, *k* is the rate constant of the exchange process. For a symmetric two-site exchange, the rate constant for the process A → B and B → A will be equal. The value of *k,* as well as the difference in resonance frequency ratios in the two environments is important when considering what effect the exchange will have on the NMR spectrum. If the value of *k* is roughly the same as the difference in resonance frequency ratios in the two environments, the system is said to be in the intermediate exchange regime. Two other types of exchange can be identified: slow exchange and fast exchange.

Slow exchange is applicable in situations where the transitions between the two molecular states do not happen very often. It is therefore infrequent, rather than actually slow. The random transitions cause changes in the precession frequency of the nuclear spin, which then causes dephasing of the transverse magnetization. This leads to a decay of the transverse magnetization. Faster exchange leads to faster decay, which causes broadening of the NMR peaks. The point where the signals coalesce is termed the crossover point. At this point, the rate of exchange is equal to the difference in chemical shift frequency of the starting signals.[5,22]

When the exchange rate constant *k* increases past the crossover point, the system is in the fast exchange regime. The changes between the molecular states happen very frequently, and since significant precession only takes place after a time interval in which a large number of changes have occurred, the average precession frequency is recorded, rather than two different frequencies. This then leads to slower decay of the total transverse magnetization, which causes the NMR signals to narrow.[5]

Experimental spectra which are recorded in the broader intermediate exchange regime are very sensitive to changes in the dynamics. The changes are commonly effected by changing

the temperature at which the spectrum is recorded. The spectra recorded at different temperatures can be used to obtain an accurate estimate of the exchange rate constant *k*. Once *k* has been obtained, either the Arrhenius equation or the Eyring equation can be used to calculate the Gibbs free energy of this exchange process at a specific temperature.[1]

In this chapter we discuss the use of variable temperature NMR to investigate the conformational changes exhibited by the cyclo-octadiene ligand in some of the complexes prepared in this thesis.

3.2 Results and discussion

3.2.1 Investigation of the imine proton resonance

As stated in Chapter 2, the shift of the imine proton resonance in the ^{1}H NMR spectrum after the complexation of **L2.2** to rhodium to form **C2.3** was uncharacteristically large. The complex is shown in Figure 3.5, while a comparison between the ^{1}H NMR spectra of the ligand and the complex is given in Figure 3.6. The signals due to the protons of the tetraphenylborate counter-ion are highlighted in grey. The assignment of the signals in the ^{1}H NMR spectrum was reported in Chapter 2, and is also supported by work on similar ligands previously reported by Haddleton *et al*.[23]

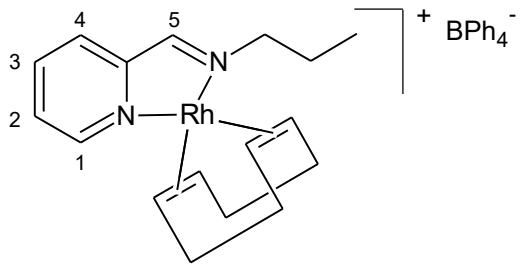

Figure 3.5 Cationic rhodium complex C2.3.

The imine proton resonance, H^5, shifted upfield by 2.22 ppm relative to the imine resonance in the free ligand. The signals due to H^1 and H^4 also show significant upfield shifts of 1.4 ppm and 1.3 ppm respectively. The signals due to H^2 and H^3 are less affected, both showing a 0.3 ppm upfield shift. In the spectrum of the complex H^2 and H^3 both partially overlap with the BPh_4^+ signals. The H^1, H^4 and H^5 protons are therefore experiencing some degree of shielding in the complex.

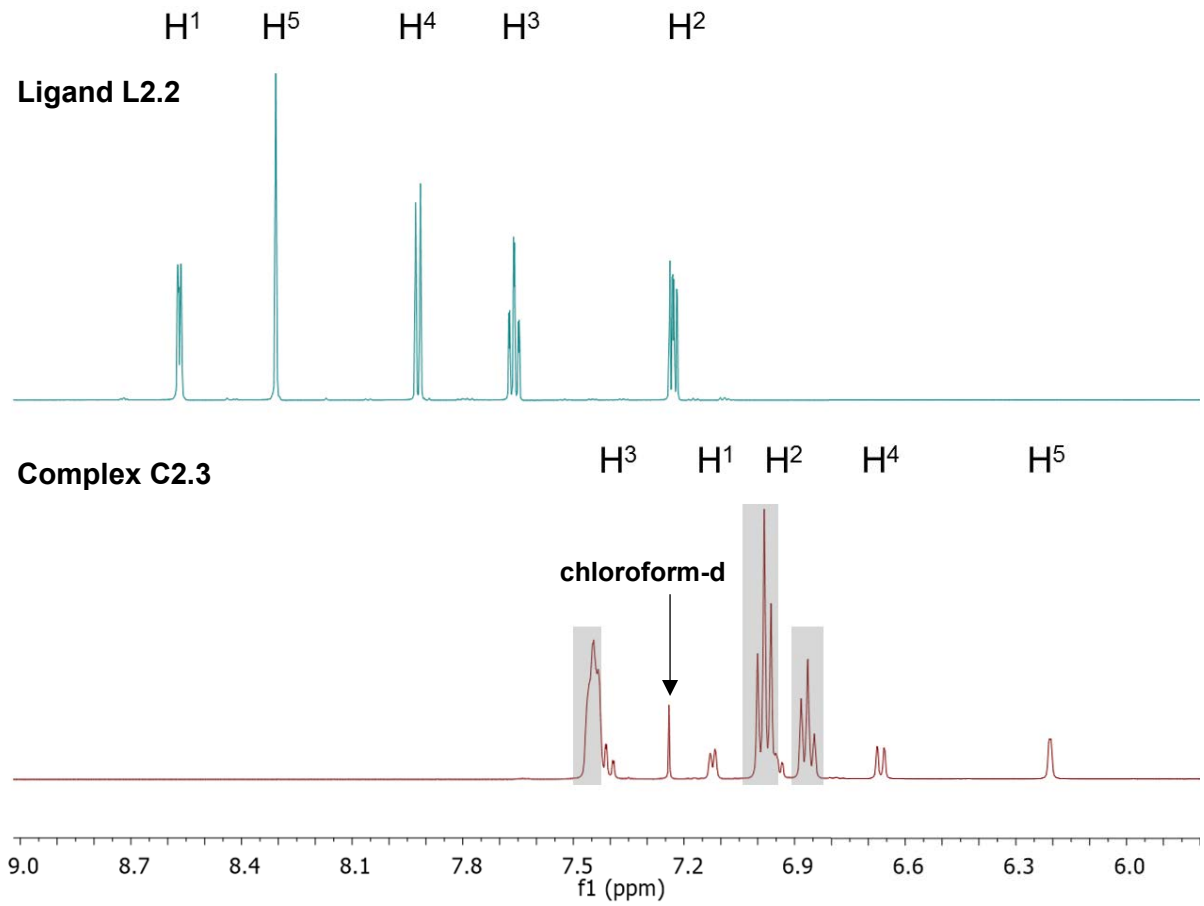

Figure 3.6 ^{1}H NMR spectra of ligand L2.2 (top) and complex C2.3 (bottom) in chloroform-*d* at room temperature. Peaks due to BPh_4^+ highlighted in grey. H^2 and H^3 show some overlap with peaks due to BPh_4^+.

This upfield shift of H^5 increased significantly on cooling of the sample, as can be seen in Figure 3.7. The imine proton signal H^5 (shown in the red box) shifts from 6.19 ppm at 20 °C to 4.74 ppm at -60 °C. H^1 also shows an upfield shift with a lowering in temperature, although it is not nearly as large as that of the imine signal. In contrast, H^4 exhibits a slight downfield shift as the temperature is decreased. H^3 and H^2 are again overlapping with counter-ion peaks, but do not seem to be significantly influenced by the change in temperature. The imine proton H^5 can therefore be said to be more affected by temperature variations than the pyridine protons.

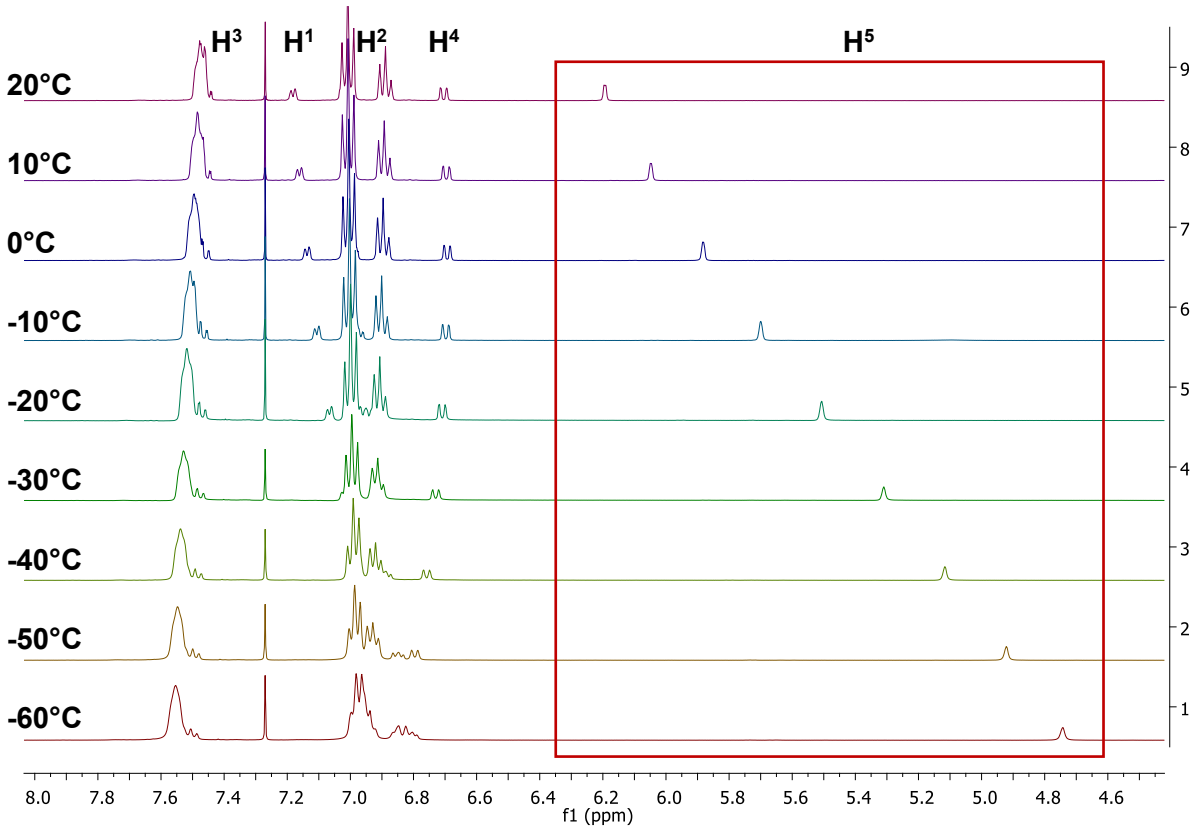

Figure 3.7 ^{1}H NMR spectrum of C2.3 from 20 °C to -60 °C in chloroform-*d*. Imine proton H^{5} shown in the red box.

Similar effects were observed for the pyridyl-triazole complex **C2.9**, with the signal for the triazole proton shifting from 8.13 ppm in the ligand to 5.79 ppm in the rhodium complex, at room temperature. As the temperature at which the ^{1}H spectrum is recorded decreases, this signal shifts more upfield to 5.01 ppm at -30°C. In contrast, a downfield shift is seen with an increase in temperature above ambient conditions. For example the signal for the triazole proton of the complex is found at 6.15 ppm when the ^{1}H NMR spectrum is recorded at 50°C. From these spectral observations it is once again clear that the aromatic rings of the tetraphenylborate counter-ion are involved in intermolecular interactions with the triazole proton.

It is possible that the type of cation-π interactions discussed in Section 3.1.2 are occurring in these molecules. Both the Schiff base complex **C2.3** and the pyridine-triazole complex **C2.9** are distorted square planer species with an electron deficient metal centre (cationic complex). Associated with these cations is the tetrahedral tetraphenylborate counter-ion. It is conceivable that some of the aromatic rings of the counter-ion would interact with the cationic complex, specifically the hydrogen atoms on some of the ligands of the cation, thereby influencing the chemical shifts of the proton signals in the ^{1}H NMR spectra of the complexes.

The cause of and influences on these shift trends were investigated using the N,N Schiff base complex **C2.3** as a model system (Figure 3.8).

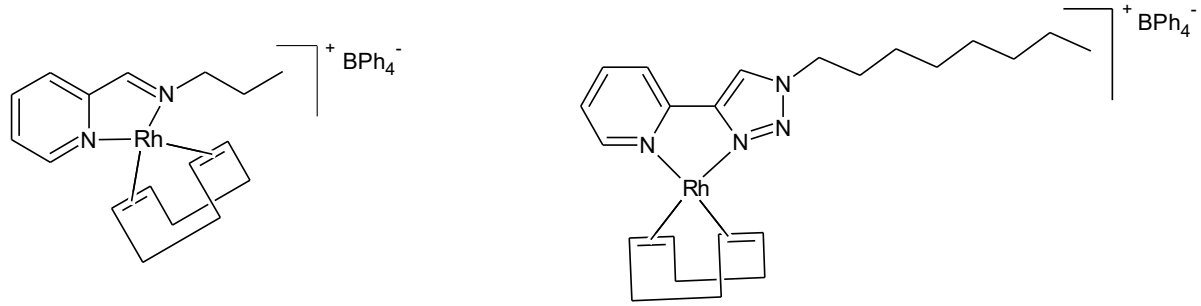

C2.3 **C2.9**

Figure 3.8 Complexes exhibiting an unusually large shift for the imine (C2.3) and triazole (C2.9) protons in chloroform-*d*.

3.2.1.1 Influence of NMR solvent

The synthesis and characterization of both a model and a siloxane functionalized N,N Schiff base complex (**C2.3** and **C2.7**) is discussed in Chapter 2. The ^{1}H NMR spectrum of **C2.3** was recorded in chloroform and that of **C2.7** was recorded in acetone, the functionalized complex being insoluble in chloroform. During this exercise it was noted that, while the signal for the imine proton of the model complex **C2.3** recorded in chloroform-d_1 exhibited the aforementioned upfield shift, the signal for the imine proton of the functionalized complex **C2.7** recorded in acetone-d_6 showed only a small downfield shift.

In order to probe this observation, it was decided to record the ^{1}H NMR spectrum of complex **C2.3** in acetone-d_6, to establish whether a similar effect on the imine proton signal observed for **C2.7** could be seen.

It was observed that the solvent indeed had a dramatic effect on the chemical shifts of several of the protons of the complex **C2.3**. This was especially the case for the aromatic protons. An upfield shift of 2.22 ppm was observed for the imine proton resonance in chloroform-*d* compared to the corresponding signal in acetone-d_6. In addition, the signal for the pyridine protons shifted between 0.81 ppm and 1.29 ppm upfield.

The resonances due to the protons in the counter-ion, BPh_4^-, were only slightly affected, appearing at only 0.13 ppm to 0.09 ppm more upfield in chloroform-d compared to what was found in acetone-d_6. The spectra for **C2.3** in the different solvents are shown in Figure 3.9, with the arrows indicating the position of the imine proton H^5.

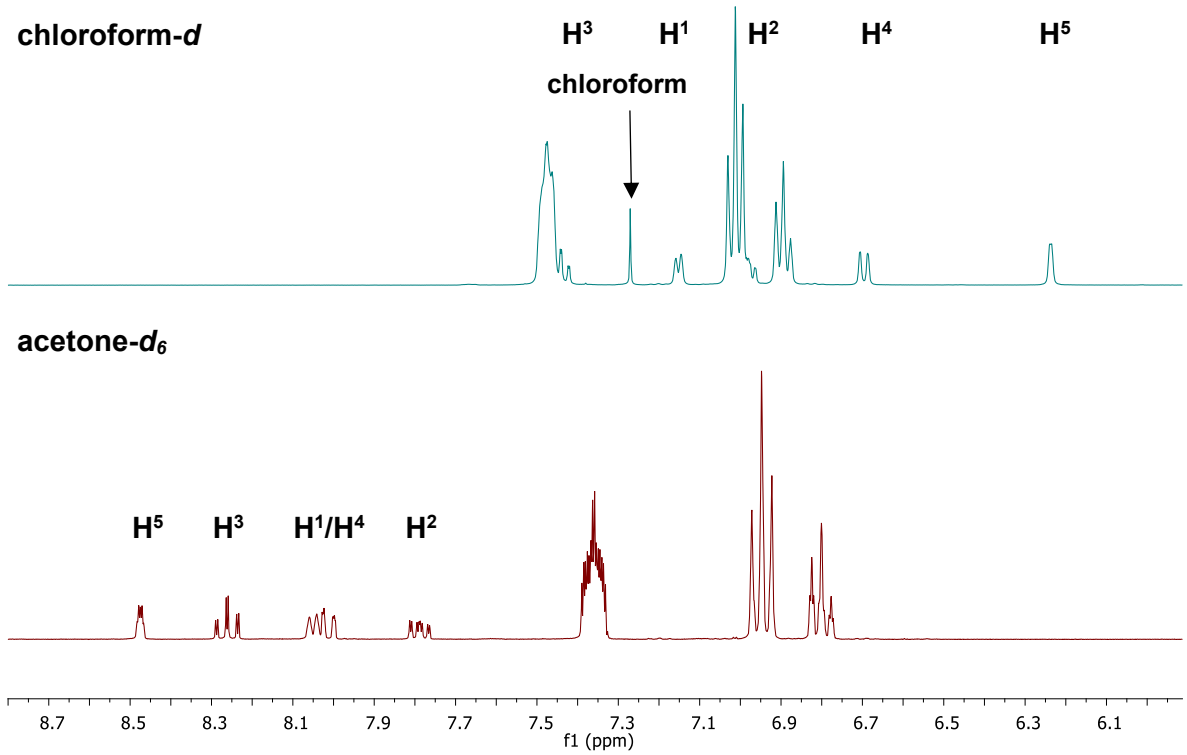

Figure 3.9 ^{1}H NMR spectra of C2.3 in chloroform-*d* (top) and acetone-d_6 (bottom) at room temperature.

A similar solvent effect was observed by Dupont *et al.* while studying an ionic liquid where tetraphenylborate was employed as anion.[24] They observed that the aromatic protons of the 1-*n*-butyl-3-methylimidazolium cation underwent significant upfield shifts in chloroform-*d* when compared to DMSO-d_6. They employed NOE spectroscopy to determine whether there would be through-space interactions between the protons of the cationic and anionic species. It was found there were interactions between one of the imidazolium protons and the protons of the counter-ion in chloroform-*d*. These interactions were absent in DMSO-d_6. This indicated that the ionic liquid behaved as a solvent-separated ion pair in DMSO, but as a contact ion pair in chloroform. The proposed structure for the contact ion pair is shown in Figure 3.10. Note the orientation of the explicitly shown hydrogen atom, directed towards one of the aromatic rings in the tetraphenylborate counter-ion. This is in agreement with the results found by Milčić *et al.*[13] As discussed in Section 3.1.2, these authors described interactions between hydrogen atoms and π systems in metal complexes where the hydrogen atom was directed towards aromatic systems.

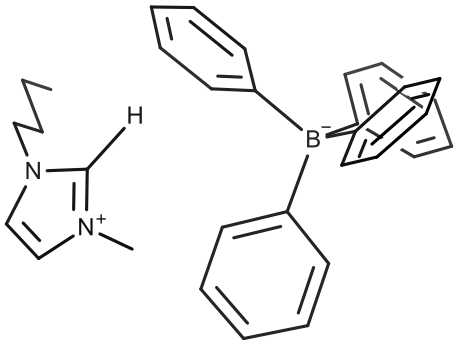

Figure 3.10 Proposed orientations of the anion and cation in chloroform-*d*, showing interaction between the aromatic rings of the anion and a hydrogen atom on the cation.[24]

This type of CH-π interaction is a known phenomenon and has been previously observed. It is a very weak type of hydrogen bond that occurs between a soft acid (the CH group) and a soft base (the π system). Evidence for this type of bonding has been obtained from thermodynamic, spectroscopic, crystallographic and computational studies.[17–19]

It is likely that a similar interaction is occurring for **C2.3**, with one or more of the hydrogen atoms of the pyridine-imine ligand in the cationic complex interacting with the phenyl rings on the anion. The imine proton H^5 showed the largest upfield shift upon complexation, and is also most affected by changes in temperature. This hydrogen atom is therefore likely oriented towards one of the phenyl rings in the counter-ion as shown in Figure 3.11. The exact orientations of the cation and anion in solution can only be speculated at this stage. At lower temperatures, the ion-pair could be more stabilised in solution, leading to closer interactions between the cation and anion. This would facilitate any CH-π interactions between the imine H^5 and the pi electron cloud of the phenyl rings of the counter-ion. This could explain why the imine proton H^5 will experience a greater degree of shielding.

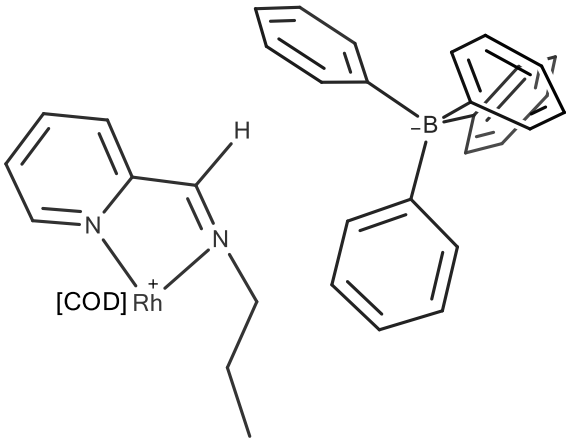

Figure 3.11 Proposed relative positions of the components of ion-pair of C2.3 in chloroform-*d*.

3.2.1.1.1 Investigation of NMR solvent effect *via* NMR titration

In order to further confirm the role of the solvent, an NMR titration was performed. In this experiment, small amounts of acetone-d_6 were added to a solution of **C2.3** in chloroform-*d*, and the ^{1}H NMR spectrum recorded after each addition. The shifts of the signals for the imine H^5, pyridine and counter-ion protons were followed throughout the experiment (Figure 3.12). The shifts were referenced to relative tetramethylsilane, due to the fact that the shifts of chloroform-*d* and acetone-d_6 also show some changes during the titration.

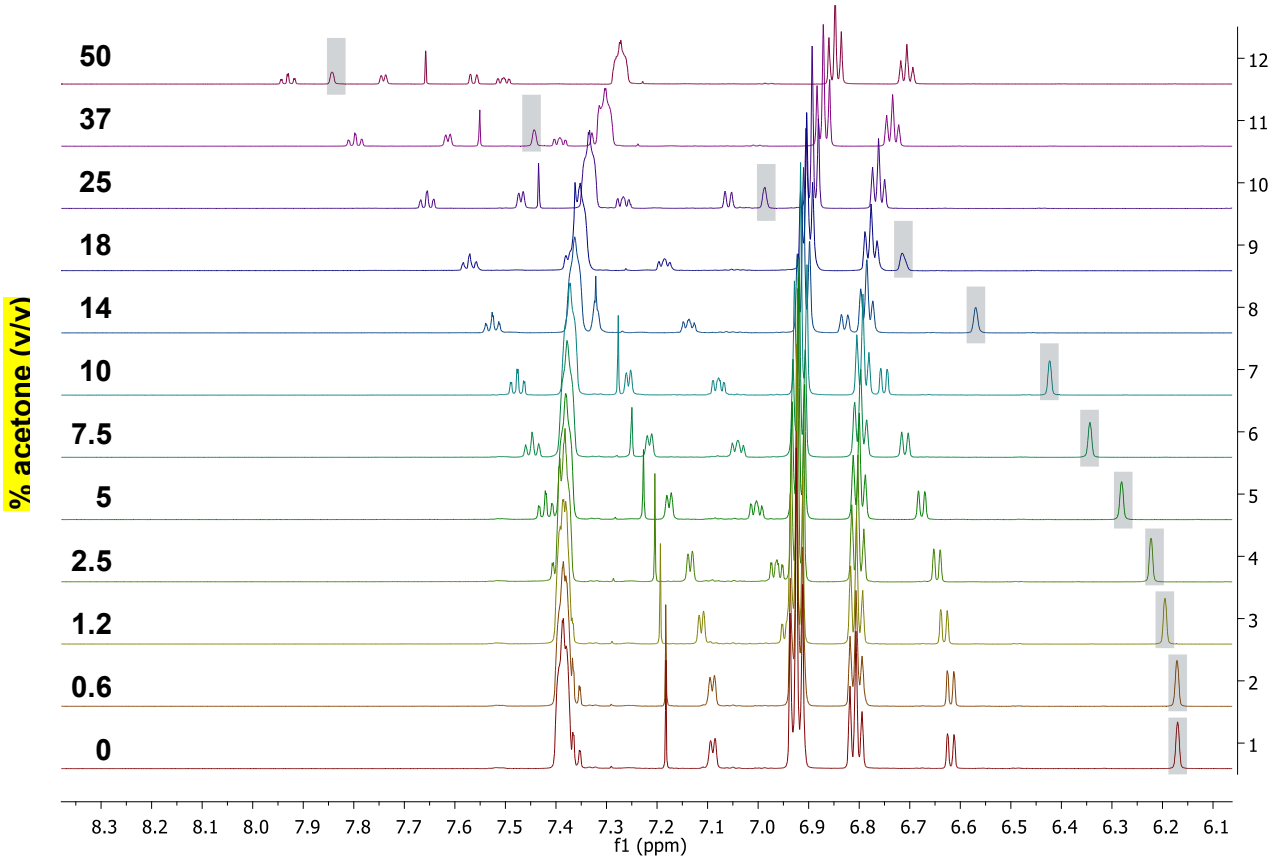

Figure 3.12 ^{1}H NMR titration of C2.3 in chloroform-*d* with acetone-d_6 at room temperature.

The results clearly show the effect that the solvent system has on the shifts of the proton resonances. The imine proton moves from 6.17 ppm in a pure chloroform solution to 7.84 ppm in a 50% chloroform/acetone solution. The pyridine protons also shifts further downfield, and the tetraphenylborate protons shift upfield very slightly.

The chemical shift of the imine proton H^5 is plotted relative to the percentage of acetone in the solution in Figure 3.13. The graph shows a clear relationship between chemical shift and the percentage acetone. It is evident that at higher acetone concentrations there are significant changes in the chemical shift of the imine proton H^5.

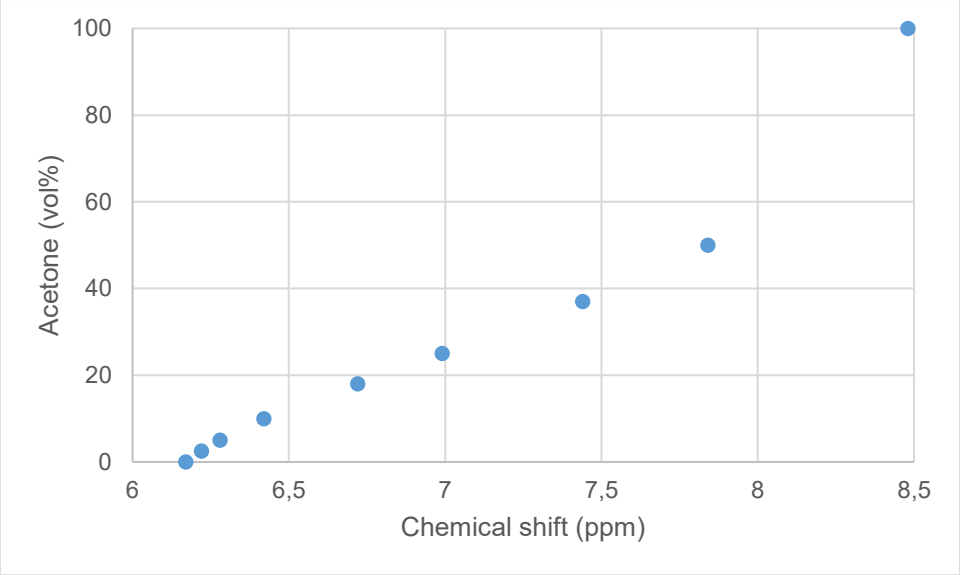

Figure 3.13 Plot of chemical shift of the imine proton H^5 *vs.* acetone content in acetone-d_6/chloroform-*d* solution.

As acetone is a more polar solvent than chloroform, it is likely that only weak ion-pairing would occur in acetone. It would therefore be more difficult for the proposed cation-π interactions to occur and the influence of the phenyl rings in the counter-ion on the proton signals of the ligand is less significant as more acetone is added to the solution.

3.2.1.2 Influence of counter-ion

In order to further confirm the influence of the tetraphenylborate counter-ion, two analogous complexes, **C3.1** and **C3.2**, were synthesized with tetrafluoroborate and hexafluorophosphate counter-ions respectively, following the method used for the synthesis of **C2.3** in Chapter 2 (Scheme 3.3). **C3.1** and **C3.2** were isolated as dark red and dark brown solids respectively.

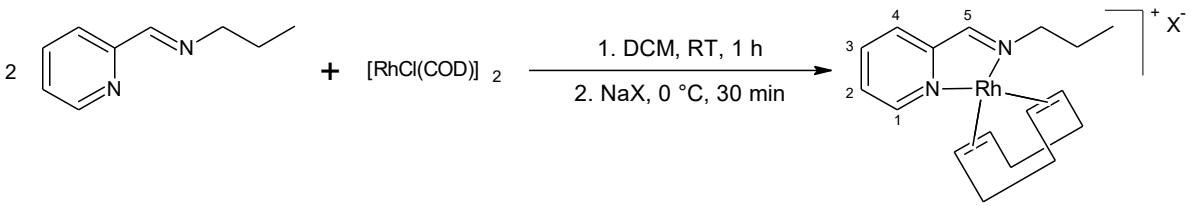

C3.1: X = BF_4
C3.2: X = PF_6

Scheme 3.3 Synthesis of complexes C3.1 and C3.2.

The ^{1}H NMR spectra of these complexes in chloroform-*d* are shown in Figure 3.14.

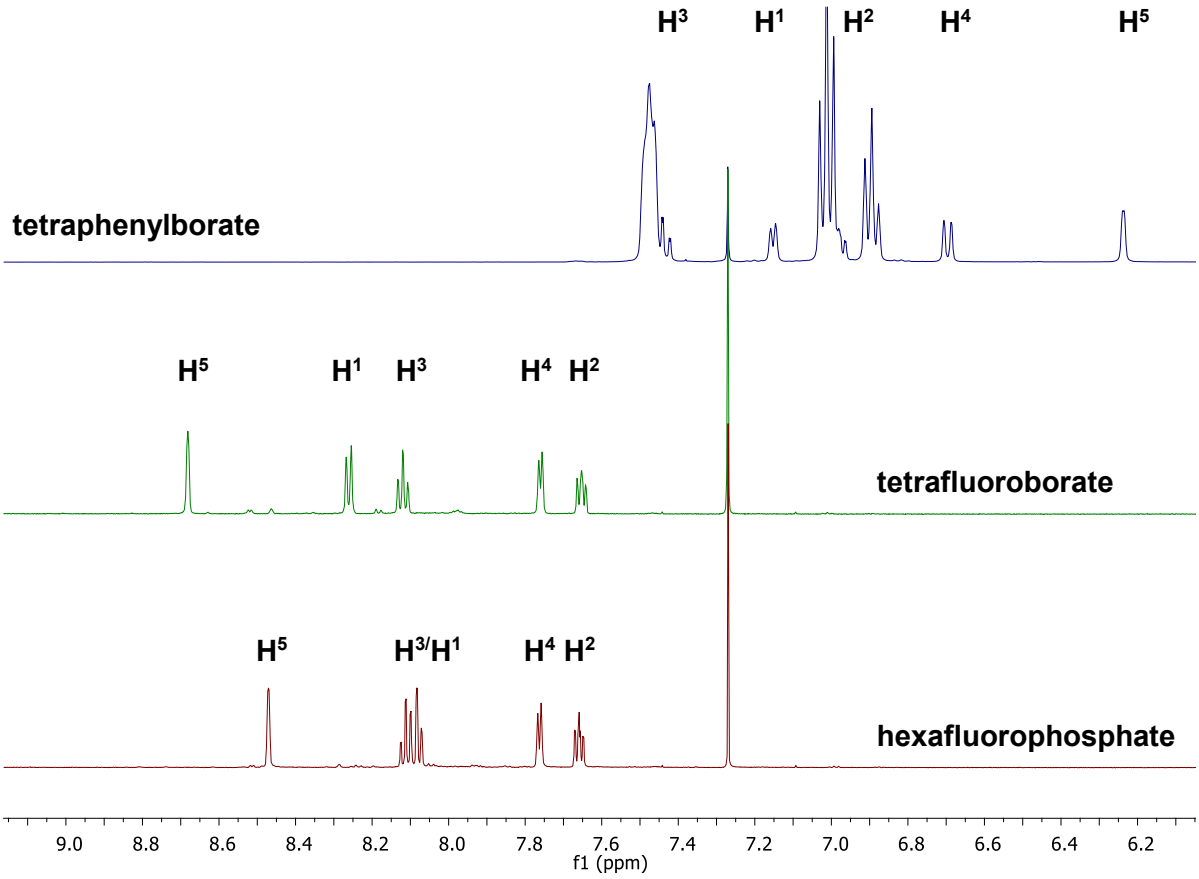

Figure 3.14 ^{1}H NMR spectra of C2.3 (top), C3.1 (middle) and C3.2 (bottom) in chloroform-*d* at room temperature.

The spectra confirm that the counter-ion used has a big influence on the ^{1}H NMR spectrum, with the signal of the imine proton H^{5} being found considerably more upfield in the ^{1}H NMR spectrum of **C2.3** than for **C3.1** and **C3.2**. The pyridine proton resonances for the former are also found further upfield in the case of **C2.3**. These resonances are found between 6.5 ppm and 7.5 ppm in the ^{1}H NMR spectrum of **C2.3**, while they can be seen between 7.6 ppm and 8.3 ppm in the ^{1}H NMR spectra of **C3.1** and **C3.2**.

The chemical shift of the imine proton H^{5} in the ^{1}H NMR spectrum in the three complexes which differs with regards to the counter-ion is summarized in Table 3.1. When tetraphenylborate is employed as counter-ion, a significant upfield shift is seen from the position of the imine proton in the ligand, whereas for the complexes utilizing tetrafluoroborate and hexafluorophosphate as counter-ions a slight downfield shift is observed.

Table 3.1 Summary of imine proton H^5 resonances in chloroform-*d* at room temperature. Note the difference in position between C2.3, and C3.1 and C3.2.

Complex	Counter-ion	Imine proton (free ligand) ppm	Imine proton (complex) ppm
C2.3	**BPh_4^-**	8.36	6.23
C3.1	**BF_4^-**	8.36	8.68
C3.2	**PF_6^-**	8.36	8.47

When the spectra of **C3.1** (BF_4^-) and **C3.2** (PF_6^-) are compared, the imine H^5 and H^1 signals are found more upfield for **C3.2** than **C3.1**. The other aromatic signals are found at similar chemical shifts in the two complexes. This would imply that these two protons are slightly more shielded in the presence of a PF_6^- counter-ion than a BF_4^- counter-ion. Aldrich *et al*. have observed some degree of hydrogen bonding between the fluorine atoms of the PF_6 anion and the ligand in a chromium complex.[25] It is therefore possible that there is hydrogen bonding between the fluorine atoms of the BF_4^- and PF_6^- counter-ions, and the hydrogen atoms H^1 and H^5 in **C3.1** and **C3.2**.

The difference in shifts in the ^1H NMR spectra can be explained by looking at the coordinating ability of the two anions towards metal cations. Since the signals of H^1 and H^5 are found more downfield when BF_4^- is used as counter-ion, it is expected that the coordinating ability of BF_4^- is greater than that of PF_6^-. Diaz-Torrez and Alvarez attempted to construct a scale to quantify the weakly coordinating character of a range of anions.[26] This was done by looking at the probability of finding the anion coordinated in the presence of a transition metal atom in a large range of crystal structures. They found that both BF_4^- and PF_6^- had weakly coordinating character, but that BF_4^- generally has a better coordinating ability than PF_6^-. This could possibly be explained by the smaller size of the BF_4^- counter-ion.

The differences in the ^1H NMR spectrum of the tetraphenylborate complex compared to those of the tetrafluoroborate and hexafluorophosphate complexes indicated that the upfield shift of the imine and pyridine protons could indeed be due to the CH-π interactions between the imine proton H^5 and the aromatic rings of the BPh_4^- anion. We attempted to investigate this using by a NOESY experiment to establish the relative positions of the cations and the anions in solution. We also employed DOSY to try and explain the differences observed in the chloroform-*d* and acetone-d_6 spectra of **C2.3** (Section 3.2.1.4).

3.2.1.3 Investigation of counter-ion effects using NOESY

The NOESY spectrum of complex **C2.3** was recorded in chloroform-*d* in order to investigate whether we could detect similar effects in our system. The spectrum is shown in Figure 3.15, with the cross-peaks between the counter-ion and the imine proton signals indicated in the black boxes. This confirmed the close interaction between the imine proton and the counter-ion. Interestingly, the NOE peak between the signal of the proton *para* to the boron atom and the imine signal is much weaker than that of the signals of the *ortho* and *meta* protons. This gives an indication of the orientation of the anion relative to the cation in solution. The spectrum also shows that there are NOE interactions between the protons of the counter-ion and the protons on the pyridine ring, which would explain the upfield shift that these proton signals undergo in the ^{1}H NMR spectrum. There is also a cross-peak between the imine H^{5} and pyridine H^{4} signals, while cross-peaks between the imine and other pyridine signals are absent. This confirms the position of H^{4} on the pyridine ring.

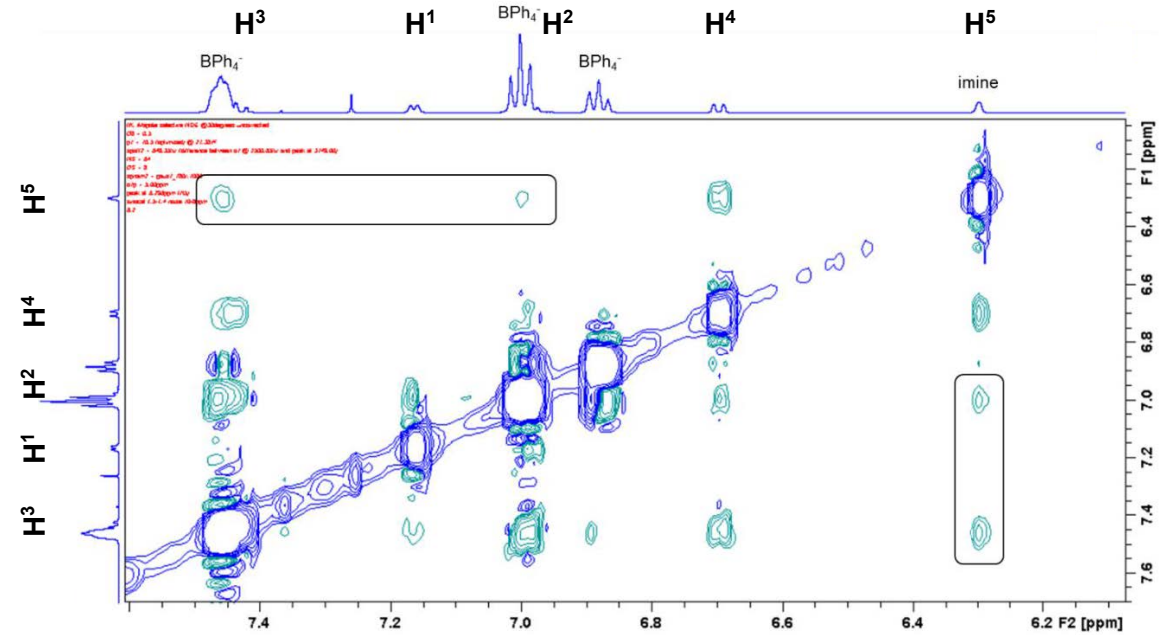

Figure 3.15 NOESY spectrum of C2.3 in chloroform. Cross-peaks between imine proton H^{5} and counter-ion protons shown in boxes.

^{1}H-^{19}F heteronuclear NOE spectroscopy was employed to investigate whether similar interactions could be observed for **C3.1** (using BF_4^- as counter-ion) and **C3.2** (using PF_6^- as counter-ion). Figure 3.16 shows the 2D HOESY spectra for **C3.1** and **C3.2**, with the resonances due to the fluorine atoms on the horizontal axis and the proton resonances on the vertical axis. The ^{19}F spectrum of **C3.2** shows a doublet due to F-P coupling. For both complexes, through-space NOE type connectivities can be observed between the fluorine atoms of the respective counter-ions and the imine proton, as well as one of the pyridine

protons. This confirms that **C3.1** and **C3.2** behave as close ion-pairs in chloroform-d, however, due to the lack of aromatic groups on these counter-ions, the same dramatic shift of the imine proton resonance as a result of CH-π interactions is not observed. It also gives an indication of where the anion is located relative to the cation in solution, due to connectivities only being observed for one of the pyridine protons, H^4. This location appears to be the same for **C2.3**, **C3.1** and **C3.2**. It appears that one of the phenyl rings of the tetraphenylborate anion (**C2.3**) or fluorine atoms of the counter-ion (**C3.1** and **C3.2**) lies in close proximity to the imine proton H^5 and the pyridine proton H^4.

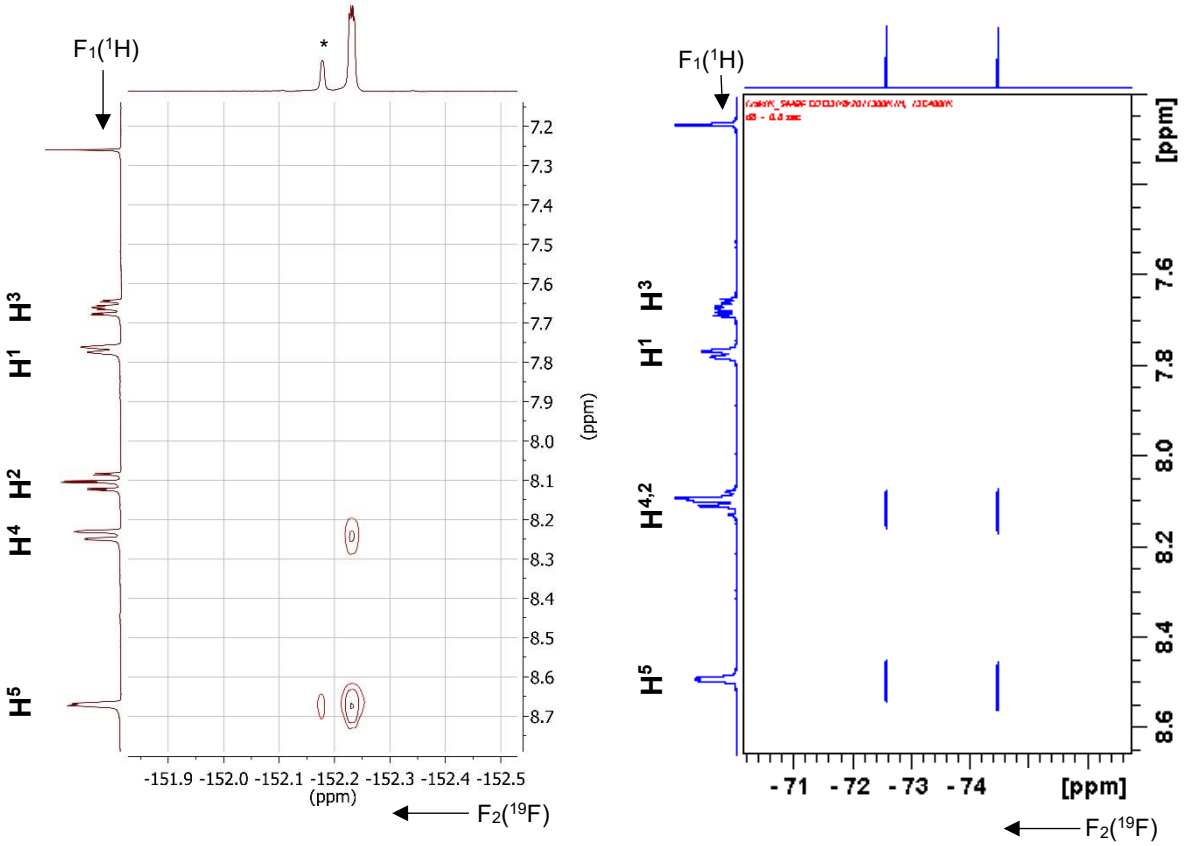

Figure 3.16 2D HOESY spectra of C3.1 (left) and C3.2 (right) recorded in chloroform-*d* at room temperature.

NOE spectroscopy has previously been employed to study interactions between cations and anions in solution. Martinez-Viviente and Pregosin looked at the interactions between the cation and anion of an iridium triflate complex in solution. They found that the cross-peaks on the ^1H-^{19}F HOESY spectra were much more intense in chloroform-*d* than in dichloromethane-d_2, indicating that the contacts between the ions were closer in chloroform-*d*. This agreed with previously obtained DOSY results, which showed that the degree of ion-pairing in chloroform-*d* was higher than in dichloromethane-d_2.[27]

Zuccaccia *et al*. used NOESY and ^1H-^{19}F HOESY to study cationic ruthenium complexes which varied in the type of anion used as counter-ion.[8] Some of the cations used in this study

were tetraphenylborate, triphenylmethylborate, hexafluorophosphate and tetrafluoroborate. They found that the counter-ion showed very specific interionic interactions in all cases, and that the counter-ion stayed in the same position relative to the cation. Quantum mechanical calculations revealed a noncentrosymmetric distribution of the electron density around the metal centre, which helped to explain the specific localization of the anions.

The experimental work done in this section, as well as previously published literature, shows that the NOESY and HOESY are excellent techniques to study transition metal complex ion pairs in solution. By making use of these techniques, we have observed through-space connectivies between certain hydrogen atoms on the cationic complex and hydrogen atoms (in the case of **C2.3**) or fluorine atoms (**C3.1** and **C3.2**) of the anions in chloroform-*d* solution. Chloroform-*d* is a non-polar solvent and is it expected that tight ion pairs will form in solution. With the anion and cation of the metal complex brought in such close proximity, interactions can occur which will affect the NMR spectra. These techniques can also be coupled with other NMR techniques like DOSY as well as quantum mechanical calculations to gain more insight into the behaviour of the complexes.

3.2.1.4 Investigation of ion-pairing using DOSY

The use of diffusion ordered spectroscopy to study ion-pairing was previously discussed in Section 3.1.12. To re-iterate briefly: a very similar or identical diffusion constant (and subsequent hydrodynamic radius) for the anion and cation would suggest that two fragments are diffusing as a unit, and can therefore said to be ion-paired. This hydrodynamic radius will also usually be larger than that of the individual ions. Different diffusion constants indicate that the anion and the cation are diffusing separately, and the ions in this case are said to be solvent-separated. A possible limitation of this technique is that the diffusion constant is related to the hydrodynamic volume of the fragment which is being studied. Should the fragments have nearly identical hydrodynamic volumes, we also would see similar diffusion constants even if ion-pairing is not occurring.

All experiments discussed below were performed at 25°C using solutions with a concentration of 4 mM, since previous work has shown that the diffusion can be affected by temperature and analyte concentration.[28] The D values were referenced to HDO in D_2O. In order to determine the diffusion coefficient of the cationic fragment, the methyl peak was monitored, whereas the protons *para* to the C-B bond were used to determine the diffusion of the anion. The experimentally obtained plots are shown in Figure 3.17 and the diffusion constants were calculated from these plots using Equation 3.1.

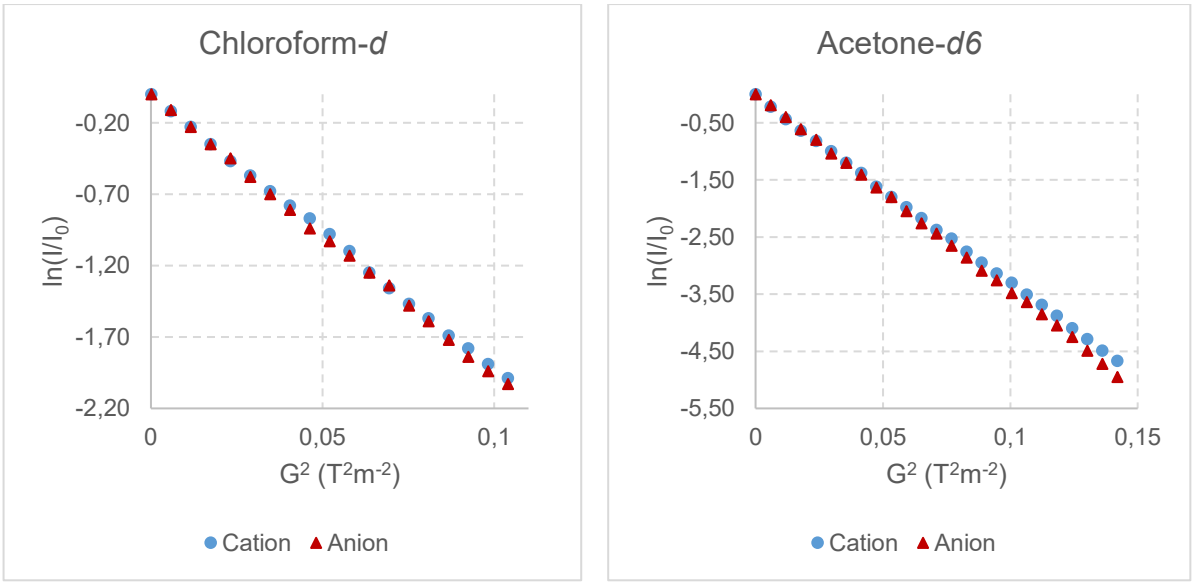

Figure 3.17 Plots of ln(I/I$_0$) *vs.* the square of the gradient amplitude for diffusion measurements on C2.3 in chloroform-*d* (left) and acetone-*d6* (right) at room temperature.

Chloroform has a viscosity of 0.58 mPa·s whereas the viscosity of acetone is 0.32 mPa·s – the ions can therefore diffuse through acetone at a faster rate than through chloroform. The hydrodynamic radii of the ions in chloroform-*d* and acetone-d_6 were calculated using the Stokes-Einstein equation in order to make a comparison of the ions in the two different solvents possible. The results are shown in Table 3.2.

Table 3.2 Diffusion constants and hydrodynamic radii of C2.3.

Fragment	Chloroform		Acetone	
	D (x 10^{-10} m^2 s^{-1})	r_H (Å)	D (x 10^{-10} m^2 s^{-1})	r_H (Å)
Cation	6.74	6.0	11.3	6.1
Anion	6.87	6.0	12.2	5.7

From the results we can see that the cation and the anion have almost identical diffusion values in chloroform, which indicates that the species forms intimate ion-pairs in solution. The close proximity of the anion and the cation in the chloroform-*d* solution would explain why we see the influence of the phenyl rings in the anion on the imine and pyridine protons of the cationic species in the ^{1}H NMR. Surprisingly, the diffusion constant and hydrodynamic radii of the anion and cation in acetone are also quite similar. One would have is expected that there would be weak or no ion-pairing in acetone, which would lead to smaller hydrodynamic radii

for the individual ions than for the tight ion-pair observed in chloroform. A similar effect for the tetraphenylborate counter-ion, where the cation and anion were found to have very similar hydrodynamic radii in acetone, has previously been observed by the group of Pregosin.[28,29]

By employing the same technique, we found a value of r_H = 5.1 Å for the tetraphenylborate anion associated with a simple cation such as Na^+ in methanol, a solvent in which one would expect minimal ion pairing to occur. This agrees with previous values reported for this species in literature.[29] Since the hydrodynamic radius of this ion in association with the cationic complex under study in this thesis is larger (5.7 Å) in acetone than for the 'free' anion (5.1 Å), we assume that some degree of ion-pairing is occurring. However, it appears that in acetone the extent of the ion pairing is not as significant as in chloroform, as is expected since acetone is a polar solvent. Thus in this case the phenyl rings of BPh_4^- has very little influence over the imine and pyridine protons.

In conclusion, the abnormally large upfield shift observed after complexation for some of the proton signals in the ^{1}H NMR spectrum of **C2.3** in chloroform-*d* has been investigated by a number of NMR techniques. It is proposed that ion-pairing takes place in chloroform-*d* and not in acetone-d_6, which explains the difference between the spectra of **C2.3** in these two solvents. Furthermore, there appears to be a specific interaction between the phenyl rings of the tetraphenylborate counter-ion and some of the hydrogen atoms on the cation. Tetrafluoroborate and hexafluorophosphate analogues of **C2.3** was synthesized. The upfield shift for the imine and pyridine protons signals of the cation was absent for these complexes, confirming the important role of the phenyl rings of the tetraphenylborate counter-ion. This interaction is likely a CH-π interaction.

3.2.2 Investigation of the 1,5-cyclooctadiene olefinic protons in C2.3, C2.4 and C2.9

Another phenomenon observed during the course of studying these cationic Rh-COD complexes was the dynamic behaviour of the COD ligand in solution. The shape of the COD signals in the ^{1}H NMR spectrum of the complexes varies dramatically depending on the nature of the chelating co-ligand. This was mentioned in Chapter 2, when discussing the characterization of these complexes. The relevant complexes are shown in Figure 3.18.

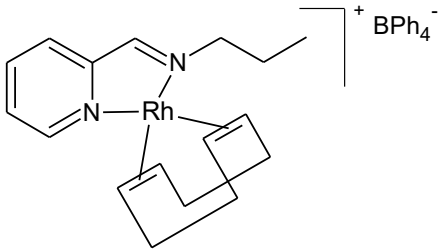

C2.3

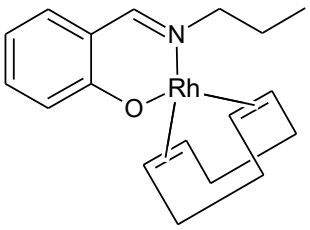

C2.4

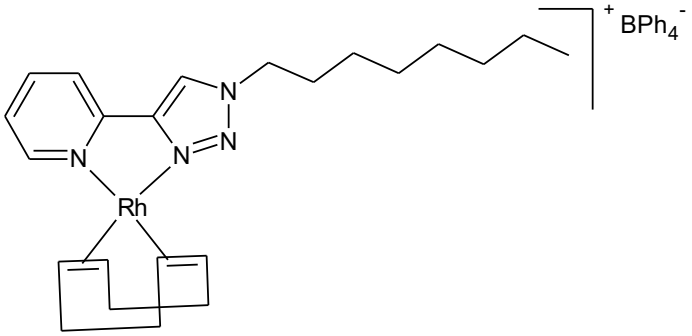

C2.9

Figure 3.18 Rhodium 1,5-cyclooctadiene complexes C2.3, C2.4 and C2.9.

C2.3 shows these protons as one narrow peak, **C2.4** as two multiplets and **C2.9** as a two very broad, flat peaks. The shapes of the peaks can be seen in Figure 3.19, with the olefinic protons of the 1,5-cyclooctadiene ligand highlighted in grey.

Initially, the difference in peak shape between **C2.3** and **C2.4** was thought to be due to the difference in donor atoms *trans* to the olefin protons – where **C2.3** has nitrogen atoms *trans* to both sets of olefin protons, and **C2.4** has two olefin protons *trans* to an oxygen atom and two *trans* to a nitrogen atom. This is consistent with what has previously been reported in literature, with the more downfield protons in the ^{1}H NMR spectrum of **C2.4** being assigned to those *trans* to the nitrogen atom and the more upfield protons corresponding to those *trans* to the oxygen atom.[30] However, after observing the shape of these protons in the ^{1}H NMR spectrum of **C2.9**, it was clear there were other factors that had to be taken into account as well.

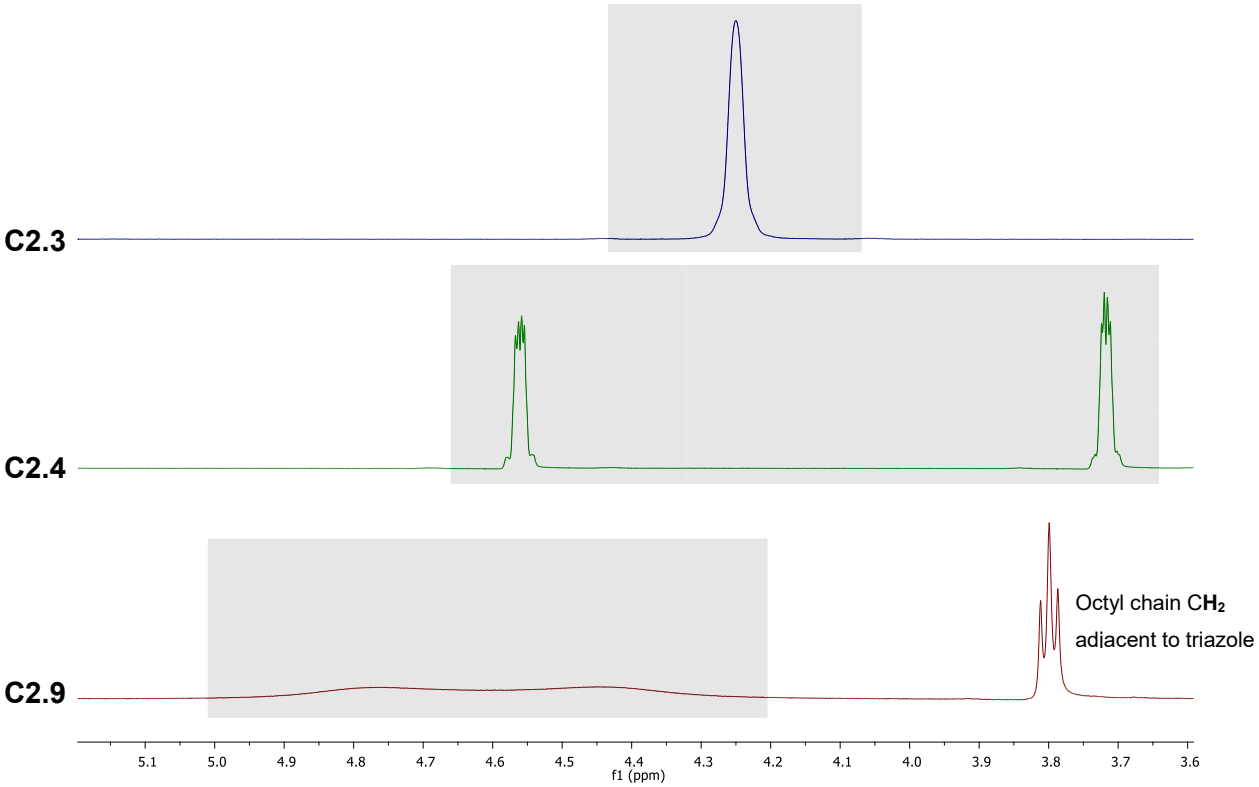

Figure 3.19 NMR spectra of C2.3 (top), C2.4 (middle) and C2.9 (bottom) in the range 5.2 ppm to 3.6 ppm in chloroform-*d* at room temperature.

3.2.2.1 Variable temperature NMR spectroscopy

Variable temperature NMR spectroscopy can be used to investigate dynamic molecular motion, given that the rate of motion is visible on the NMR timescale. The ^{1}H NMR spectrum of **C2.9** in chloroform-*d* was recorded over the range of -30°C to 50°C (Figure 3.20). The spectrum was recorded at 25°C, and the sample then cooled to -30°C, with a spectrum being recorded at 10°C intervals (starting at 20°C). The sample was subsequently allowed to warm up to 25°C and another spectrum was recorded. The sample was then heated to 50°C, and a spectrum recorded every 10°C (starting from 30°C). Finally, the sample was cooled to 25°C and the ^{1}H NMR spectrum recorded once again. The parts of interest of these spectra are shown in Figure 3.22.

The spectrum shows two phenomena of interest: Firstly, the triazole proton shows a dramatic shift over the temperature range, moving from 5.04 ppm to 6.18 ppm. This is likely due to CH-π interactions between fragments in the cationic complex and the anionic counter-ion as discussed in Section 3.2.1. At lower temperature, the degree of ion pairing is higher and greater magnetic shielding of the triazole proton occurs. As the temperature is increased, the ions are less tightly associated and the shielding is less. This is also a dynamic process and will therefore influence the NMR spectra.

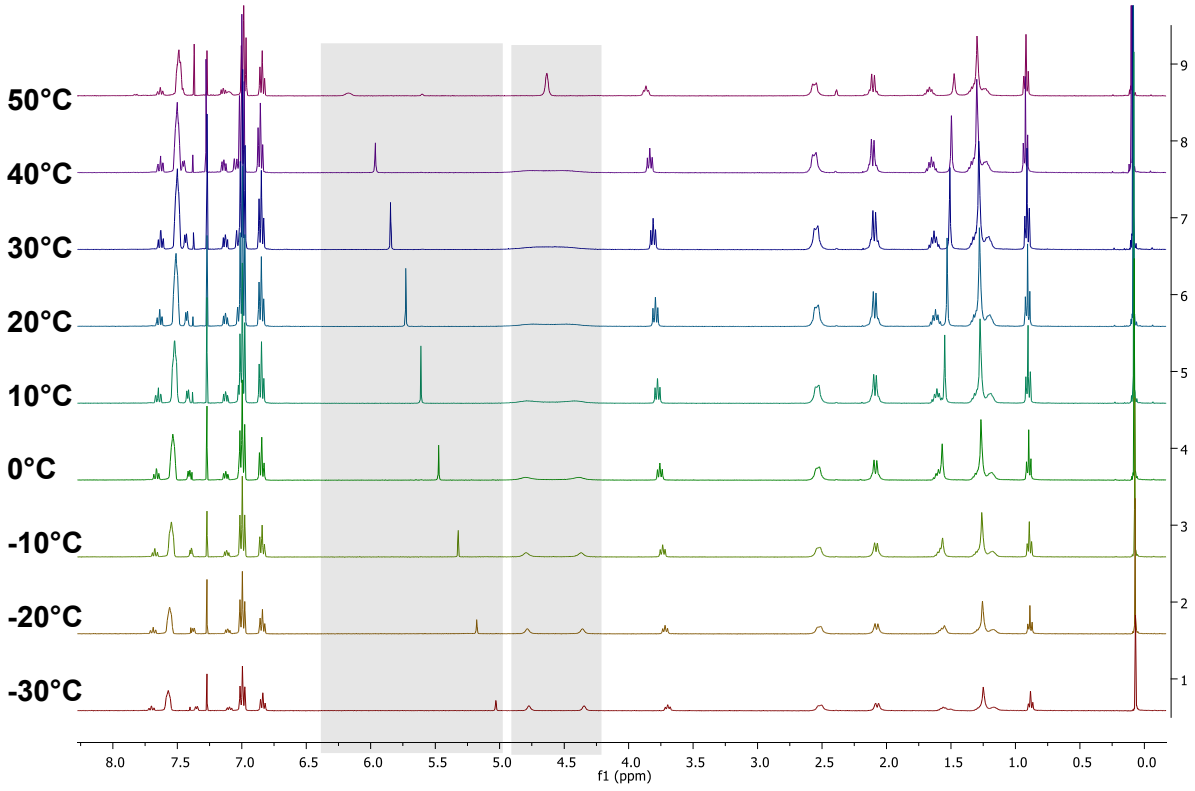

Figure 3.20 ^{1}H NMR spectroscopic array of C2.9 in chloroform-*d* (-30°C to 50°C). Grey areas indicate signals with significant structural changes and/or changes in chemical shifts.

In addition to these non-covalent interactions occurring, a second dynamic process occurs concomitantly, involving the COD ligands. The ^{1}H NMR spectrum shows the olefinic protons of the1,5-cyclooctadiene ligand as being resolved into two fairly sharp peaks, indicating the COD protons being in two different environments, at low temperature. These signals go through a transition where only a very broad, flat signal is observed, and collapse into a narrower signal at high temperature. The narrow signal is due to the system being in rapid exchange occurring faster than the NMR time-scale resulting in two indistinguishable sets of protons. This type of spectrum is consistent with a two-site exchange process. It should be noted that the signal at 50 °C is shifted slightly downfield relative to the centre of the two signals at -30 °C, indicating that the two-site exchange may not be the only process taking place. Some contribution from the ion-pairing and cation-π interactions discussed in Section 3.2.1 is also highly likely.

This type of exchange for the 1,5-cyclooctadiene ligand has been observed previously.[31,32] Gomes *et al.* studied a [Ni(η-Ind)(η^{4}-COD)]BF_4 complex using variable temperature ^{1}H spectroscopy. The authors reported that the four olefinic COD proton resonances merged into a single resonance at 5.09 ppm at room temperature in dichloromethane-d_2. As the

temperature was decreased, the resonances collapsed with a coalescence temperature at -15°C. At -80°C, two new resonances, at 5.43 ppm and 4.57 ppm, were observed. In this study, as in ours, the single resonance at higher temperature appears at a position more downfield than the midpoint between the positions of the two resonances observed at low temperature. It should also be noted that dichloromethane-d_2 is expected stabilise the formation of tight ion pairs.

The olefinic protons on carbons 1 and 2 in Figure 3.21 exchange with protons on carbons 5 and 6, respectively.

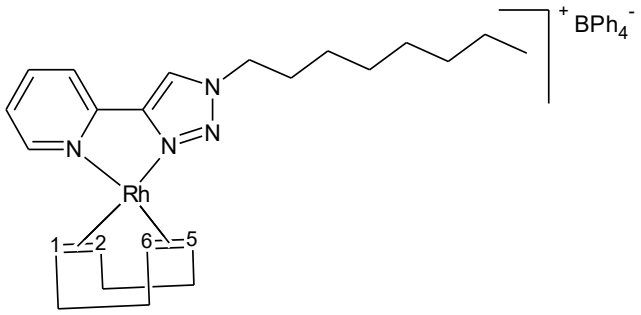

Figure 3.21 Complex C2.9, showing the protons undergoing exchange.

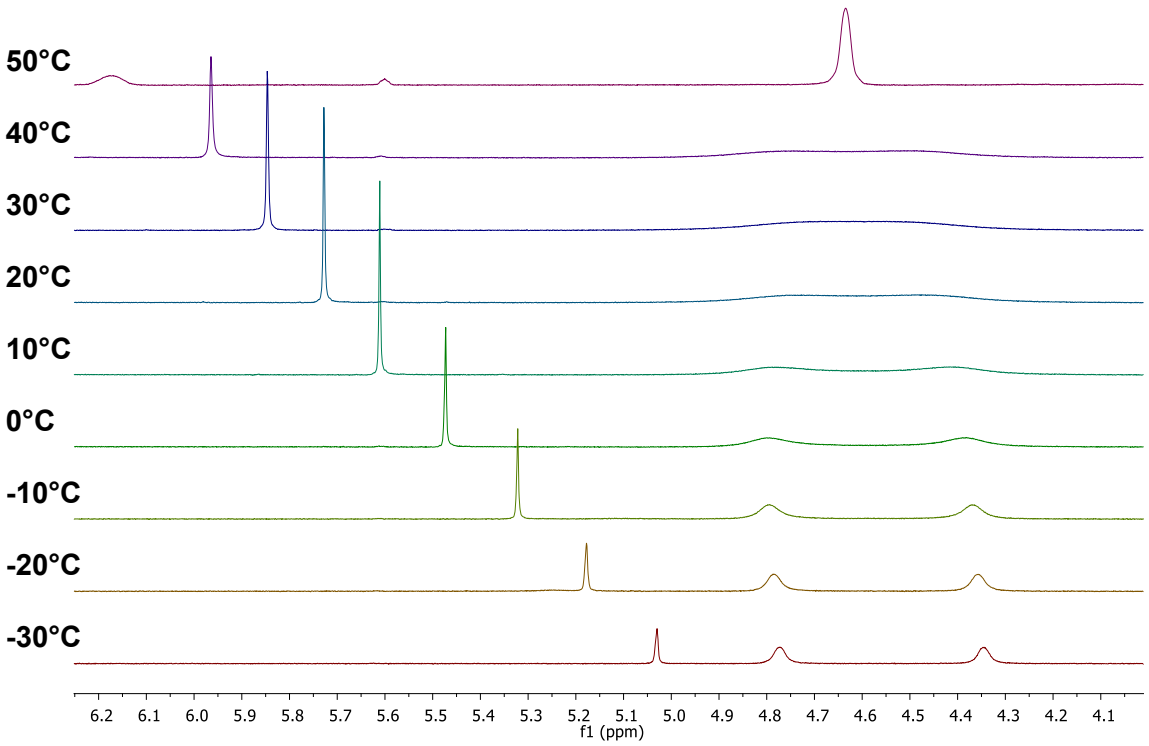

Figure 3.22 ^{1}H NMR spectroscopic array of triazole proton and olefinic 1,5-cyclooctadiene signals of C2.9 in chloroform-*d* (-30°C to 50°C).

3.2.2.1.1 Modelling the symmetric two-site exchange model

An in-house program, NMRfitv12, was employed to model the symmetric two-site exchange between the 1,5-cyclooctadiene protons. The calculations used in the program are based on work by Vallurupalli.[33] The calculations are used extensively in the literature and the calculation details are therefore not discussed here.[34–36] The program does not explicitly model symmetric site-exchange, but since the forward and reverse rate constants for such a process must be the same, the model can be applied to the symmetric site-exchange. The program was written by one of our collaborators and further details can be found in the thesis of O'Kennedy.[37]

The program was used to determine line fit plots for the calculated data. These are shown relative to the experimental data in Figure 3.23. The experimental data fit the model quite well, with only minor differences being observed in the baseline of some of the spectra. The forward and reverse rate constants at each temperature were found to be similar (Table 3.3), confirming the symmetric nature of the exchange.

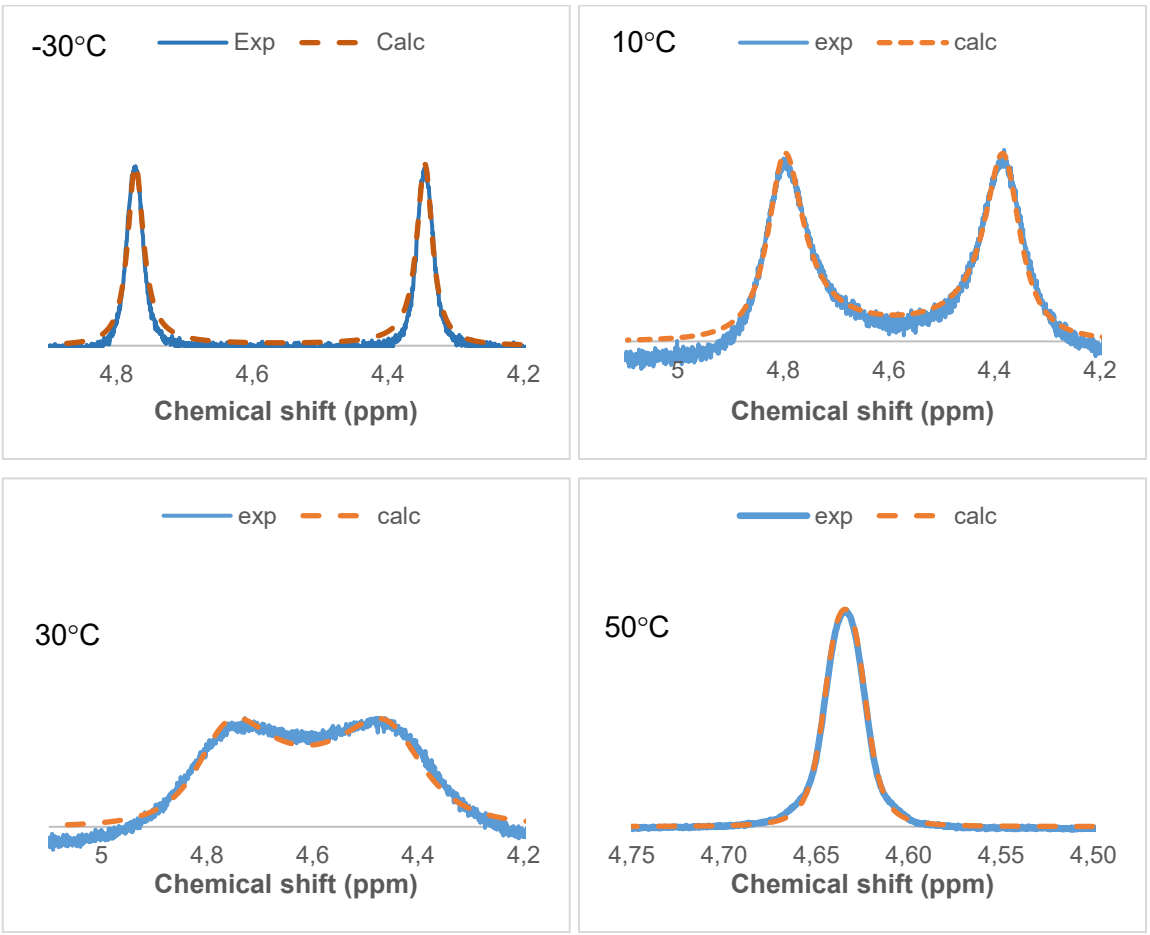

Figure 3.23 Plots showing correlation between experimental and calculated NMR spectra of C2.9 in chloroform-*d* at different temperatures.

At -30 °C, the 1,5-cyclooctadiene methine signals are observed as two peaks at 4.34 and 4.77 ppm. These signals are representative of a static system with no two-site exchange occurring. The signals remain relatively narrow at -20, -10 and 0 °C. At 10 °C, the signals are seen at 4.40 and 4.80 ppm and appear to be broadening. At 30 and 40 °C the signal is very broad. At this point, the methine sites are exchanging so fast that an average signal of the two sites is seen. The sharpening of the signal is quite sudden, with a narrower peak being observed at 50 °C. This signal appears at 4.64 ppm.

Table 3.3 Forward and reverse rate constants for C2.9 in chloroform-*d* at various temperatures.

Temperature (°C)	k_1 (s^{-1})	k_2 (s^{-1})
-30	30.988	30.500
-20	34.775	34.775
-10	51.810	52.411
0	100.242	99.933
10	179.316	166.571
20	247.173	222.702
30	250.238	242.334
40	289.749	281.349
50	310.283	304.867

3.2.2.1.2 Examining the nature of the exchange of COD

Various causes for this observed exchange have been proposed for similar cases in the literature. These include a) the dissociation of one of the donor atoms of the chelating ligand and subsequent rotation of the ligand around the remaining metal to ligand bond and b) interconversion between conformations of the 1,5-cyclooctadiene ligand while it remains coordinated.[32]

In order to determine which of these processes was responsible for the site-exchange, the energy barrier for the conformational change of the COD ligand was calculated. The enthalpy ($\Delta H^{\ddagger}$), entropy ($\Delta S^{\ddagger}$) and Gibbs free energy of activation ($\Delta G^{\ddagger}$) were obtained from Eyring plots constructed using the calculated rate constants. The Eyring plot, shown Figure 3.24, depicts

the reaction rate constant as a function of temperature (Equation 3.3). The enthalpy and entropy of activation were calculated from the slopes and intercepts of these graphs (Equations 3.4 and 3.5), while the activation energy was calculated with Equation 3.6.

$$\boldsymbol{ln\frac{k}{T} = -\frac{\Delta H^{\ddagger}}{R}\frac{1}{T} + \frac{\Delta S^{\ddagger}}{R} + ln\frac{k_B}{h}} \quad \textbf{(3.3)}$$

$$slope: -\frac{\Delta H^{\ddagger}}{R} \quad \textbf{(3.4)}$$

$$intercept: \frac{\Delta S^{\ddagger}}{R} + ln\frac{k_B}{h} \quad \textbf{(3.5)}$$

$$\Delta G^{\ddagger} = \Delta H^{\ddagger} - T\Delta S^{\ddagger} \quad \textbf{(3.6)}$$

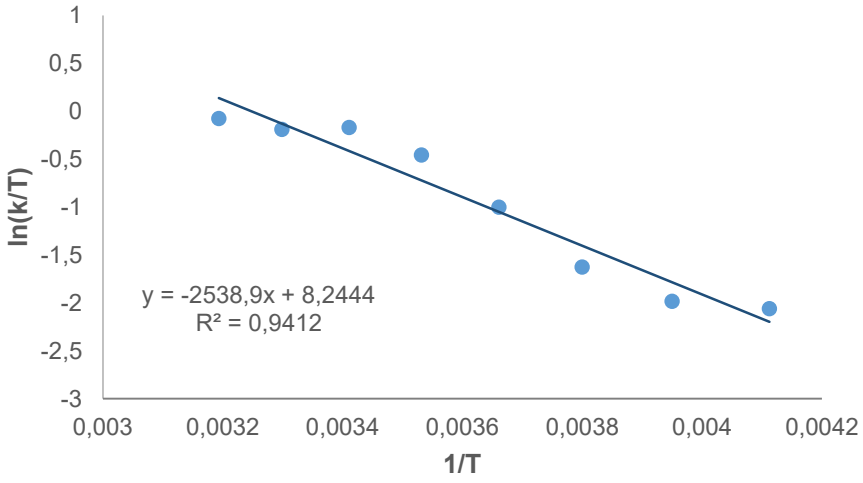

Figure 3.24 Eyring plot of exchange process in C2.9 in chloroform-*d*.

The results calculated from these plots are tabulated below in Table 3.4.

Table 3.4 Thermodynamic data calculated from Eyring plots of C2.3 and C2.9. Data obtained from spectra collected in chloroform-*d*.

Complex	$\Delta H^{\ddagger}$ (kJ.mol^{-1})	$\Delta S^{\ddagger}$ (kJ.mol^{-1})	$\Delta G^{\ddagger}$ (kJ.mol^{-1})
C2.3 (imine)	8.1	-0.1	48.5
C2.9 (triazole)	21.1	-0.1	60.2

From the experimental data, we can see that the energy of activation is lower for complex **C2.3** than for complex **C2.9**. The complexes are shown in Figure 3.25. This correlates with the observed NMR spectra – in the spectrum of **C2.3** we observe one signal at 25°C, indicating relatively fast exchange. This is in contrast with the spectrum of **C2.9**, where we observe two peaks due to the COD protons in two different environments, which is indicative of slower exchange. Using a similar method, Gomes *et al.* calculated the Gibbs free energy of activation for the process occurring in their study to be 43.5 kJ.mol^{-1}.[32] With the above data in hand, we could compare the activation energies to the energy barriers of the various proposed mechanisms for the exchange process. It is clear from the variable temperature ^{1}H NMR spectra of **C2.3** and **C2.9** (Figure 3.7 and Figure 3.20) that the cation-anion interaction is also greatly influenced by temperature, evidenced by the large shifts seen for the imine and triazole protons. These interactions could also have an effect on the dynamic process involving the COD hydrogen atoms.

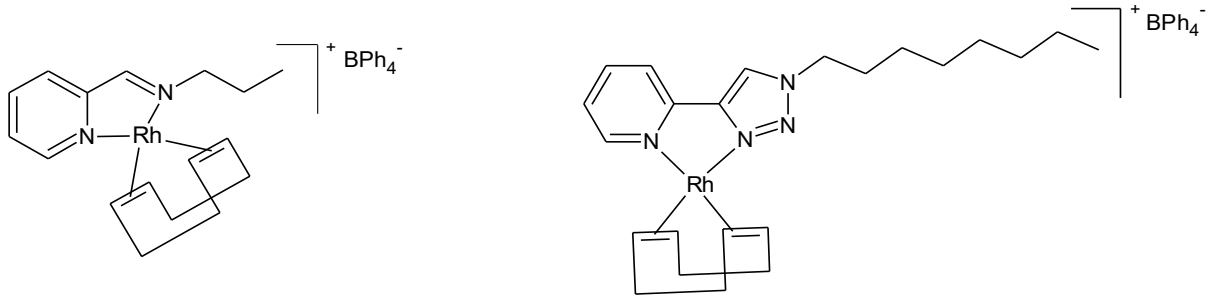

C2.3 **C2.9**

Figure 3.25 Rhodium complexes C2.3 and C2.9.

First, we looked at the interconversion of COD ligand between the two twist-boat conformations possible for that ligand. The free energy profile for the process was determined by means of DFT calculations and is shown in Figure 3.26. Note that the calculations were performed on the entire complexes, but only the COD ligand is shown below for simplicity.

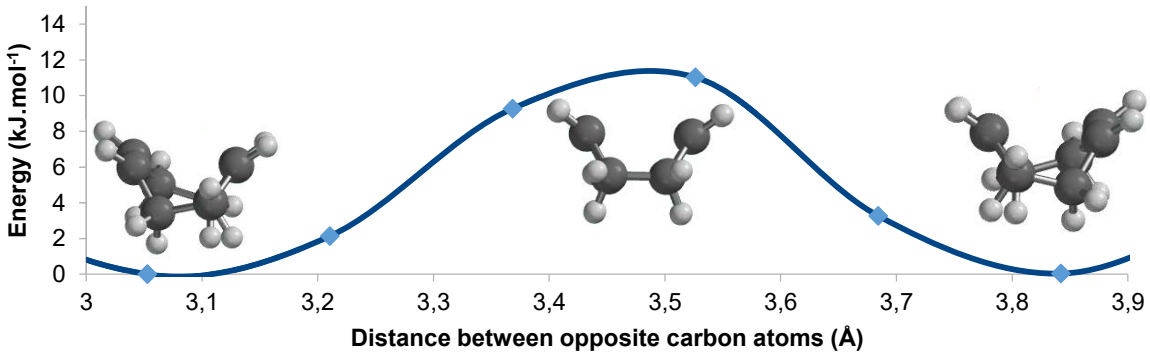

Figure 3.26 Energy barrier profile for COD interconversion of complex C2.9. DFT calculations were performed on the entire complex C2.9 but only the COD ligand is shown for clarity.

The activation energy for the conformational change was calculated to be 14.79 kJ.mol^{-1} for **C2.9** and 12.38 kJ.mol^{-1} for **C2.3**. These values are much lower than the experimentally determined values and the COD interconversion process is probably occurring too fast to be observable on the NMR timescale. While this does not rule out that the interconversion of the COD ligand is occurring in solution, it is clearly not the only process contributing to the effects we see in the NMR spectrum.

Valentini *et al*. proposed a breaking of a non-COD ligand-metal bond and subsequent rotation and re-coordination of the chelating ligand.[31] This process is illustrated for our complexes in Scheme 3.4. The first step involves the breaking of a Rh-N bond (N_2), to form a three-coordinate species. Rotation of the ligand then takes place around the remaining Rh-N bond (N_1). A new bond is then formed between the metal and the donor atom (N_2) where the original bond breakage took place. While the complex is essentially re-formed, the positions of the olefinic protons 1 and 2, and 5 and 6, relative to the different nitrogen donor atoms are changed. This sequence is expected to be relatively slow, especially the rotation of a large structural fragment that takes place in step 3. This process would therefore be slow enough to be observed on the NMR timescale.

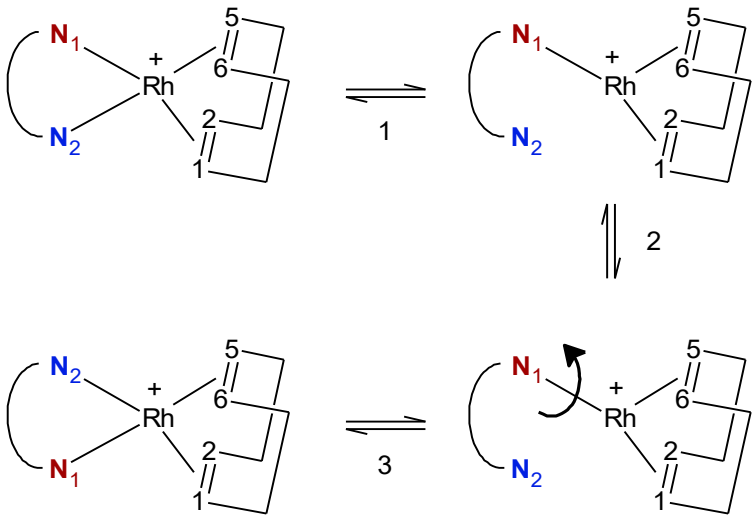

Scheme 3.4 Possible mechanism of the dynamic process proposed for C2.3 and C2.9.[31]

It is also possible that the COD ligand undergoes partial dissociation and rotation in a manner similar to the N,N ligand as proposed above. Quantum mechanical calculations could possibly be used to determine whether the N,N ligand or the COD ligand is more likely to undergo partial dissociation and rotation, but this falls outside the scope of this thesis.

The role that the counter-ion plays in this process must also be considered. Gomes *et al.* proposed the stabilisation of the three-coordinate metal species formed after partial dissociation by the tetrafluoroborate counter-ion.

The question then remains: why do we observe a difference in the rate of activation, and therefore the room temperature ^{1}H NMR spectra between complex **C2.3** and **C2.9**? A possible determining factor could be the relative bond strengths of the different nitrogen-rhodium bonds in both complexes. A full investigation into the factors responsible for the difference is outside the scope of this thesis.

3.3 Conclusions

Two ^{1}H NMR phenomena were investigated in this Chapter. The ^{1}H NMR spectrum of complex **C2.3** showed an unusually large upfield shift of the imine proton relative to the ligand in chloroform, but not in acetone. The shift was determined to be the result of CH-π interactions between the imine proton on the cation and the phenyl rings of the BPh_4^- counter-ion. The reason for this occurring in chloroform-*d* and not in acetone-d_6 was proposed to be due to the fact that tight ion-pairs would form in the non-polar chloroform-*d* while acetone-d_6 is a polar solvent and would promote the formation of solvent-separated ion-pairs. The complex was further studied by 2 dimensional NMR techniques. NOE spectroscopy indicated through-space connectivities between the imine proton H^5 as well as one of the pyridine protons and the *ortho*

and *meta* hydrogen atoms on the tetraphenylborate counter-ion, giving more insight into the relative orientation of the cation and anion in solution. The ion-pairing was further investigated by using DOSY and it was found that the cation and anion behaves as an intimate ion-pair in chloroform, as is expected for a non-polar solvent. The ion-pairing phenomenon is of interest in this project, as it may have an effect on catalysis using these complexes as precursors. Cation-anion interactions of metal complexes are also often studied in solid phase by making use of crystallographic data and it would have been interesting to compare

We also observed that signal for the olefinic 1,5-cyclooctadiene protons differed depending on the nature of the co-ligands in the complex. Using variable temperature ^{1}H NMR and computational techniques, the differences in the peak shapes were partly attributed to a symmetric two-site exchange. The exact nature of the exchange could not be determined conclusively, but there are indications that it might involve a metal-ligand bond breakage and subsequent rotation of the ligand around the remaining metal-ligand bond involving the chelating ligand. The reason for the difference in Gibbs free energy of activation between the imine (**C2.3**) and triazole (**C2.9**) complexes could not be determined at this stage. A large shift in the positions of the imine (**C2.3**) and triazole (**C2.9**) proton signals was observed in the variable temperature ^{1}H NMR, with the signal shifting upfield at lower temperatures. This was attributed to stronger CH-π interactions and possible aggregation of two or more complexes at low temperature.

3.4 Experimental

3.4.1 General remarks and instrumentation

All reactions were carried out under a nitrogen atmosphere making use of standard Schlenk techniques. Highly air-sensitive materials were stored in a nitrogen purged glovebox and all manipulations with these materials were carried out in the glovebox to prevent decomposition or oxidation. A CEM Discover microwave reactor was used for certain reactions.

Fourier transform infrared (FR-IR) spectra were recorded using an ATR accessory on a Nicolet Avatar 330 FT-IR spectrometer. ^{1}H and ^{13}C NMR spectra were recorded on an Agilent Inova instrument at 300, 400 and 600 MHz for ^{1}H and 75, 100, 150 MHz for ^{13}C.

3.4.2 Materials and methods

Reagents were purchased from Sigma-Aldrich and used as received. Solvents were purchased from Sigma-Aldrich and Kimix Chemicals and were dried over alumina molecular sieves in Sigma Aldrich Innovative Technology solvent purifiers in the case of dichloromethane (DCM), tetrahydrofurane (THF), diethyl ether, toluene and hexane, and by refluxing over dry magnesium turnings and iodine in the case of ethanol and methanol.

^{1}H NMR spectra were recorded on an Agilent Inova instrument at 600 MHz. The ^{19}F, ^{1}H HOESY measurements were acquired using the standard HOESY pulse program on a Bruker Avance III 400 MHz spectrometer equipped with a 5 mm PABBO BB-1H/D ZGRD probe. A mixing time of 1200 ms was used for measuring the spectrum of **C3.1** while the mixing time for **C3.2** was 600 ms. The number of scans used was 16 and the number of increments in the F1 dimension was 128.

Samples of 4 mM were prepared in 0.5 mL of deuterated solvent for the DOSY spectra. The spectra were recorded using the Dbppste_cc pulse sequence on an Agilent Inova 600 MHz instrument fitted with a IDpfg 5mm broadband probe. The gradient power level was varied from 500 to 25 000 over 25 increments. The data obtained were used to calculate the *D* values of the samples, according to the literature.[38]

Density functional theory calculations were done using ORCA 3.0.3 suite. The geometry optimization and numerical frequency calculations were done with a PBE/def-TVZ-ZORA basis set with atom-pairwise Grimme D3 dispersion correction.[39,40] Relaxed geometry optimization scans of reaction coordinates were conducted using the same basis sets and functionals as the original optimizations.

3.4.3 Synthesis of rhodium complexes C3.1 and C3.2

L2.2 (0.2 mmol) was dissolved in dry DCM (2 mL) and added dropwise to a stirring solution of $[RhCl(COD)]_2$ (0.1 mmol) in dry DCM (4 mL). Upon addition of the ligand, the solution changed colour from yellow to dark purple. The solution was stirred at room temperature for 1 hour. The solvent was removed, leaving a residue which was dissolved in dry methanol (8 mL) and cooled to 0°C. $NaBF_4$ (**C3.1**) or $NaPF_6$ (**C3.2**) (0.2 mmol) was added and a dark precipitate formed in the solution. The reaction was stirred for a further 30 minutes at 0°C after which the solid was filtered off and washed with dry methanol.

Tetrafluoroborate complex **C3.1**: Dark red solid, yield 62%. Mp: 75°C - 77°C. IR: FT-IR, ν/cm^{-1}: 1633 (w, imine, C=N), 1595 (m, pyridine, C=N). ^{1}H NMR (300 MHz, $CDCl_3$): δ (ppm) = 1.00 (t, $^{3}J_{H\text{-}H}$ = 7.6 Hz, 3H, $NCH_2CH_2C\mathbf{H_3}$), 1.79 (m, 2H, $NCH_2C\mathbf{H_2}CH_3$), 2.10 (m, 4H, C**H$_2$**-*COD*), 2.58 (m, 4H, C**H$_2$**-*COD*), 3.33 (t, $^{3}J_{H\text{-}H}$ = 7.6 Hz, 2H, $NC\mathbf{H_2}CH_2CH_3$), 4.49 (s, 4H, C**H**-*COD*), 7.65 (t, $^{3}J_{H\text{-}H}$ = 5.9 Hz, 1H, Ar), 7.77 (d, $^{3}J_{H\text{-}H}$ = 5.3, 2H, Ar), 8.12 (td, $^{3}J_{H\text{-}H}$ = 7.7 Hz and $^{4}J_{H\text{-}H}$ = 1.2 Hz, 1H, Ar), 8.26 (d, $^{3}J_{H\text{-}H}$ = 7.7 Hz, 1H, Ar), 8.68 (s, 1H, *imine*-C**H**).

Hexafluorophosphate complex **C3.2:** Dark brown solid, yield 62%. Mp: 78°C - 81°C. IR: FT-IR, ν/cm^{-1}: 1630 (w, imine, C=N), 1593 (m, pyridine, C=N). ^{1}H NMR (300 MHz, $CDCl_3$): δ (ppm) = 0.98 (t, $^{3}J_{H\text{-}H}$ = 7.6 Hz, 3H, $NCH_2CH_2C\mathbf{H_3}$), 1.76 (m, 2H, $NCH_2C\mathbf{H_2}CH_3$), 2.09 (m, 4H, C**H$_2$**-

COD), 2.56 (m, 4H, C**H$_2$**-*COD*), 3.31 (t, $^3J_{H-H}$ = 7.6 Hz, 2H, NC**H$_2$**CH$_2$CH$_3$), 4.49 (s, 4H, C**H**-*COD*), 7.66 (t, $^3J_{H-H}$ = 5.9 Hz, 1H, Ar), 7.77 (d, $^3J_{H-H}$ = 5.3, 2H, Ar), 8.08 (d, $^3J_{H-H}$ = 7.7 Hz, 1H, Ar), 8.11 (td, $^3J_{H-H}$ = 7.7 Hz and $^4J_{H-H}$ = 1.2 Hz, 1H, Ar), 8.47 (s, 1H, *imine*-C**H**).

3.5 References

1 H. Gunther, *NMR spectroscopy: Basic Principles, concepts and applications in chemistry*, John Wiley & Sons LTD, 1995.

2 L. Frydman, A. Lupulescu and T. Scherf, *J. Am. Chem. Soc.*, 2003, **125**, 9204–9217.

3 E. E. Kwan and S. G. Huang, *European J. Org. Chem.*, 2008, 2671–2688.

4 R. Huo, R. Wehrens, J. Van Duynhoven and L. M. C. Buydens, *Anal. Chim. Acta*, 2003, **490**, 231–251.

5 M. H. Levitt, *Spin Dynamics: Basics of Nuclear Magnetic Resonance*, Wiley, 2001.

6 A. Macchioni, *Chem. Rev.*, 2005, **105**, 2039–2073.

7 P. S. Pregosin, *Prog. Nucl. Magn. Reson. Spectrosc.*, 2006, **49**, 261–288.

8 C. Zuccaccia, G. Bellachioma, G. Cardaci and A. Macchioni, *J. Am. Chem. Soc.*, 2001, **123**, 11020–11028.

9 P. S. Pregosin, *Magn. Reson. Chem.*, 2016, **55**, 405–413.

10 E. A. Meyer, R. K. Castellano and F. Diederich, *Angew. Chem. Int. Ed.*, 2003, **42**, 1210-1250.

11 I. Richter, J. Minari, P. Axe, J. P. Lowe, T. D. James, K. Sakurai, D. Bull and J. S. Fossey, *Chem. Comm.,* 2008, 1082–1084.

12 N. Zacharias and D. A. Dougherty, *Trends Pharmacol. Sci.,* 2002, **23**, 281–287.

13 K. Milčić, Z. D. Tomic and D. Zaric, *Inorg. Chem. Acta.,* 2004, **357**, 4327–4329.

14 Z. Zhang, J. Tan, C. Luo, J. Xie, H. Cai, L. Yang, X. Liu, J. Zhou and C. Ni, *Synth. Met.*, 2014, **195**, 147–153.

15 X. Xiao, J. Liu, K. Chen, Q. Zhu, S. Xue and Z. Tao, *J. Am. Chem Soc.,* 2010, 195, 2956–2961.

16 V. A. Afanas, L. A. Glinskaya, D. A. Piryazev, S. A. Gromilov, P. E. Plyusnin and L. A. Sheludyakova, *Inorg. Chem. Commun.*, 2017, **83**, 70–75.

17 D. Kruk, A. Korpala, E. Rossler, K. A. Earle, W. Medycki and J. Moscicki, *J. Chem. Phys.*, 2012, **136**, 1–9.

18 L. E. Kay, *J. Mol. Biol.*, 2016, **428**, 323–331.

19 W. Setaka, A. Koyama and K. Yamaguchi, *Org. Lett.*, 2013, **15**, 5092–5095.

20 C. Ji, S. Li, F. Deng, S. Liu, M. A. Asghar, Z. Sun, M. Hong, J. Luo, L. Shenhui, F. Deng, S. Liu, M. A. Asghar, Z. Sun, M. Hong and J. Luo, *Phys. Chem. Chem. Phys.*, 2016, **18**, 10868–10872.

21 A. D. Bain, *Prog. Nucl. Magn. Reson. Spectrosc.*, 2003, **43**, 63–103.

22 R. S. Macomber, *A Complete Introduction to Modern NMR Spectroscopy*, John Wiley & Sons LTD, 1998.

23 D. M. Haddleton, D. J. Duncalf, D. Kukulj, M. C. Crossman, S. G. Jackson, S. A. F. Bon, A. J. Clark and A. J. Shooter, *Eur. J. Inorg. Chem.*, 1998, 1799–1806.

24 J. Dupont, P. A. Z. Suarez, R. F. De Souza, R. A. Burrow and J.-P. Kintzinger, *Chem. - A Eur. J.*, 2000, **6**, 2377–2381.

25 K. E. Aldrich, B. S. Billow, D. Holmes, R. D. Bemowski and A. L. Odom, *Organometallics*, 2017, **36**, 1227–1237.

26 R. Diaz-Torrez and S. Alvarez, *Dalton Trans.*, 2011, **40**, 10742–10750.

27 E. Martínez-Viviente and P. S. Pregosin, *Inorg. Chem.*, 2003, **42**, 2209–2214.

28 A. Moreno, P. S. Pregosin, B. Fuentes, L. F. Veiros, A. Albinati and S. Rizzato, *Organometallics*, 2009, **28**, 6489–6506.

29 D. Schott, P. S. Pregosin, B. Jacques, M. Chavarot, F. Rose-Munch and E. Rose, *Inorg. Chem.*, 2005, **44**, 5941–5948.

30 M. Enamullah, M. A. Islam and C. Janiak, *J. Mol. Struct.*, 2016, **1122**, 331–340.

31 M. Valentini, K. Selvakumar, M. Wo and P. S. Pregosin, *J. Organomet. Chem.*, 1999, **587**, 244–251.

32 C. S. B. Gomes, S. I. Costa, L. F. Veiros and P. T. Gomes, *Polyhedron*, 2016, **116**, 162–169.

33 P. Vallurupalli, "Chemical exchange workshop series on NMR and related topics:, TIFR Mumbai, 2009.

34 F. Bloch, *Phys. Rev.*, 1946, **70**, 460–474.

35 J. Ashcroft, M. Besnard, V. Aquada and J. Jonas, *Chem. Phys. Lett.*, 1984, **110**, 420–424.

36 D. F. Hansen, P. Vallurupalli and L. E. Kay, *J. Phys. Chem. B*, 2008, **112**, 5898–5904.

37 S. J. O'Kennedy, *A Kinetic Thermodynamic Study of Procyanidin Oligomer Conformation by 1H NMR and DFT*, Stellenbosch University, 2015.

38 A. Moreno, P. S. Pregosin, L. F. Veiros, A. Albinati and S. Rizzato, *Chem. - A Eur. J.*, 2009, **15**, 6848–6862.

39 D. A. Pantazis, X. Chen, C. R. Landis and F. Neese, *J. Chem. Theory Comput.*, 2008, **4**, 908–919.

40 S. Grimme, J. Antony, S. Ehrlich, H. Krieg, S. Grimme, J. Antony, S. Ehrlich and H. Krieg, *J. Chem. Phys.*, 2010, **132**, 154104.

CHAPTER 4 : IMMOBILIZATION OF RHODIUM COMPLEXES ONTO MCM-41 AND SBA-15

4.1 Introduction

In the past two decades there has been considerable interest in the synthesis and application of mesoporous silica materials. These materials have high specific surface areas, thermal and mechanical stability, uniform, tuneable pores, and are easy to functionalize. Mesoporous silica has been applied as pollutant absorbents, templates for other porous materials, in targeted drug delivery and as supports in catalysis to name but a few uses.[1–4] It is this latter application that is of interest in the current project.

As discussed in Chapter 1, the recovery and re-use of metal catalysts is an area of great current research interest. One method that is often followed is the modification and immobilization of an inherently homogeneous catalyst onto a solid support. These catalysts are then said to be 'heterogenized' and are regarded to be in a different phase than the reagents and products. The catalysts can therefore easily be separated from the product mixture and potentially be recycled. They have the additional potential to be used in continuous flow processes, making the catalysts attractive from an industrial point of view.[4]

Mesoporous silica materials are often the catalyst support of choice in academic research. They are commonly synthesized by making use of an organic template which is usually a surfactant molecule. The templating molecules form a liquid crystal array in solution, and a silica source is added to the reaction as shown in Figure 4.1. The silica condenses around the templating molecules, and a hybrid mesoporous structure is formed. The silica is then washed with water and finally calcined to remove the templating molecules.[5]

There are many factors that can affect the exact properties of the silica that is obtained. These include the type of surfactant, the pH of the solution, the presence of additives, surfactant and silica concentrations, the specific silica source and the temperature. Silica from the family known as M41S which includes Mobil Composition of Matter No. 41 (MCM-41), for example, is synthesized *via* a direct interaction between a cationic surfactant and a negatively charged silica source in a basic environment. Conversely, Santa Barbara amorphous (SBA) materials

are made by using a polymeric based organized system which interacts indirectly with a positively charged silica source in acidic medium.[5–8]

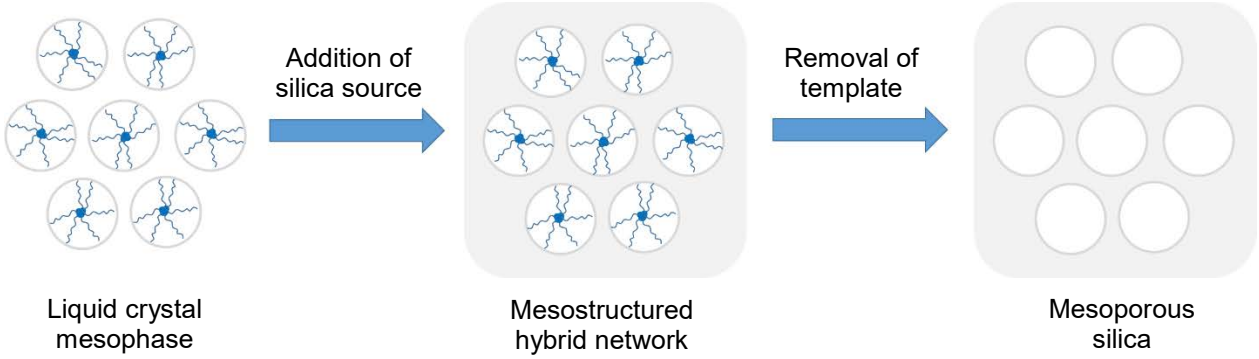

Figure 4.1 Synthesis of mesoporous silica *via* the templating method.[5]

MCM-41 and SBA-15 are commonly used as supports in catalysis and some examples will be discussed below.

4.1.1 Mesoporous silicas MCM-41 and SBA-15 used a catalyst supports

Pastva *et al*. studied ruthenium-based complexes with quaternary ammonium tags which were immobilized onto MCM-41, SBA-15 and amorphous silica.[9] The immobilized catalysts were applied in olefin metathesis. The group assumed that the strong interaction between the ammonium groups and the surface silanols present in the silica materials would prevent catalyst leaching. The catalyst is shown in Figure 4.2.

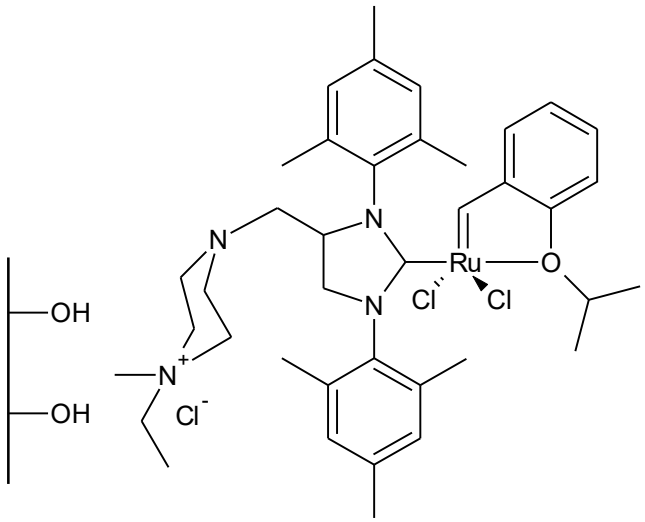

Figure 4.2 Electrostatically immobilized ruthenium catalyst used by Pastva *et al*.[9]

The immobilized catalyst was characterized by powder X-ray diffraction, nitrogen adsorption and ICP-OES (inductively coupled plasma optical emission spectrometry). The catalysts were then employed in the ring-closing metathesis of (-)-*β*-citronellene. It was found that the reactivity decreased in the following order: homogeneous catalyst > SBA-15 > MCM-41 > silica

gel. The reaction rate for the catalyst immobilized onto SBA-15 was almost as high as that observed for the homogeneous catalyst. It was also observed that 2.6% of the initial amount of ruthenium was leached from the support after 5 hours.

Veisi *et al*. immobilized palladium complexes onto SBA-15, and tested these complexes in Suzuki-Miyaura coupling reactions.[10] The complexes were covalently anchored onto the silica support following the sequential immobilization method (as discussed in Chapter 2). The final immobilized catalyst is shown in Figure 4.3.

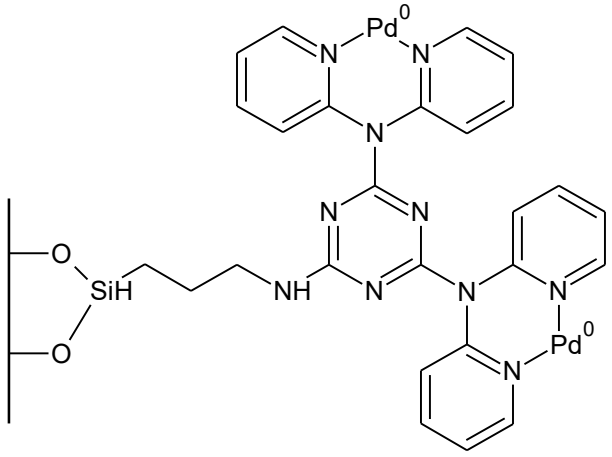

Figure 4.3 Covalently immobilized palladium catalyst used by Veisi *et al*.[10]

The immobilized catalyst was characterized using FT-IR spectroscopy, nitrogen adsorption, powder x-ray diffraction and scanning and transmission electron microscopy. The catalyst was applied in the Suzuki reaction between iodobenzene and phenylboronic acid. Various parameters such as solvent, the nature of the base and temperature were tested in order to obtain the optimum reaction conditions. The catalyst could also be recycled eight times without significant loss of catalytic activity.

The above examples show that there is a variety of ways that catalyst immobilization can be achieved. A number of solid-state commonly applied characterization methods is mentioned as well.

This chapter describes the synthesis of MCM-41 and SBA-15 using published methods, followed by the immobilization of the siloxane-functionalized complexes described in Chapter 2 onto both types of silica. The native silica as well as the immobilized catalysts were characterized using a range of solid-state characterization methods.

4.2 Results and discussion

4.2.1 Synthesis and characterization of mesoporous silicas MCM-41 and SBA-15

The targeted mesoporous silica materials, MCM-41 and SBA-15, were synthesized using adapted procedures previously reported by Cai and Zhao.[8,11] MCM-41 was synthesized using the surfactant cetyltrimethylammonium bromide (CTAB) in a basic solution (pH ~ 12) with the addition of tetraethyl orthosilicate (TEOS). For the synthesis of SBA-15, poly(propelyneglycol)-block-poly(ethyleneglycol) was used as surfactant and the synthesis was carried out in an acidic solution, using TEOS as silica source once again. The SBA-15 was also aged for 24 hours – a step that leads to thicker pore walls. Both types of silica were isolated as fine white powders after filtration, washing with distilled water and drying. The silica was then calcined at 550 °C for 8 hours to remove the surfactant molecules that acted as templating agents during the synthesis of the material.

4.2.1.1 Characterization of native MCM-41 and SBA-15

The synthesized silica materials were analyzed by infrared spectroscopy, powder x-ray diffraction, nitrogen adsorption, scanning electron microscopy, transmission electron microscopy and thermal gravimetric analysis. These techniques give information on a wide range of properties of the materials, from the chemical structure to surface characteristics, crystallinity and pore properties.

4.2.1.1.1 Characterization of MCM-41 and SBA-15 by means of FT-IR spectroscopy (ATR)

FT-IR spectroscopy was used to investigate the chemical properties of the synthesized materials. The samples were dried at 100 °C for 1 hour before recording the spectra in order to remove any water that could be absorbed on the silica surface. The obtained spectra are shown in Figure 4.4. The only difference between the two spectra is that MCM-41 has an extra weak band at 1242 cm^{-1}. This band could be due to the longitudinal-optic splitting of the vibrational mode as described by Innocenzi.[12] The longitudinal-optic modes are not always observed by reflectance infrared spectroscopy, but is sometimes seen in materials with a high porosity. The bands in the region of 799 cm^{-1} to 805 cm^{-1} and 1063 cm^{-1} and 1067 cm^{-1} are attributed to the symmetric and asymmetric Si-O-Si stretch vibrations and are characteristic of a condensed silica network.[10,12,13]

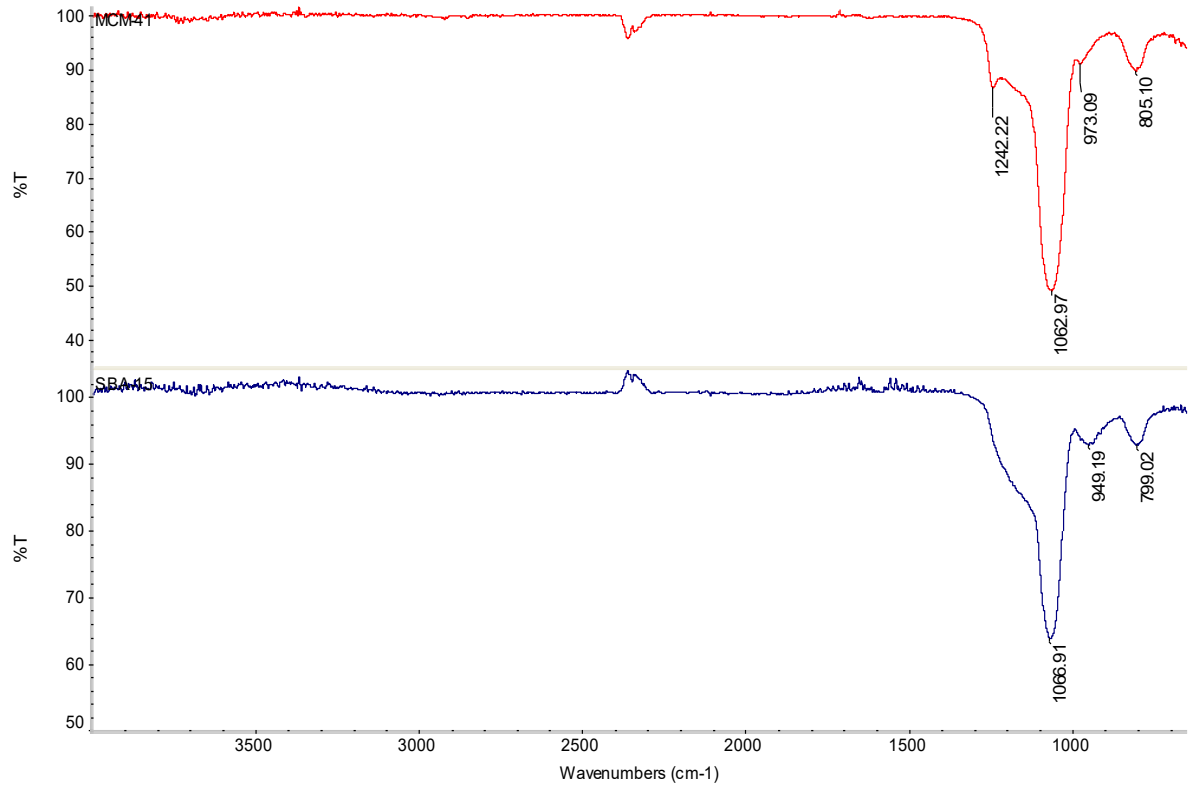

Figure 4.4 Infrared spectra of MCM-41 (top) and SBA-15 (bottom).

4.2.1.1.2 Characterization of MCM-41 and SBA-15 by means of powder X-ray diffraction

The powder X-ray diffraction patterns for MCM-41 and SBA-15 are shown in Figure 4.5 and Figure 4.6. Both patterns show three well resolved peaks that can be indexed as the (100), (110) and (200) diffractions, consistent with a 2-D hexagonal symmetry. This indicates that the materials have a well-ordered mesostructure.[14]

For MCM-41 these peaks occur at 2θ = 2.40° (100), 4.15° (110) and 4.78° (200) as is typical for this material.[11] Furthermore, a less well resolved peak can be seen at 2θ = 6.30° and this is assigned to the (210) reflection plane. The peaks for SBA-15 occur at lower angles than those of MCM-41. The peaks are seen at 2θ = 0.95° (100), 1.63° (110) and 1.87° (200).[8] There is also a less well resolved peak present at 2θ = 2.4° which is assigned to the (210) reflection plane. The presence of the fourth peak indicates that the synthesized material is of good quality in terms of crystallinity. The diffraction patterns are consistent with what is reported for these materials in literature.

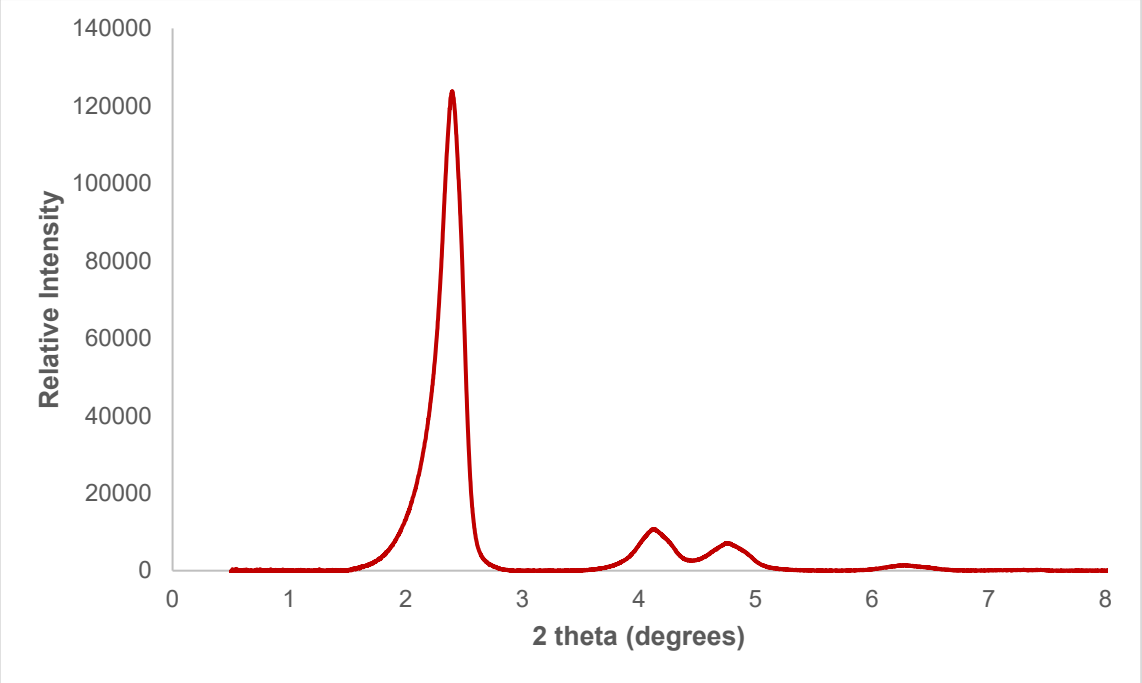

Figure 4.5 Powder XRD spectrum of MCM-41.

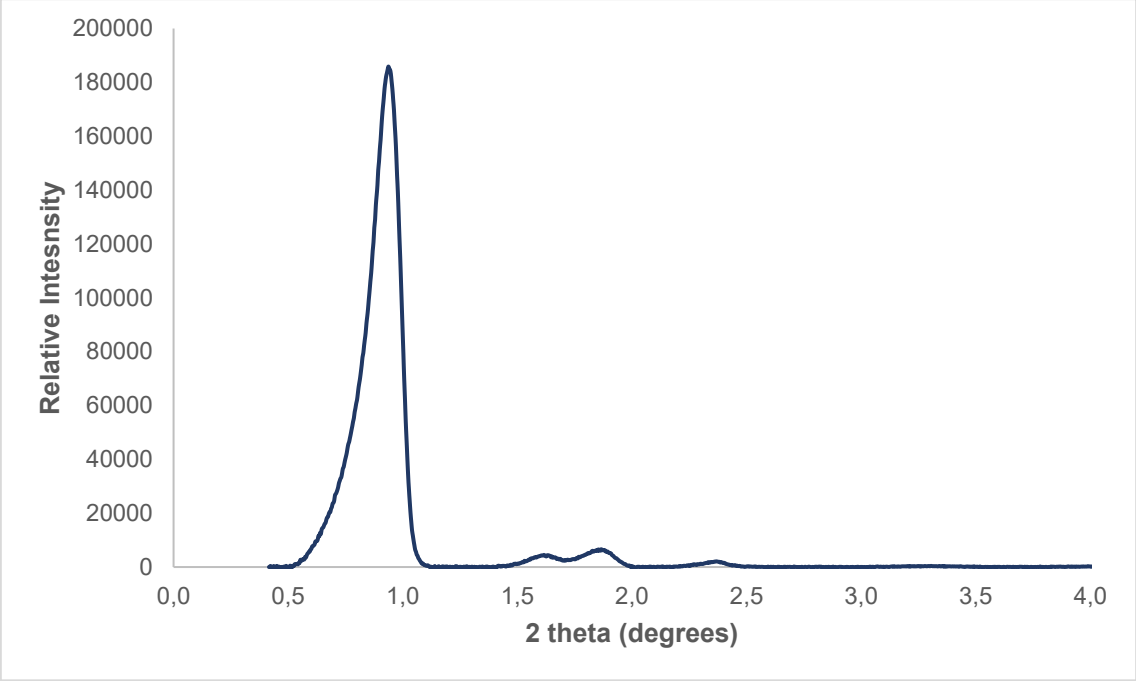

Figure 4.6 Powder XRD spectrum of SBA-15.

The angles for the diffraction peaks of MCM-41 and SBA-15 are summarized in Table 4.1.

Table 4.1 2 Theta values from powder XRD plots of MCM-41 and SBA-15.[a]

Material	(100)	(110)	(200)	(210)
MCM-41	2.41	4.25	4.81	6.34
SBA-15	0.98	1.64	1.87	2.38

[a] Angles given as degrees 2 theta

Bragg's equation (Equation 1) can be used to calculate the interplanar spacing for the (100) reflection plane of the materials. For MCM-41 the calculated *d* spacing for the reflection plane d_{100} was found to be 36.78 Å and for SBA-15 the value was 92.88 Å (λ = 1.5106 Å and *n* for d_{100} = 1). From these values the unit cell parameter *a* was calculated to be 42.47 Å for MCM-41 and 107.25 Å for SBA-15 respectively (Equation 2). This compares well to the unit cell parameters of 45.95 Å for MCM-41 and 120 Å for SBA-15 obtained by Beck and Zhao respectively.[7,8]

$$2dsin\theta = n\lambda \quad (1)$$

$$a = 2d/\sqrt{3} \quad (2)$$

4.2.1.1.3 Characterization of MCM-41 and SBA-15 by means of BET (Brunauer Emmett Teller) surface analysis

The surface area and average pore diameter of the supports were determined using BET surface analysis. This technique involves the adsorption and desorption of gas molecules onto the surface and into the pores of the material. Various gases can be used for this analysis, but the most common gas, which was also used in our analysis, is nitrogen.

Six types of adsorption isotherms are described by IUPAC and are illustrated in Figure 4.7.[15] The types are microporous (type I), nonporous or macroporous (types II, III and VI), or mesoporous (types IV and V). The point indicated by 'B' in the figure for isotherms II and IV is the point where monolayer adsorption is considered to be complete and multilayer adsorption is about to begin. The type IV isotherm is most commonly observed for mesoporous materials. It often includes a hysteresis loop, which is associated with capillary condensation occurring in the pores.

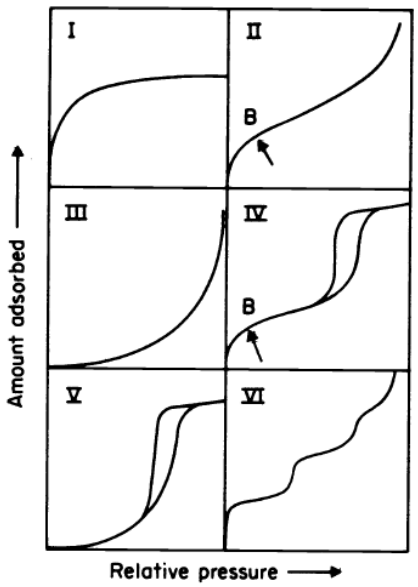

Figure 4.7 Adsorption isotherms described by IUPAC.[15]

The silica samples MCM-41 and SBA-15 were degassed at 150 °C for 24 hours prior to the analysis to ensure that the samples were completely dry. The pressure was then increased from 0 to 1 relative pressure (P/P_0) and nitrogen was allowed to adsorb onto the surface of the silica at a temperature of 77 K. Both MCM-41 and SBA-15 gave characteristic type IV isotherm plots which are shown in Figure 4.8. The volume for nitrogen gas adsorbed onto MCM-41 is higher than for SBA-15, which indicates that MCM-41 has a larger surface area than SBA-15.

The hysteresis loop for SBA-15 is quite large, while it is barely visible in the plot of MCM-41. Materials with large pores of constant cross-section are known to produce isotherm plots with larger hysteresis loops. It has previously been reported that the hysteresis loops in the case of nitrogen adsorption only appears below temperatures of 70 K, or when the material has a pore diameter greater than 40 Å.[16,17] Our analyses were carried out at 77 K, which then indicates that our MCM-41 would have pores with a diameter of less than 40 Å.

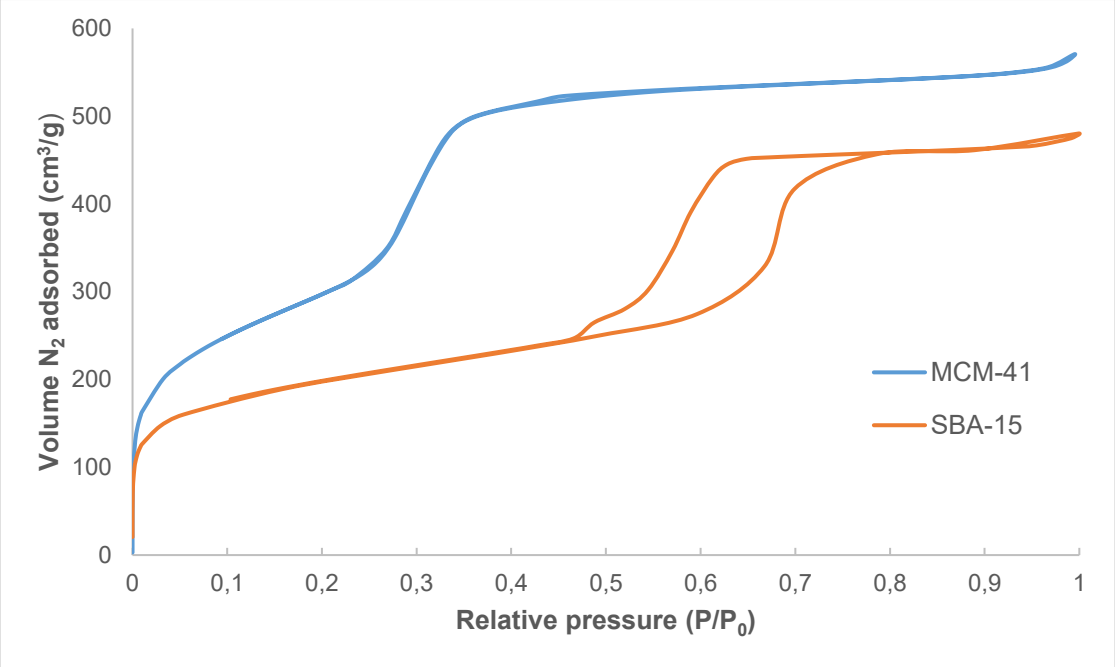

Figure 4.8 Isotherm plots for MCM-41 and SBA-15. The plot for SBA-15 has a prominent hysteresis loop, typical of mesoporous materials.

The pore-filling steps are visualized on the isotherm as areas with a much steeper slope than the rest of the isotherms. For MCM-41, this occurs between P/P_0 0.24 - 0.35 relative pressure while it occurs between P/P_0 0.46 – 0.64 relative pressure for SBA-15. The pores in MCM-41 are therefore filled over a smaller pressure range than for SBA-15, and this indicates that MCM-41 has a narrower pore distribution than SBA-15. This is confirmed when looking at the pore size distributions plotted in Figure 4.9.

The surface area, average pore diameter and total pore volume data calculated from the BET analysis for MCM-41 and SBA-15 are shown in Table 4.2. The calculated data shows that MCM-41 has a higher total surface area than SBA-15. It also confirms that MCM-41 has pores with a diameter of less than 40 Å, as indicated by the lack of a hysteresis loop in the isotherm plot. SBA-15, on the other hand, has quite as large average pore diameter. The total pore volume is fairly similar for the two materials. The results obtained are consistent with results reported in literature.[11,18,19]

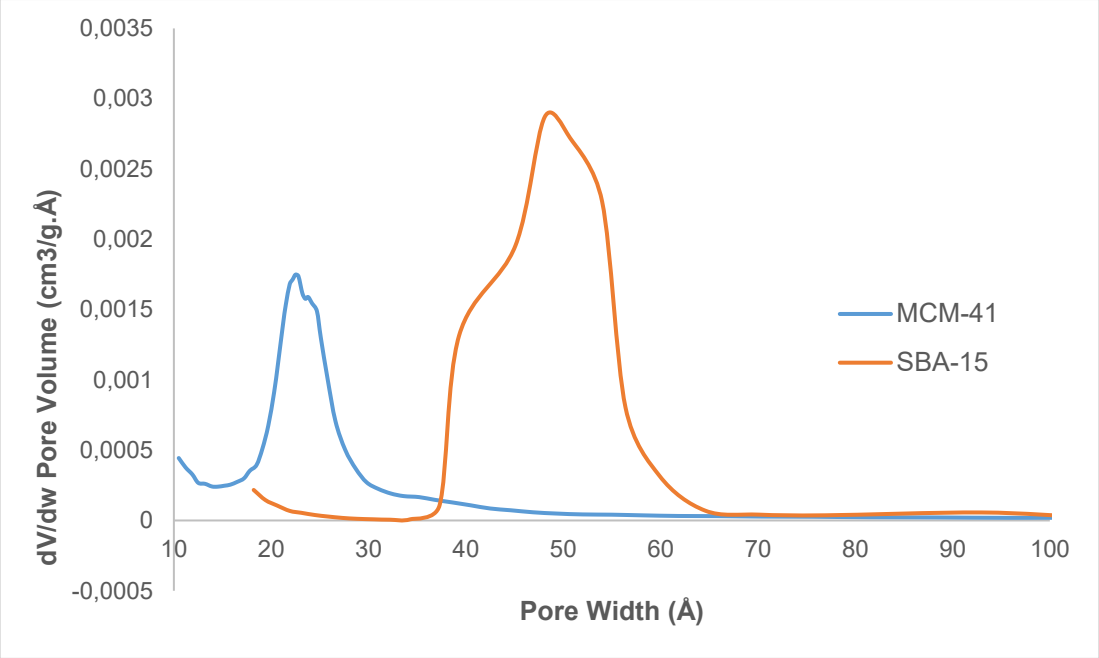

Figure 4.9 Pore size distribution plots of MCM-41 and SBA-15.

Table 4.2 Summary of BET surface area, average pore diameter and total pore volume for MCM-41 and SBA-15.

Material	BET Surface Area (m^2/g)	Average Pore Diameter (Å)	Total Pore Volume (cm^3/g)
MCM-41	1100.66	24.33	0.74
SBA-14	702.61	58.24	0.77

4.2.1.1.4 Characterization of MCM-41 and SBA-15 by means of microscopic studies (SEM and TEM)

The morphology of the materials were studied using electron microscopy and the micrographs are shown in Figure 4.10 and 4.11. The MCM-41 silica consists of small, flat roughly hexagonal particles. The particles are fairly uniform in size, with some aggregates also being present. This is consistent with the literature method used for the synthesis of MCM-41.[11] The SBA-15 particles are more rod-like, and tend to arrange in large chain-like structures.

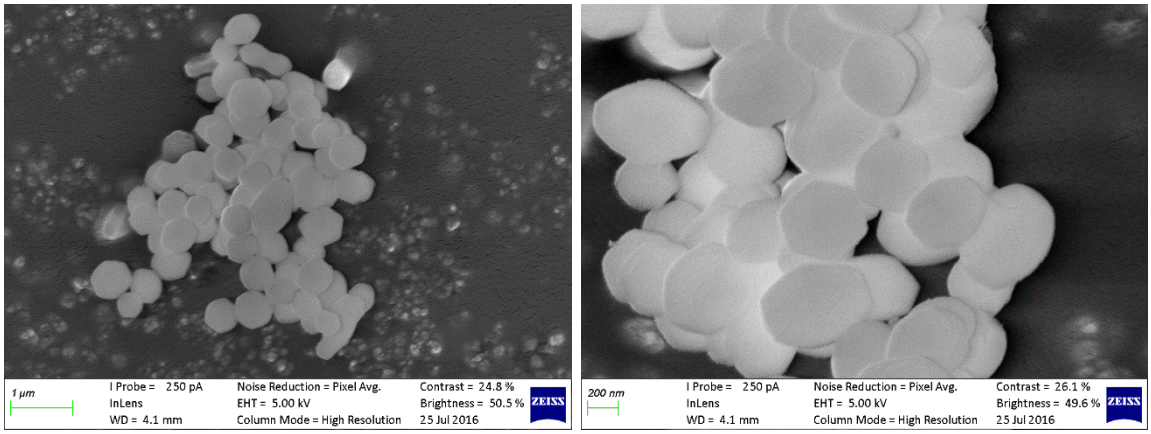

Figure 4.10 Scanning electron micrographs of MCM-41.

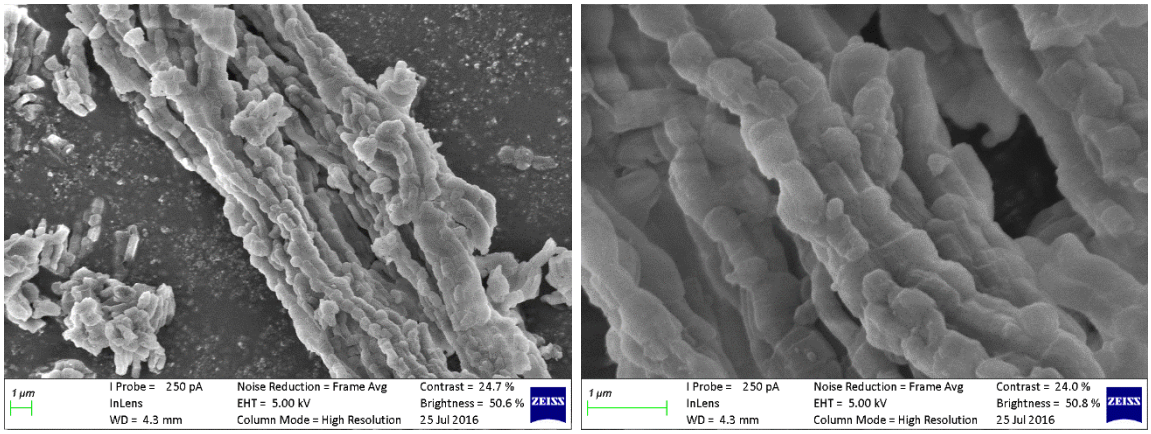

Figure 4.11 Scanning electron micrographs of SBA-15.

The physical appearance of mesoporous silica is highly dependent on the exact synthetic method used, as discussed by Cool and co-workers in an overview article on the synthesis of mesoporous silica.[5] They compared various published methods of the synthesis of mesoporous silicas, and also listed the characterization data obtained with each method. They found that, while BET and powder XRD characterization data was largely similar when comparing different synthetic methods for MCM-41 and SBA-15 respectively, dramatic changes in the physical appearance were observed. The appearance of MCM-41, for example, ranges from rod-like particles, to glass-like agglomerates, to hexagonal particles (as is seen in our material).

The TEM micrographs of MCM-41 and SBA-15 show the regular arrays of mesoporous channels expected for these materials. The pores are more pronounced for SBA-15 than for MCM-41. This can be ascribed to the aging process that was included in the synthesis of SBA-15. The micrographs are shown in Figure 4.12 and 4.13.

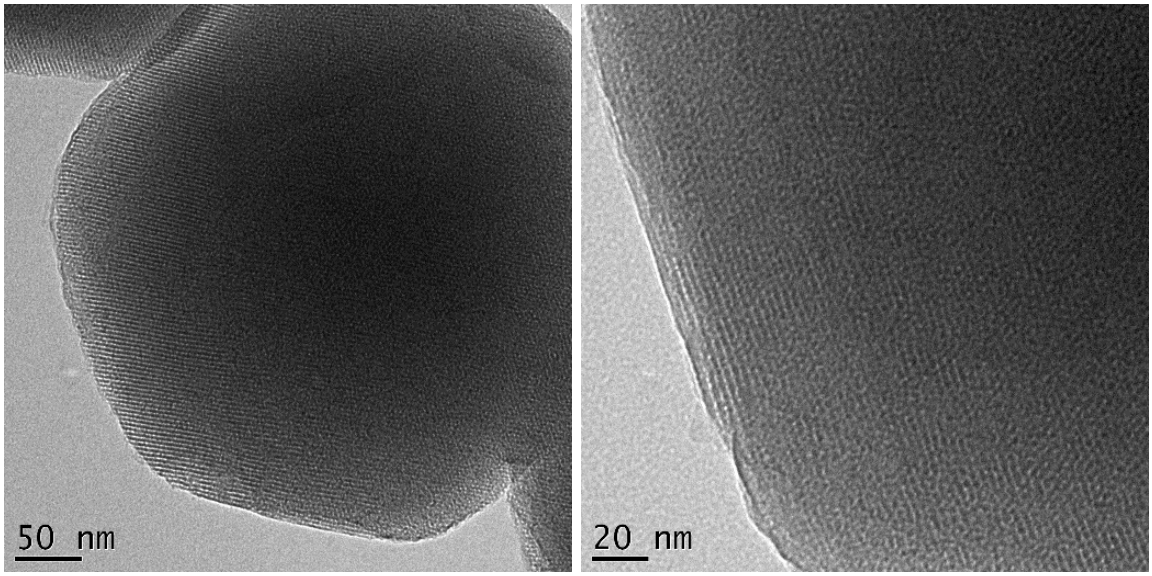

Figure 4.12 Transmission electron micrographs of MCM-41 showing mesoporous channels present in the material.

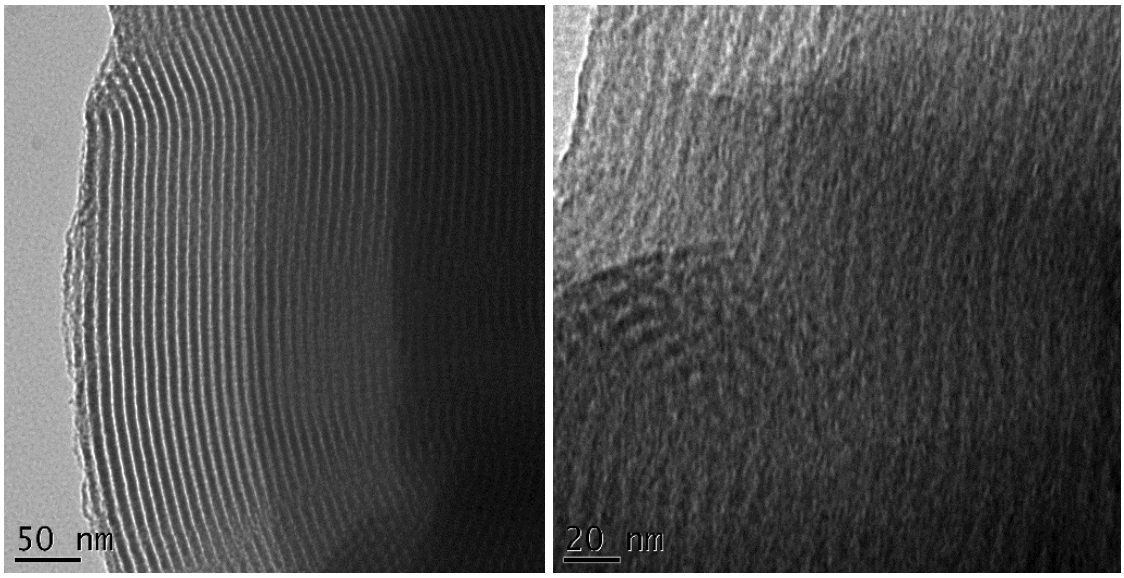

Figure 4.13 Transmission electron micrographs of SBA-15 showing mesoporous channels present in the material.

The pores of SBA-15 are larger than those of MCM-41, which corroborates the unit cell parameters calculated from the powder XRD results as well as the results obtained from BET analysis.

4.2.1.1.5 Characterization of MCM-41 and SBA-15 by means of thermal gravimetric analysis (TGA)

Thermal gravimetric analysis was used to study the thermal stability of the silicate materials (Figure 4.14). An initial weight loss is observed below 100°C and was attributed to loss of the water absorbed onto the surface of the materials, with the loss being slightly more for SBA-15 than for MCM-41. No further significant weight loss is observed between 100°C and 600°C.

This confirms that these materials have good thermal stabilities, a useful characteristic in a catalyst support. The weight loss between 100°C and 600°C is roughly 2-2.5% over the temperature range and can be attributed to the decomposition of small amounts of TEOS or templating agent as well as the condensation of the silanol groups.

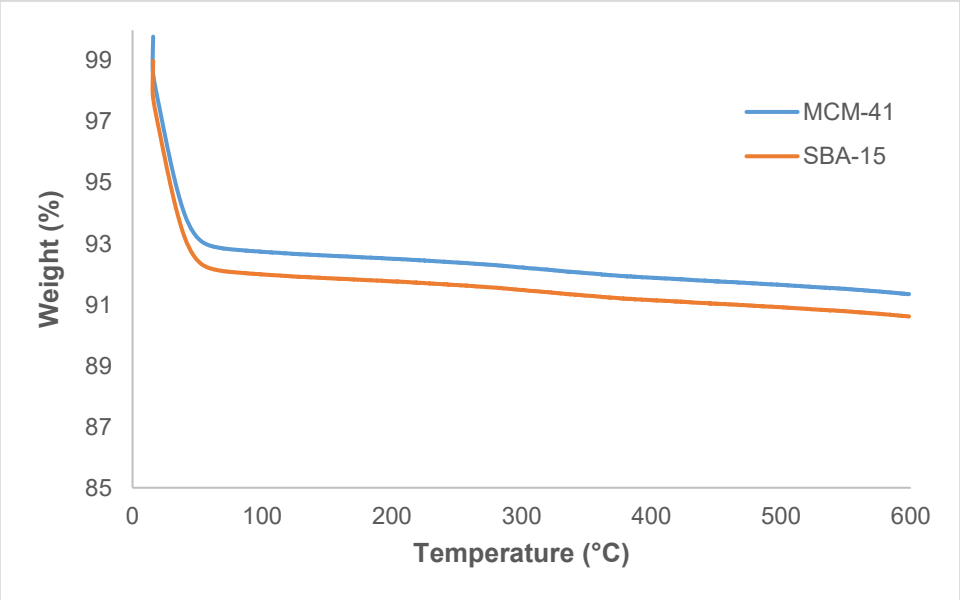

Figure 4.14 Thermal gravimetric analysis plot for MCM-41 and SBA-15.

4.2.2 Synthesis and characterization of immobilized catalysts

The siloxane functionalized catalysts discussed in Chapter 2 were immobilized onto the synthesized silica supports in order to obtain the immobilized catalysts. In this study, 10 weight % of the siloxane functionalized complex relative to the silica support was utilized to obtain the immobilized catalysts. The expected weight % of rhodium on the immobilized catalysts was between 1 and 2%. The native silica was dried at 100°C for four hours before use. The catalysts were immobilized by adding the functionalized complex dissolved in the appropriate solvent to a stirring slurry of the appropriate silica in toluene. Due to the differences in solubility of the complexes, either toluene, THF or chloroform was employed to dissolve the complexes prior to the addition of the complex to the silica support. The slurries were stirred at reflux (110°) for 24 hours. After 24 hours, the silica was filtered off while still hot, washed with the appropriate solvent and dried. The immobilized catalysts were obtained as light orange or yellow powders.

The immobilization is illustrated by using the neutral complex **C2.5** in Scheme 4.1.

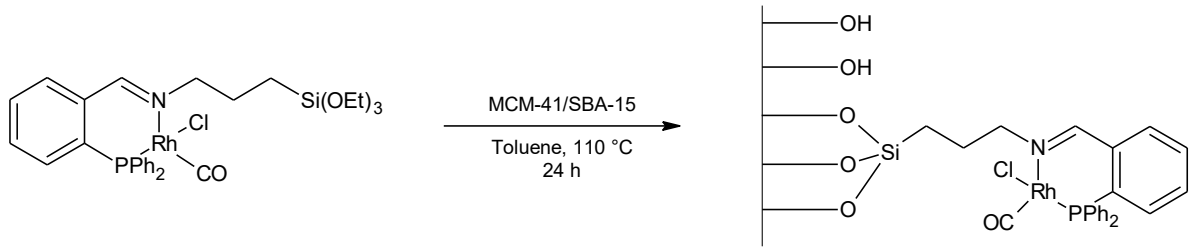

Scheme 4.1 Immobilization of complex C2.5.

Ten immobilized catalysts were prepared by reacting the five functionalized complexes with either MCM-41 or SBA-15. The immobilized catalyst systems are listed in Figure 4.15.

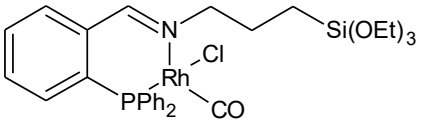

IC4.1: MCM-41
IC4.2: SBA-15

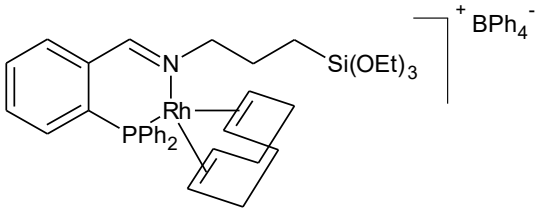

IC4.3: MCM-41
IC4.4: SBA-15

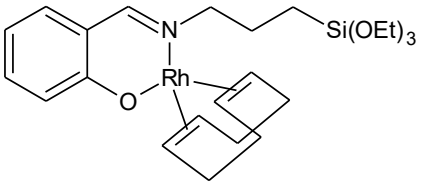

IC4.5: MCM-41
IC4.6: SBA-15

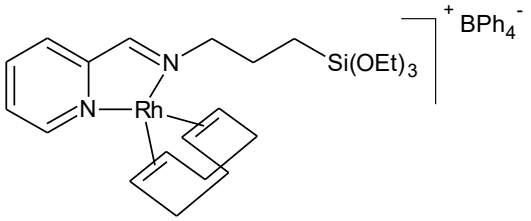

IC4.7: MCM-41
IC4.8: SBA-15

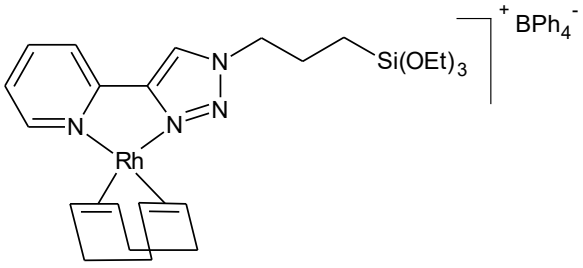

IC4.9: MCM-41
IC4.10: SBA-15

Figure 4.15 Immobilized catalysts prepared in this study.

4.2.2.1 Characterization of immobilized catalysts IC4.1 – IC4.10

4.2.2.1.1 Characterization of immobilized catalysts IC4.1-4.10 by means of FT-IR spectroscopy (ATR)

The infrared spectra for the immobilized compounds are shown in Figures 4.16 to 4.19. No significant changes are observed when the spectra of the immobilized catalysts are compared with the spectra of the native silica. The most characteristic peak for identifying the complexes is the imine peak around 1600 cm^{-1}, but this signal is only observed as a broad band for IC4.7 in Figure 17, and is absent in the spectra of the other immobilized complexes. The low intensity of the signal is explained by the low loading of the complex on the support. The spectra are therefore dominated by the very strong absorption bands of the silica support.

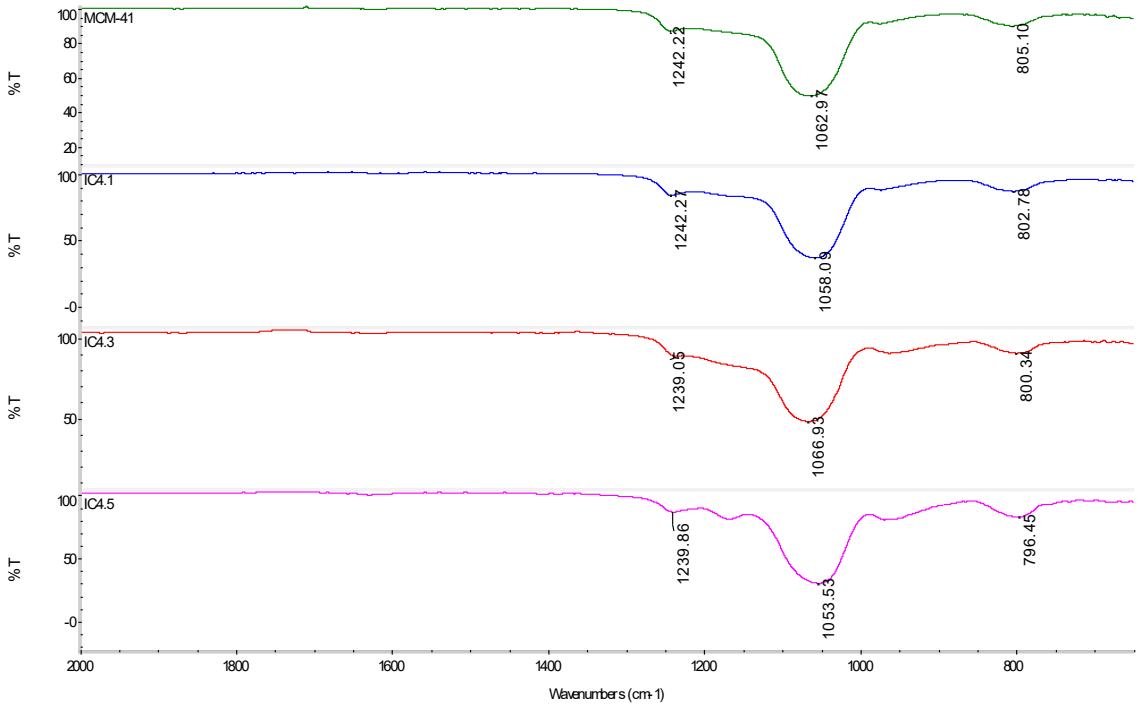

Figure 4.16 Infrared spectra of MCM-41, IC4.1, IC4.3 and IC4.5.

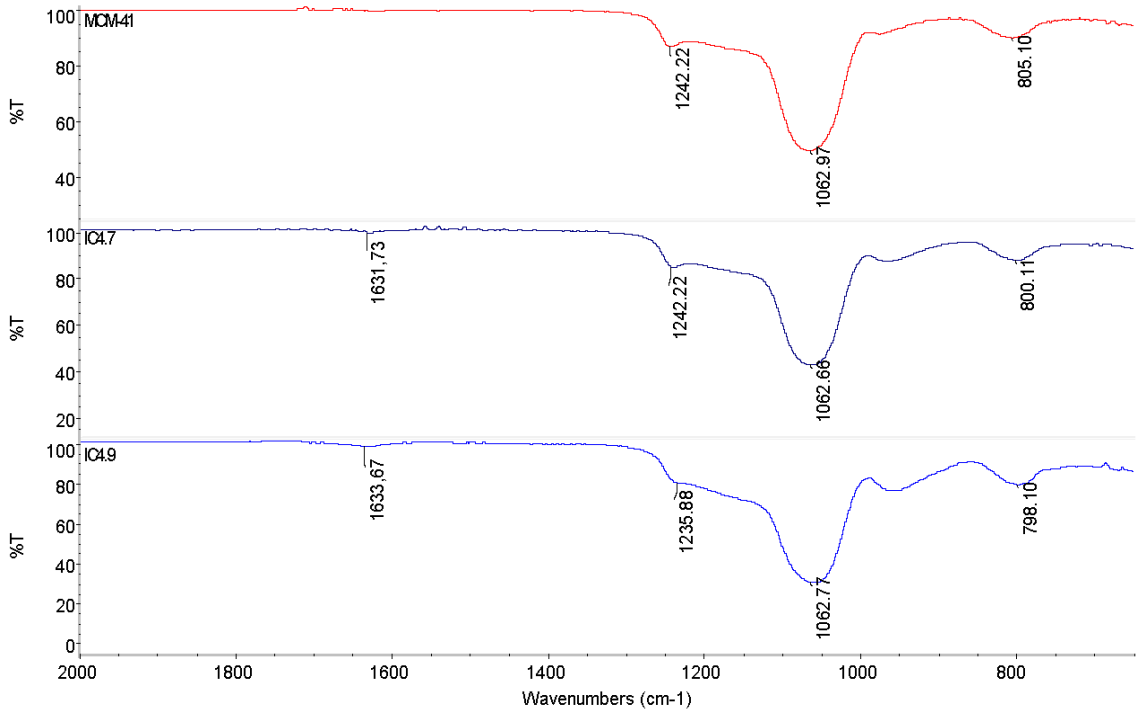

Figure 4.17 Infrared spectra of MCM-41, IC4.7 and IC4.9.

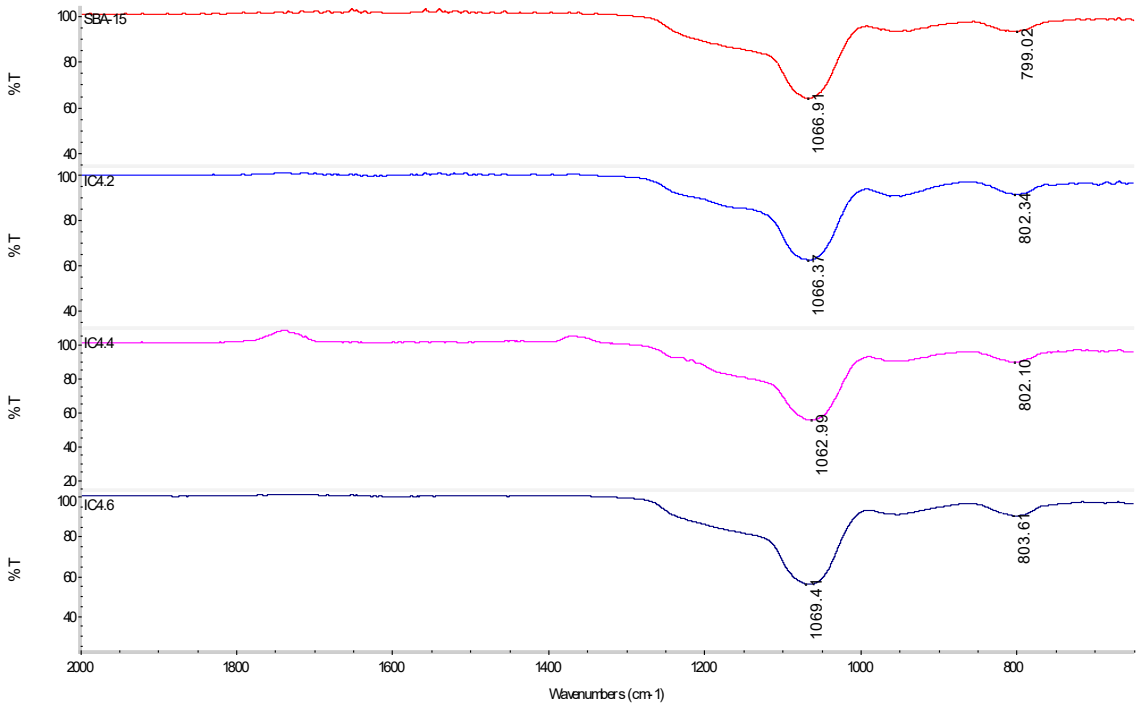

Figure 4.18 Infrared spectra of SBA-15, IC4.2, IC4.4 and IC4.6.

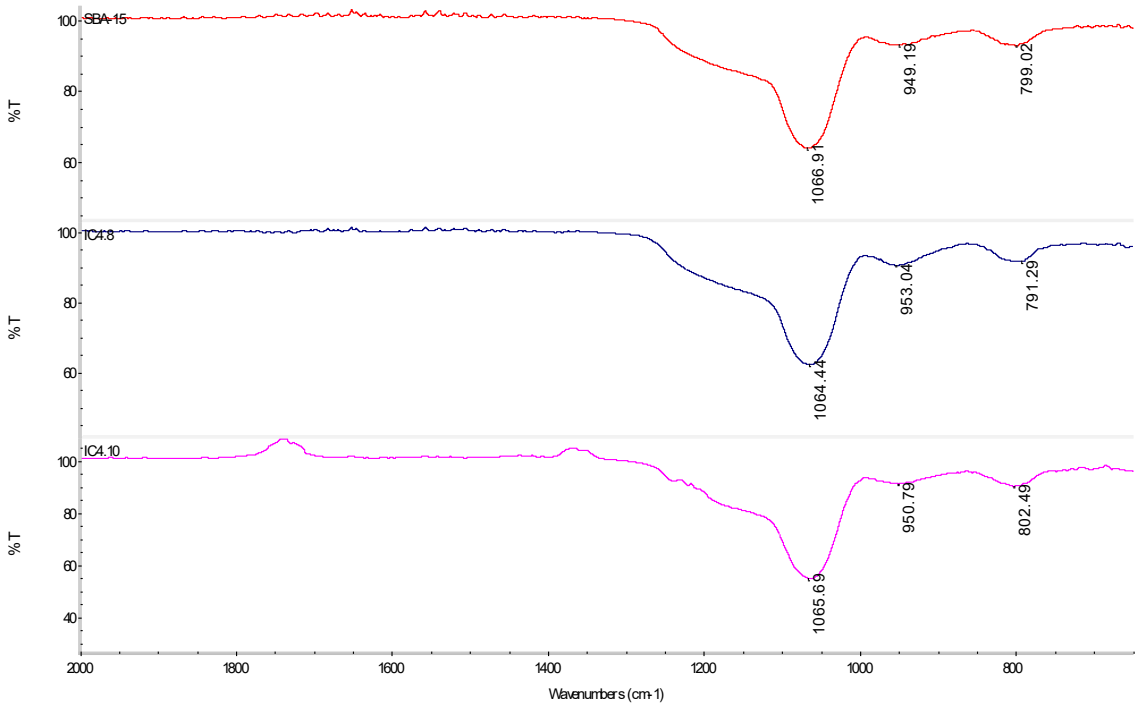

Figure 4.19 Infrared spectra of SBA-15, IC4.8 and IC4.10.

4.2.2.1.2 Characterization of immobilized catalysts IC4.1-4.10 by means of powder X-ray diffraction

The diffraction patterns of the immobilized catalysts do not differ greatly from that of the native supports. In the case of MCM-41 (Figure 4.20 and 4.21), there is a decrease in intensity of the peaks after immobilization. The decrease in the powder diffraction intensity can be attributed to a change in the degree of ordering of the silicate material due to the immobilization process. Some percentage of the material may have lost its crystalline character after being subjected to the conditions used during immobilization. The first three refraction peaks are, however, still visible in all cases which indicates that some degree of crystallinity is retained.

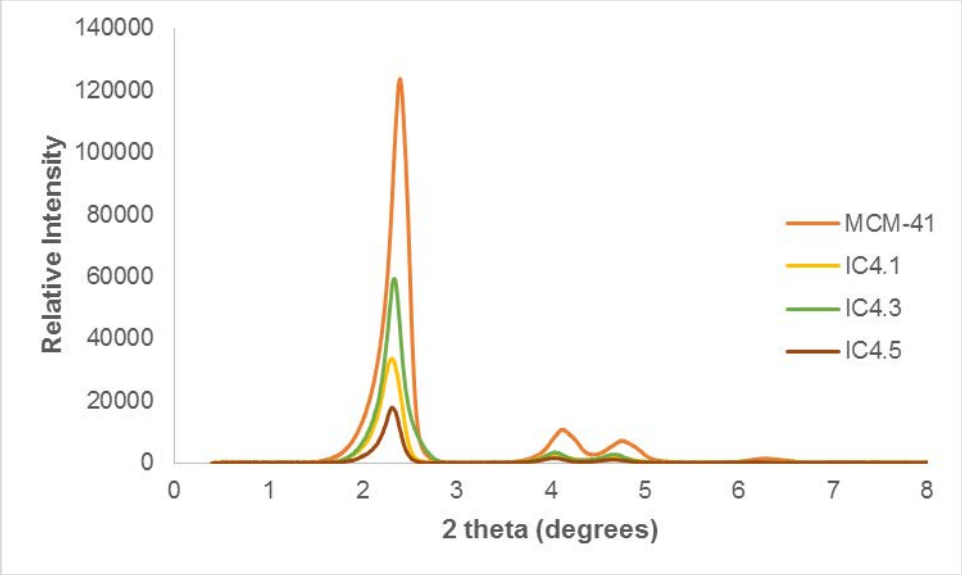

Figure 4.20 Powder XRD plots for MCM-41 immobilized catalysts IC4.1, IC4.3 and IC4.5.

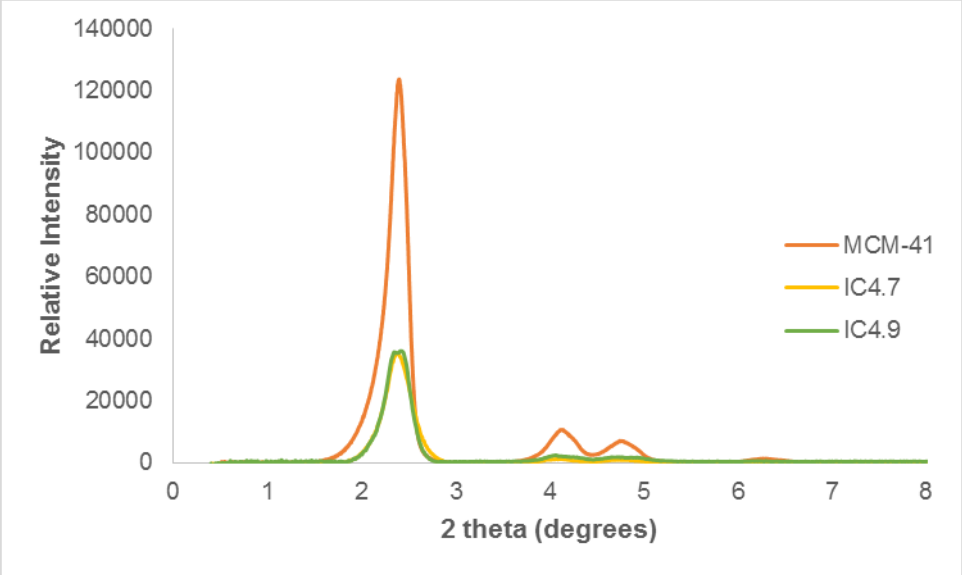

Figure 4.21 Powder XRD plots for MCM-41 immobilized catalysts IC4.7 and IC4.9.

For SBA-15, only minor differences in the intensity of the d_{100} peak at 2θ = 0.95° is seen for the immobilized catalysts (Figures 4.22 and 4.3). The weak peak at 2θ = 2.4° is seen in four of the five immobilized catalysts. This indicates that the materials have retained their well-ordered mesoporous structure after immobilization of the catalysts.

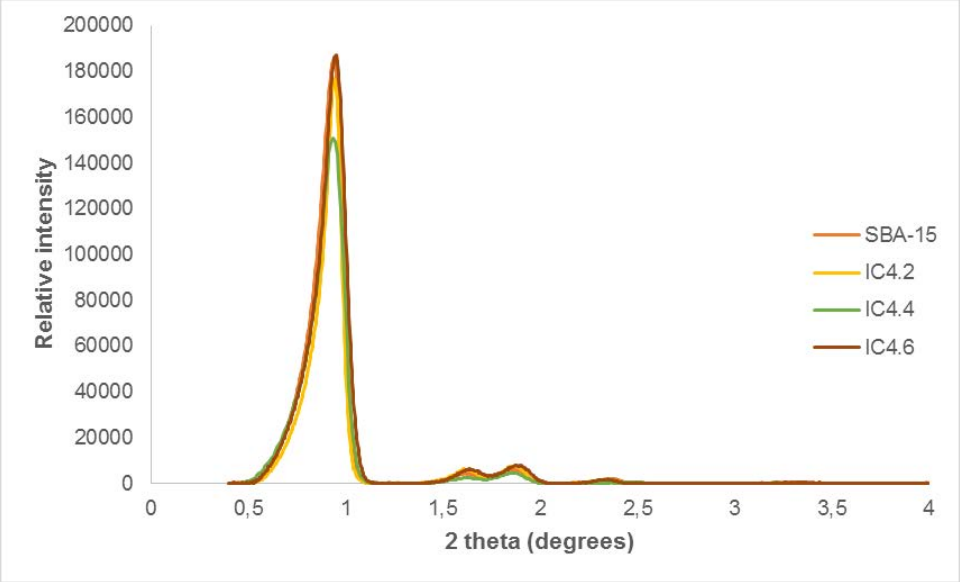

Figure 4.22 Powder XRD plots for SBA-15 immobilized catalysts IC4.2, IC4.4 and IC4.6.

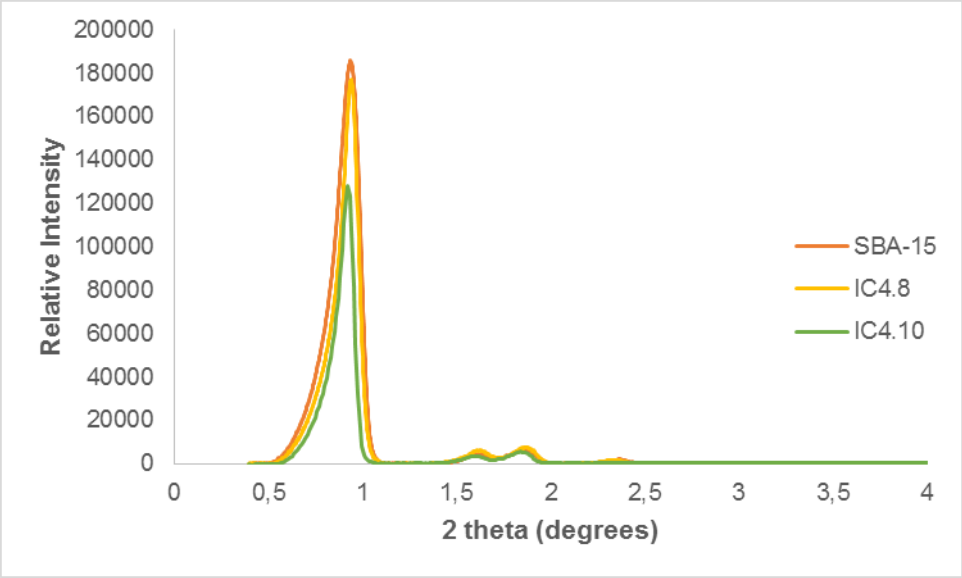

Figure 4.23 Powder XRD plots for SBA-15 immobilized catalysts IC4.8 and IC4.10.

4.2.2.1.3 Characterization of immobilized catalysts IC4.1-4.10 by means of BET (Brunauer Emmett Teller) surface analysis

Type IV isotherms were obtained for all immobilized catalysts, as is expected for mesoporous materials with cylindrical channels. The hysteresis loops are more pronounced for the catalysts immobilized onto SBA-15 than those immobilized onto MCM-41. This was also the case for the native supports. The isotherms of the immobilized catalysts **IC4.1** – **IC4.10** as well as the native supports are shown in Figure 4.24 to 4.27. The volume of nitrogen adsorbed onto the surface of the immobilized catalysts is less that what is adsorbed onto the native silica

supports. This can be attributed to the fact that the immobilized complexes occupy some space on the surface of the supports.

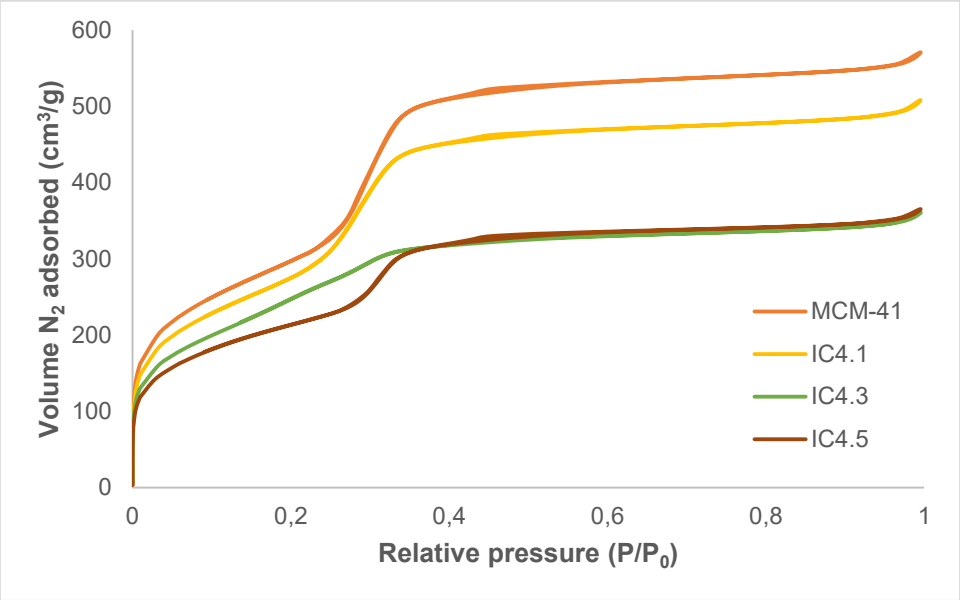

Figure 4.24 Isotherm plots for MCM-41 immobilized catalysts IC4.1, IC4.3 and IC4.5.

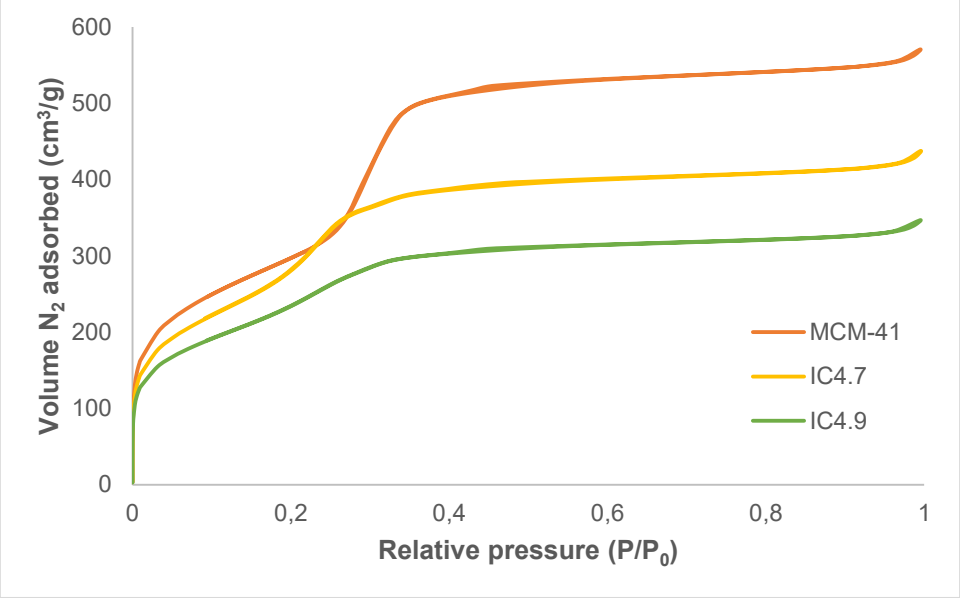

Figure 4.25 Isotherm plots for MCM-41 immobilized catalysts IC4.7 and IC4.9.

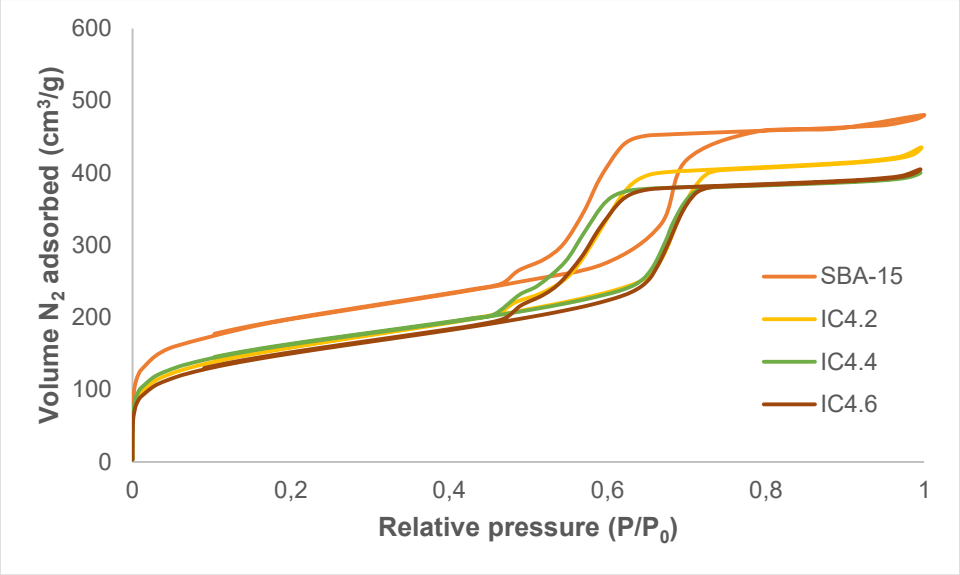

Figure 4.26 Isotherm plots for SBA-15 immobilized catalysts IC4.2, IC4.4 and IC4.6.

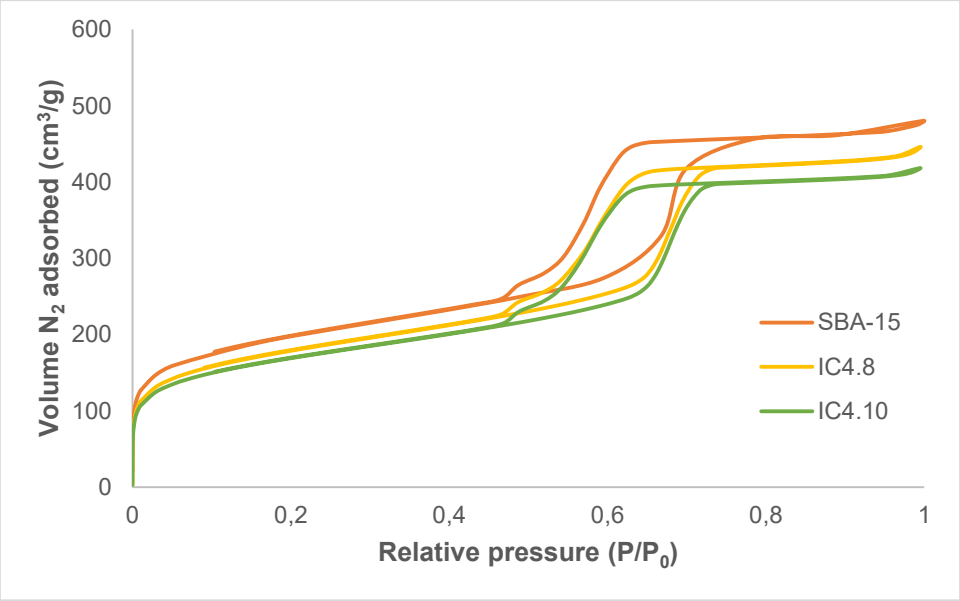

Figure 4.27 Isotherm plots for SBA-15 immobilized catalysts IC4.8 and IC4.10.

The surface areas, pore sizes and pore volumes of the immobilized catalysts are summarized in Table 4.3. The loss in BET surface area is quite varied in the case of MCM-41, ranging from 58.76 m^2/g for **IC4.1** to 342.93 m^2/g for **IC4.5**. This gives a rough indication of the amount of complex immobilized onto the support surface, although analysis with ICP-OES was used to obtain a more accurate measurement (p 122). In the case of SBA-15 the difference in surface area between the native and immobilized catalyst ranges from a difference of 55.75 m^2/g for **IC4.8** to 161.15 m^2/g in the case of **IC4.6**. The difference in surface area is generally larger for MCM-41 compared to SBA-15.

The average pore diameter, as well as the total pore volume, decreases for all the immobilized catalysts, with the exception of **IC4.3** which shows a slight increase in the average pore diameter. The decrease in pore volume is to be expected after immobilization of the siloxane functionalized complexes onto the silica, and suggests that some of the complex was immobilized inside or at the entrance of the pores of the support.

Table 4.3 Summary of BET nitrogen adsorption/desorption results for immobilized catalysts IC4.1 to IC4.10.

Material	Adsorption/Desorption Measurements		
	BET surface area (m^2/g)	Average pore diameter (Å)	Total pore volume (cm^3/g)
MCM-41	1100.66	24.33	0.74
IC4.1	1041.90	23.64	0.65
IC4.3	932.86	26.61	0.56
IC4.5	757.73	23.68	0.44
IC4.7	1038.20	21.15	0.54
IC4.9	899.38	23.90	0.53
SBA-15	702.61	58.24	0.77
IC4.2	570.25	56.80	0.60
IC4.4	580.20	55.45	0.46
IC4.6	541.46	54.62	0.56
IC4.8	646.86	55.22	0.59
IC4.10	599.95	55.64	0.54

4.2.2.1.4 Characterization of immobilized catalysts IC4.1-4.10 by means of inductively-coupled plasma optical emission spectroscopy (ICP-OES)

ICP-OES was used to determine the amount of rhodium present in each immobilized catalyst. To analyse the samples, a certain mass (0.035 g – 0.040 g) of each catalyst was digested in aqua regia at high temperature. The experimentally determined loading is generally quite low, ranging between 10% and 46% of the expected loading. This could be due to the low solubility of some of the complexes in toluene, the solvent employed during the immobilization process. It should be noted that full recovery of rhodium is often not attained after digestion in aqua regia.

Table 4.4 Rhodium loading of immobilized catalysts IC4.1 to IC4.10 as determined by ICP-OES.

Material	Theoretical loading (wt%)[a]	Actual loading (wt%)
IC4.1 (NP-CO-MCM)	1.56	0.53
IC4.3 (NP-cod-MCM)	1.01	0.29
IC4.5 (NO-cod-MCM)	1.92	0.31
IC4.7 (NN-cod-MCM)	1.22	0.37
IC4.9 (NN-tri-MCM)	1.17	0.17
IC4.2 (NP-CO-SBA)	1.56	0.72
IC4.4 (NP-cod-SBA)	1.01	0.34
IC4.6 (NO-cod-SBA)	1.92	0.67
IC4.8 (NN-cod-SBA)	1.22	0.43
IC4.10 (NN-tri-SBA)	1.17	0.20

[a] mg Rh per 100 mg silica

4.2.2.1.5 Characterization of immobilized catalysts IC4.1-4.10 by means of microscopic studies (SEM and TEM)

Figures 4.28 and 4.29 shows the scanning electron micrographs of the immobilized catalysts **IC4.1** to **IC4.10**. There are no significant changes in the physical appearance of the silica after immobilization, with the MCM-41 still showing flat, roughly hexagonal structures and the SBA-15 particles appearing as agglomerated rod-like shapes.

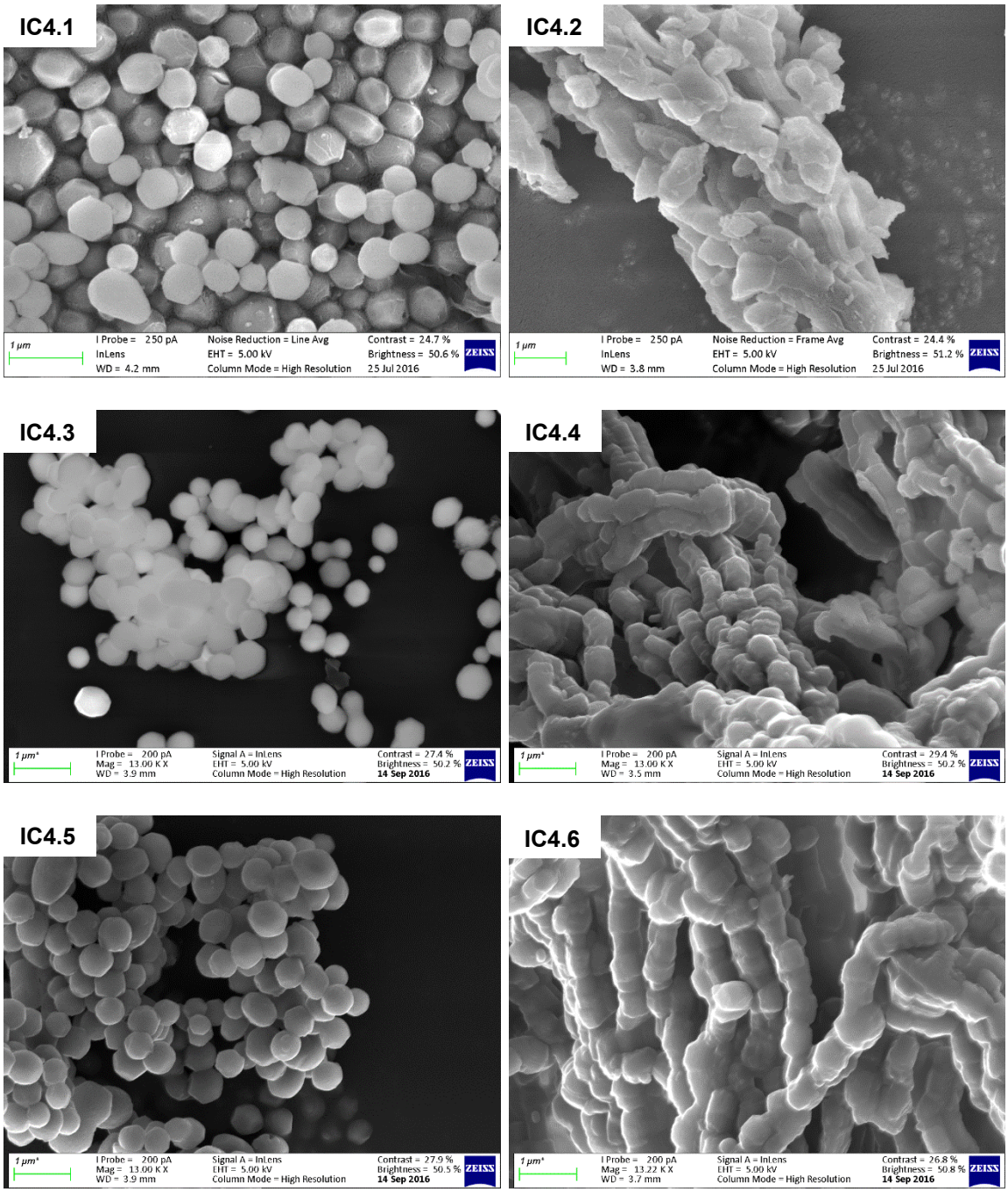

Figure 4.28 SEM micrographs of MCM-41 (left) and SBA-15 (right) immobilized catalysts.

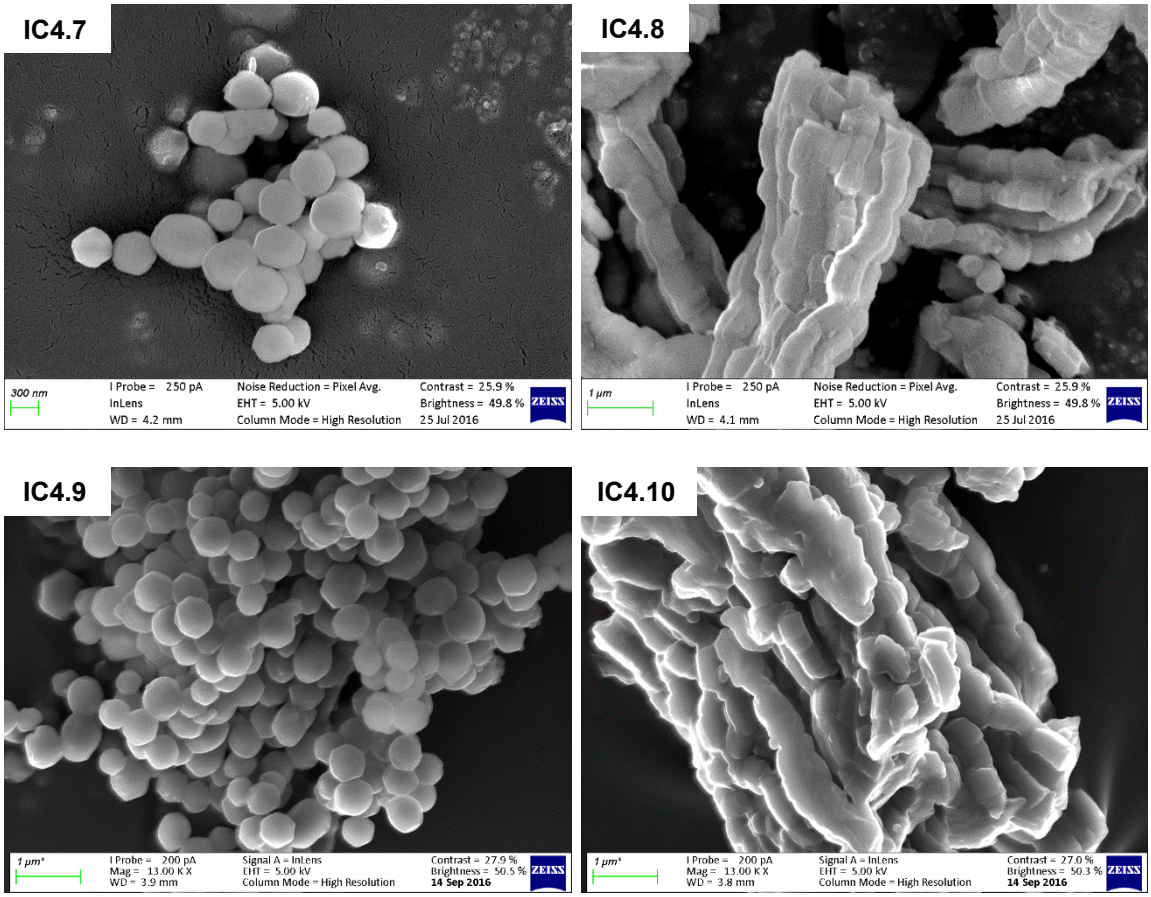

Figure 4.29 SEM micrographs of MCM-41 (left) and SBA-15 (right) immobilized catalysts.

The transmission electron micrographs of the immobilized catalysts are shown in Figures 4.30 and 4.31. No difference is observed in the micrographs after immobilization. The regular pore structure is still visible for both MCM-41 and SBA-15. The image for **IC4.8** shows a top-down view of the pores through the silica.

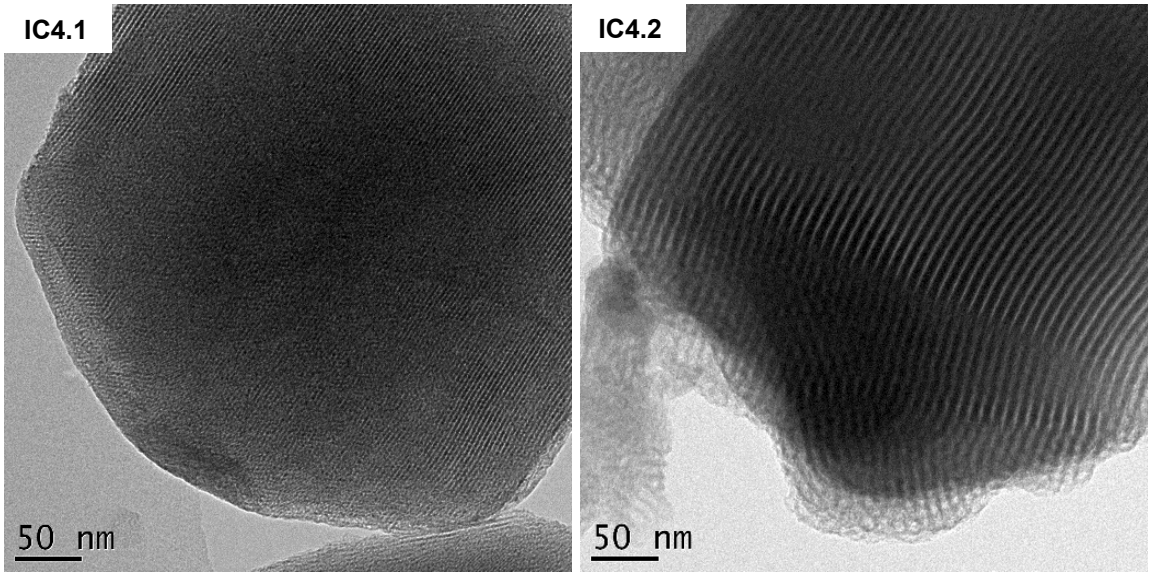

Figure 4.30 TEM micrographs of MCM-41 (left) and SBA-15 (right) immobilized catalysts.

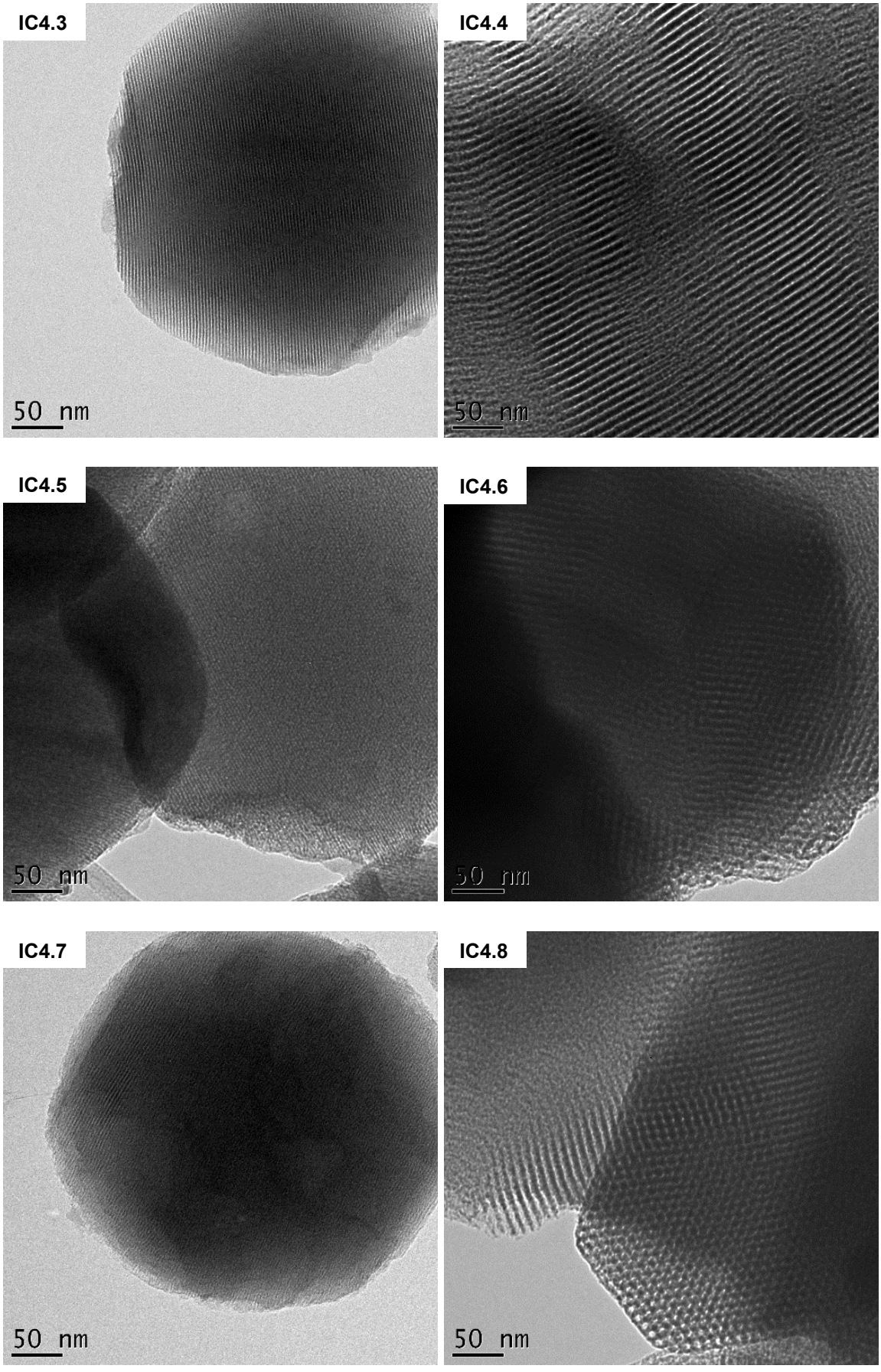

Figure 4.31 TEM micrographs of MCM-41 (left) and SBA-15 (right) immobilized catalysts.

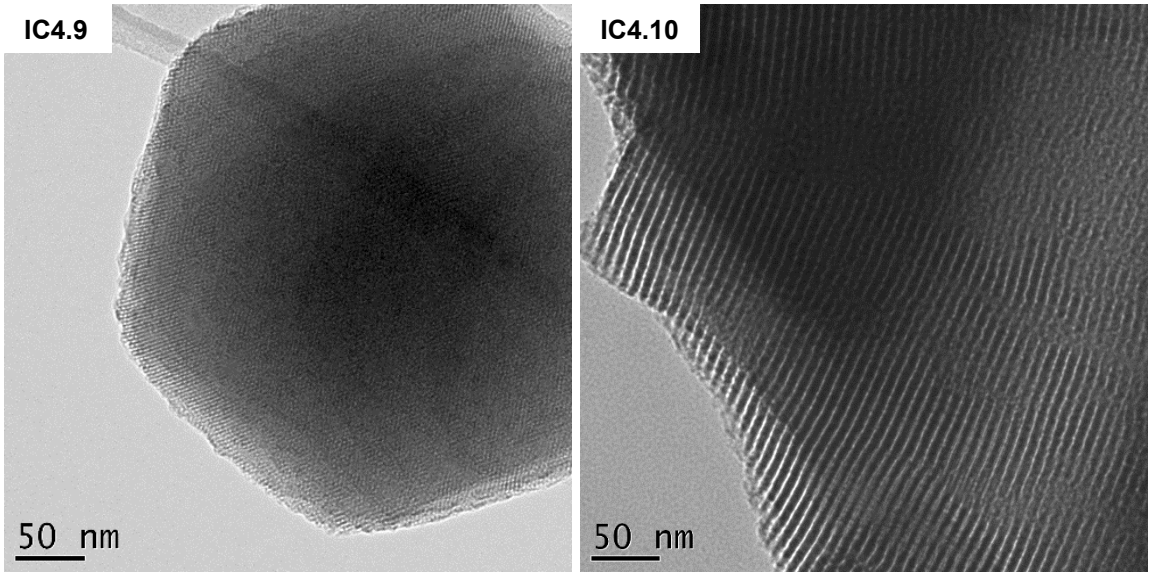

Figure 4.32 TEM micrographs of MCM-41 (left) and SBA-15 (right) immobilized catalysts.

SEM-EDS shows the presence of rhodium on the supports after immobilization. This method can however only give an indication of the rhodium on the surface of the support. Furthermore, the method can only analyse certain regions of the catalyst surface and does not give an indication of the overall composition. This, combined with the fact that the loading of complex on silica is only 10 weight %, means that we do not expect to see a large rhodium peak for the immobilized catalysts. The EDS spectra of native MCM-41 (Figure 4.33) and **IC4.5** (Figure 4.34) are compared below.

In the spectrum of the native MCM-41, carbon, nickel and copper is detected due to the Ni-Cu grid with a carbon film used to support the samples during microscopy, and silicon and oxygen is seen due to the silica.

In the EDS spectrum of **IC4.5**, the previously seen peaks are again observed. Additionally, two small peaks indicating the presence of rhodium can be seen at roughly 2.6 keV and 20.5 keV. As previously stated, we do not expected to see a large amount of rhodium using this method, since only a certain point on the surface of the catalyst is analysed.

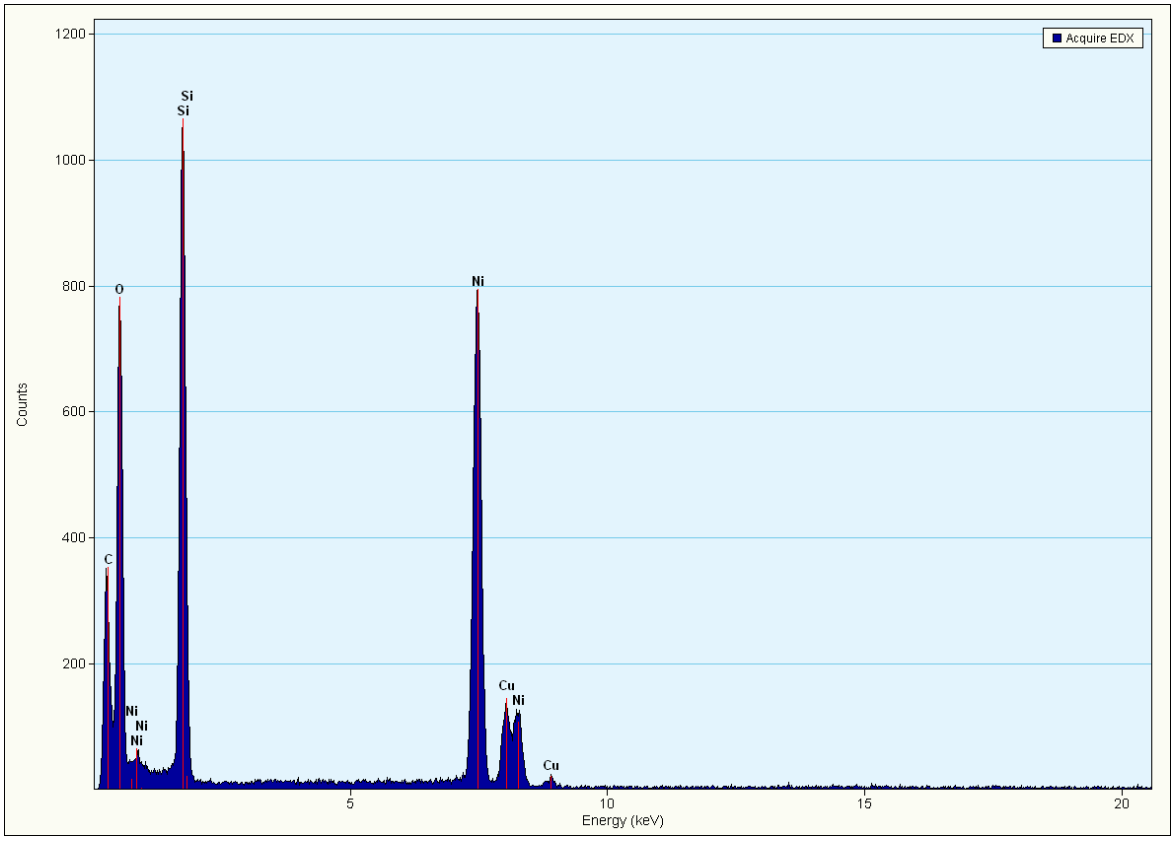

Figure 4.33 EDS spectrum of MCM-41.

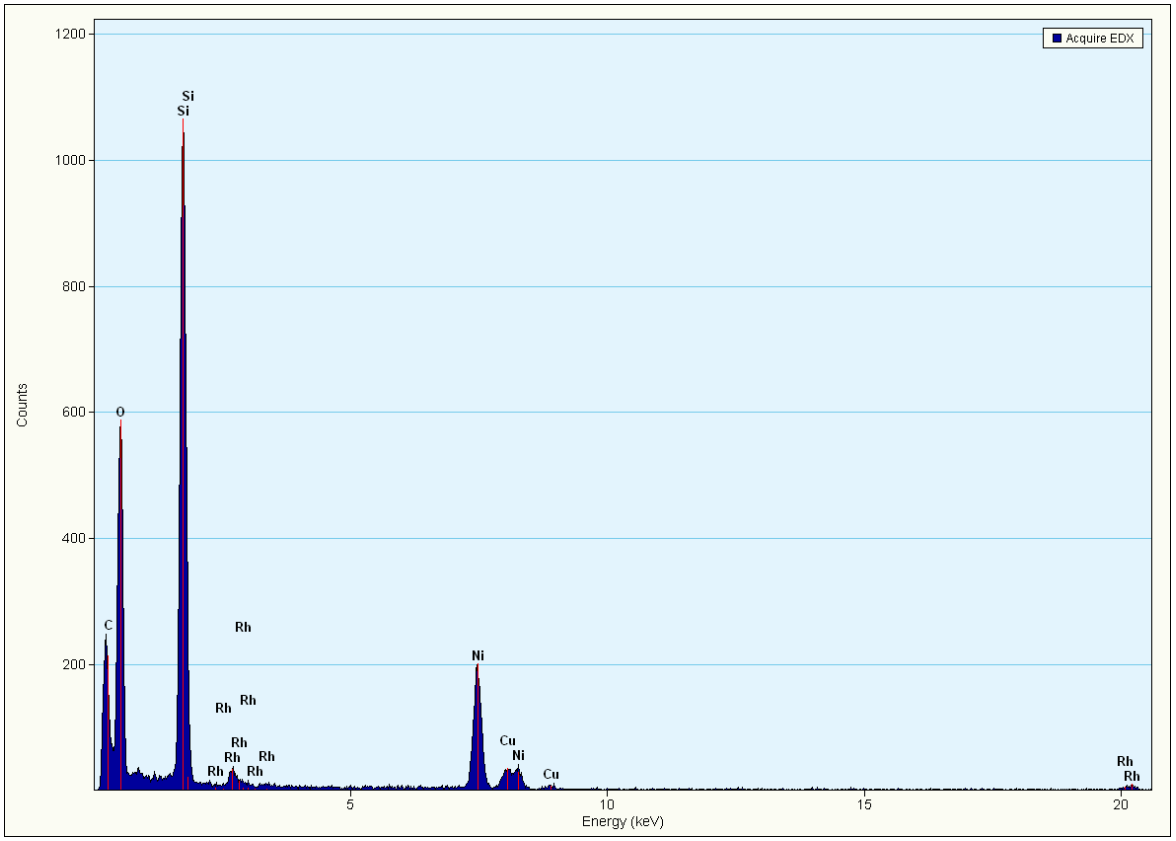

Figure 4.34 EDS spectrum of IC4.5 showing the presence of rhodium.

4.2.2.1.6 Characterization of immobilized catalysts IC4.1-4.10 by means of thermal gravimetric analysis

TGA plots of selected immobilized catalysts compared with the native supports are shown in Figure 4.35 and Figure 4.36. Both the native supports and the immobilized catalyst show an initial weight loss at a temperature below 100°C. This loss was attributed to a loss of absorbed atmospheric moisture, since silica is known to absorb water very easily.

For the immobilized catalysts, a gradual weight loss is seen between 100°C and 300°C, with a steeper weight loss curve starting around 300°C. This is attributed to the decomposition of the organic part of the immobilized complexes. The % weight loss between 100°C and 600°C is around 5% for the immobilized catalysts (after the weight loss of the native supports over the same temperature range were taken into account). Since the loading of the complex on the silica is 10 weight %, one would intuitively expect a loss of 10 weight %, however, the metal in the complex is most likely oxidized to rhodium oxide which is not volatile and should be entrenched in the pores of the support unlike the organic framework of the immobilized complexes. The rhodium could also be reduced to rhodium metal which would remain on the support.

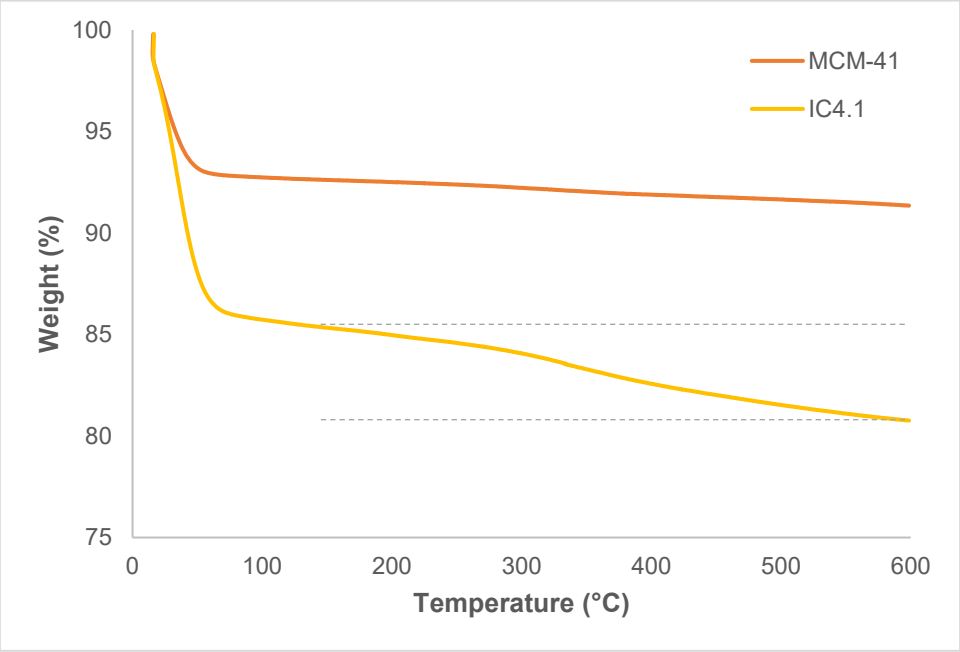

Figure 4.35 Thermal gravimetric analysis plot for MCM-41 and IC4.1.

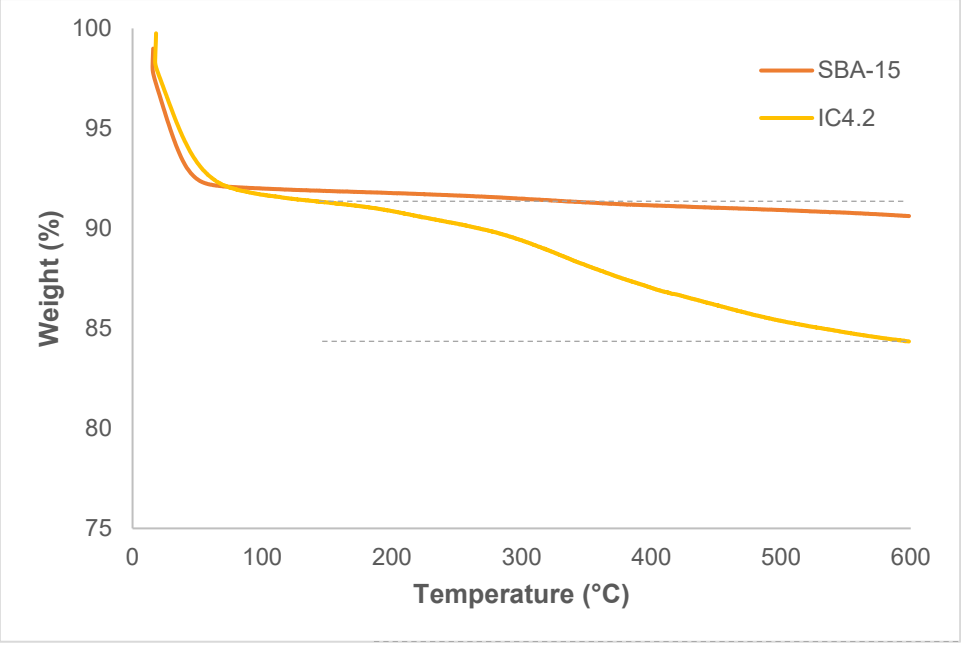

Figure 4.36 Thermal gravimetric analysis plot for SBA-15 and IC4.2.

4.2.2.1.7 Characterization of immobilized catalysts IC4.1-4.10 by means of solid-state NMR spectroscopy

The native supports, MCM-41 and SBA-15, as well as some selected immobilized catalysts were analyzed by means of solid-state ^{29}Si MAS NMR spectroscopy. This technique gives insight into the environment of the silicon nuclei in the material. Through deconvolution of the spectra, peaks at -90 ppm, -100 ppm and -110 ppm could be identified. These peaks were assigned to silicon nuclei with different numbers of O-Si bonds to each nucleus, termed Q^2 $[(SiO)_2(SiOH)_2]$, Q^3 $[(SiO)_3SiOH]$ and Q^4 $[(SiO)_4]$.[21,22] The environment of the silicon nuclei are illustrated in Figure 4.37.

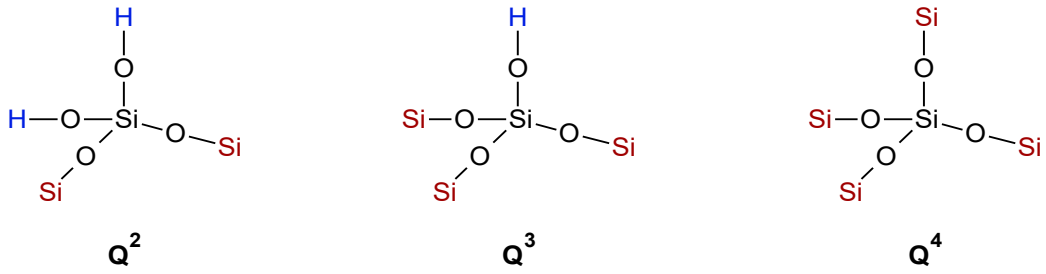

Figure 4.37 Q^2, Q^3 and Q^4 silicon nuclei.

The *Global Spectral Deconvolution* tool from MestReNova was used to deconvolute the silica spectra. From these spectra, the relative abundance of Q^2, Q^3 and Q^4 sites can be obtained. The spectra for native MCM-41 and SBA-15 are shown in Figure 4.38 and Figure 4.39.

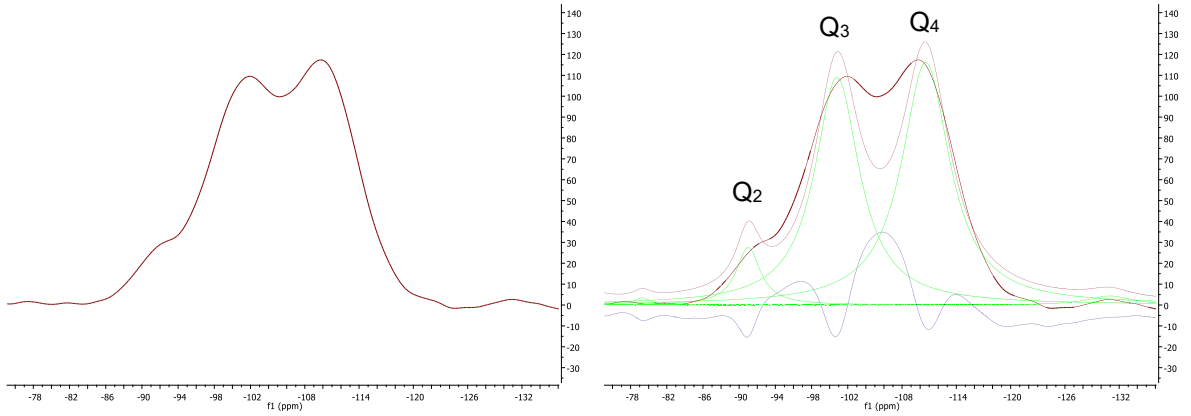

Figure 4.38 Solid-state ^{29}Si single-pulse MAS NMR spectra of MCM-41: experimental (left) and deconvoluted (right).

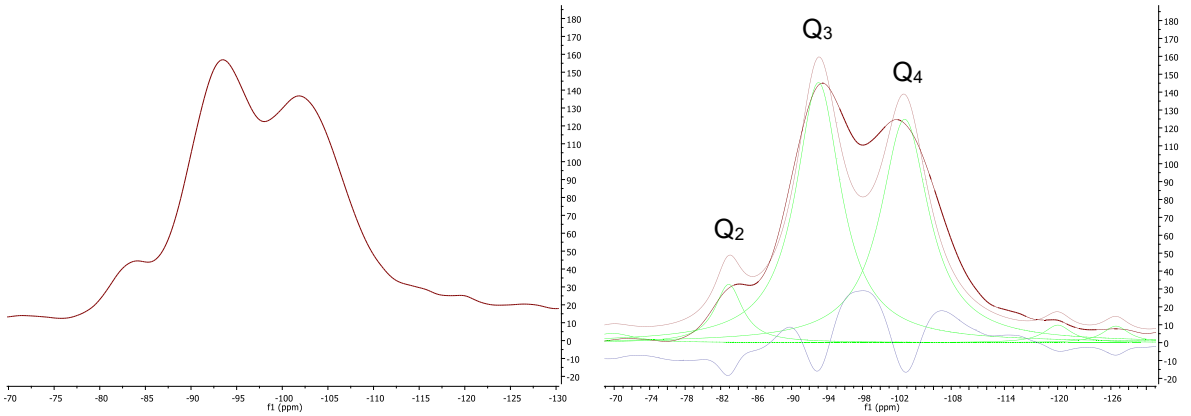

Figure 4.39 Solid-state ^{29}Si single-pulse MAS NMR spectra of SBA-15: experimental (left) and deconvoluted (right).

For both MCM-41 and SBA-15 the Q^3 and Q^4 sites are fairly equal while only a small number of Q^2 sites are observed (6% and 7% for MCM-41 and SBA-15 respectively). 49% of the silicon nuclei in SBA-15 are Q^3 sites, while this number is 44% for MCM-41. It should be noted that there is a quite a large degree of uncertainty (up to 5%) in these numbers due to the use of deconvolution techniques.

Selected samples were also analyzed after immobilization. A decrease in the amount of Q^3 sites is expected, due to the free silanol groups on the silica surface being used to anchor the functionalized complexes. The deconvoluted spectra for **IC4.9** and **IC4.10** are shown in Figure 4.40.

A decrease in the Q^3 sites is indeed observed for both **IC4.9** and **IC4.10**. The effect is more dramatic for the SBA-15 immobilized catalyst **IC4.10**, with the percentage of Q^3 sites decreasing from 49% to 39% after immobilization. For MCM-41 a slight decrease is observed, from 44% to 40%. However, taking into account the degree of error, the decrease in the Q^3 sites for MCM-41 is thus not significant. From the ICP results we observe that the SBA-15

immobilized catalysts generally have a higher rhodium loading than the MCM-41 immobilized catalysts. This may be attributed to the higher percentage of Q^3 sites available on the SBA-15 support.

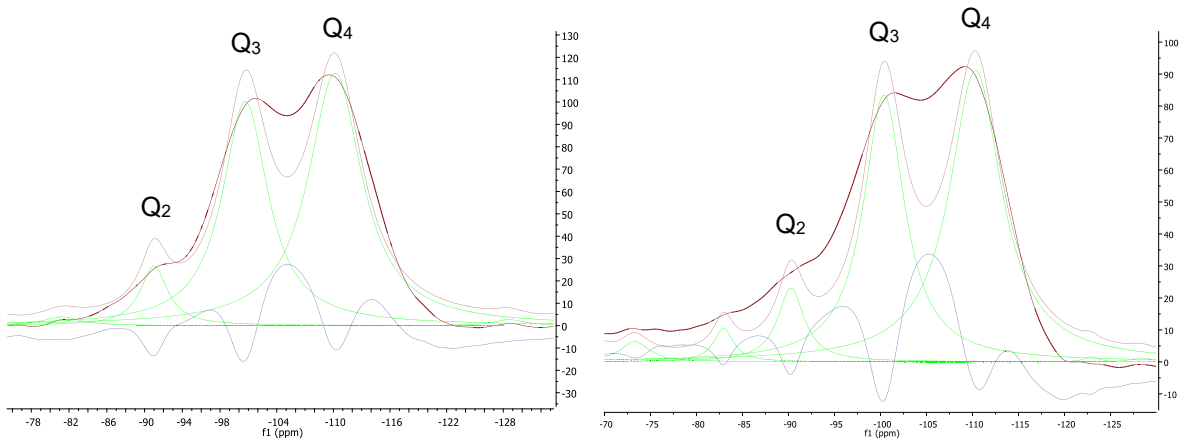

Figure 4.40 Solid-state ^{29}Si single-pulse MAS NMR spectra of MCM-41 and SBA-15 immobilized catalysts IC4.9 (left) and IC4.10 (right).

The decrease in Q^3 sites (and related increase in Q^4 sites) indicate that **IC4.10** has a lower proportion silanol groups when compared to the native support SBA-15. This is an indication that immobilization had taken place. The technique is unfortunately not sensitive enough to give conclusive information on the decrease of Q^3 sites and thus the immobilization for **IC4.9**. A summary of the changes in the silica framework for MCM-41 and SBA-15 and the analogous immobilized catalysts is shown in Table 4.5.

Table 4.5 Summary of the obtained Q^2, Q^3 and Q^4 sites in native silica and immobilized catalysts.

Material	Silica framework		
	Q^2 (%)	Q^3 (%)	Q^4 (%)
MCM-41	6	44	50
IC4.9	7	40	53
SBA-15	7	49	44
IC4.10	7	39	54

4.3 Concluding Remarks

Two types of mesoporous silica, MCM-41 and SBA-15 were synthesized according to literature procedures. The silica supports were characterized using FT-IR, powder X-ray diffraction, BET surface analysis, SEM, TEM and TGA. The powder X-ray diffraction and BET analyses results were compared to literature results to confirm that the syntheses resulted in the particular type of silica (MCM-41 and SBA-15) that was aimed for. The mesoporous silica supports exhibited high surface areas, with 1100 m^2/g and 703 m^2/g obtained for MCM-41 and SBA-15 respectively. The formation of mesopores was confirmed by the powder X-ray diffraction, BET and TEM analyses.

The five siloxane functionalized complexes synthesized in Chapter 2 were immobilized onto the mesoporous silica supports MCM-41 and SBA-15 to afford ten immobilized catalysts **IC4.1** – **IC4.10**. This was done by dissolving each complex in an appropriate high boiling point solvent and adding the solutions to a slurry of either MCM-41 or SBA-15 in the same solvent. After filtration, the silica was washed with hot solvent in an attempt to remove any unreacted siloxane functionalized complex. ICP-OES analysis of the filtrate at this stage could have given an indication of the presence of unreacted complex.

The immobilized catalysts were subjected to the same analyses as the native silica supports, with the addition of EDS, ICP-OES and solid-state ^{29}Si analysis. The immobilization was confirmed by monitoring the change in surface area by BET analysis. The BET analysis together with powder XRD analysis also gave a good indication of the pore structure of the catalysts before and after immobilization. TEM-EDS was used to confirm the presence of rhodium in the immobilized catalyst **IC4.5** – however this technique could not give information on the amount of rhodium present in the immobilized catalysts. ICP-OES was used to estimate the amount of rhodium present in the samples. This information will be used to compare the homogeneous and immobilized catalyst systems during catalytic investigations. Solid-state ^{29}Si NMR was used to investigate the change in Q^3 and Q^4 silica sites between the native silica and immobilized catalyst. Unfortunately, due to the low loading of catalyst and the relatively low sensitivity of the technique, the information obtained with this technique was not as valuable as expected.

4.4 Experimental Section

4.4.1 General remarks and instrumentation

Fourier transfer infrared (FT-IR) spectra were recorded using an ATR accessory on a Nicolet Avatar 330 FT-IR spectrometer. Solid-state NMR spectra were recorded on an Agilent VNMRS 500 MHz wide bore solid state NMR spectrometer using a 4.0 mm HX MAS {^{15}N-^{31}P} broadband probe. Powder X-ray diffraction was done using a Bruker D8 Advance

diffractometer fitted with a LynxEye detector. Nitrogen adsorption measurements were done using a Micromeritics 3Flex Surface Characterization instrument.

Scanning electron microscopy imaging of the samples was accomplished using a Zeiss MERLIN Field Emission Scanning Electron Microscope in conjunction with Zeiss SmartSEM software. Prior to imaging, the samples were mounted on a stub with double sided carbon tape. The samples were then coated with gold to make the samples electrically conductive. The images were collected using a Zeiss SE1 (inLens) detector with a 5kV beam. Transmission electron micrographs were collected using an FEI Tecnai G2 20 field-emission gun TEM, operated in bright field mode at an accelerating voltage of 200 kV. The samples were prepared by sonicating a small amount of the sample in ethanol and placing a drop of the liquid on a carbon-coated nickel-copper grid.

Energy dispersive x-ray spectra were collected using an EDAX liquid nitrogen cooled lithium doped silicon detector. Rhodium content of the immobilized catalysts was determined using a Thermo ICap 6200 ICP-AES. The instrument was calibrated using NIST traceable standards purchased from Inorganic Ventures to quantify selected elements. A NIST-traceable quality control standard from De Bruyn Spectroscopic Solutions was analysed to verify the accuracy of the calibration before sample analysis, as well as throughout the analysis to monitor drift. TGA analysis was performed on a Perkin Elmer TGA 7 instrument.

4.4.2 Materials

Reagents were purchased from Sigma-Aldrich and Merck and used as received. These include cetyltrimethylammonium bromide (CTAB), tetraethylorthosilicate (TEOS) and poly(ethylene)-*block*-poly(propylene)-*block*-poly(ethylene). Solvents were purchased from Sigma-Aldrich and Kimix Chemicals and were dried in Pure Solv^{TM} Micro solvent purification systems fitted with activated alumina columns.

4.4.3 Synthesis of solid silica supports MCM-41 and SBA-15

4.4.3.1 Synthesis of MCM-41

Cetyltrimethylammonium bromide (CTAB) (3.996 g) was added to a solution of ammonia (410 mL, 25% w/v) and distilled water (540 mL). The solution was heated to 50°C whilst stirring. After the CTAB had completely dissolved, tetraethylorthosilicate (20 mL) was added. A white slurry formed roughly 5 minutes after the addition of the tetraethylorthosilicate and the mixture was stirred for a further 2 hours at 50°C. The mixture was then left to cool to room temperature and subsequently filtered and washed with 1100 mL of distilled water. The obtained white solid was left to dry overnight. The solid was then calcined at 550°C (temperature slowly increased) for 8 hours.

Yield: 3.820 g

4.4.3.2 Synthesis of SBA-15

Poly(ethylene)-*block*-poly(propylene)-*block*-poly(ethylene) (8.050 g) was added to a solution of HCl (360 mL, 2M) and distilled water (60 mL). The solution was heated to 35°C and was stirred until the surfactant had dissolved completely. TEOS (18.2 mL) was added to the solution. A white slurry formed roughly 10 minutes after the addition of the silica source and the mixture was stirred at 35°C for 20 hours. The temperature was then increased to 80°C and the mixture was left to age without stirring for 24 hours. The mixture was left to cool to room temperature and subsequently filtered and washed with 1000 mL of distilled water. The obtained white solid was left to dry overnight. The solid was then calcined at 550°C (temperature slowly increased) for 8 hours.

Yield: 5.922 g

4.4.4 Synthesis of immobilized catalysts IC4.1 – IC4.10

4.4.4.1 Synthesis of immobilized catalysts IC4.1 – IC4.6

The appropriate dried silica, MCM-41 or SBA-15 (0.450 g) was suspended in toluene (8 mL) and stirred to yield a slurry. The appropriate complex (0.045 g) was dissolved in toluene (2 mL) and added to the slurry, which changed colour from white to yellow. The reaction was heated to 110°C and stirred under reflux for 24 hours. The reaction was then filtered while hot, and washed with toluene. It was subsequently dried under vacuum to yield a light yellow powder.

4.4.4.2 Synthesis of immobilized catalysts IC4.7 and IC4.8

The appropriate dried silica, MCM-41 or SBA-15 (0.450 g) was suspended in toluene (8 mL) and stirred to yield a slurry. The appropriate complex (0.045 g) was dissolved in THF (2 mL) and added to the slurry, which changed colour from white to yellow. The reaction was heated to 110°C and stirred under reflux for 24 hours. The reaction was then filtered while hot, and washed with THF. It was subsequently dried under vacuum to yield a light yellow powder.

4.4.4.3 Synthesis of immobilized catalysts IC4.9 and IC4.10

The appropriate dried silica, MCM-41 or SBA-15 (0.450 g) was suspended in toluene (8 mL) and stirred to yield a slurry. The appropriate complex (0.045 g) was dissolved in chloroform (2 mL) and added to the slurry, which changed colour from white to yellow. The reaction was heated to 110°C and stirred under reflux for 24 hours. The reaction was then filtered while hot, and washed with chloroform. It was subsequently dried under vacuum to yield a light yellow powder.

4.5 References

1 A. Walcarius and L. Mercier, *J. Mater. Chem.*, 2010, **20**, 4478–4511.

2 J. Lee, S. Han and T. Hyeon, *J. Mater. Chem.*, 2004, **14**, 478–486.

3 J. M. Rosenholm, C. Sahlgren and M. Linden, *Nanoscale*, 2010, **2**, 1870–1883.

4 A. Corma and H. Garcia, *Adv. Synth. Catal.*, 2006, **348**, 1391–1412.

5 V. Meynen, P. Cool and E. F. Vansant, *Microporous Mesoporous Mater.*, 2009, **125**, 170–223.

6 H. Zhang, J. Sun, D. Ma, X. Bao, A. Klein-Hoffmann, G. Weinberg, D. Su and R. Schlögl, *J. Am. Chem. Soc.*, 2004, **126**, 7440–7441.

7 J. S. Beck, J. C. Vartuli, W. J. Roth, M. E. Leonowicz, C. T. Kresge, K. D. Schmitt, C. T.-W. Chu, D. H. Olson, E. W. Sheppard, S. B. McCullen, J. B. Higgins and J. L. Schlenkert, *J. Am. Chem. Soc.*, 1992, **114**, 10834–10843.

8 D. Zhao, J. Feng, Q. Huo, N. Melosh, G. Fredrickson, B. Chmelka and G. Stucky, *Science.*, 1998, **279**, 548–52.

9 J. Pastva, K. Skowerski, S. J. Czarnocki, N. Zilkova, J. Cejka, Z. Bastl and H. Balcar, *ACS Catal.*, 2014, **4**, 3227–3236.

10 H. Veisi, M. Hamelian and S. Hemmati, *J. Mol. Catal. A Chem.*, 2014, **395**, 25–33.

11 Q. Cai, W.-Y. Lin, F.-S. Xiao, W.-Q. Pang, X.-H. Chen and B.-S. Zou, *Microporous Mesoporous Mater.*, 1999, **32**, 1–15.

12 P. Innocenzi, *J. Non. Cryst. Solids*, 2003, **316**, 309–319.

13 S. M. Alahmadi, S. Mohamad and M. J. Maah, *Int. J. Mol. Sci.*, 2012, **13**, 13726–13736.

14 S. D. Kirik, V. A. Parfenov and S. M. Zharkov, *Microporous Mesoporous Mater.*, 2014, **195**, 21–30.

15 K. S. W. Sing, D. H. Everett, R. A. W. Haul, L. Moscou, R. A. Pierotti, J. Rouquerol and T. Siemieniewska, *Pure Appl. Chem.*, 1985, **57**, 603–619.

16 P. L. Llewellyn, Y. Grillet, F. Schuth, H. Reichert and K. K. Unger, *Microporous Mater.*, 1994, **3**, 345–349.

17 V. B. Fenelonov, V. N. Romannikov and A. Y. Derevyankin, *Microporous Mesoporous Mater.*, 1999, **28**, 57–72.

18 Z. Luan, J. A. Fournier, J. B. Wooten and D. E. Miser, *Microporous Mesoporous Mater.*, 2005, **83**, 150–158.

19 M. Hartmann and A. Vinu, *Langmuir*, 2002, **18**, 8010–8016.

20 N. E. Botterhuis, Q. Sun, P. C. M. M. Magusin, R. A. Van Santen and N. A. J. M. Sommerdijk, *Chem. - A Eur. J.*, 2006, **12**, 1448–1456.

21 J. Tre, J. W. Wiench, S. Huh and V. S. Lin, *J. Am. Chem. Soc.*, 2005, **127**, 2023–2030.

CHAPTER 5 : THE HYDROFORMYLATION OF 1-OCTENE

5.1 Introduction

The hydroformylation of alkenes, as discussed in Chapter 1, is an important organic transformation and one of the few examples where homogeneous catalysis is being applied on a relatively large scale in industry. As shown in Scheme 5.1, two main oxygenated products are obtained from the hydroformylation reaction – either the linear aldehyde, or one of various branched aldehydes. If the specific catalyst used has a high reducing ability, alcohols can also be produced. Alternatively, the aldehyde can subsequently be reduced in order to yield the alcohol.

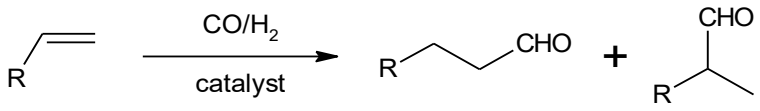

Scheme 5.1 General hydroformylation of alkenes.

In this chapter the use of rhodium complexes (both model and immobilized) as pre-catalysts in the hydroformylation reaction will be discussed, together with an investigation of the possible effects of various parameters on the reaction. In order to gain a better understanding of the process, a brief look at the mechanism of the reaction is necessary.

5.1.1 Catalytic cycle of rhodium-catalyzed hydroformylation

The catalytic cycle of the rhodium-catalyzed hydroformylation of alkenes has been well studied and an overview of the generally accepted mechanism, first proposed by Wilkinson and co-workers, is given below (Scheme 5.2).[1] In the case of Wilkinson's catalyst, the active species is a four-coordinate hydride species (**2**). The vinyl substrate is coordinated to form the π complex (**3**). The alkene is then inserted into the Rh-H bond to give an alkyl-rhodium intermediate (**4a**). It is this step that determines the regioselectivity of the reaction.

The alkyl moiety then migrates onto a CO ligand coordinated to the rhodium *via* migratory "insertion" to yield the acyl-rhodium species (**6**). Subsequently, oxidative addition of hydrogen to the rhodium metal centre takes place, followed by the reductive elimination of the aldehyde product and the regeneration of the rhodium hydride species.[2]

The rate of the reaction can be influenced by a variety of factors, including temperature, pressure and the type of ligands for the rhodium complex employed. Generally, using electron-donating ligands leads to less active catalysts due to a higher degree of back-donation to carbon monoxide which leads to stronger binding of the carbonyl ligands to the rhodium centre.[3,4] This leads to slower formation of species **2** and ultimately **6** in the cycle shown in Scheme 5.2.

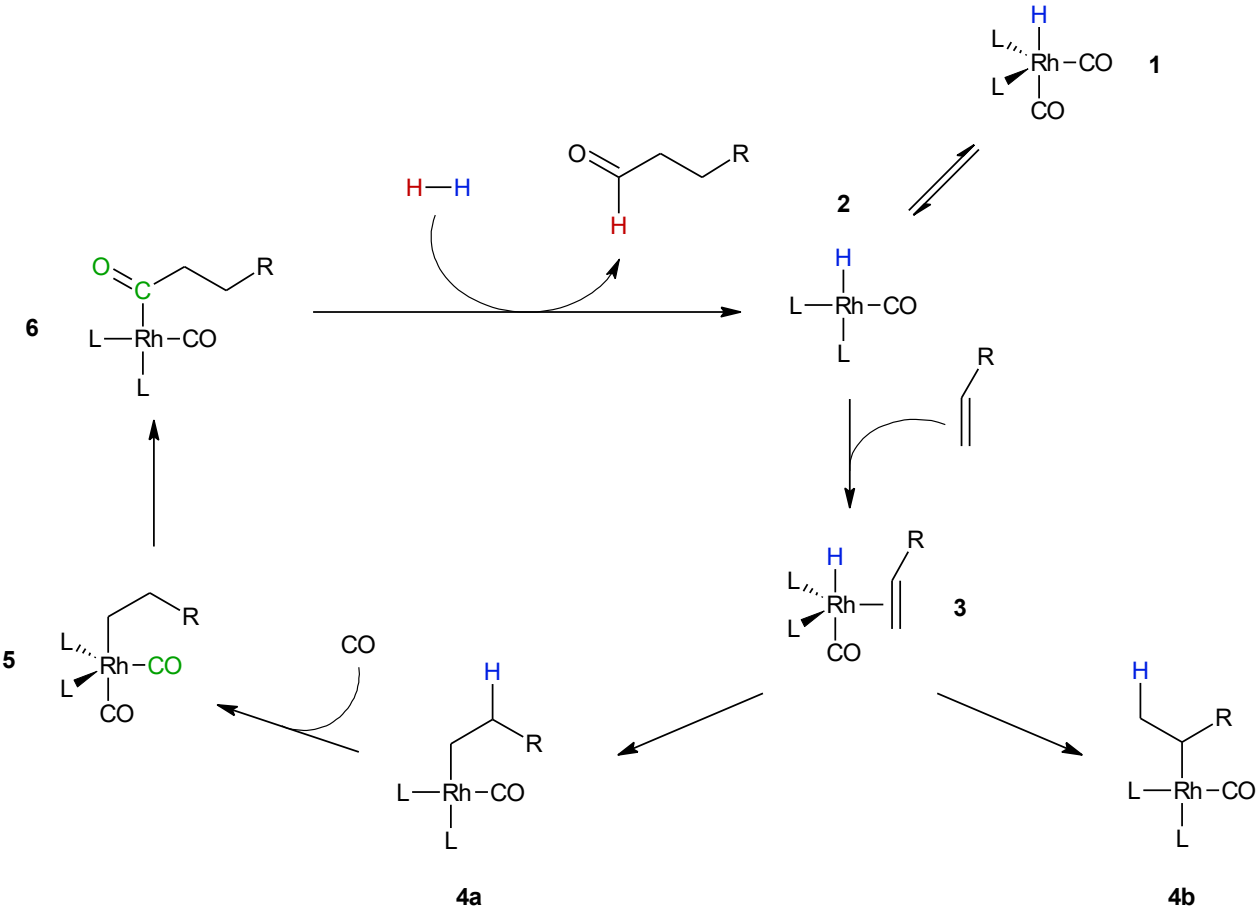

Scheme 5.2 Rhodium-catalyzed hydroformylation reaction.[2] Phosphines or phosphites are typically used as ligands.

There are also unwanted secondary processes that can take place during the reaction, as illustrated by species **4b** above. The branched aldehyde can be formed from this intermediate. The alkyl species can also undergo β-hydride elimination to form internal octene products. These octenes themselves can then undergo hydroformylation and form more branched aldehydes.[5] This isomerisation process is depicted in Scheme 5.3.

When an unmodified rhodium catalyst i.e. a rhodium precursor without ligands is used, the ratio of linear to branched (l:b) aldehydes produced is usually close to 1:1 at full conversion of the substrate (when using an α-olefin as substrate).[6] Ideally, one would want a catalyst that

can selectively produce either the linear or the branched aldehyde, depending on the final application of the hydroformylation product. Process conditions as well as different ligands are employed in order to drive selective formation of a particular product.

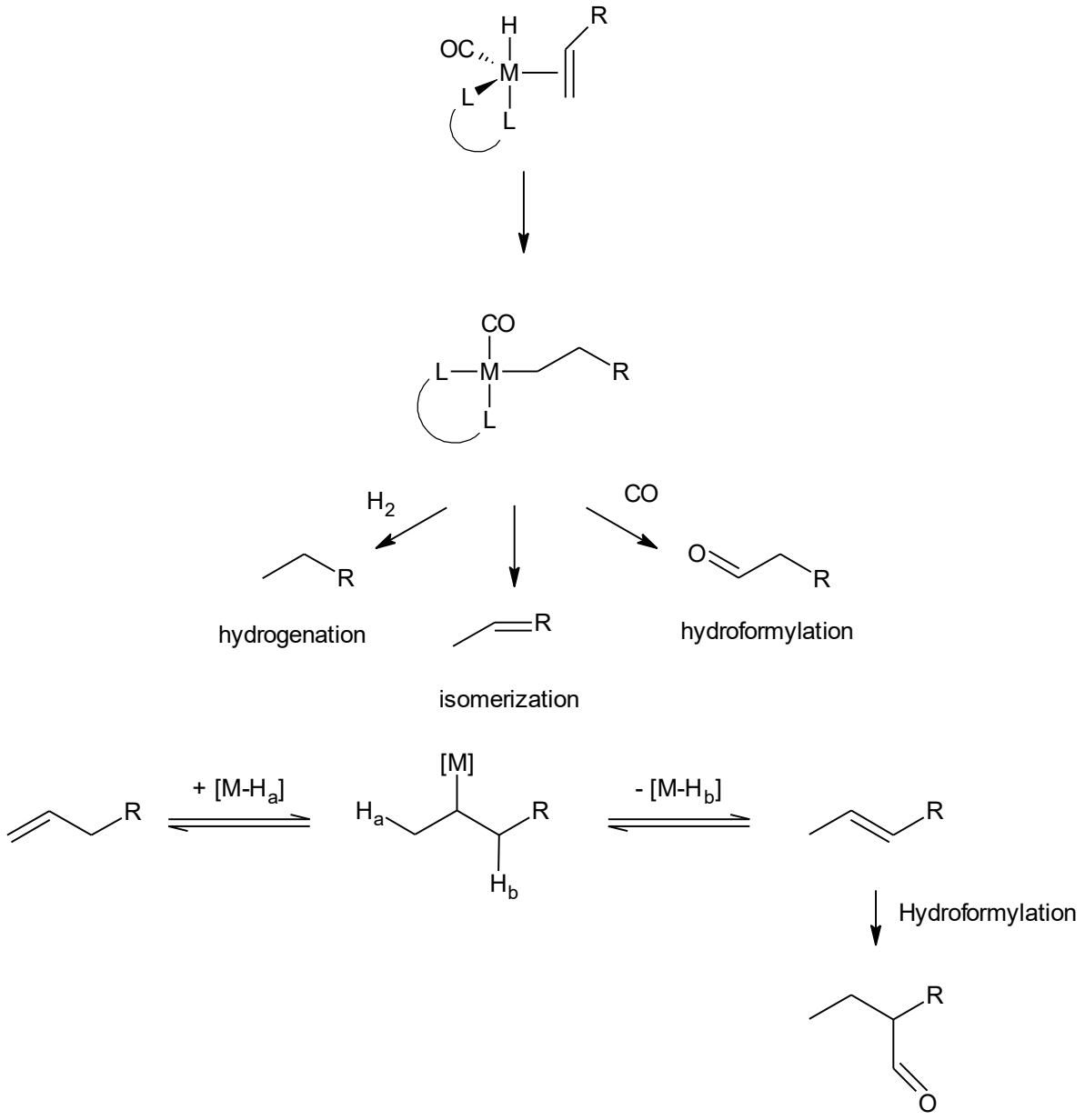

Scheme 5.3 Metal-assisted isomerization of alkenes.

The factors governing the regioselectivity of the hydroformylation reaction are complex and are still not fully understood. A number of steric and electronic ligand effects can play a role in determining the regioselectivity of the formed products. The ligands used in this study differ with regards to donor atoms, steric influences and charge, and we would expect to see variations in the selectivity when using different complexes as pre-catalysts.

Although some ligand systems with N,N chelating donor atoms are reported in literature, there is little known about the mechanism in which these systems play a role.[7–9] In order for hydroformylation to take place, a carbonyl hydride species (similar to **1** in Scheme 5.2) must be formed as active species. In this chapter, we report some preliminary studies on the formation of such species and the possible nature of the active catalyst derived from pre-catalysts based on the N,N chelating systems.

In addition to probing the possible mechanism of these systems in hydroformylation, we also investigated the problem catalyst recovery and reuse. As discussed in Chapter 1, the homogeneous nature of rhodium catalysts in the hydroformylation reaction makes recovery of the valuable rhodium metal difficult. It is envisioned that the silica-immobilized rhodium catalysts could potentially be re-useable, and also facilitate rhodium recovery. The mesoporous nature of the silica supports could also have an effect on the selectivity of the reactions.

5.2 Results and discussion

5.2.1 General procedure for the hydroformylation of 1-octene

The reaction conditions used throughout were modelled on those used by Antonels *et al*.[7] The catalyst (0.0034 mmol) was dissolved in toluene (5 mL) in a 20 mL high-pressure reactor and 1-octene (5 mmol, 0.800 mL) was added to the solution. The amount of catalyst used was therefore 0.07 mole %. The reaction was heated to the required temperature while stirring at 500 rotations per minute, after which it was pressurized with syngas (CO/H_2 ratio 1:1). The reaction was then left to proceed for the allotted time, after which it was cooled to room temperature. The reactor was depressurized and samples were taken for analysis by GC-FID.

In the case of the immobilized catalysts, the solution containing the immobilized catalyst suspended in toluene after the reaction was placed in a centrifuge tube after depressurizing the reactor, and centrifuged for 30 minutes at 4 000 revolutions per minute. With the silica settled in the bottom of the tube, a sample was taken from the mother liquor for analysis. The mother liquor was removed by decantation, and the silica was dried before re-use.

It should be noted that the relative mass of rhodium used as catalyst was kept constant throughout the reactions – in the case of the immobilized catalysts this was established by ICP-OES analysis as discussed in Chapter 4. All reactions were done at least in duplicate, and the reported results represent the average values obtained from two reactions where the results differed by no more than 4%. Error bars indicate the standard deviation from the mean value of the results obtained from two reactions.

The term ‘conversion’ is used throughout to refer to the conversion of 1-octene to all products. ‘Selectivity’ refers to the products formed and is followed by the specific product or products referenced. The term ‘aldehydes’ refers to nonanal, 2-methyloctanal and other branched C9 aldehydes. In our experiments, nonanal and 2-methyloctanal were the main aldehydes detected.

5.2.2 Model complexes C2.1 – C2.5 and immobilized catalysts IC4.1 – IC4.10 employed as catalyst precursors in the hydroformylation of 1-octene

The model complexes and immobilized catalysts used as hydroformylation pre-catalysts are shown in Figure 5.1 and Figure 5.2 respectively.

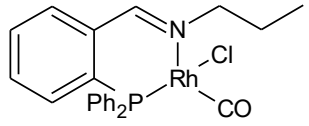

C2.1

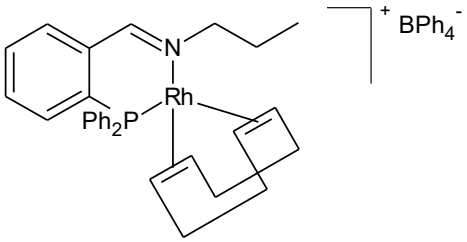

C2.2

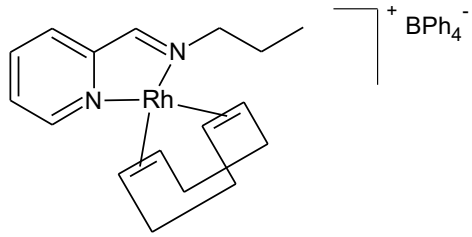

C2.3

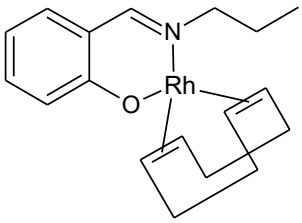

C2.4

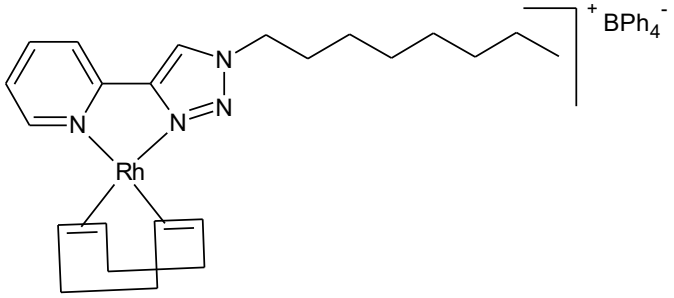

C2.9

Figure 5.1 Model complexes C2.1 - C2.4 and C2.9 used for the hydroformylation reactions.

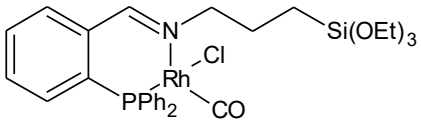

IC4.1: MCM-41
IC4.2: SBA-15

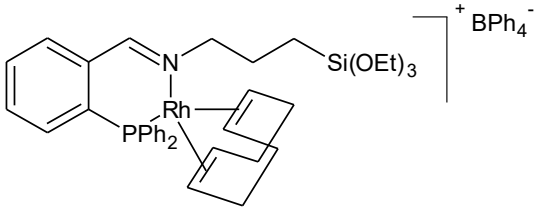

IC4.3: MCM-41
IC4.4: SBA-15

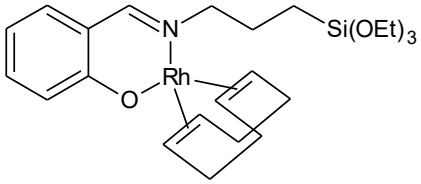

IC4.5: MCM-41
IC4.6: SBA-15

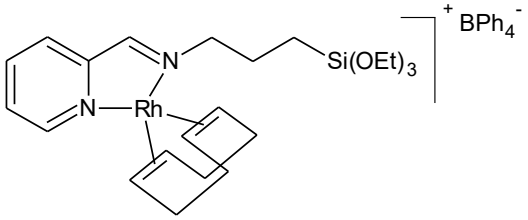

IC4.7: MCM-41
IC4.8: SBA-15

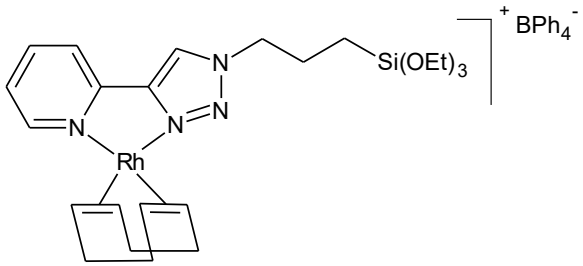

IC4.9: MCM-41
IC4.10: SBA-15

Figure 5.2 Immobilized complexes IC4.1 - IC4.10 used for the hydroformylation reactions.

5.2.3 Establishing baseline catalysis conditions

Various parameters, namely time, temperature and pressure were changed in order to observe how this would affect the reaction in terms of conversion, chemoselectivity and regioselectivity. The model N,N Schiff base complex **C2.3** was used in these initial studies.

5.2.3.1 Effect of time on the hydroformylation of 1-octene

The first parameter that was investigated was the effect of time on the reaction. Because a batch reactor was employed, this investigation was carried out by investigating five different reactions, each conducted over a different period of time, rather than sampling from the same reaction at different time intervals. The results are depicted in Figure 5.3, showing that after one hour, the conversion of 1-octene is already almost 50%. The conversion gradually increases to 84% after eight hours. Between 4 and 8 hours, the increase in conversion is only

about 10%. This could either indicate a drop in activity of the catalyst, or it could be a function of the substrate being consumed.

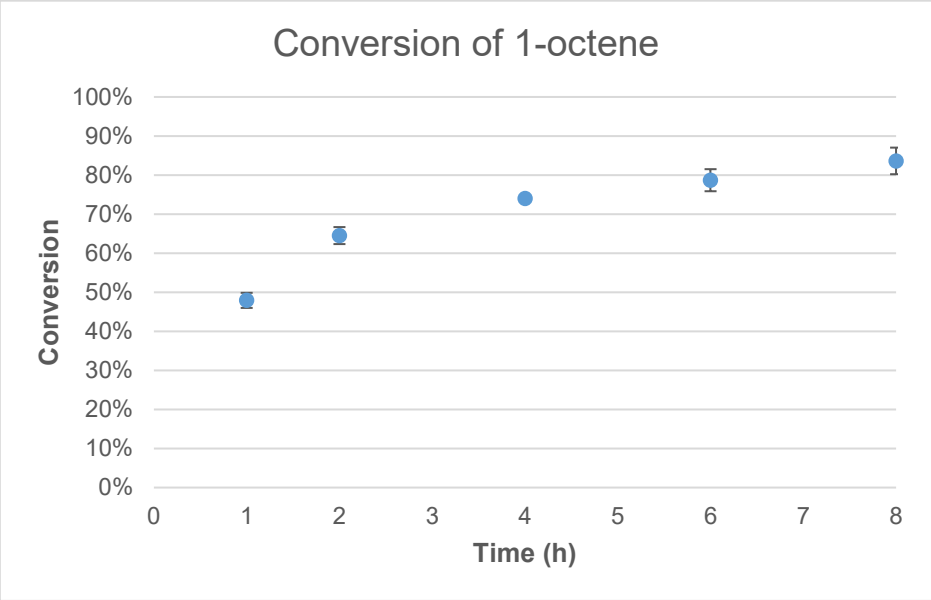

Figure 5.3 Conversion of 1-octene to all products at different time intervals.
Reaction conditions: 0.07 mol% rhodium (**C2.3**), 1-octene (5 mmol), toluene (5 mL), 30 bar syngas ($CO:H_2$ ratio 1:1), 75°C

The turnover frequency (TOF), determined as the mole 1-octene consumed per mole catalyst per hour, is shown in Figure 5.4. At 1 hour, the TOF is almost 700 $mol.mol^{-1}.h^{-1}$. The value decreases over the time period to just over 150 $mol.mol^{-1}.h^{-1}$. Turnover frequency gives a good indication of the behaviour of a catalyst over time. The catalyst used in this reaction shows deactivation over a time period of 8 hours.

The selectivity towards the various products formed, shown in Figure 5.5, indicates an interesting trend. It should be noted that a small amount of octane, the hydrogenation product, was formed in all reactions. Initially, a large portion of the products formed are internal octenes, indicating facile isomerization of the α-olefin during the initial stages of the reaction. During this initial phase it is clear that the rate of isomerization exceeds the rate of hydroformylation as the percentage aldehyde is just over 40% of the product stream after 8 hours.

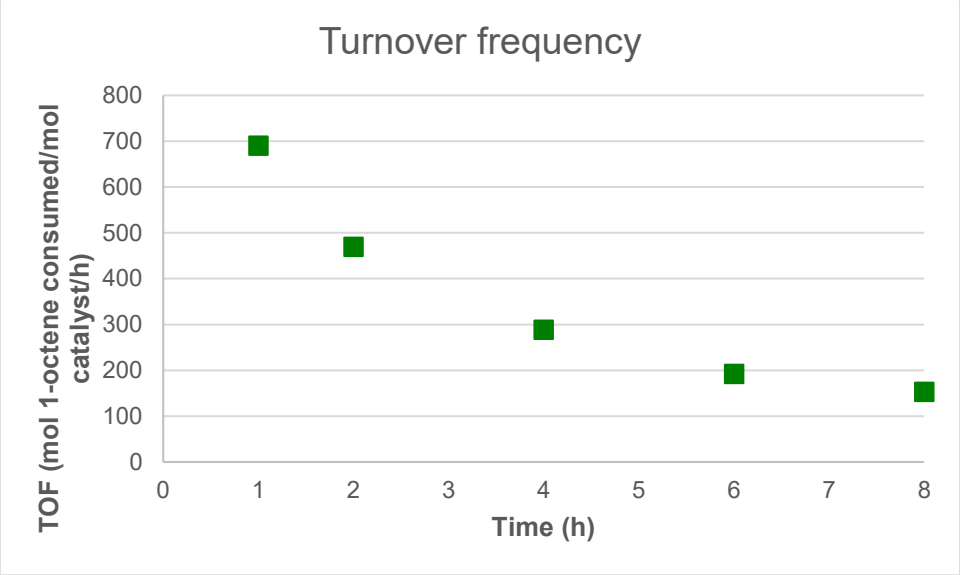

Figure 5.4 Turnover frequency in terms of mol 1-octene consumed per mol catalyst per hour. Reaction conditions: 0.07 mol% rhodium (C2.3), 1-octene (5 mmol), toluene (5 mL), 30 bar syngas (CO:H2 ratio 1:1), 75°C. Turnover defined as mmol 1-octene consumed per mmol rhodium used per hour.

As the reaction proceeds, the amount of internal octenes, formed by isomerization during the initial stages of the reaction, decreases almost linearly with a concomitant increase in the amount of aldehydes. After eight hours, only 13% of the products formed are internal alkenes, while 84% of the products streams are aldehydes. This is in good agreement with the results obtained by Makhubela *et al.* with a similar rhodium complex.[10] These authors report 16% internal octenes and 84% aldehydes under similar reaction conditions.

Along with the decrease in internal octenes, we see a significant increase in the amount of *iso*-aldehydes formed. It is therefore apparent that the *iso*-aldehydes are formed *via* the hydroformylation of these internal octenes. The amount of nonanal formed also increases slightly over time until it makes up about 44% of the formed products.

The *n:iso* ratio is higher at shorter time periods but steadily decreases over time and reaches 1.1:1 after eight hours reaction time. This indicates that the amount of nonanal formed is almost equal to the amount of branched aldehydes obtained. Makhubela *et al*. reported an even lower *n:iso* ratio of 0.7:1 under these conditions. The catalyst is therefore not very selective to the linear product, nonanal, under these conditions – at shorter times, the internal octenes dominate, and at longer times there is an almost equal amount of the branched aldehyde being formed.

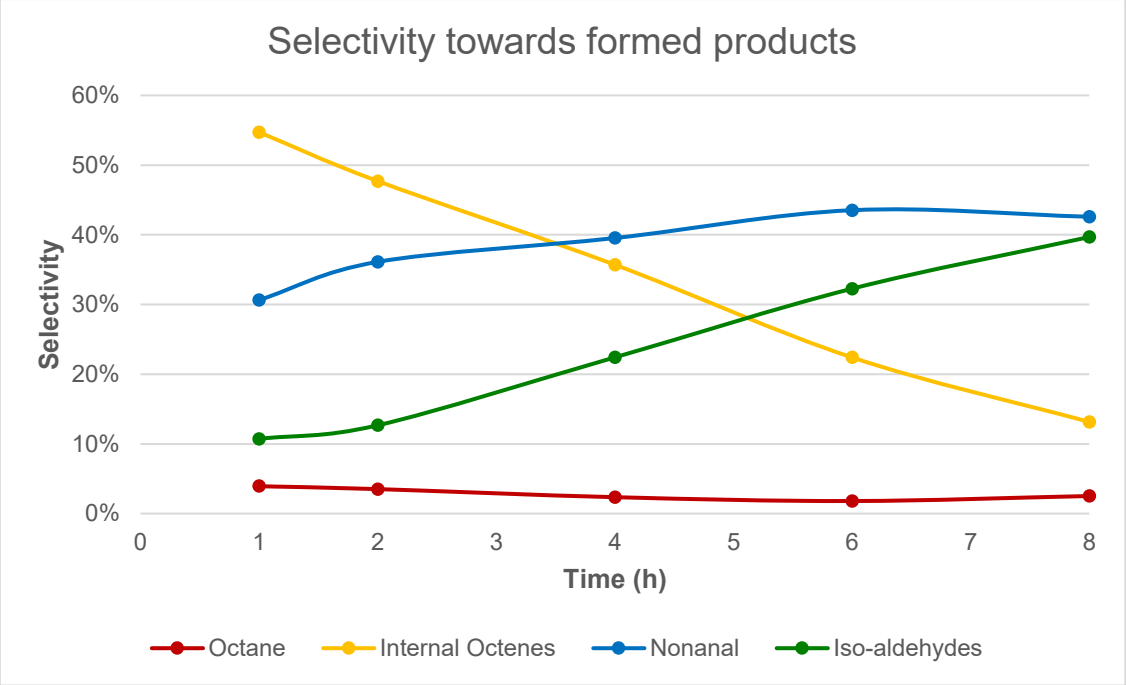

Figure 5.5 Product selectivity over time.
Reaction conditions: 0.07 mol% rhodium (C2.3), 1-octene (5 mmol), toluene (5 mL), 30 bar syngas (CO:H2 ratio 1:1), 75°C

5.2.3.2 Effect of temperature on the hydroformylation of 1-octene

The catalyst was evaluated at different temperatures in order to establish the effect on the conversion and selectivity. The results are shown in Figure 5.6. At 65°C the overall conversion is quite low, being just under 30%. The low conversion at low temperatures is not uncommon for rhodium-catalyzed hydroformylation.[11] The conversion more than doubles when the reaction temperature is increased to 75°C. Interestingly, the conversion at 85°C and 95°C is very close to the conversion at 75°C. This could possibly be due to the complex being unstable at these temperatures, thus leading to slight deactivation of the catalyst system.

When one looks at the selectivity at different temperatures, as shown in Table 5.1, it is clear that there is a slight increase in the rate of isomerization with increased temperature. At 65°C, 41% of the formed products are internal octene isomers, with 52% of the products being aldehydes. At 95°C, on the other hand, 54% of the products are isomers and only 46% are aldehydes. This is in contrast of what was reported by Makhubela *et al*., who observed a sharp increase in the amount of aldehydes formed at higher temperatures. The amount of branched aldehydes formed also increases with an increase in temperature, leading to a decrease in the *n:iso* ratio. This is most probably due to the increased hydroformylation of the internal octenes produced during the initial stages of the reaction.

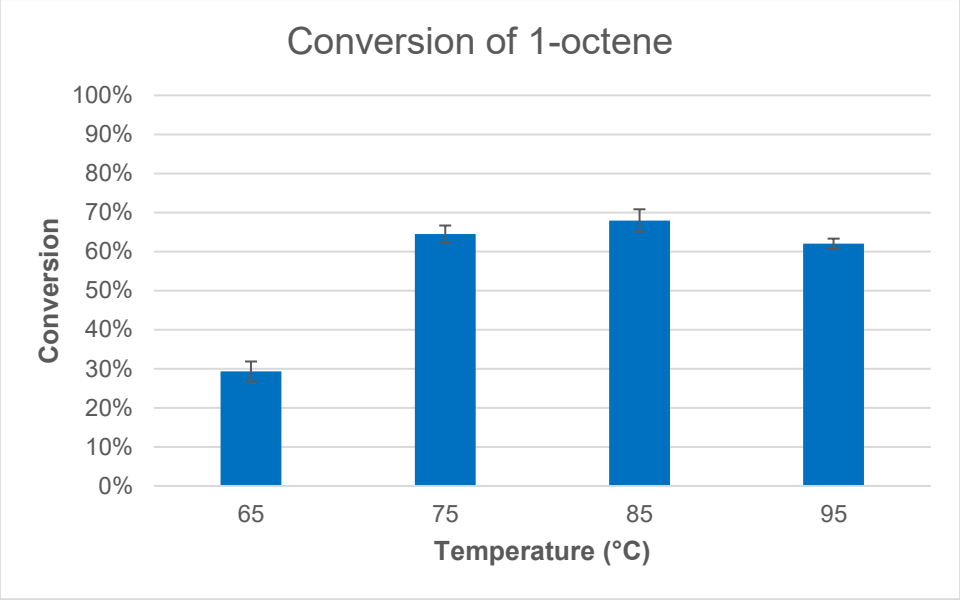

Figure 5.6 Conversion of 1-octene to all products at different temperatures.
Reaction conditions: 0.07 mol% rhodium (C2.3), 1-octene (5 mmol), toluene (5 mL), 30 bar syngas (CO:H2 ratio 1:1), 2 h

Table 5.1 Selectivity of 1-octene hydroformylation at different temperatures.

Temp (°C)	Conversion (%)	Selectivity (%)			*n:iso* ratio
		Octane	Internal octenes	Aldehydes*	
65	29	6	41	52	2.65
75	65	4	48	49	2.85
85	68	0	55	45	1.70
95	62	0	54	46	1.21

Reaction conditions: 0.07 mol% rhodium (**C2.3**), 1-octene (5 mmol), toluene (5 mL), 30 bar syngas ($CO:H_2$ ratio 1:1), 2 h
*Nonanal and other branched C9 aldehydes

5.2.3.3 Effect of pressure on the hydroformylation of 1-octene

The effect of syngas pressure on the reaction was studied (Figure 5.7). There is not a significant difference between the overall conversions at pressures of 20 and 30 bar. At 40 bar, the conversion is increased to 81%. This could possibly be due to the higher concentration of syngas in the reaction mixture.

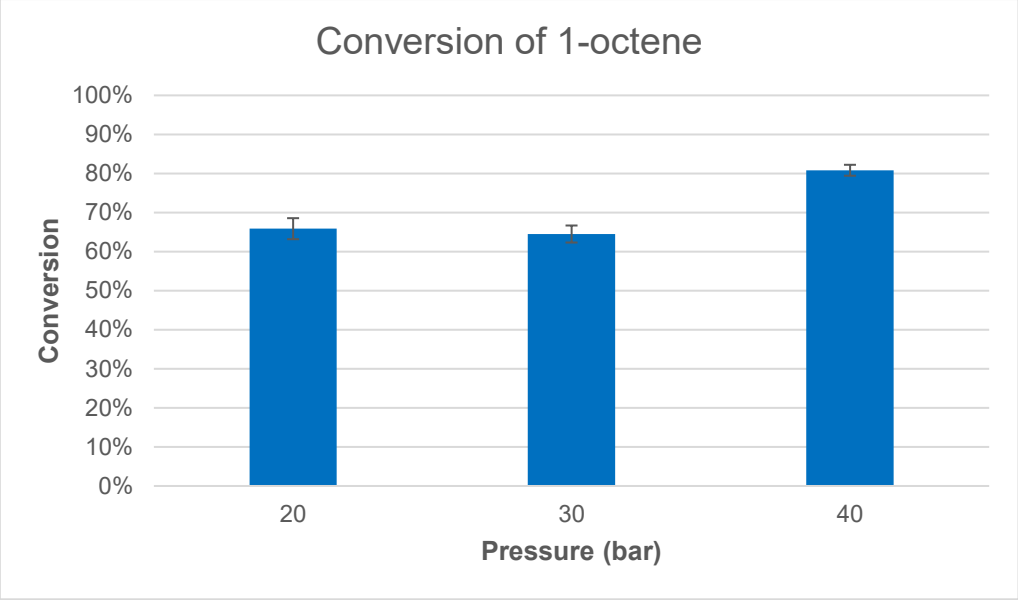

Figure 5.7 Conversion of 1-octene to all products at different pressures.
Reaction conditions: 0.07 mol% rhodium (C2.3), 1-octene (5 mmol), toluene (5 mL), syngas (CO:H2 ratio 1:1), 75°C, 2 h

It is clear from Table 5.2 that the syngas pressure has a significant influence on the type of products formed. At 20 bar, the largest proportion of the products formed are internal octenes, with the total amount of aldehydes formed being less than 30%. At pressures of 30 and 40 bar, more aldehydes compared to internal octenes are observed, with nonanal being the major product formed at 40 bar.

The increase in aldehyde formation as opposed to alkene isomerization is due to the higher concentration of carbon monoxide available in these reactions. A high concentration of carbon monoxide is expected to facilitate carbon monoxide coordination to the four-coordinate rhodium species **5** in Figure 1 which would subsequently favour migratory insertion of the carbonyl into the alkyl group to form the acyl species over competitive β-hydride elimination involving the metal-alkyl species.[12] Makhubela *et al*. also reported an increase in the formation of aldehydes with an increase in pressure, over a pressure range of 5 – 30 bar.

The *n:iso* ratio is consistently found to be above 2.4:1 at all pressures tested. This indicates that more nonanal is formed, and that under these conditions there is less hydroformylation of internal octenes taking place.

Table 5.2 Selectivity of 1-octene hydroformylation at different pressures.

Pressure (bar)	Conversion (%)	Selectivity (%)			*n:iso* ratio
		Octane	Internal octenes	Aldehydes*	
20	66	4	69	28	2.46
30	65	4	48	49	2.85
40	81	3	37	60	2.73

Reaction conditions: 0.07 mol% rhodium (**C2.3**), 1-octene (5 mmol), toluene (5 mL), syngas ($CO:H_2$ ratio 1:1), 75°C, 2 h
*Nonanal and other branched C9 aldehydes

5.2.4 Effect of different counter-ions of the catalyst precursor complex on the hydroformylation of 1-octene

In Chapter 3, it was briefly mentioned that cationic complexes that differ only with regard to the counter-ion used may exhibit different catalytic properties. The two N,N Schiff base complexes synthesized in Chapter 3, with tetrafluoroborate (**C3.1**) and hexafluorophosphate (**C3.2**) counter-ions respectively were tested in the hydroformylation of 1-octene, and the results were compared to the results obtained when using the tetraphenylborate analogue **C2.3**. It was found that the hexafluorophosphate analogue **C3.2** was insoluble in toluene, and therefore gave much poorer conversion of 1-octene than **C2.3** and **C3.1**. These results did thus not give much information on the effect of the counter-ion on catalysis.

Hydroformylation reactions using the different catalyst precursors were repeated using dioxane as solvent, which has only a slightly higher dielectric constant than toluene and the results are shown in Figure 5.8. All three complexes are soluble in dioxane at room temperature and solvent effects therefore played less of a role than in the case of toluene. It was found that the tetrafluoroborate and hexafluorophosphate complexes **C3.1** and **C3.2** gave almost quantitave conversion after a 1 hour period, while the conversion using the tetraphenylborate complex **C2.3** was only 53%. The lower conversion found for **C2.3** was ascribed to the presence of the bulky tetraphenylborate anion which could inhibit the binding of the substrate to the metal.

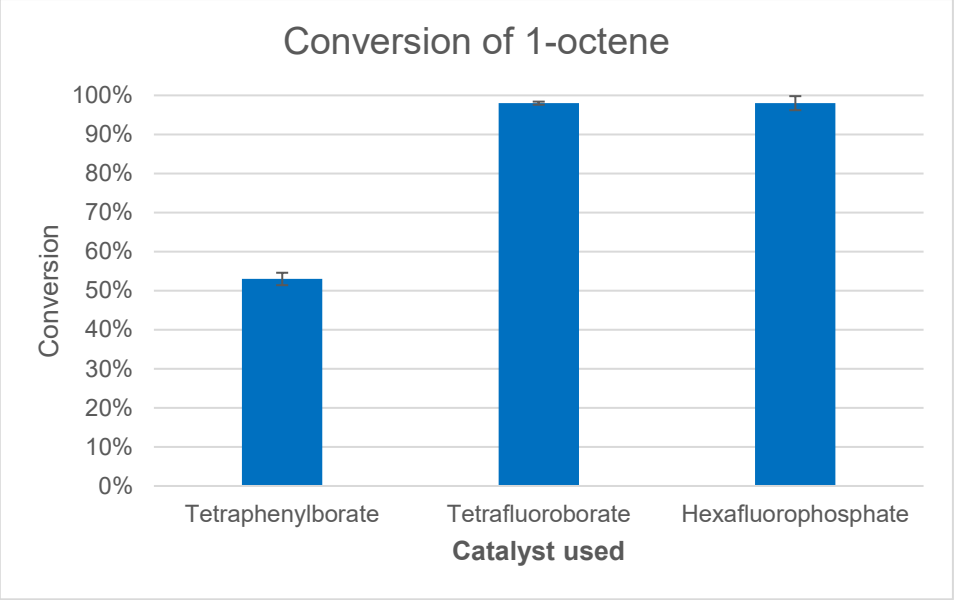

Figure 5.8 Conversion of 1-octene to all products using different anions using dioxane as solvent.
Reaction conditions: 0.07 mol% rhodium, 1-octene (5 mmol), solvent (5 mL), syngas (CO:H2 ratio 1:1), 75°C, 1 h

The selectivities for the reactions is shown in Table 5.3. The chemoselectivity for the three complexes is quite similar, with slightly more aldehydes being formed than internal octenes in all cases. When the regioselectivities are compared, it can be seen that **C2.3** favoured the formation of the linear aldehyde with an *n:iso* ratio of 2.69. This can be attributed to presence of the bulky counter-ion close to the active metal centre, which favours insertion of the alkene substrate in an orientation that would lead to the formation of the linear aldehyde.

Table 5.3 Selectivity of 1-octene hydroformylation using different counter-ions in dioxane.

Counter-ion	Complex	Conversion (%)	Selectivity (%)			*n:iso* ratio
			Octane	Internal octenes	Aldehydes*	
BPh_4	**C2.3**	53	0	42	58	2.69
BF_4	**C3.1**	98	4	45	51	1.55
PF_6	**C3.2**	98	4	46	50	1.66

Reaction conditions: 0.07 mol% rhodium, 1-octene (5 mmol), solvent (5 mL), syngas ($CO:H_2$ ratio 1:1), 75°C, 1 h
*Nonanal and other branched C9 aldehydes

A suitable solvent with a high dielectric constant, a boiling point above 80°C and in which all the complexes were adequately soluble could not be found. In a solvent with a high dielectric constant ion-pairing would be disfavoured and a tight ion-pair would be less likely to form. The counter-ion may therefore theoretically have less of an effect on the regioselectivity.

5.2.5 Comparison of model catalysts C2.1 – C2.4 and C2.9 in the hydroformylation of 1-octene

The five model catalysts were tested as pre-catalysts in the hydroformylation of 1-octene with the aim of probing the effect of the ligand. The results are shown in Figure 5.9. The conversion after 2 hours varies quite a lot, ranging from 37% in the case of the neutral N,P system, **C2.1**, to 86% for the cationic pyridyl-triazole complex **C2.9** which has 1,5-cyclooctadiene as co-ligand. Both steric and electronic properties of ligands coordinated to rhodium can influence the conversion and selectivity of the hydroformylation reaction.[12]

The complexes containing 1,5-cyclooctadiene as co-ligand all show higher conversion of 1-octene compared to the neutral complex **C2.1**, which has one carbonyl and one chloride ligand in addition to the Schiff base ligand. As reported in literature and illustrated later in this chapter (Section 5.2.7.1), the replacement of the COD ligand by two carbonyl moieties is a facile and rapid reaction (Scheme 5.4).[10] It would thus be more likely to regard the complexes containing the COD ligand as having two carbonyl ligands when the catalytic properties of the complexes are considered.

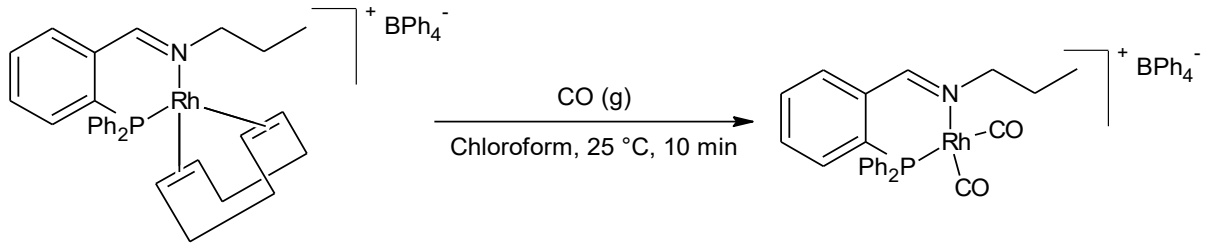

Scheme 5.4 Displacement of 1,5-cyclooctadiene co-ligand with carbonyl ligands.

Comparing the two complexes containing N,P donor ligands, **C2.1** and **C2.2**, our experimental results show that the conversion of 1-octene is far higher for **C2.2** (79%) than for **C2.1** (37%). This may be due to the fact that **C2.2** is cationic while **C2.1** is neutral, and the rhodium centre in **C2.2** is therefore more electrophilic. This would facilitate coordination of the alkene substrate to the metal centre. Another factor could be the difference between the monodentate ligands on the two complexes. Carbonyl ligands are well known to be good π-acceptor ligands, and π-back-donation is likely to occur from the rhodium to the carbonyl ligands. In **C2.1** there is only one carbonyl ligand (the other monodentate ligand being a chloride ligand), while **C2.2** has two carbonyl ligands. The π-back-donation would thus be spread across two ligands in **C2.2** while in **C2.1** it is concentrated on one ligand, making the metal-carbonyl bonds weaker in **C2.2** than in **C2.1**. This may lead to faster formation of species **1** and **5** as shown Scheme 5.2 and their equilibrium concentration will increase.[12]

A very important step in the catalytic cycle is the formation of the rhodium hydride (Scheme 5.2). It is generally accepted that the molecular hydrogen approaches the metal centre in a side-on fashion, forming a 3-centered intermediate.[13,14] Rh-H bonds start forming, and the H-H bond starts to break with concomitant formation of the rhodium hydride. It can be reasonably assumed that the metal centre in complex **C2.1** has a higher electron density than complex **C2.2**. We would therefore expect that it can back-donate more electron density to the σ^* orbitals of the hydrogen atom, leading to faster H-H bond breakage and thus faster hydride formation. However, since **C2.2** shows better conversion of 1-octene than **C2.1**, it would suggest that the hydride formation is not the rate-determining step in reactions where these complexes are involved in hydroformylation. This would suggest that another step in the catalytic cycle, for example hydride migration, alkene coordination or migratory CO insertion could be rate limiting.[2]

The cationic pre-catalysts **C2.2**, **C2.3** and **C2.9** also show higher conversion than the neutral complexes **C2.1** and **C2.4**, although **C2.3** only shows slightly higher conversion than **C2.4**. The metal centre in the cationic complexes is more electron deficient than those in the neutral complexes, making it more electrophilic and thus facilitating alkene coordination. It can therefore be expected that the cationic complexes would show generally higher conversion than the neutral complexes over the same time period. While one would need kinetic evidence to confirm this, the simple conversion data for the reactions performed would suggest that alkene coordination rather than hydride formation is more likely to be the rate-determining step.

The highest conversion is achieved with the triazole complex **C2.9**, followed by the cationic N,P complex **C2.2**. The conversion for complexes **C2.3** and **C2.4** is similar.

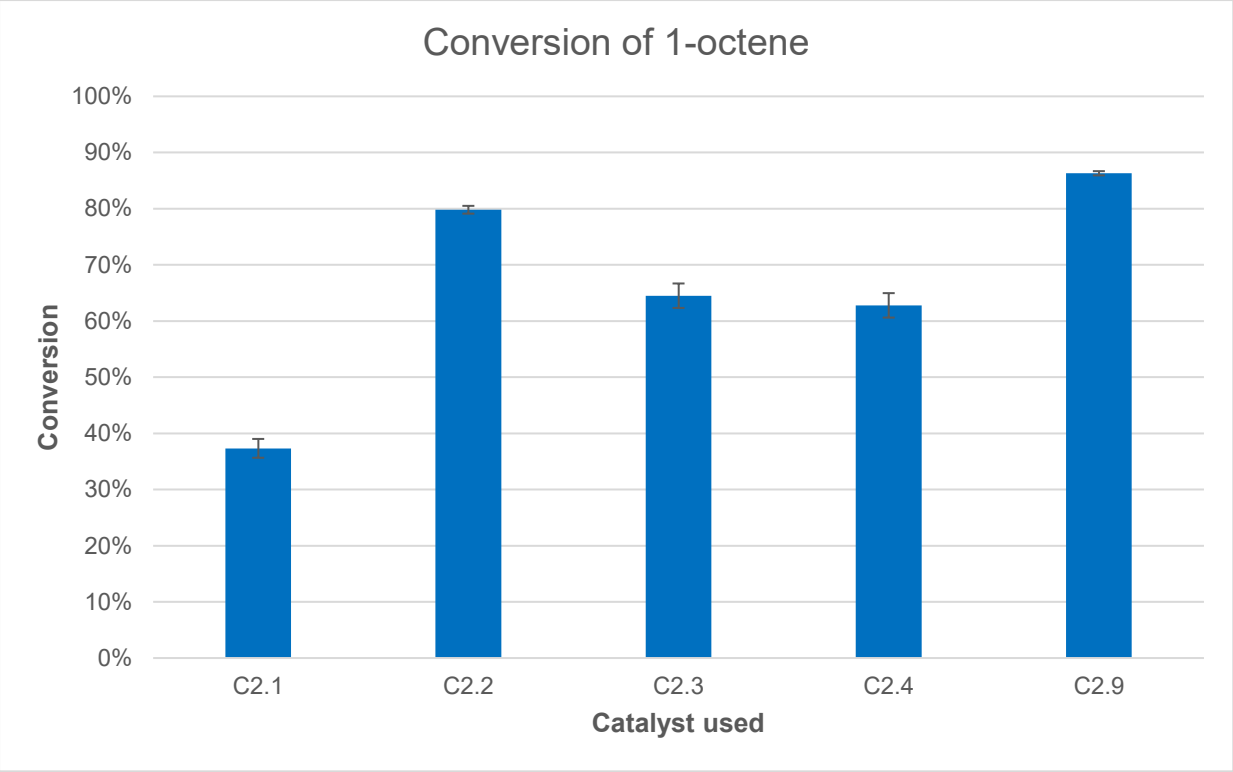

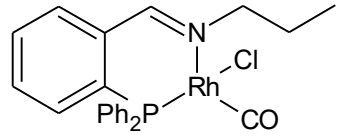

C2.1

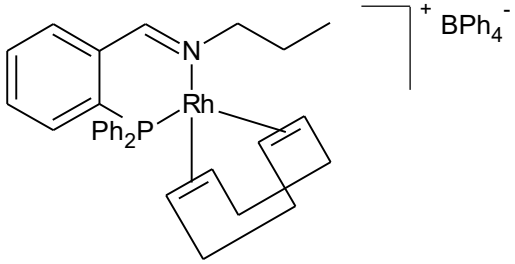

C2.2

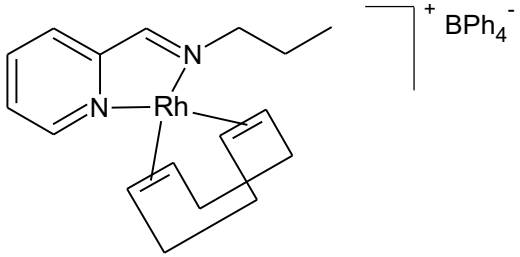

C2.3

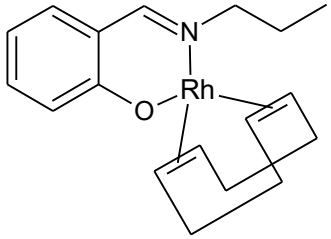

C2.4

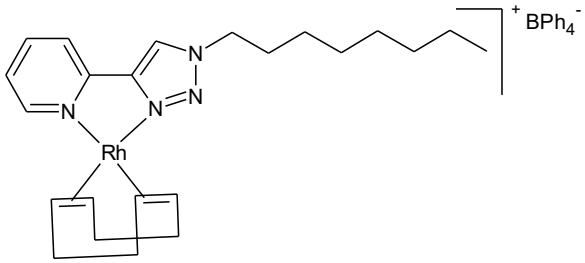

C2.9

Figure 5.9 Conversion of 1-octene to all products using complexes C2.1 – C2.4 and C2.9

From the selectivities towards the different products achieved with the different catalyst precursors (Table 5.4), we can see some similar trends than what was already observed in that an increase in the amount of aldehydes formed is accompanied by a decrease in the *n:iso* ratio. A small amount of octane, the hydrogenation product, is obtained in all cases. The selectivity towards aldehydes is generally not high, with **C2.2** being the exception (72% selectivity towards aldehydes). This catalyst also shows the lowest *n:iso* ratio, 1.33:1, while all the other catalysts giving *n:iso* ratios in the range of 2.40:1 to 3.00:1. The chemo- and regioselectivity of **C2.2** at two hours (72% aldehydes with an *n:iso* ration of 1.33:1) is similar to that of **C2.3** at 6 hours (76% aldehydes with an *n:iso* ratio of 1.36:1), indicating that **C2.2** can more accurately be called a more *active* catalyst than a more *selective* catalyst than **C2.3**.

The pyridyl-triazole catalyst, **C2.9**, shows the highest conversion of 1-octene to all products with 86%, but a very low selectivity towards aldehydes, with only 33% of the products that are formed being aldehydes. When comparing the selectivities of, for example, **C2.2** to **C2.9**, we can say that **C2.2** is more selective towards nonanal than **C2.9**.

Table 5.4 Selectivity of 1-octene hydroformylation using different catalysts.

Catalyst	Conversion (%)	Selectivity (%)			*n:iso* ratio
		Octane	Internal octenes	Aldehydes*	
C2.1	37	6	59	35	3.00
C2.2	80	2	26	72	1.33
C2.3	65	4	48	49	2.85
C2.4	63	4	53	43	2.87
C2.9	86	3	64	33	2.40

Reaction conditions: 0.07 mol% rhodium, 1-octene (5 mmol), toluene (5 mL), 30 bar syngas ($CO:H_2$ ratio 1:1), 75°C, 2 h
*Nonanal and other branched C9 aldehydes

5.2.6 Employing immobilized catalysts IC4.1 – IC4.10 in the hydroformylation of 1-octene

Following the study on the model homogeneous catalysts, the catalyst precursors immobilized onto MCM-41 and SBA-15 were tested in 1-octene hydroformylation. The immobilized catalyst precursors are shown in Figure 5.10.

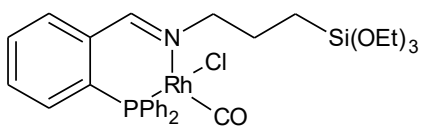

IC4.1: MCM-41
IC4.2: SBA-15
Analogue: **C2.1**

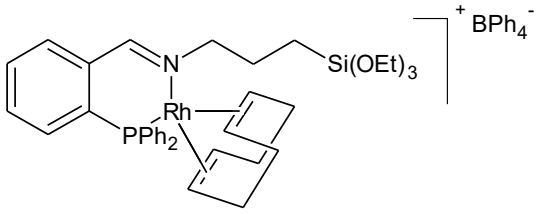

IC4.3: MCM-41
IC4.4: SBA-15
Analogue: **C2.2**

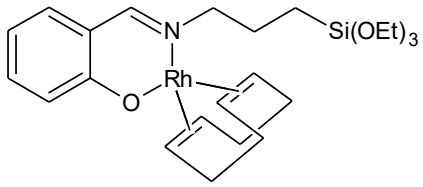

IC4.5: MCM-41
IC4.6: SBA-15
Analogue: **C2.4**

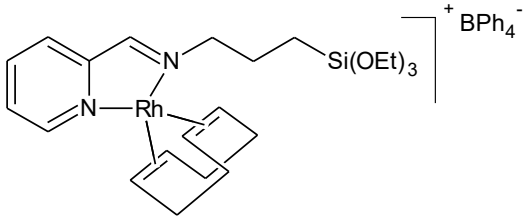

IC4.7: MCM-41
IC4.8: SBA-15
Analogue: **C2.3**

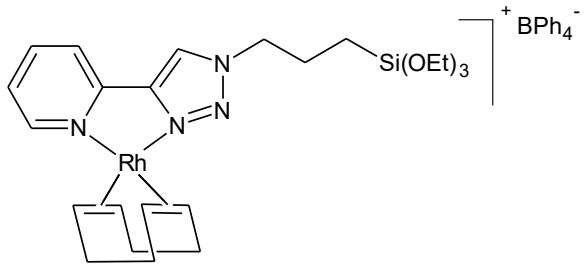

IC4.9: MCM-41
IC4.10: SBA-15
Analogue: **C2.9**

Figure 5.10 Immobilized catalysts IC4.1 - IC4.10 and abbreviations for homogeneous analogues used in the hydroformylation of 1-octene.

Some initial test reactions with the immobilized catalysts indicated that the conversion of 1-octene was generally higher with the immobilized catalysts than is the case for the model catalysts. The catalyst loading was therefore halved to 0.035 mol% in the evaluation of the immobilized catalysts. Along with this lower metal loading, reaction parameters of 30 bar syngas pressure, 75°C and 2 hours were chosen for the testing of the immobilized catalysts. New catalytic experiments were also carried out using the model catalysts at the lower loading, in order to be able to compare the model and immobilized catalysts at the same metal loading, 0.035 mol%.

From Figure 5.11 it can be seen that the activity of the immobilized catalysts is significantly higher than that of their analogous homogeneous counterparts. Apart from the neutral N,P

immobilized complexes (**IC4.1** and **IC4.2**), there are only slight differences in the turnover numbers when comparing the catalysts immobilized onto MCM-41 and SBA-15, with the immobilized complexes containing SBA-15 generally being more active.

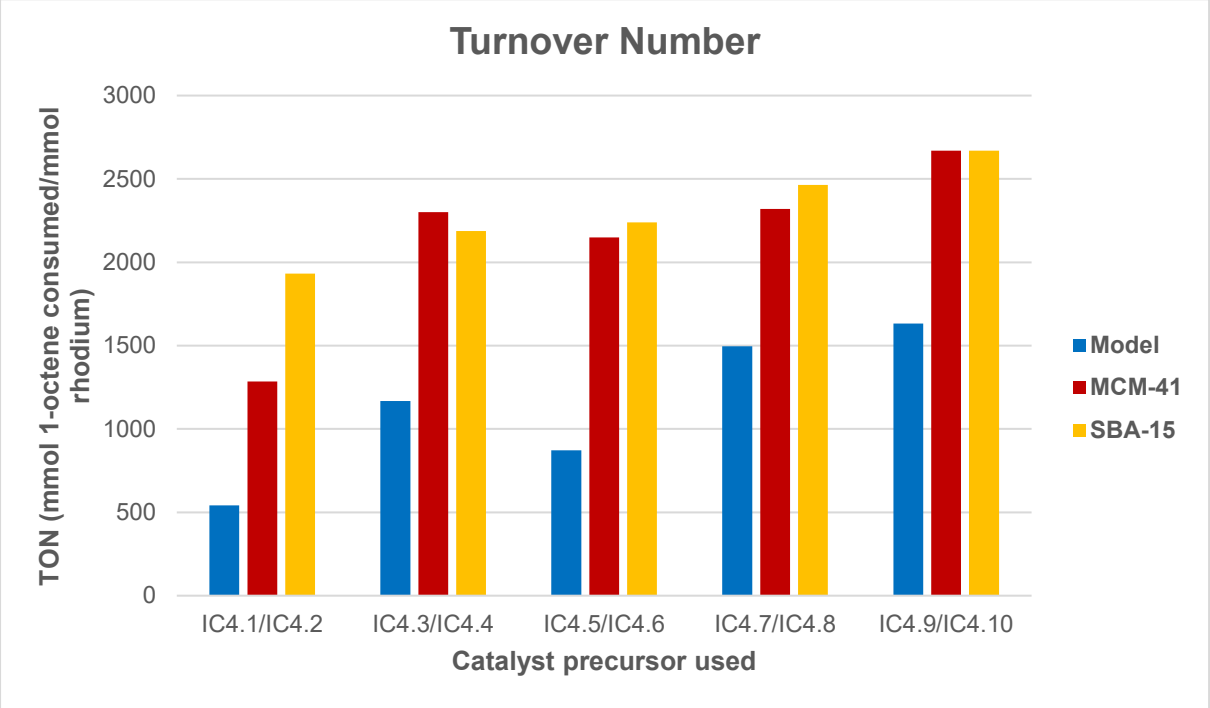

Figure 5.11 Conversion using different immobilized catalysts.
Reaction conditions: 0.035 mol% rhodium, 1-octene (5 mmol), toluene (5 mL), 30 bar syngas (CO:H2 ratio 1:1), 75°C, 2 h

Marras *et al*. found that a SBA-15 supported xantphos-type rhodium catalysts outperformed an analogous homogeneous complex under some conditions.[15] This was tentatively attributed to a reduction in the formation of inactive dinuclear rhodium species due to site-isolation in the immobilized catalyst (Figure 5.12). These carbonyl bridges dimers can form more readily in solution resulting in the deactivation of the catalytically active sites.

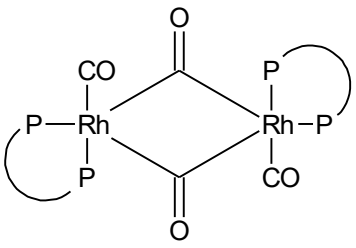

Figure 5.12: Inactive dinuclear rhodium species proposed by Marras et al.[15]

The chemo- and regioselectivities of the immobilized catalysts show some interesting results when compared to their homogeneous counterparts as discussed below. For both the neutral and cationic complexes containing the bidentate N,P ligand, there is not much difference between the selectivities of the homogeneous and the immobilized (**C2.1** vs. **IC4.1**, **IC4.2** and

C2.2 vs. **IC4.3** and **IC4.4**) catalysts, as can be seen in Figure 5.13. This indicates that the ligand environment around the metal site is essentially not impacted by the immobilization; thus being the same for both the homogeneous and heterogenized catalyst. The different mesoporous silica supports also do not seem to have a significant effect on the selectivity of the catalysts.

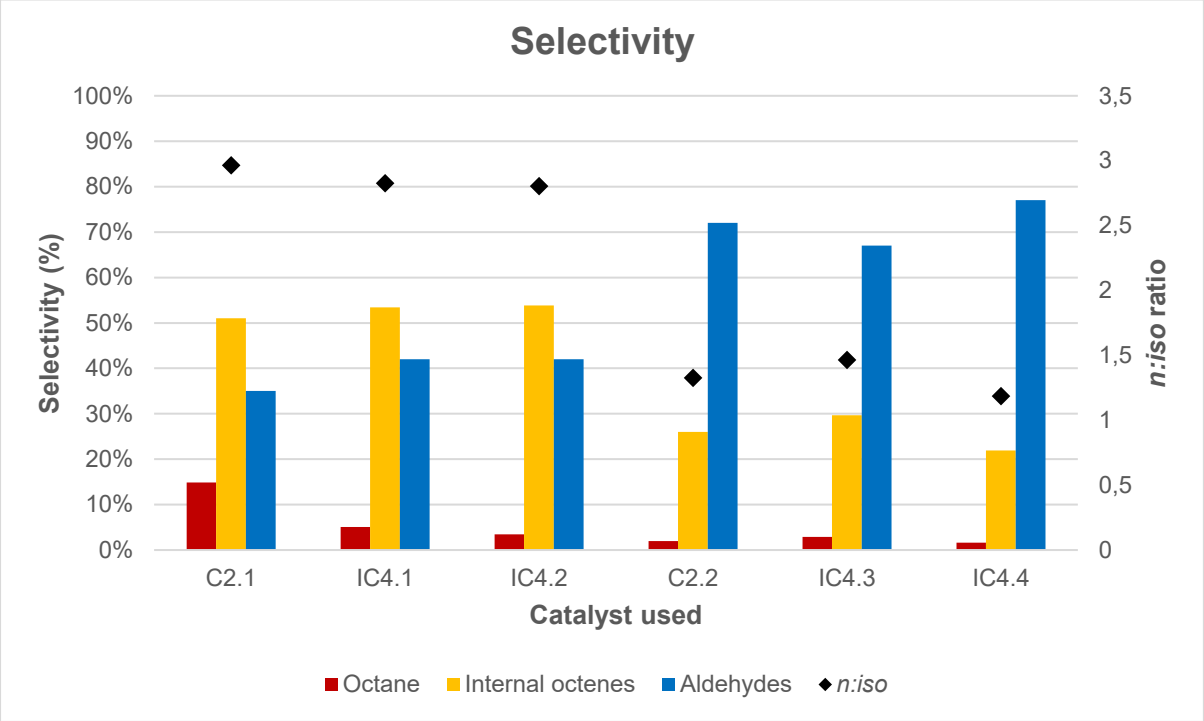

Figure 5.13 Selectivity of model and immobilized N,P catalysts.
Reaction conditions: 0.035 mol% rhodium, 1-octene (5 mmol), toluene (5 mL), 30 bar syngas (CO:H2 ratio 1:1), 75°C, 2 h
'Aldehydes' refers to nonanal and other branched C9 aldehydes

The other three immobilized catalysts, (**IC4.5 – IC4.10**) generally do show a difference in selectivity when the immobilized systems are compared with the homogeneous catalysts and this data is plotted in Figure 5.14. The homogeneous neutral N,O catalyst, **C2.4**, for example, shows an 58% selectivity towards internal octenes while the MCM-41 and SBA-15 immobilized catalysts (**IC4.5** and **IC4.6**) favours alkene isomerization to a much lesser extent, resulting in 30% and 23% internal octenes respectively. There is a concomitant increase in the amount of aldehydes formed (36% and 68% vs. 74%) when using these immobilized catalysts. We also see a decrease in the *n:iso* ratio from 2.94:1 in the case of the homogeneous catalyst to 1.41:1 and 1.17:1 for the two immobilized catalysts. This trend agrees with what was previously observed for the homogeneous catalysts with aldehyde formation increasing over time (Section 5.2.3.1, p. 155). Similar trends are also seen with several catalyst precursors which have higher overall activity. In these cases higher overall activity leads to an increase in the formation of aldehyde products, but a decrease in *n:iso* ratio as more branched aldehydes are

formed. On the whole, the overall rate of hydroformylation in terms of conversion of 1-octene to all formed products per mmol of rhodium tends to be higher when using the immobilized catalysts than the homogeneous catalyst.

A noticeable exception to the above-mentioned selectivity trend is found for the pyridyl-triazole complex immobilized on MCM-41, **IC4.9**. This complex shows the expected increase in activity after immobilization, with a turnover number increase of approximately 1000 mmol 1-octene per mmol rhodium being observed after immobilization. Both immobilized complexes also show remarkable selectivity towards aldehydes when compared to the homogeneous complex, with 87% of the products formed with **IC4.9** being aldehydes.

In the case of the complex immobilized on SBA-15, **IC4.10**, we see the usual decrease in *n:iso* ratio, while the higher *n:iso* ratio is retained for the complex immobilized on MCM-41. We would expect that the size of the immobilized pyridyl-triazole complex would be larger than that of the pyridine-imine and salicylaldimine complexes. Since the average pore diameter of SBA-15 (58.2 Å) is more than double that of MCM-41 (24.3 Å), it is likely that **IC4.10** contains more of the complex inside the silica pores than **IC4.9**.

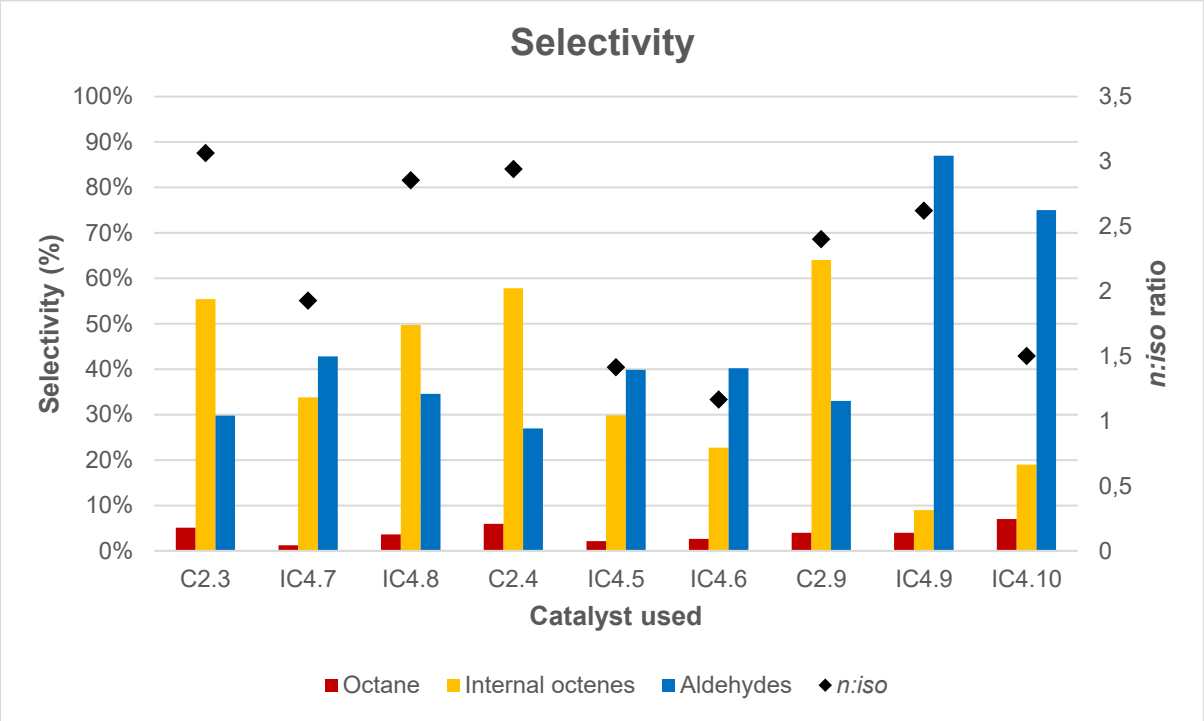

Figure 5.14 Selectivity of 1-octene hydroformylation using immobilized catalysts IC4.5 – IC4.10.
Reaction conditions: 0.035 mol% rhodium, 1-octene (5 mmol), toluene (5 mL), 30 bar syngas (CO:H2 ratio 1:1), 75°C, 2 h
'Aldehydes' refers to nonanal and other branched C9 aldehydes

5.2.6.1 The role of the support materials MCM-41 and SBA-15 in the hydroformylation of 1-octene

In order to investigate the role of the silica supports, native silica was added to model pre-catalyst. The mass of the silica added was kept equal to that of the total mass of the immobilized catalyst used.

In Figure 5.15 the turnover number (in terms of 1-octene consumed per mmol of rhodium) obtained with the model catalyst and its immobilized analogues is compared to the turnover number (TON) using the homogeneous catalyst in the presence of native silica. It is clear that we can increase the turnover number by simply adding some silica. A similar effect has previously been observed in our group for the oxidative cleavage of alkenes using ruthenium catalysts. The increase in conversion was attributed to the stabilizing effect of the surface silanol groups on the active species, RuO_4.[16] In our case the increase in TON could possibly be due to the presence of the silica leading to better dispersion of the rhodium complexes, leading to less catalyst deactivation as discussed in Section 5.2.6.

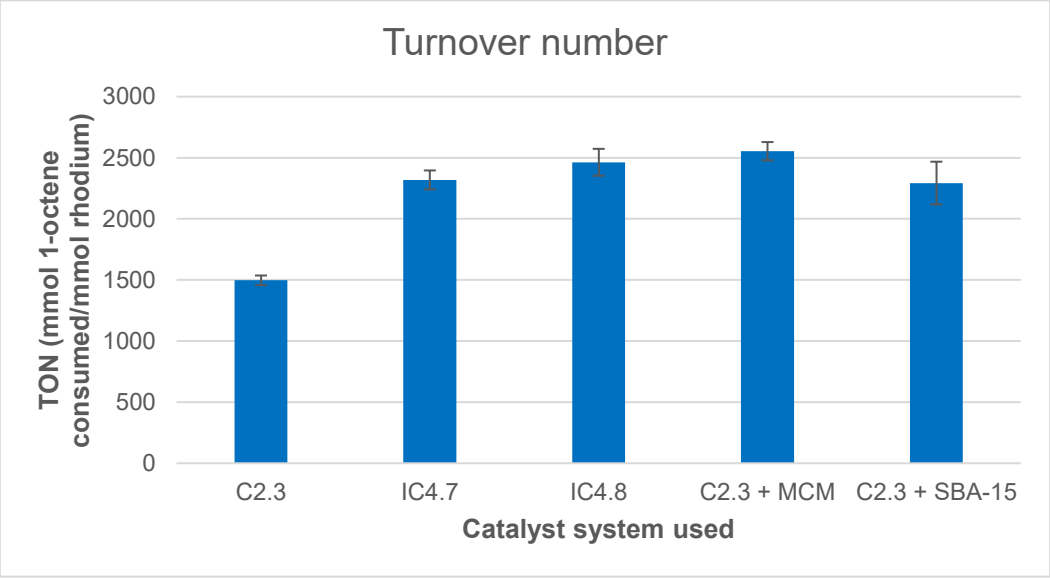

Figure 5.15 Turnover number obtained with model catalyst C2.3, its immobilized analogues and the model catalyst in presence of silica.
Reaction conditions: 0.035 mol% rhodium, 1-octene (5 mmol), toluene (5 mL), 30 bar syngas (CO:H2 ratio 1:1), 75°C, 2 h

Table 5.5 Selectivity of 1-octene hydroformylation using model catalyst C2.3, its immobilized analogues and the model catalyst in the presence of silica.

Catalyst	Conversion (%)	Selectivity (%)			*n:iso* ratio
		Octane	Internal octenes	Aldehydes*	
C2.3	54	5	55	40	3.06
IC4.7	82	1	34	65	1.93
IC4.8	56	4	50	47	2.86
C2.3 + MCM	90	3	35	62	1.50
C2.3 + SBA	81	3	20	77	1.41

Reaction conditions: 0.035 mol% rhodium, 1-octene (5 mmol), toluene (5 mL), 30 bar syngas ($CO:H_2$ ratio 1:1), 75°C, 2 h

*Nonanal and other branched C9 aldehydes

5.2.6.2 Attempted recycling studies

The immobilized catalysts were re-used in order to determine whether heterogenizing the complexes on silica could produce recyclable catalysts. The catalyst was recovered from the reaction mixture after catalysis by centrifuge from the mother liquor. The recovered solid was washed with fresh toluene to remove any residual octenes or hydroformylation products from the silica, and the mixture was centrifuged a second time, followed by removal of the mother liquor and the recovered catalyst was dried before re-use. We observed a discoloration of the mother liquor after the first use of the catalysts, which suggested the possibility of rhodium leaching from the silica support.

Figure 5.16 depicts the TON of the reaction after recycling. The amount of rhodium used for the TON calculations was determined by estimating at the amount of rhodium leached from the reaction after recycling. The mother liquor was analysed by ICP-OES and the results are shown in Table 5.6 on p. 174. A general decrease in the turnover number is observed for the reactions using the recycled immobilized catalyst.

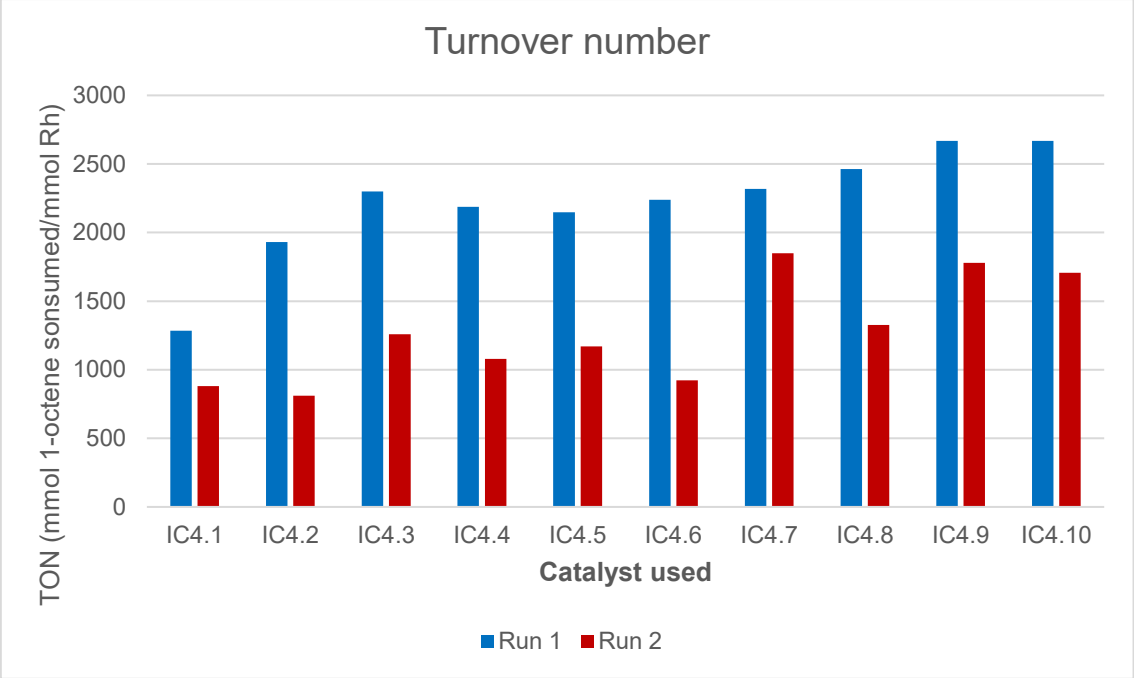

Figure 5.16 TON using and re-using immobilized catalysts.
Reaction conditions: 0.035 mol% rhodium, 1-octene (5 mmol), toluene (5 mL), 30 bar syngas (CO:H2 ratio 1:1), 75°C, 2 h. TON defined as mmol 1-octene consumed per mmol Rh used.

The selectivities obtained using the immobilized catalysts with N,P chelating ligands (**IC4.1 – IC4.4**) and their recycled counterparts are shown in Figure 5.17. The *n:iso* ratio is indicated by the black dots and are plotted on the secondary (right-hand) axis. The selectivity for the immobilized neutral N,P complex (**IC4.1** and **IC4.2**) stays fairly constant after recycling. This indicates that the nature of the catalytic species is not significantly altered after recycling.

In the case of the immobilized cationic N,P COD complex (**IC4.3** and **IC4.4**), a big change in selectivity for both the MCM-41 and SBA-15 complex is observed after recycling, with the selectivity towards the aldehyde decreasing dramatically and the relative proportion of internal octenes increasing significantly. The *n:iso* ratio is also higher after recycling. This is indicative of a less active catalyst – it is likely that, over a longer time period, the internal alkenes probably undergo hydroformylation and that an increase in aldehyde formation with a corresponding decrease in *n:iso* ratio would be observed.

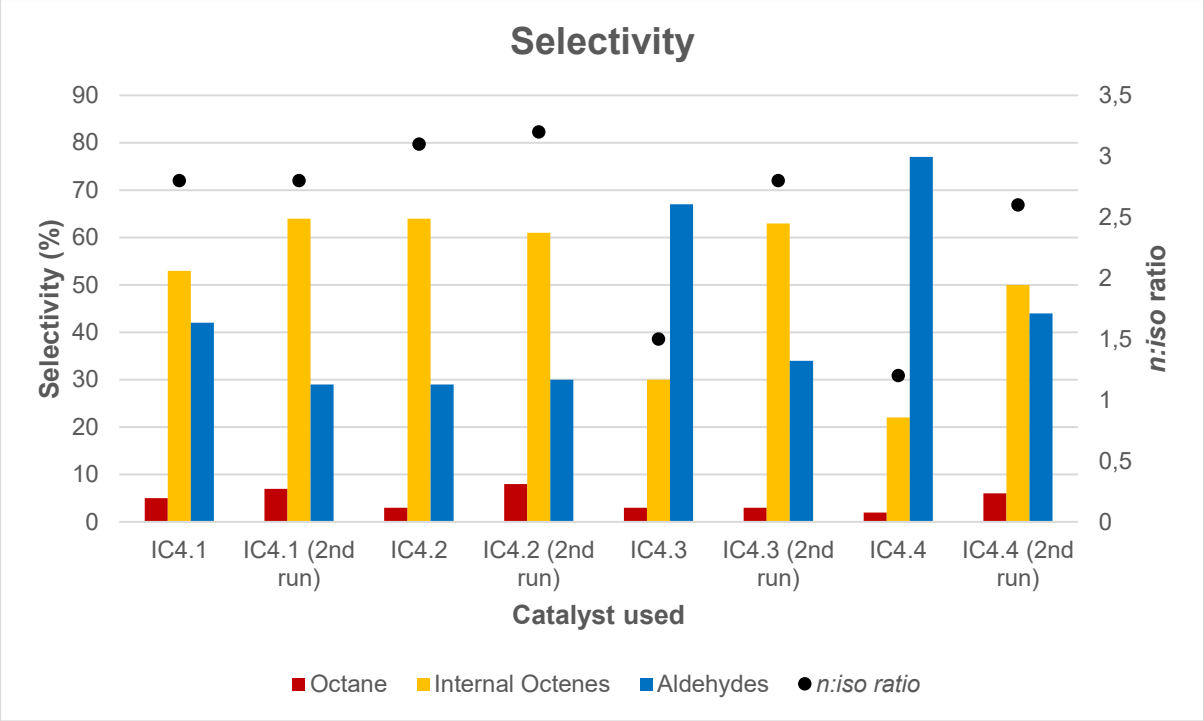

Figure 5.17 Selectivity using and re-using immobilized catalysts IC4.1 - IC4.4.
Reaction conditions: 0.035 mol% rhodium, 1-octene (5 mmol), toluene (5 mL), 30 bar syngas (CO:H2 ratio 1:1), 75°C, 2 h
'Aldehydes' refers to nonanal and other branched C9 aldehydes

A similar chart is depicted in Figure 5.18 for the immobilized catalysts with N,O and N,N chelating ligands (**IC4.5 – IC4.10**). **IC4.5**, **IC4.6** and **IC4.7** show a similar, though less dramatic, change in selectivity when compared to **IC4.3** and **IC4.4**, with once again an increase in internal octenes being observed after recycling. As is the case for **IC4.3** and **IC4.4**, the *n:iso* ratio increases after recycling, an indication that less of the internal octene isomers have been hydroformylated. For **IC4.8**, **IC4.9** and **IC4.10**, the changes in selectivity after recycling is minimal.

The pyridyl-triazole complex (**IC4.9** and **IC4.10**) still show excellent selectivity towards aldehydes even after recycling, which distinguishes it from the other complex systems. All the other immobilized catalysts which show selectivity towards the aldehydes (**IC4.3** - **IC4.7**) lose this selectivity after recycling, resulting in more internal octenes being formed during the 2nd runs. The immobilized pyridine-triazole complexes possibly have a degree of steric hindrance around the active sites, which could discourage the migratory insertion of the coordinated alkene in the orientation that would lead to branched aldehydes or β-hydride elimination to the internal octene isomers (**3a** in Scheme 5.5).

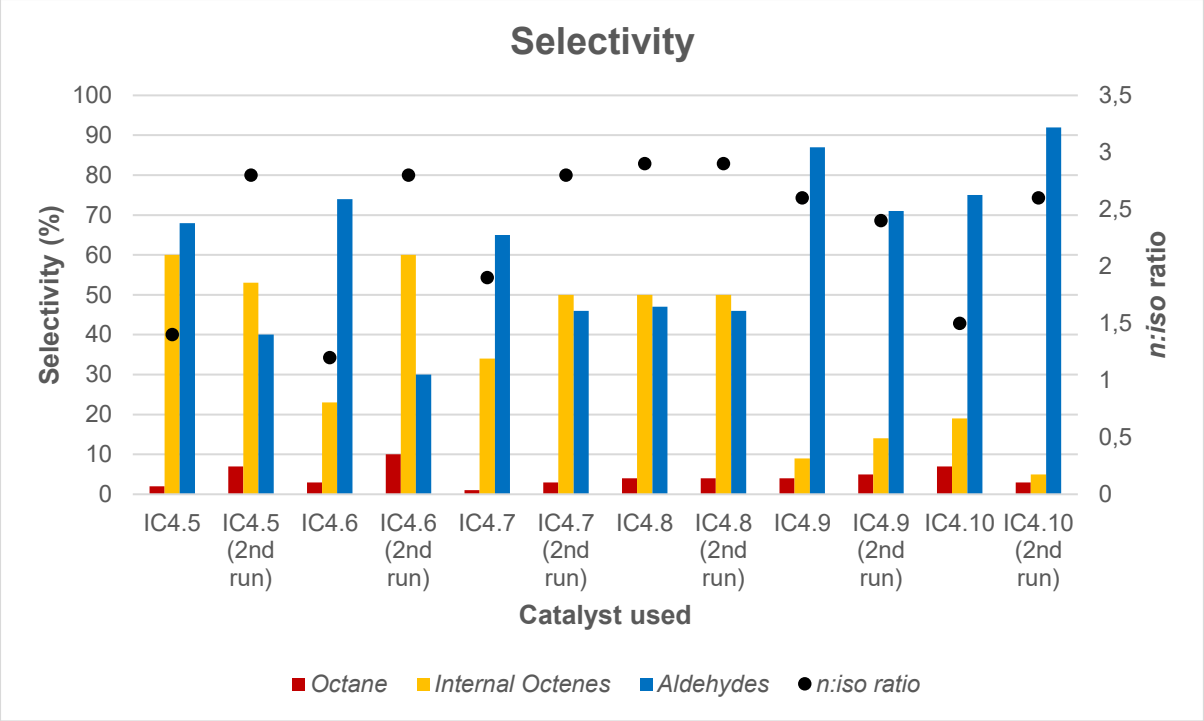

Figure 5.18 Selectivity using and re-using immobilized catalysts IC4.5 - IC4.10.
Reaction conditions: 0.035 mol% rhodium, 1-octene (5 mmol), toluene (5 mL), 30 bar syngas (CO:H2 ratio 1:1), 75°C, 2 h
'Aldehydes' refers to nonanal and other branched C9 aldehydes

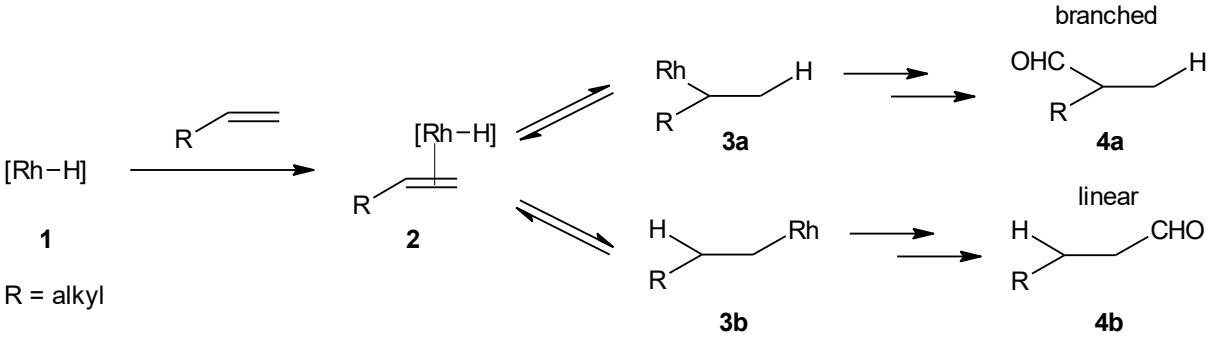

Scheme 5.5 Reaction pathway explaining the formation of branched and linear aldehydes.[17]

In a situation with a higher degree of steric hindrance around the rhodium centre, the migratory insertion of the alkene resulting in the metal-alkyl with the orientation shown in **3b** may be more likely than the process leading to **3a**, since the side chain on the alkene is further away from the metal in **3b**. As shown in Scheme 5.5, this orientation leads to the formation of linear aldehydes and could explain the higher selectivity towards nonanal exhibited by **IC4.9** and **4.10**.

After each initial run, the filtrate was isolated and analyzed by ICP-OES to determine the amount of rhodium present. The correlation between the loss of conversion and the amount of rhodium in the filtrate is fairly good and is shown in Table 5.6. **IC4.1**, **IC4.7** and **IC4.8** all

show a loss of conversion of less than 20%, and have low rhodium leaching (less than 1 ppm). **IC4.6** shows the biggest difference in conversion upon re-use (62%) and also has the highest amount of rhodium in the filtrate, 14.5 ppm. It therefore appears that the decrease in conversion is a consequence of the leaching of rhodium from the immobilized catalyst. The formation of inactive rhodium dimers as postulated by Marras *et al.* as discussed in Section 5.2.6 could also contribute to the loss of conversion.[15]

Table 5.6 Loss of conversion and rhodium leaching of immobilized catalysts after one use.

Catalyst	Loss of conversion of 1-octene (%)	Rhodium in filtrate (ppm)	Residual rhodium on support (ppm)
IC4.1	15	0.9	30.3
IC4.2	46	6.7	24.6
IC4.3	43	4.4	26.8
IC4.4	44	4.2	27.1
IC4.5	37	2.5	28.7
IC4.6	62	14.5	16.8
IC4.7	18	0.4	30.9
IC4.8	11	0.4	30.9
IC4.9	34	1.4	29.9
IC4.10	44	5.3	26.0

The above results make it clear that these catalysts are unfortunately not suitable for re-use, as there is a significant loss in conversion for all the catalysts after only one re-use. This could either be due to incomplete immobilization of the complexes onto the silica, or due to the transformation of the catalyst precursor to a soluble rhodium species. It is possible that the metal dissociates from the ligand during the catalytic cycle to form rhodium tetracarbonyl hydride, and this metal would thus be lost into the filtrate during recycling of the catalyst.[18] In order to investigate the cause of the low recyclability, we attempted to probe the mechanism of our hydroformylation reactions more closely.

5.2.7 Preliminary mechanistic studies

It is well known that the active catalyst in the rhodium-catalyzed hydroformylation reaction is a rhodium hydride species with one or more carbonyl ligands also present on the rhodium metal centre.[12] We were therefore interested in investigating the transformation of our catalyst precursors into the active catalyst.

5.2.7.1 Formation of the carbonyl species

The majority of our pre-catalysts contain a 1,5-cyclooctadiene co-ligand and under gaseous CO the replacement of this ligand with carbonyl ligands is reported to be facile.[10] We set out to confirm this assumption by attempting to replace the 1,5-cyclooctadiene ligand with carbonyl groups.

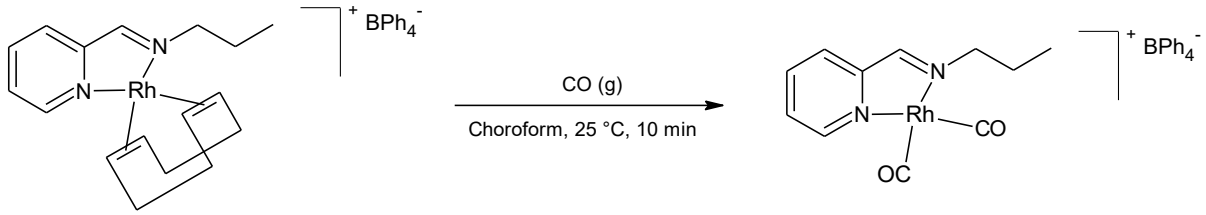

Scheme 5.6 Displacement of COD ligand with carbon monoxide.

Complex **C2.3** was dissolved in chloroform in a sealable NMR tube equipped with a J. Young valve, which allows for control of the atmosphere above the sample. The air was removed from the tube by evacuation, and re-filled with carbon monoxide at atmospheric pressure and room temperature. The tube was periodically inverted to mix the contents. The colour of the solution started to change from red-purple to orange within minutes, and after 10 minutes the solution was a bright orange colour. We also observed that, if the complex was dissolved in chloroform in a glass vial and the gas bubbled through the solution, a similar colour change happened within a few seconds due to the improvement in mixing. The ^{1}H NMR spectrum of the orange solution is compared to that of the complex in Figure 5.19 below.

In the spectrum of the complex, the olefinic protons of the COD ligand are found at 4.22 ppm, while the aliphatic protons can be seen as two resonances at 2.46 ppm and 1.98 ppm. These resonances are absent in the spectrum of the complex after treatment with carbon monoxide. Two new peaks can be observed at 5.58 ppm and 2.36 ppm, indicating the olefinic and aliphatic protons of free COD respectively. This was confirmed by looking at the ^{1}H NMR of a authentic sample of 1,5-cyclooctadiene.

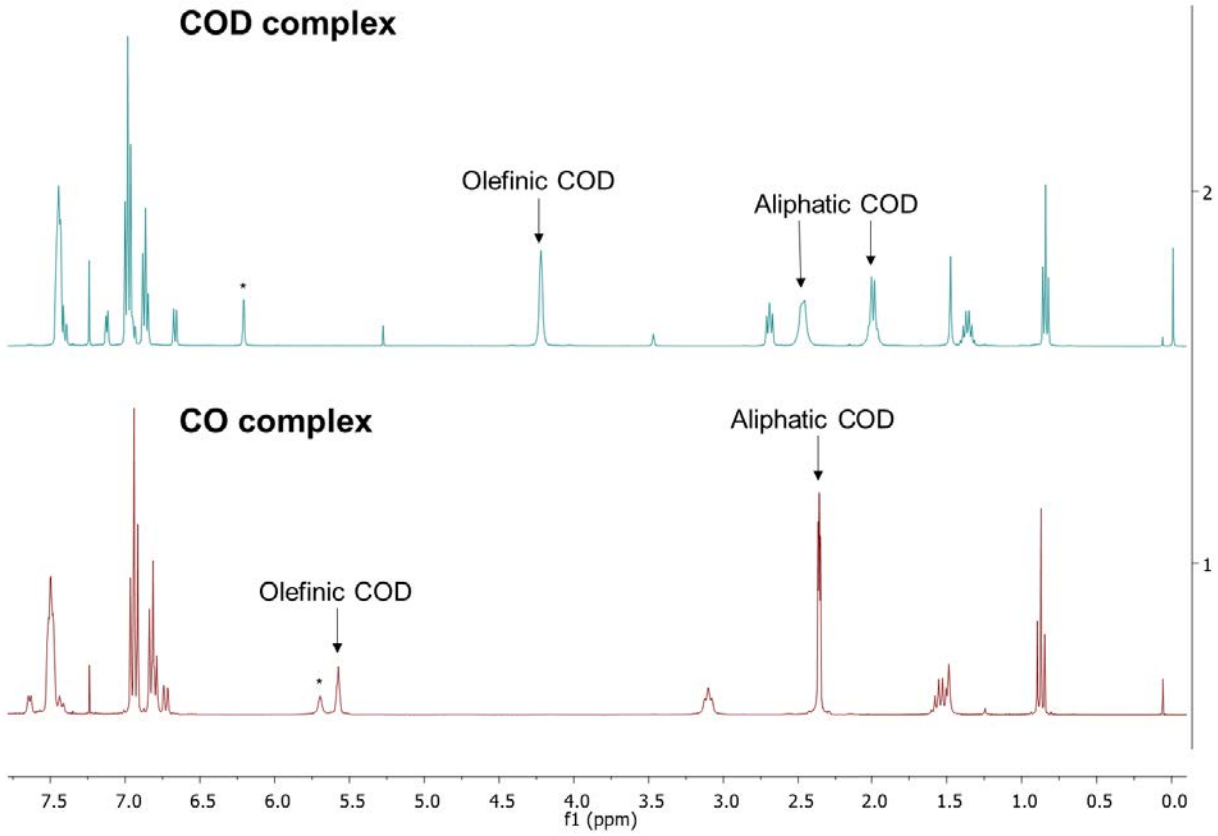

Figure 5.19 ^{1}H NMR of C2.3 (top) and C2.3 after reaction with CO (bottom). Note the changes in COD proton peaks. Imine proton marked by *.

We also see some small shifts as various other protons are affected by the exchange. Notably, the imine proton (marked with a *) shifts from 6.21 ppm to 5.70 ppm. There is also a significant downfield shift of the pyridine proton resonance at in **C2.3** to in the carbonyl complex, while the other pyridine proton resonances only show slight shifts. This proton has unambiguously been assigned as the proton *ortho* to the pyridine nitrogen. This is expected to be the most affected pyridine proton when the co-ligand COD is replaced by carbonyl ligands bound to rhodium.

We were able to isolate red needle-shaped crystals from the chloroform-*d* solution after the solution was left at low temperature. These crystals were air-sensitive and decomposed on prolonged exposure to air. The crystals were analyzed by single crystal X-ray diffraction and the asymmetric unit is shown in Figure 5.20, showing this complex to indeed be the dicarbonyl analogue of **C2.3**.

The geometry around the metal centre is distorted square planar, with both the N-Rh-C angles being larger than the N-Rh-N and C-Rh-C angles. Only small differences are observed in the N-Rh bond lengths. The geometry around the boron atom of the counter-ion is tetrahedral as expected.

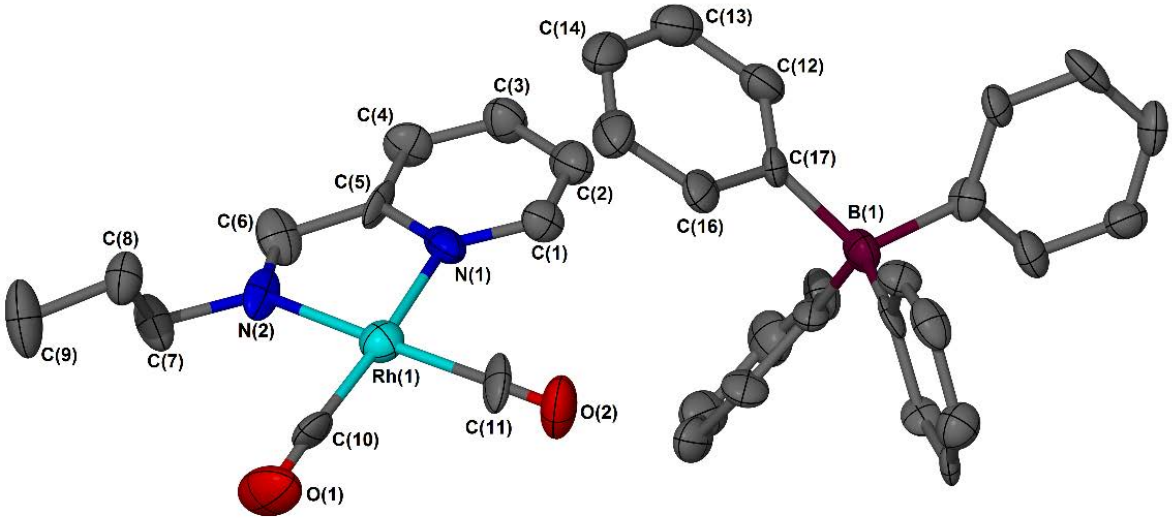

Figure 5.20 Crystal structure of C2.3 with CO ligands.

Table 5.7 Selected bond lengths and angles for the molecular structure of complex C2.3 with CO ligands

Atoms	Interatomic Distances (Å)	Angles (°)
Rh(1) – N(1)	2.092(16)	-
Rh(1) – N(2)	2.063(17)	-
Rh(1) – C(10)	1.83(3)	-
Rh(1) – C(11)	1.91(2)	-
C(10) – O(1)	1.16(3)	-
C(11) – O(2)	1.08(3)	-
N(1) – Rh(1) – C(11)	-	100.7(9)
C(11) – Rh(1) – C(10)	-	86.0(10)
C(10) – Rh(1) – N(2)	-	94.9(9)
N(2) – Rh(1) – N(1)	-	78.4(8)

5.2.7.2 Formation of the rhodium hydride

Based on the proposed mechanism for hydroformylation, we would expect after the formation of the rhodium carbonyl species, the formation of a metal hydride which is the active catalyst in the hydroformylation reaction. We therefore set out to spectroscopically identify this species using high-pressure NMR spectroscopy. From the available literature the ^{1}H NMR signal of a

rhodium hydride is expected to appear between -8 ppm and -12 ppm in the ^{1}H NMR spectrum.[11,19,20]

A high pressure sapphire NMR tube was used for these experiments. This type of tube is was first introduced by Roe in 1985 and allows for the recording of NMR spectra at pressures higher than atmospheric pressure.[21] The tube has a fairly simple design and is somewhat limited in that mixing is not automatically achieved as in a bubble tube.[20] It is however possible to shake or invert the tube to achieve the desired degree of mixing.

A known mass of catalyst was introduced into the tube in the presence of deuterated solvent. The tube was then flushed with 5 bar syngas and finally pressurized to 30 bar syngas. At this stage the tube was inverted in order to promote mixing of reactants. The reaction was heated at 80°C in an oil bath for 2 hours. NMR spectra were then recorded at 25°C and 75°C. The spectra were recorded over a wide spectral range (up to -30 ppm), in case the hydride appeared somewhere in this range.

Toluene-d_8 was used as solvent, since this is the solvent that is used in the hydroformylation reactions. Unfortunately, at the concentrations necessary for NMR spectra, the solubility of our complexes in toluene were poor and the peak intensities were quite low. An NMR spectrum of **C2.3** in toluene is shown below, with an inset showing a closer look at the area where hydrides are usually observed (Figure 5.21). No hydride peaks could be observed, which suggests that the rhodium hydride is possibly present in low abundance in the solution, or alternatively is extremely short-lived relative to the NMR time-scale. Dissolved molecular hydrogen can be seen at 4.52 ppm.

Next, we wanted to observe how the complex would react in the presence of syngas and substrate. Due to the low solubility of the complex in toluene, we decided to use chloroform-*d* in the place of toluene-d_8 for these NMR experiments. A small amount of 1-octene was added to the NMR tube after addition of the complex. We observed a similar colour change from red-purple to bright orange, as was seen for the experiments in Section 5.2.7.1 when carbon monoxide was bubbled through a chloroform-d solution of **C2.3**. This suggests that the COD ligand is displaced by carbon monoxide in the presence of syngas, as expected.

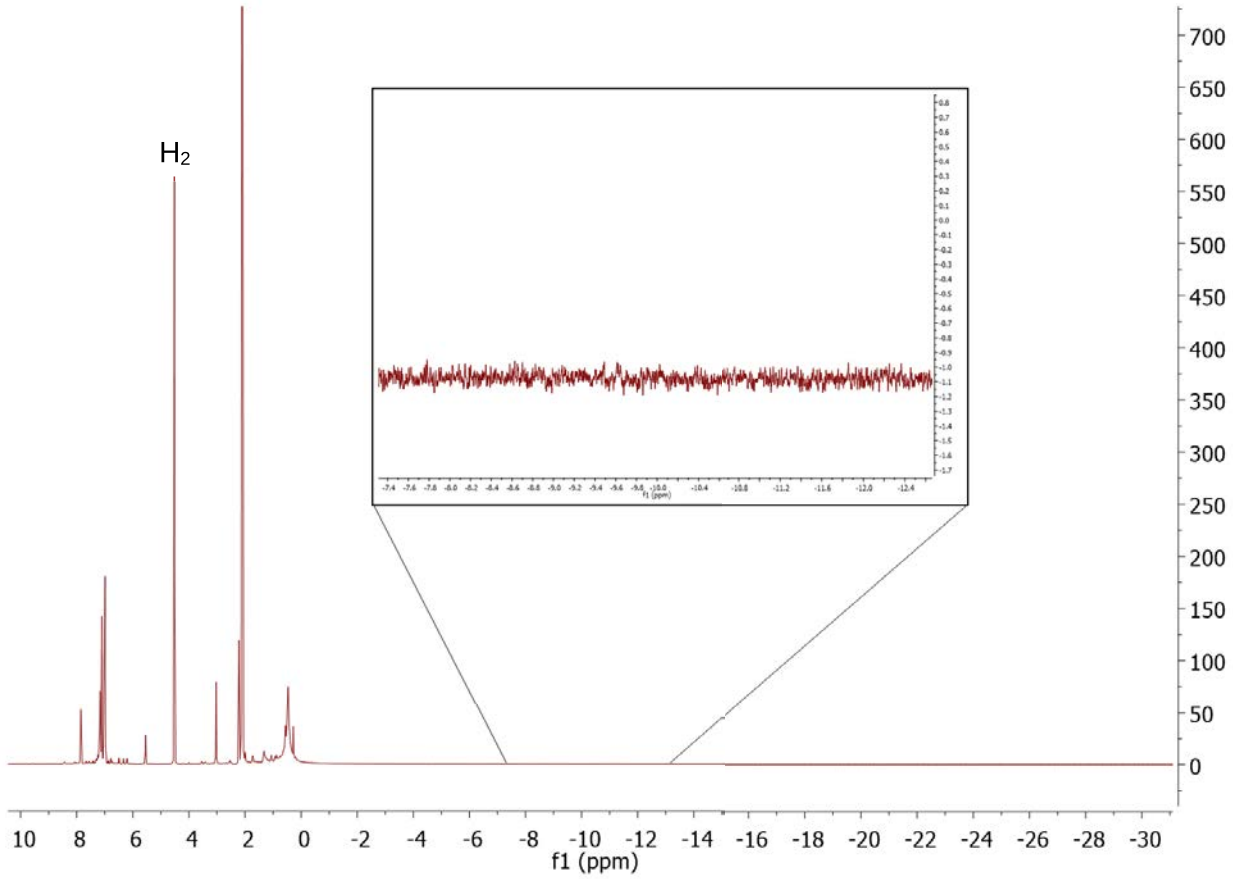

Figure 5.21 ^{1}H NMR spectrum of C2.3 in toluene-d_8 in the presence of 30 bar syngas.

The tube was inverted to improve mixing and subsequently heated at 55°C for 2 hours. As the boiling point of chloroform-d is 61°C, the sample could not be heated to the normal reaction temperature of 75°C usually employed for catalytic hydroformylation reaction. A ^{1}H NMR spectrum was initially recorded at 25°C. The sample was then heated to 55°C in the NMR instrument and spectra were recorded every 30 minutes over a 90 minute period.

Several changes could be observed in the NMR spectra over the time period. The full ^{1}H NMR spectra are depicted in Figure 5.22. The most important changes are the decrease in intensity of the olefinic protons in region 2 and the formation of new peaks in the aldehyde region (4). The regions numbered 1 – 4 in the image will each be discussed in detail below.

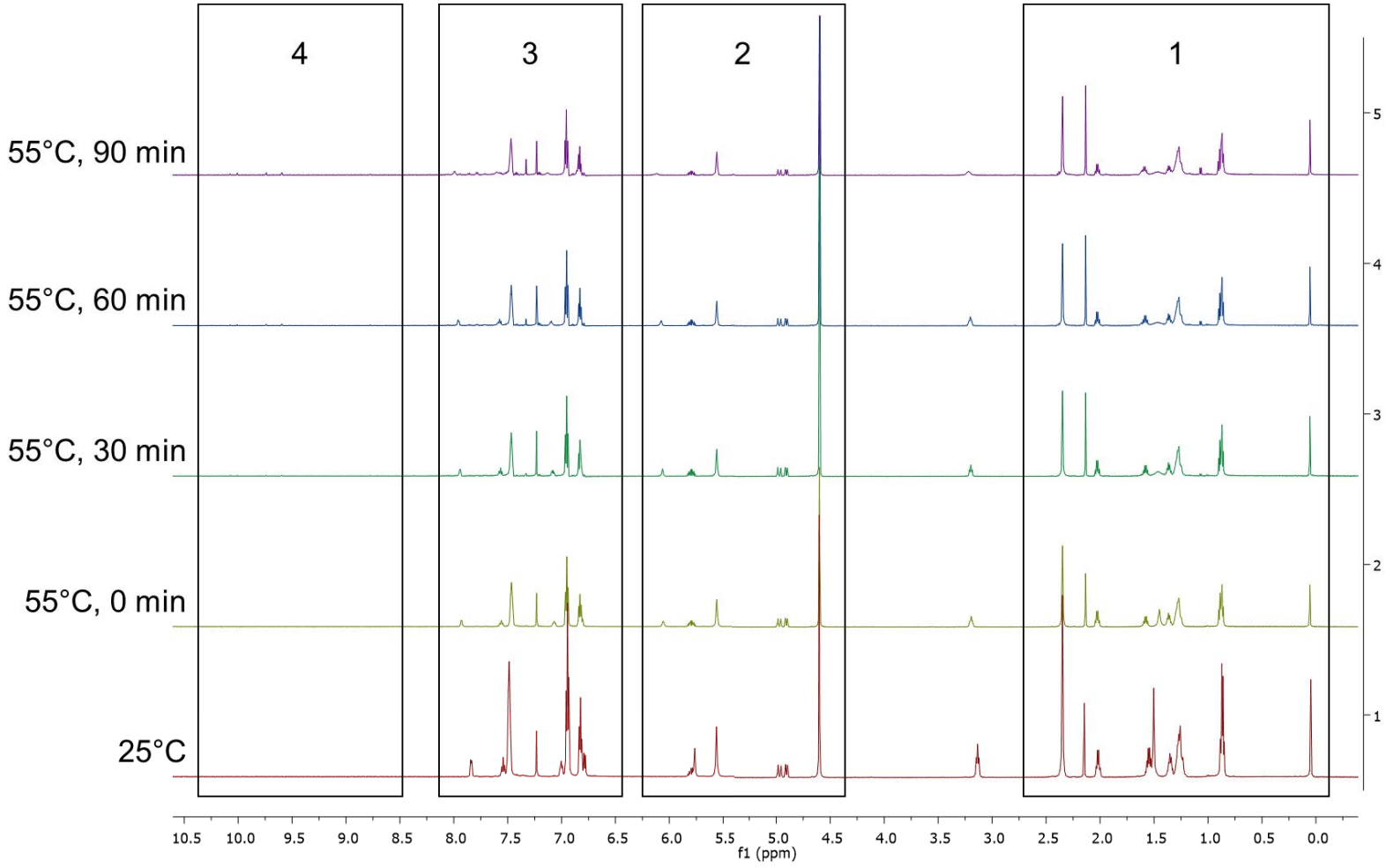

Figure 5.22 High-pressure ^{1}H NMR spectrum of C2.3 in the presence of 30 bar syngas and 1-octene. Areas in black boxes show significant changes and are expanded and discussed in the following pages.

Region 1. The aliphatic region (Figure 5.23) shows the presence of the substrate, 1-octene, with peaks due to its aliphatic hydrogen atoms appearing at 0.85 ppm, 1.25 ppm, 1.35 ppm and 2.25 ppm (indicated by the grey boxes). Water and acetone impurities are visible at 1.5 ppm and 2.17 ppm. The aliphatic protons of the free COD are also visible at 2.35 ppm, confirming that the COD ligand has been displaced.

Over time, a new small doublet, indicated in the red box, is formed at 1.05 ppm. The peak at 0.85 ppm shows a change in shape over the recorded time period.

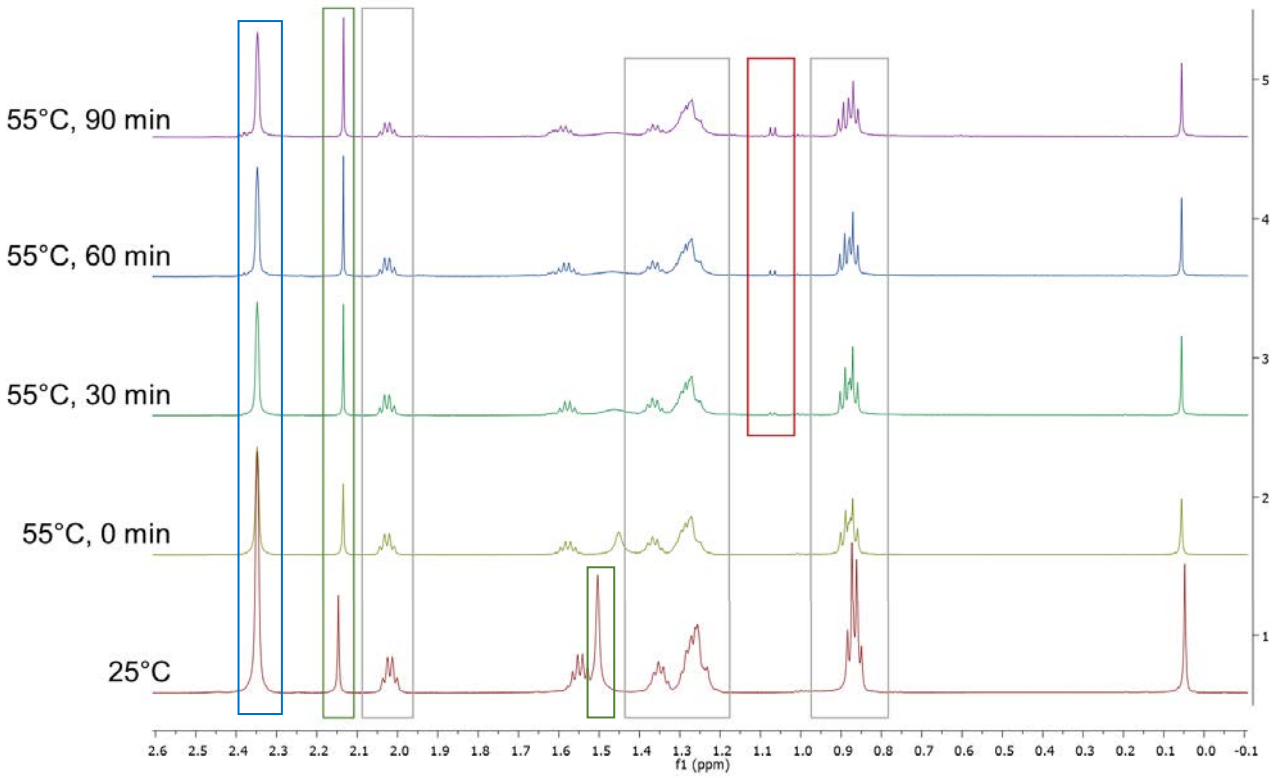

Figure 5.23 High-pressure ^{1}H NMR spectrum of C2.3 in the presence of 30 bar syngas and 1-octene (0 ppm – 2.6 ppm). Peaks due to aliphatic protons of 1-octene shown in grey. Water and acetone shown in green. Aliphatic COD protons shown in blue. New peak shown in red.

Region 2. The region between 4.2 ppm and 6.2 ppm shows the dissolved hydrogen as expected at 4.6 ppm in Figure 5.24 (indicated by the grey box). The resonance due to the imine is seen at 5.76 ppm at 25°C and is indicated with a blue arrow. This resonance shows a shift to 6.08 ppm after heating, and shifts slightly downfield over the recorded time period. The intensity of this resonance also decreases significantly over time. These changes indicate that the ligand does undergo change during the catalytic reaction.

The olefinic protons of the 1-octene substrate are seen between 5.0 and 4.85 ppm and are found in the red box in Figure 5.24. The intensity of these peaks decrease over time, as is expected with the substrate being consumed to form aldehydes.

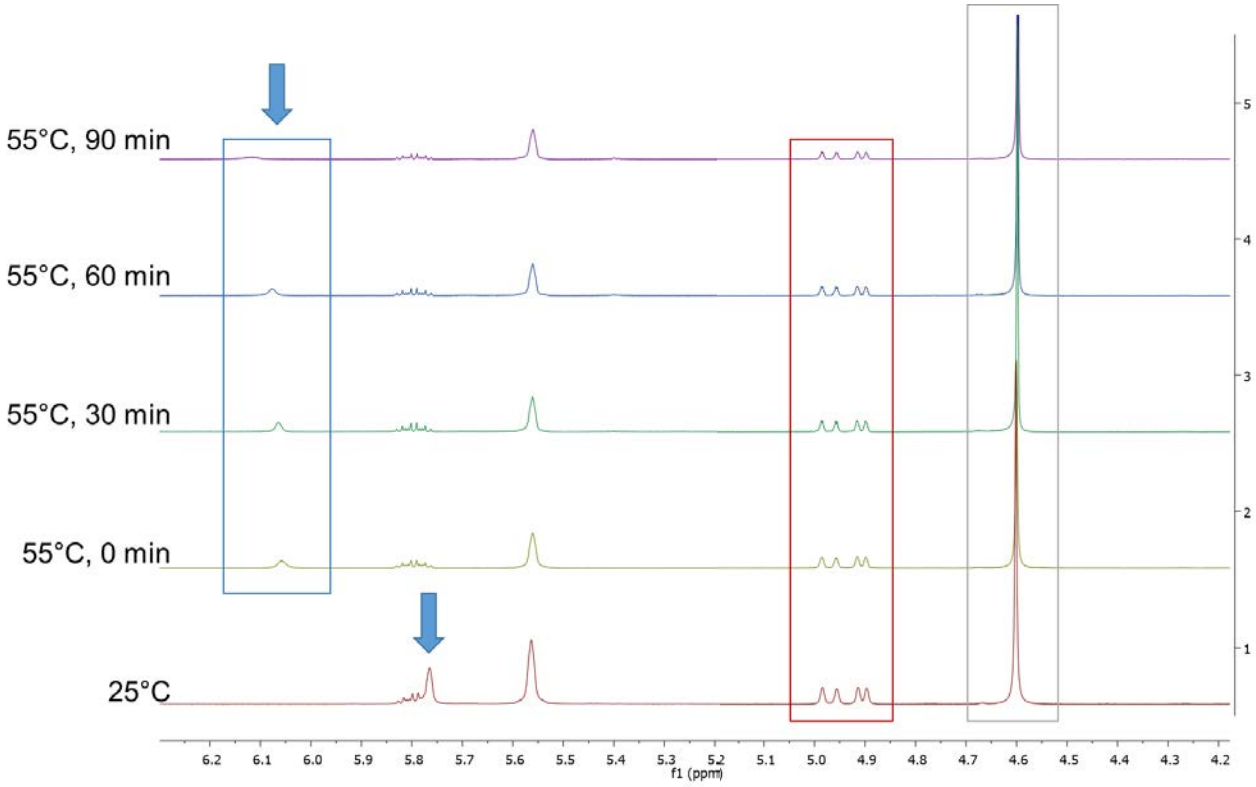

Figure 5.24 High-pressure ^{1}H NMR spectrum of C2.3 in the presence of 30 bar syngas and 1-octene (4.2 ppm – 6.2 ppm). Blue arrows indicate imine peak. Hydrogen shown in grey box. 1-octene olefinic protons shown in the red box.

Region 3. The aromatic region shown in Figure 5.25 contains the proton resonances of the pyridine ring as well as the tetraphenylborate counter-ion. The resonances due to the pyridine protons all show a gradual downfield shift over the recorded time period. The intensity of these signals also decrease over time.

The formation of a new peak at 7.33 ppm is observed as well. This is likely due to the formation of benzene resulting from the hydrolysis of the tetraphenylborate counter-ion with the residual hydrochloric acid often found in chloroform-*d*. It should be noted that the actual catalytic reactions were performed in toluene and we therefore do not expect this process to occur under these reaction conditions.

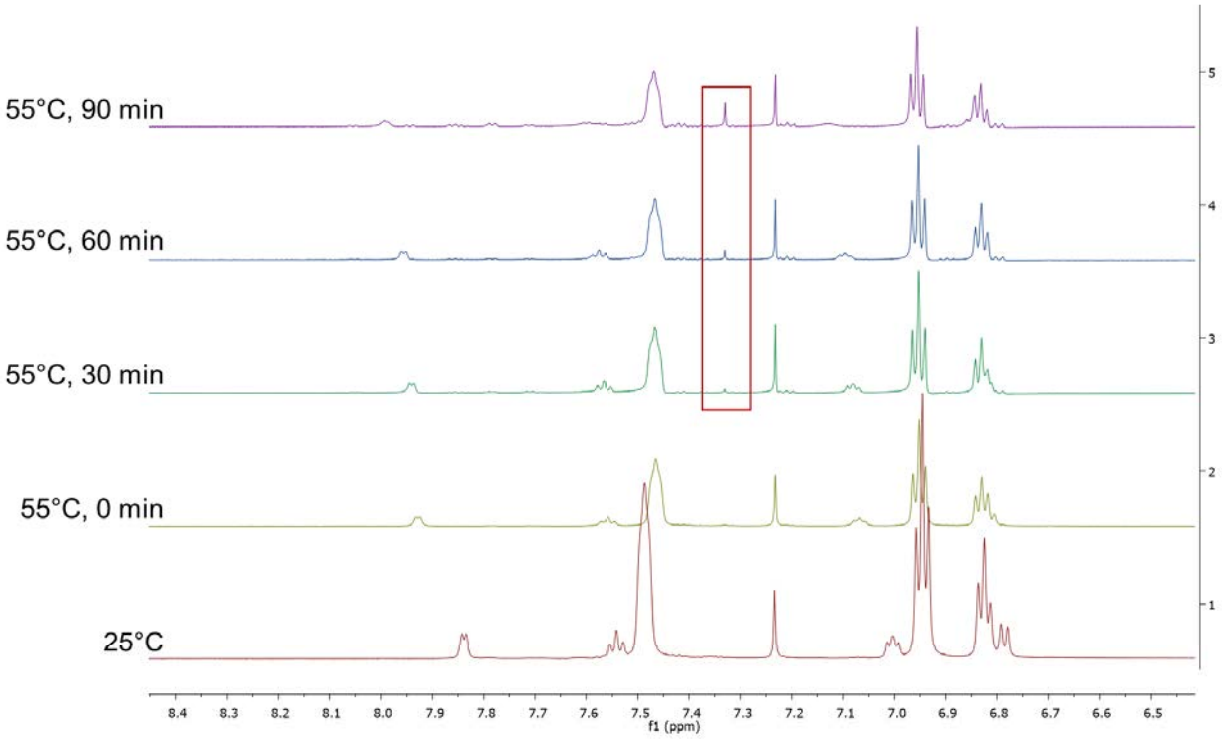

Figure 5.25 High-pressure ^{1}H NMR spectrum of C2.3 in the presence of 30 bar syngas and 1-octene (6.5 ppm – 8.4 ppm). New peak, likely due to hydrolysis of tetraphenylborate, shown in red box.

Region 4. The region downfield of 9 ppm initially shows no peaks (Figure 5.26). After 30 minutes at 55°C, four small peaks start to appear at 9.55 ppm, 9.70 ppm, 10 ppm and 10.10 ppm. The intensity of these peaks increase over the time period. The peaks appear at the same time as the doublet at 1.1 ppm (Figure 5.23). The newly formed peaks are found in the aldehyde region and may be indicative of the products, nonanal and branched aldehydes, forming as part of the hydroformylation process. The ^{1}H NMR spectrum of nonanal was recorded and it was found that the aldehyde proton signal appears at 9.66 ppm.

From the above observations it is clear that the rhodium precursor mediates the transformation of the 1-octene substrate to a mixture of aldehydes.

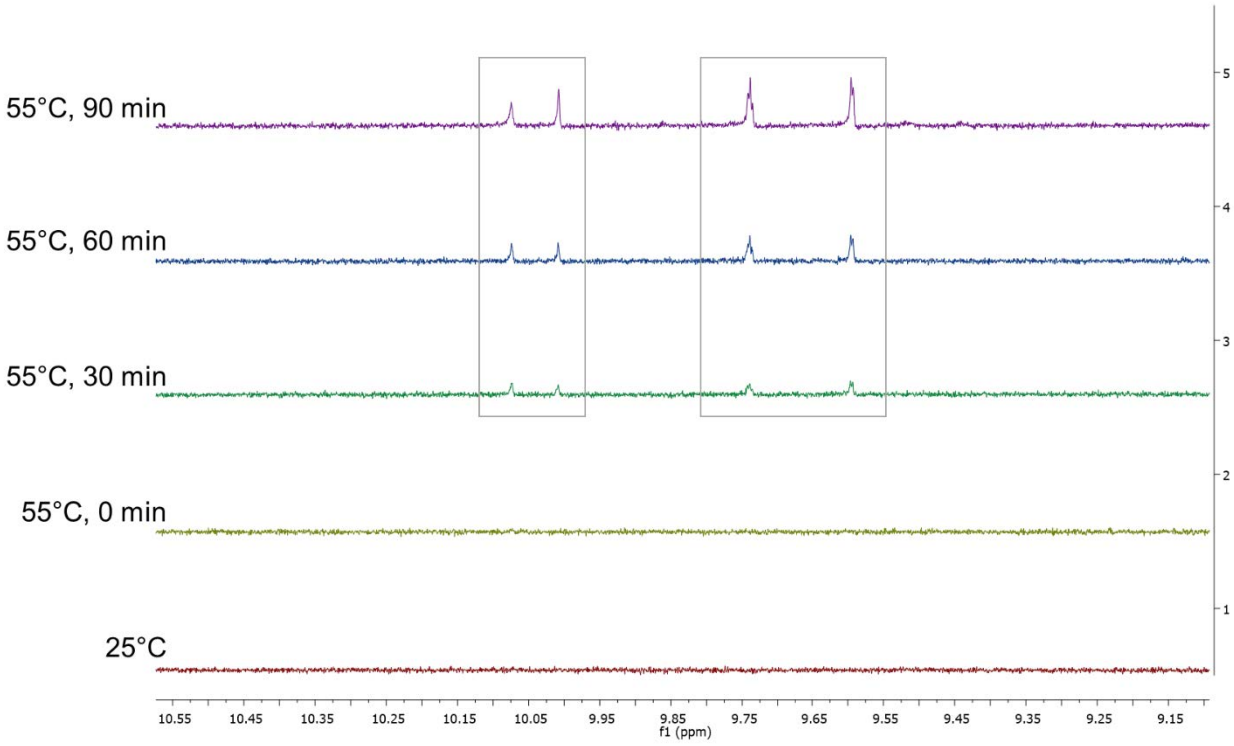

Figure 5.26 High-pressure ^{1}H NMR spectrum of C2.3 in the presence of 30 bar syngas and 1-octene (9.15 ppm – 10.55 ppm). New peaks due to aldehyde formation are shown in grey boxes.

5.3 Concluding remarks

In this chapter, five different pre-catalysts for rhodium-catalyzed hydroformylation of 1-octene were investigated. The complexes were generally not selective catalysts, forming a mixture of octane, isomerized octene species, nonanal, and branched aldehydes. The major products were isomerized octene species and nonanal for most of the complexes, while nonanal and 2-methyloctanal were the major products formed for complex **C2.9**. Reaction parameters such as time, temperature and pressure influenced the conversion of 1-octene, as well as the type

of products formed. An increase in reaction pressure from 30 bar to 40 bar lead to an increase in 1-octene conversion from 65% to 81%, with an accompanying increase in selectivity towards aldehydes from 49% to 60% and without any substantial decrease in *n:iso* ratio. In contrast, an increase in temperature lead to higher selectivity towards internal octenes as well as a decrease in the *n:iso* ratio. It is therefore recommended that, for these complexes, the hydroformylation reaction be carried out at 75°C in the presence of 40 bar syngas.

The cationic N,P complex, **C2.2** and the N,N triazole complex **C2.9** gave the highest conversion of 1-octene, with **C2.2** being quite selective towards aldehydes. The reason for the differences in conversion and selectivity of the complexes could not be conclusively established. It is proposed that alkene coordination may most likely be the rate-limiting step, which would explain the higher conversions of 1-octene obtained with the cationic complexes as these are more electron-deficient.

Ten immobilized catalysts were evaluated. The turnover numbers obtained using these immobilized catalysts was found to be generally higher than that of their analogues homogeneous complexes. This could possibly be due to fewer inactive rhodium dimers being formed for the immobilized catalysts. Unfortunately, attempts at recycling were not entirely successful with the immobilized complexes exhibiting a significant drop in turnover number after only one re-use. ICP-OES analysis of the reaction mixture revealed that some of the rhodium had leached from the immobilized catalyst. It is possible that ligand dissociation could have occurred during the catalytic reaction resulting in free metal being released into solution. Any unbound metal species have been removed from the silica during isolation of the used catalyst. Another possibility is that there could have been some catalyst deactivation during the catalytic reaction.

Preliminary mechanistic investigations confirmed that the replacement of the 1,5-cyclooctadiene ligand with carbonyl ligands is a facile reaction. The formation of this species was confirmed by ^{1}H NMR spectroscopy and by the isolation of the dicarbonyl species. The structure of the latter was determined by single-crystal x-ray diffraction. Attempts to observe a rhodium hydride species using high pressure ^{1}H NMR were unsuccessful, leading to the conclusion that the hydride species has a short life-time. High pressure ^{1}H NMR experiments using catalyst precursor **C2.3**, syngas and 1-octene showed the formation of a number of aldehyde species over a two hour time period, with a concomitant decrease in substrate.

5.4 Experimental section

5.4.1 General remarks and instrumentation

Hydroformylation reactions were performed in a Celcius high pressure reactor using syngas (CO/H_2 ratio 1:1). ^1H spectra were recorded on a Varian Unity Inova instrument at 600 MHz for ^1H. High pressure ^1H spectra were recorded on the same instrument using a Roe sapphire NMR tube. Single X-ray diffraction intensity data were collected on a Bruker SMART Apex 2 diffractometer with a CCD area detector using graphite monochromated Mo-Kα radiation (λ = 0.71073 Å).[20] Data collection, reduction and refinement were performed using SMART and SAINT software.[21] Absorption corrections and other systematic errors were accounted for using SADABS.[22,23] All structures were solved by Direct Methods using SHELXS-97 and refined using SHELXL-97.[24] The program X-Seed was used as a graphical interface for the SHELX program.[25] All non-hydrogen atoms were refined anisotropically. High resolution molecular diagrams were produced using the program POV-Ray.[26] The reaction products were analyzed using a Varian 3900 Gas Chromatograph equipped with Cyclosil-B column with dimensions 30 m x 0.25 mm x 0.25 µm. Helium was used as carrier gas at a flowrate of 1.1 mL/min.

5.4.2 Materials and methods

Reagents were purchased from Sigma-Aldrich and used as received. Solvents were purchased from Sigma-Aldrich and Kimix Chemicals and were dried over alumina molecular sieves in Sigma Aldrich Innovative Technology solvent purifiers.

5.4.3 General catalytic procedure

5.4.3.1 Model catalysts

The relevant complex (0.0034 mmol) was dissolved in toluene (5 mL) in a 50 mL high-pressure reactor. 1-octene (5 mmol, 0.800 mL) was added to the solution. The reactor was sealed and the reaction was heated to the required temperature (usually 75°C) while stirring at 500 rotations per minute, after which it was pressurized with syngas (CO/H_2 ratio 1:1). The reaction was then left to proceed for the allotted time, after which it was cooled to room temperature. The reactor was depressurized and a sample was taken for analysis by GC-FID.

5.4.3.2 Immobilized catalysts

The relevant amount of immobilized catalyst (as determined by ICP-OES) was weighed off and placed into a 50 mL high-pressure reactor. Toluene (5 mL) and 1-octene (5 mmol, 0.800 mL) was then added. The reactor was sealed and the reaction was heated to 75°C while stirring at 500 rotations per minute. The reactor was then pressurized to 20 bar using (CO/H_2 ratio 1:1). The reaction was allowed to proceed for 2 hours and the reactor was then cooled

to room temperature and depressurized. The suspension containing the suspended immobilized catalyst was placed in a centrifuge tube, and was then centrifuged for 30 minutes at 4 000 revolutions per minute. With the silica settled in the bottom of the tube, a sample was taken from the mother liquor for analysis by GC-FID. The mother liquor was then decanted, and the silica was dried before re-use.

5.5 References

1 J. A. Osborn, G. Wilkinson and J. F. Young, *Chem. Comm.*, 1965, 17–17.

2 E. Zuidema, L. Escorihuela, T. Eichelsheim, J. J. Carbó, C. Bo, P. C. J. Kamer and P. W. N. M. Van Leeuwen, *Chem. - A Eur. J.*, 2008, **14**, 1843–1853.

3 J. K. MacDougall, M. C. Simpson, M. J. Green and D. J. Cole-Hamilton, *Dalton Trans.*, 1996, 1161–1172.

4 A. Buhling, P. C. J. Kamer, P. W. N. M. Van Leeuwen, K. Goubitz and J. Fraanje, 1997, **23**, 3027–3037.

5 M. Vilches-Herrera, L. Domke and A. Börner, *ACS Catal.*, 2014, **4**, 1706–1724.

6 R. Lazzaroni, R. Settambolo, G. Alagona and C. Ghio, 2010, **254**, 696–706.

7 N. C. Antonels, J. R. Moss and G. S. Smith, *J. Organomet. Chem.*, 2011, **696**, 2003–2007.

8 B. C. E. Makhubela, A. Jardine and G. S. Smith, *Green Chem.*, 2012, **14**, 338–347.

9 E. B. Hager, B. C. E. Makhubela and G. S. Smith, *Dalton Trans.*, 2012, **41**, 13927–13935.

10 B. C. E. Makhubela, A. M. Jardine, G. Westman and G. S. Smith, *Dalton Trans.*, 2012, **41**, 10715–10723.

11 P. C. J. Kamer, A. Van Rooy, G. C. Schoemaker and P. W. N. M. Van Leeuwen, *Coord. Chem. Rev.*, 2004, **248**, 2409–2424.

12 B. R. James, P. W. N. M. Van Leeuwen, S. D. Ittel, A. Nakamura, R. L. Richards and A. Yamamoto, *Rhodium Catalyzed Hydroformylation*, Kluwer Academic Publishers, 2002.

13 D. M. Heinekey and W. J. Oldham, *Chem. Rev.*, 1993, **93**, 913–926.

14 N. V Belkova, L. M. Epstein, O. A. Filippov and E. S. Shubina, *Chem. Rev.*, 2016, **116**, 8545–8587.

15 F. Marras, J. Wang, M.-O. Coppens and J. N. H. Reek, *Chem. Commun.*, 2010, **46**, 6587–6589.

16 H. Kotzé, *Immobilized Ru(II) Catalysts for Transfer Hydrogenation and Oxidative Alkene Cleavage Reactions*, Ph.D. Thesis, Stellenbosch University, 2015.

17 R. Lazzaroni, R. Settambolo, G. Alagona and C. Ghio, *J. Mol. Catal. A. Chem.*, 2012, **356**, 1–13.

18 C. Li, L. Chen, E. Widjaja and M. Garland, 2010, **155**, 261–265.

19 G. Ball, W. R. Cullen, M. D. Fryzuk, W. J. Henderson, B. R. James and K. S. MacFarlane, *Inorg. Chem.*, 1994, **33**, 1464–1468.

20 A. Torres, N. Molina Perez, G. Overend, N. Hodge, B. T. Heaton, J. A. Iggo, J. Satherley, R. Whyman, G. R. Eastham and D. Gobby, *ACS Catal.*, 2012, **2**, 2281–2289.

21 D. C. Roe, *J. Magn. Reson.*, 1985**, 63**, 388–391.

22 Apex2, *Data Collect. software*, Bruker AXS, 2010.

23 SAINT, *Data Reduct. software*, Bruker AXS, 2003.

24 R. H. Blessing, *Acta Crystallogr. A.*, 1995, **51**, 33–38.

25 SADABS, *Version 2.05*, Bruker AXS, 2002.

26 G. M. Sheldrick, *Acta Crystallogr. Sect. A Found. Crystallogr.*, 2007, **64**, 112–122.

27 L. J. Barbour, *J. Supramol. Chem.*, 2001, **1**, 189–191.

28 POV-Ray, *Version 3.6*, Williamstown, Australia, Persistence of vision ray

CHAPTER 6 : CONCLUDING REMARKS AND FUTURE PROSPECTS

6.1 Concluding remarks

In Chapter 1 of this thesis, four aims for the thesis were listed. This chapter will evaluate to what extent these aims were achieved successfully.

Aim 1: To synthesize a range of ligands with N,P, N,N and N,O donor atoms, with some of these incorporating a siloxane tether and to use these ligands to synthesize both neutral and cationic rhodium complexes.

One class of ligands featured Schiff base ligands that varied in terms of the chelating atoms on the ligand. The siloxane functionality was incorporated in a fairly conventional way by using 3-aminopropyltriethoxysilane as amine in the Schiff base condensation reactions. A less common approach was also followed, where 'click' chemistry was used to synthesize a pyridyl-triazole ligand *via* microwave-assisted azide-alkyne Huisgen cycloaddition. In this case the siloxane functionality was situated on the nitrogen **1** of the triazole ring. The siloxane functionalized ligands were not stable in air for long periods of time, but were reasonably stable when stored in a nitrogen-purged glovebox.

Both neutral and cationic complexes were synthesized by reacting the obtained ligands with rhodium precursors $[RhCl(CO)_2]_2$ or $[RhCl(COD)]_2$. A microwave-assisted method for the synthesis of $[RhCl(COD)]_2$ was developed. By using this method, the reaction time could be decreased to 5 minutes, and the yield was increased from around 60% to roughly 70%. In the synthesis of the cationic complexes the chloride counter-ion was exchanged with a tetraphenylborate ion, resulting in a more stable salt thus facilitating the isolation of the complexes.

An attempt was made to expand the ligand series by synthesizing a triazole compound that incorporated both an aldehyde and a siloxane functionality. It was envisioned that this compound could be reacted with various amines (varied in terms of steric and electronic properties) to produce a series of N,N ligands, which could then be reacted with $[RhCl(COD)]_2$ to form cationic complexes. To this end, propargyl alcohol was reacted with

3-azidotriethoxysilane in the presence of a copper catalyst to yield the alcohol-functionalized triazole compound. Various attempts were made to oxidize the alcohol functionality to an aldehyde, but unfortunately only low amounts of the target aldehyde product could be obtained and attempts to increase the aldehyde yield lead to extensive hydrolysis of the siloxane functionality. After unsuccessfully attempting several different protocols to perform the oxidation of the alcohol, this initiative was finally abandoned.

During the characterization of the complexes prepared as part of this thesis by ^{1}H NMR, two interesting phenomena were observed, both involving the Schiff base imine complex **C2.3** and the pyridyl-triazole complexes **C2.9**. Firstly, a rather large upfield shift in the signal of the imine and the triazole protons were observed after complexation of both ligands to the rhodium precursor. An initial search of the available literature yielded only one case where something similar was reported, but unfortunately the authors never discussed this in any detail. A closer examination of the literature revealed that NMR spectra of these types of cationic complexes were usually reported in acetone or DMSO, whereas our complexes, as well as the other case found in the literature where a large shift was observed, were recorded in chloroform. This realization prompted us to investigate the NMR behaviour of **C2.3** in acetone. In addition we also synthesized analogous cationic complexes with different counter-ions, as we speculated that the aromatic rings of the tetraphenylborate counter-ion was having a shielding effect on the imine and some of the pyridine protons. NOESY and DOSY experiments were conducted to investigate possible ion-pairing between the constituent ions of the complex with the hope of explaining why the unusual NMR behaviour was observed in chloroform and not in acetone. These experiments indeed confirmed our suspicions.

The second observation made when investigating the NMR behaviour was a rather large difference in the shape of the olefinic proton signals of the 1,5-cyclooctadiene ligand in the ^{1}H NMR spectra of **C2.3** and **C2.9**. For **C2.3**, the signal was in the shape of a single peak, while two very broad, flat peaks were observed for **C2.9**. This was ascribed to dynamic behaviour of the complexes in solution, and variable temperature ^{1}H NMR was used to confirm that indeed we were dealing with a dynamic system. The variable temperature NMR data enabled us to use an Eyring plot to determine the energy involved during the dynamic process. Computational methods were used to look at the interconversion of the 1,5-cyclooctadiene ligand from one twist-boat conformation to another, but it was determined that this interconversion would be too fast to observed on the NMR timescale. The dynamic behaviour observed was tentatively attributed to the breaking of a N-Rh bond, followed by rotation of the ligand about this bond, and then re-forming of the bond. This type of process has previously been invoked in the literature to explain the type of changes observed in the ^{1}H NMR spectra.[1]

The first aim was thus successfully achieved, although the number of complexes synthesized in the end were rather limited, and a synthetic methodology which could lead to a larger library of rhodium complexes was not found. In addition to synthesizing and characterizing the complexes, some unusual ^{1}H NMR behaviour of the complexes in solution was investigated using some advanced NMR techniques.

Aim 2: To immobilize the siloxane functionalized complexes onto mesoporous silica and characterize these immobilized catalyst systems.

The mesoporous silica supports, MCM-41 and SBA-15, were synthesized according to literature procedures.[2,3] The complexes were immobilized by refluxing them with a slurry of the silica in toluene. Some of the siloxane functionalized complexes were insoluble in toluene, and therefore had to be solubilized in THF or chloroform before addition to the silica slurry. The immobilized complexes were obtained as yellow powders. A range of solid state analytical techniques were used in order to characterize the native silica supports as well as the immobilized catalysts. FT-IR and ^{29}Si solid-state NMR spectroscopy gave insight into the chemical structure of the silica supports, although the solid-state NMR technique was not sensitive enough to enable us to make definite conclusions regarding the MCM-41 immobilized catalyst analysed. Powder XRD showed that the structural integrity and degree of crystallinity of the supports were maintained after immobilization of the functionalized complexes. BET surface analysis indicated that there was a decrease in surface area after immobilization of the complexes, and was also a valuable tool in determining the sizes of the pores in the two different silica supports. SEM and TEM were used to monitor the morphology of the supports and by using these methods it was confirmed that the morphology remained unchanged after immobilization. ICP-OES was employed to determine the metal content on the supports. This was crucial to know, in order to be able to directly compare the model and immobilized complexes in terms of rhodium loading. However, due to the method used for digesting the rhodium-containing silica, it is suspected that not all the rhodium was extracted into solution, possibly leading to lower than expected rhodium values.

As part of this aim we successfully prepared and characterized the targeted silica supports. Immobilization of the rhodium complexes was also achieved. Some of the techniques used to characterize the immobilized catalyst systems, namely the ICP-OES and solid-state ^{29}Si NMR, did not give us as definitive results as expected, and more thought could have gone into the application of these techniques.

Aim 3: To apply the catalysts in the hydroformylation of 1-octene and compare the activity and selectivity of the different catalyst systems.

The complexes were evaluated in the hydroformylation of 1-octene. Initially, complex **C2.3** was used to evaluate a range of reaction conditions in order to establish optimized conditions in terms of 1-octene conversion and both chemo- and regioselectivity. At short reaction times (1 to 2 hours), olefin isomerization predominated. Over time, the internal octenes were hydroformylated to produce branched aldehydes. The amount of linear aldehydes formed showed a slight increase over a period of eight hours. When the different model complexes were evaluated as pre-catalysts, it was observed that the cationic complexes **C2.2** and **C2.9** showed the highest conversion of 1-octene. **C2.2** was quite selective towards the formation of aldehydes, however a low *n:iso* ratio was observed. The pyridyl-triazole complex **C2.9** exhibited a high selectivity towards the formation of internal octenes over a two hour period, with a higher *n:iso* ratio. It is likely that, over a longer time period, the hydroformylation of the internal octenes would dominate.

The heterogenized catalysts were generally more active in the hydroformylation of 1-octene than their homogeneous counterparts. This could possibly be ascribed to deactivation of the homogeneous catalyst as a result of active site agglomeration. This is often a problem for homogeneous catalysts in solution. Catalyst deactivation could be retarded in the case of the heterogenized catalysts as the silica support could serve to isolate active metal centres. For the immobilized complexes **IC4.5** – **IC 4.7**, **IC4.9** and **IC4.10** a change in selectivity was observed when compared to the homogeneous analogues, indicating either a change in catalyst structure during immobilization, or an influence of the silica support during catalysts.

The third aim was achieved in that the different catalyst systems were compared with each other.

Aim 4: To attempt the recycling of the immobilized catalysts in order to determine to what extent they could be re-used in the hydroformylation reaction.

Unfortunately, these immobilized catalysts showed reduced activity after recycling, with the activity being roughly halved in some cases. Rhodium leaching was suspected after observing discolouration of the reaction mother liquor. In addition, the presence of rhodium in the filtrate after recovering the immobilized catalysts was confirmed by means of ICP-OES. It is suspected that, during the catalytic cycle, the rhodium metal dissociates from the ligand system, and that some of this rhodium is lost into the solution phase. Furthermore, the rhodium

remaining on the support may form inactive rhodium dimers during the first reaction cycle, leading to a loss in activity after recycling.

Some preliminary mechanistic investigations were carried out in an attempt to gain insight into the hydroformylation mechanism in the presence of these N,N ligands. It was shown that the 1,5-cyclooctadiene ligand is very easily replaced by two carbonyl ligands. This was confirmed by ^{1}H NMR as well as single crystal XRD. An attempt was made to detect a rhodium hydride complex, the proposed active species, by using high pressure ^{1}H NMR spectroscopy, but this species was not observed. It is therefore likely that this species has a short life-time under the conditions investigated. The complex **C2.3** was also subjected to high syngas pressure in the presence of 1-octene in a high pressure NMR tube, and ^{1}H NMR spectra was recorded over a time period of 2 hours. A decrease in the olefinic proton signal intensities with the concomitant formation of new peaks in the aldehyde region was observed over time. This confirmed the formation of hydroformylation products.

The experiments needed to achieve the fourth aim were carried out, however the results were disappointing. It is clear that the catalyst systems discussed in this thesis are not suitable for recycling. It may be that phosphine or phosphite ligand systems are more suited to this type of recycling and recovery due to the fact that rhodium coordinates more strongly to phosphorous donor atoms than to nitrogen donor atoms. Another possible parameter to investigate could be the number of free ligands bound to the silica – increasing the ratio of ligands to metal could conceivably increase retention of the metal.

6.2 Future prospects

A few questions arose during this project, which could possibly be explored more fully in the future.

In terms of elaborating the scope of ligands, formyl derivatives of triazole compounds should be investigated. Attempts at one such ligand *via* the oxidation of triazole alcohols were not successful. The oxidation of the siloxane functionalized triazole alcohol could possibly be achieved by making use of a catalytic oxidation procedure. The use of the 2,2,6,6-tetramethylpipyridyl-oxyl radical (TEMPO) could be investigated, as it has been shown to effectively oxidize alcohols to aldehydes under mild conditions.[4]

Cation-anion interactions of metal complexes can be studied in solid state by means of crystallography. A study of the crystal structures of complexes **C2.3, C3.1** and **C3.2**, and subsequent comparison of the solution-state and solid-state interactions may leads to new insights regarding the interactions. We are however aware that more often than not, direct correlation between solid-state and solution does not hold.

The exact cause of the dynamic behaviour in complexes **C2.3** and **C2.9** could be investigated by computational means. It would also be interesting to synthesize a number of other N,N bidentate ligands with varying steric and electronic properties and investigate whether the complexes of these ligands display similar behaviour.

Due to time constraints, it was only possible to do some preliminary mechanistic investigations on the N,N complexes. More work is needed to establish exactly what happens to these complexes during the hydroformylation reactions – there is for example the possibility of hydrogenation of the imine functionality to an amine. Results from such experiments could also possibly help to shed light on the route by which the rhodium metal is leached from the silica supports, and possibly give insight into which types of ligands to use to prevent metal leaching.

6.3 References

1 M. Valentini, K. Selvakumar, M. Wo and P. S. Pregosin, *J. Organomet. Chem.*, 1999, **587**, 244–251.

2 J. S. Beck, J. C. Vartuli, W. J. Roth, M. E. Leonowicz, C. T. Kresge, K. D. Schmitt, C. T.-W. Chu, D. H. Olson, E. W. Sheppard, S. B. McCullen, J. B. Higgins and J. L. Schlenkert, *J. Am. Chem. Soc.*, 1992, **114**, 10834–10843.

3 D. Zhao, J. Feng, Q. Huo, N. Melosh, G. Fredrickson, B. Chmelka and G. Stucky, *Science.*, 1998, **279**, 548–52.

4 P. Gamez, I. W. C. E. Arends and R. A. Sheldon, *Chem. Comm.*, 2003, 2414–2415.